Response of high resolution silicon photodetectors coupled to CsI(Tl) or $LaBr_3$(Ce)

DISSERTATION
zur Erlangung des Grades eines Doktors
der Naturwissenschaften

vorgelegt von
Dipl.-Phys. Dieter Michael Schlosser

eingereicht bei der Naturwissenschaftlich-Technischen Fakultät
der Universität Siegen
Siegen 2014

Gutachter der Dissertation:
Prof. Dr. Lothar Strüder
Prof. Dr. Ullrich Pietsch

Datum der mündlichen Prüfung:
8. Juli 2014

Gedruckt auf alterungsbeständigem holz- und säurefreiem Papier.

Zusammenfassung

Das Ziel der vorliegenden Arbeit ist es, die Detektorantwort und die zugrundeliegenden Prozesse eines Röntgen- und γ-Detektors, bestehend aus einer SDD (Silizium Drift Detektor) Zelle gekoppelt an einen CsI(Tl) bzw. einen $LaBr_3$(Ce) Szintillator und einem SDD Array bzw. einem pnCCD (pn Charged Coupled Device) gekoppelt an einen CsI(Tl) Szintillator zu analysieren, um die Grenzen und Verbesserungsmöglichkeiten für Spektroskopie - und Bildgebungsanwendungen aufzuzeigen.

Für das System SDD / pnCCD + Szintillator fehlt bisher eine Systembeschreibung, die die relevanten Beiträge zur Energie- und Ortsauflösung auflistet und deren Werte angibt. Ergebnisse aus Berechnungen und Simulationen deuten darauf hin, dass für den einzelligen SDD + Scintillator der Hauptbeitrag zur Energieauflösung von der nicht proportionalen Bildung von Szintillationsphotonen in Abhängigkeit zur deponierten Energiedichte herrührt. Die Inhomogenität und die Effizienz der Licht- und Ladungssammlung erzeugen nach Ergebnissen aus Simulationen für die gewählten Detektorparameter nur einen kleinen Beitrag zur Energieauflösung, falls ein CsI(Tl) Szintillator verwendet wird. Diese und die restlichen Beiträge werden für γ-Energien in dem Bereich 6 keV - 662 keV presentiert.

γ-Kameras bestehend aus einem SDD array mit 77 hexagonalen Zellen mit einer Fläche von 8.7 mm^2 pro Zelle, gekoppelt an einen 5 mm dicken CsI(Tl) Szintillator wurden in Bezug auf ihre Orts- und Energieauflösung für γ-Photonen mit Energien von 60 keV und 122 keV untersucht. Diese Kameras wurden für potentielle Anwendungen im medizinischen Bereich wie zum Beispiel die Emissionstomographie bei Kleintieren entwickelt. Die intrinsische Ortsauflösung erreicht Werte von 1.1 mm (60 keV) und 0.5 mm (122 keV) und eine relative Energieauflösung von ca. 0.37. Ergebnisse aus Simulationen reproduzieren die Messwerte und deuten darauf hin, dass die Hauptbeiträge zur Energieauflösung durch den geringen Abstand des Signals zum Schwellenwert der Datenerfassung und durch die Abhängigkeit der Signalhöhe von der Erzeugungstiefe der Szintillationsphotonen im Szintillator bestimmt werden. Die Simulationen zeigen, dass eine Reduzierung der Szintillatordicke und insbesondere des elektronischen Rauschens, was auch eine Verringerung des derzeitigen Schwellenwertes der Datenerfassung ermöglicht, die Energie und Ortsauflösung verbessern.

Die Kombination eines pnCCDs mit einer Pixelgröße von 75 x 300 μm^2 bzw. 300 x 300 μm^2 gekoppelt an einen 0.7 mm bzw. 1 mm dicken CsI(Tl) Szintillator als γ-Detektor für den Energiebereich von 1 keV - 150 keV wurde mittels Simulationen untersucht, um dessen Eignung als Detektor mit einer ausreichenden Energie und Ortsauflösung für Strukturanalysen an Materialien mit Hilfe von Röntgenbeugung zu prüfen. Die Quanteneffizienz von pnCCDs, die zu Energien größer als 10 keV exponentiell abnimmt, wird durch die Ankopplung eines Szintillators an den pnCCD wieder vergrößert. Das gekoppelte System wird von der pnCCD Seite her bestrahlt, um weiterhin die sehr gute Energie und Ortsauflösung des pnCCDs bei niedrigeren Energien auszunutzen. Höherenergetische Photonen durchdringen den pnCCD und generieren im Szintillator Photonen. Die Ergebnisse aus den Simulationen deuten darauf hin, dass der Detektor, bestehend aus pnCCD + CsI(Tl), bei passender Wahl der Detektorparameter geeignet ist, Röntgenbeugungsmuster in ausreichender Energie- und Ortsauflösung im Energiebereich von 1 keV - 150 keV darzustellen.

Abstract

The intention of this work is to analyze the detector response and the participating processes of a X- and γ-ray detector consisting of a single Silicon Drift Detector (SDD) cell coupled to a CsI(Tl) or $LaBr_3$(Ce) scintillator and a SDD array or pn-Charged Coupled Device (pnCCD) coupled to a CsI(Tl) scintillator in order to define limitations of the detector performance and possibilities to improve it.

For the system, SDD / pnCCD + CsI(Tl) or $LaBr_3$(Ce) scintillator, the relevant contributions to the energy and spatial resolution are investigated and their values are determined from results of measurements, calculations and simulations, which have not been presented in literature yet.

Results indicate, that the main contribution to the energy resolution for a single SDD cell coupled to CsI(Tl) or $LaBr_3$(Ce) originates from the so called scintillator non-proportionality. Simulations show that the light and charge collection efficiency inside the system generate only a minor contribution to the energy resolution, if CsI(Tl) is used as scintillator. These and the remaining contributions are presented for incident γ-rays in the range from 6 keV to 662 keV.

A γ-camera consisting of a SDD array with 77 hexagonal cells and an active area of 29 x 26 mm^2, which is coupled to a 5 mm thick CsI(Tl) scintillator, has been investigated with respect to the spatial and energy resolution for γ-rays with an energy of 60 keV and 122 keV. These detectors have been developed for medical applications, e.g. emission tomography for small animals, with a sub millimeter spatial resolution in the energy range of interest. The spatial resolution reaches values of 1.1 mm for 60 keV and 0.5 mm for 122 keV photons. The relative energy resolution has a value of about 0.37. Results from simulation reproduce these results and indicate that the main contributions to the energy resolution originate from a high data acquisition threshold, due to the increased electronic noise and the dependence of the number of signal electrons on the generation depth of the scintillation photons inside the scintillator. A reduction of the scintillator thickness and especially the decrease of the electronic noise, which enables a lowering of the data acquisition threshold, improves the spatial and energy resolution.

The combination of a pnCCD with a pixel size of 75 x 300 μm^2 or 300 x 300 μm^2 and a CsI(Tl) scintillator of 0.7 mm or 1 mm thickness respectively were investigated by simulations for their suitability as a γ-camera in the energy range of 1 keV - 150 keV. In particular the application as a detector for X and γ-ray diffraction pattern analysis with sufficient spatial and energy resolution was of interest. By coupling a scintillator onto the pnCCD a higher quantum efficiency of the system is reached. The coupled system will be irradiated from the pnCCD side to utilize the good performance of the pnCCD in the low X-ray energy range up to several 10 keV. The pnCCD is almost transparent for hard X- and γ-ray photons, which generate scintillation photons inside the scintillator. Results from simulations indicate that the detector, pnCCD + CsI(Tl), is suitable to detect diffraction patterns in the energy range 1 keV - 150 keV, if detector parameters are chosen and set properly.

Contents

Glossary

E	energy
Z	atomic number
A	atomic weight
m	mass
ρ	density
Φ	cross section
μ	mass absorption coefficient
α, l=1/α	absorption coefficient, absorption length
dE/dx	energy loss per unit path length
I	mean excitation energy
$\overline{w}$	mean energy to create an electron hole pair
N_{eh}	number of electrons hole pairs
N_e	number of signal electrons
E_g	energy gap in semiconductors and insulators
E_{ph}	phonon energy
F	Fano factor
N_{ph}	number of photons
E_{Stokes}	energy of the Stokes Shift
H	Hyang-Rhys parameter
T_{emp}	temperature
T	transfer efficiency
FWHM	full width at half maximum
R	relative energy resolution
$\widetilde{R}$	spatial resolution
ENC_{el}	equivalent noise charge in units of electrons
n	refraction index
Var(X)	variance of X
v(X)	relative variance of X: Var(X)/X^2
σ	standard deviation
R_{efl}	reflectance
T_{ARC}, T_{ew}	transmittance through the entrance window
λ	wavelength
QE	quantum efficiency
CCE	charge collection efficiency
K	collection efficiency of scintillation photons
η	system quantum efficiency for scintillation photons
A_{sv}	absorption efficiency
C	conversion efficiency of E inside the scintillator into eh-pairs
G	conversion efficiency of E inside the SDD into eh-pairs
P	power
W	transition probability
t	time
t_S	shaping time

1. Introduction

The detection of hard X- and γ-rays is interesting in different fields such as astrophysics, medical applications, material science, monitoring the radiation in nuclear power plants and fusion plasmas or simply the detection of radioactive sources. Ionization chambers belong to the first detectors for radioactive radiation. The energy deposited by the radiation is detected directly inside the gas volume. These detectors can be defined as direct detectors. The first ionization chambers have been invented in 1908 by Rutherford and Geiger [1].

In the 1950s and 1960s a second type of direct detector, the solid-state detector with a higher stopping power than the gas chambers, emerged and have been steadily improved in the following decades [2]. Especially detectors consisting of silicon (Si) and germanium (Ge), which could be fabricated in a high purity have been produced for direct X- and γ-ray detection. Si-detectors can be used for direct X-ray detection up to 30 keV, because of its low atomic number, Z = 14, and density, $\rho = 2.33$ g/cm^3 [3]. The stopping power of Ge-detectors for X- and γ-radiation is higher compared to Si-detectors, due to its higher atomic number, Z = 32, and density $\rho = 5.32$ g/cm^3. Their disadvantage is the high leakage current at room temperature, hence the high electronic noise, because of the small band gap of 0.67 eV at 300 K [4]. To reduce the electronic noise to an acceptable value, the detector has to be cooled down to the temperature of liquid nitrogen. Other, larger band gap semiconductor materials like HgI_2, CdTe and CdZnTe, which have the potential of room temperature $\gamma-$ray semiconductor detectors have been investigated. Drawbacks of these materials are their poorer spectral resolution compared to Ge-detectors, due to charge trapping [5, 6, 7]. Furthermore, these materials are difficult to fabricate and to process.

After the invention of the photomultiplier tube (PMT) by Kubetsky in the year 1930 a different type of radiation detectors, consisting of a scintillator coupled to a PMT, appeared. In these detectors the energy of the γ-radiation is deposited inside the scintillator, where it is converted into scintillation photons (generally from the ultra violet, UV, and visible range, Vis), which are detected by a photodetector, which is sensitive to scintillation photons. This detector type can be defined as indirect detector and it is operated at moderate cooling temperatures compared to Ge-detectors. There are a number of scintillators with a higher stopping power compared to the materials of which room temperature $\gamma-$ray semiconductor detectors consist of.

The energies of Vis, UV, X- and $\gamma-$ray photons are illustrated in Fig. 1.1, which shows a part of the electromagnetic spectrum.

Scintillator + PMT detectors have been the first choice for γ-ray detectors until the 1990s. Their disadvantage is their high sensitivity to magnetic fields, so that they cannot be used in medical applications and in instruments for fundamental research, where magnetic fields are required. Furthermore the bias voltage is several kilo volts. Hybrid photon detectors (HPD) are an alternative for PMTs, but they

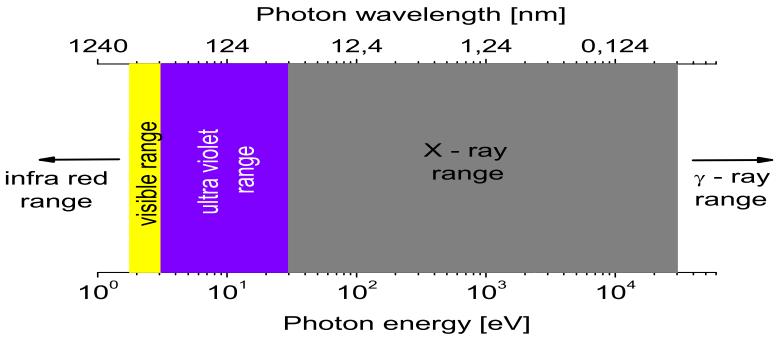

Figure 1.1.: *Part of the electromagnetic spectrum.*

have to struggle with the same disadvantages.

Photodiodes (PDs) have substituted the PMTs in several applications, due to a higher quantum efficiency, QE, and low sensitivity to magnetic fields. The detector performance can be improved with an avalanche photo diode (APD) as photodetector, because of a higher signal to electronic noise ratio than PDs, due to the internal gain. The disadvantages of APDs compared to PDs are the higher sensitivity to bias, temperature change and an additional contribution to the energy resolution originating from the internal gain. Another promising photodetector candidate is the silicon photomultiplier (SiPM). It has the potential to exceed the performance of the other photodetectors. (Compared to APDs, SiPMs are operated in Geiger mode, which reduces the contribution of the internal gain to the energy resolution). Yet some technological issues have to be solved. The high number of dark counts, the optical cross talk have to be reduced and the fill factor, which limits the quantum efficiency, has to be increased.

Advantages of a detector system consisting of a scintillator + silicon photodetector are on the one hand the possibilities to choose between a variety of scintillators with properties, i.e. the atomic number Z, density, range of the scintillation spectrum, shape and thickness of the scintillator, which fit best the overall detector and photodetector requirements. On the other hand the outstanding properties of approved and established silicon photodetectors can be maintained. Furthermore, these detectors are more compact compared to the detector systems, scintillator + PMTs.

The use of a silicon drift detector (SDD) as photodetector for scintillation photons has the following advantages: a lower electronic noise compared to PDs, a lower sensitivity to bias voltage and temperature change compared to APDs. Furthermore, there is no internal gain degrading the energy resolution. In addition the SDD capacitance does not depend on the detector area. The reason for these advantages results from the SDD working principle. There is also the possibility to design the SDD entrance window (EW), which consists of an antireflection coating (ARC) and which can be optimized to ensure a high quantum efficiency for scintillation photons of the used scintillators.

Silicon Drift Detectors, first presented in 1984 by Gatti et al. [8] for X-ray detection, are nowadays being used in a rising number of different applications. As

a result of the continuous improvements in the detector technology developed by PNSensor and Politecnico di Milano, SDDs are established as state-of-the-art detectors for energy dispersive X-ray (EDX) spectroscopy [9].

Detector systems consisting of SDDs with an ARC-Window in combination with scintillators, such as CsI(Tl) and $LaBr_3$(Ce), have also been developed by PNSensor GmbH and Politecnico di Milano. Theses detectors have been investigated for the first time as γ-ray detectors for spectroscopy and imaging in the years 1997 and 2000 [10, 11]. Spectroscopic investigations presented in [12] showed a superior energy resolution for gamma energies above 100 keV in comparison to photodiodes and photomultipliers (PMTs). The spatial resolution of the imaging γ-ray detectors consisting of SDD arrays coupled to CsI(Tl) belong to the best ever measured [13].

The aim of this work is to understand the X- and γ-ray detector system consisting of a SDD / pnCCD (pn Charged Coupled Device) coupled to a scintillator in order to determine limitations of the detector performance and to find possibilities to improve its energy and spatial resolution.

To achieve this goal, measurements have been performed with SDDs coupled to the scintillators, CsI(Tl) and $LaBr_3$(Ce), to determine the energy resolution, the number of detected signal electrons inside the SDD, the electronic noise, the quantum efficiency and the spatial resolution. Results from these experiments are then compared with results from calculations and Monte Carlo simulations. The calculated so called scintillator "non-proportionality" contribution of CsI(Tl) and $LaBr_3$(Ce) to the energy resolution for incident γ-rays in the energy range from 6 keV to 662 keV is presented for the first time in this work. Furthermore the contribution of the light and charge collection efficiency to the energy resolution in the system scintillator, reflector, entrance window for the scintillation light are determined. The detector response of SDD arrays and pnCCD pixel detectors coupled to CsI(Tl) has also been investigated.

The composition of this work is as follows: After the introduction in Chap. 1, in Chap. 2 basic information on the interaction of photons with the detector materials is given. The interaction process of X- and γ-ray photons in CsI and $LaBr_3$ crystals, the generation of scintillation photons in CsI(Tl) and $LaBr_3$(Ce) and the detection of photons from the near ultra-violet and visible range in a silicon are analyzed.

In Chap. 3 the concept and operation of a SDD and the principles of hard X- and γ-ray detection with a SDD in direct detection mode or a SDD coupled to a scintillator are depicted.

In Chap. 4 one of the basic equations of this thesis, the energy resolution formula in terms of the full width at half maximum FWHM(E) respectively R(E) = FWHM(E)/E is deduced for the case of a solid - state detector coupled to a scintillator, describing all relevant contributions to R(E).

The quantum efficiency of the SDD for X-rays and scintillation photons is discussed in Chap. 5. The energy dependence of the quantum efficiency, which is determined by the entrance window, is investigated for X-rays and photons from the near ultra-violet and visible range. The values of the quantum and charge collection efficiency are calculated. Also the angle dependent quantum efficiency is examined.

In Chap. 6 the results of the energy dependent light yield and energy resolution of spectroscopic measurements and simulations in the range from 6 to 662 keV are

discussed for the detector system consisting of a single SDD cell coupled to CsI(Tl) or $LaBr_3$(Ce). The relevant noise contributions are investigated and their values are determined. The contributions of the light and charge collection efficiency and the scintillator non-proportionality to the energy resolution of CsI(Tl) and $LaBr_3$(Ce) coupled to a single SDD are analyzed in detail.

In Chap. 7 detectors consisting of SDD arrays or pnCCDs coupled to one CsI(Tl) scintillator covering all cells are examined. Measurements and simulations of the spatial and energy resolution have been performed for a 77 cell SDD array with the dimensions 29 x 26 mm^2 and a hexagonal cell size of 8.7 mm^2 coupled to one 5 mm thick CsI(Tl) scintillator. The spatial resolutions for incident photons of 59.5 keV and 122 keV and the energy resolutions for 59.5 keV, 88 keV and 122 keV photons have been determined. A spatial resolution of 1.1 mm and 0.5 mm have been determined at 59.5 keV and 122 keV and an energy resolution of about 0.37. From Monte Carlo simulations the main contribution to the energy resolution are determined and possibilities to improve it are proposed.

Also a pixel detector consisting of a pnCCD coupled to CsI(Tl) has been investigated theoretically by simulations as a detector, which extends the energy range of the pnCCD X-ray camera into the hard X- and γ-ray range. The examined pnCCD has pixel sizes of 75 x 300 μm^2 and 300 x 300 μm^2 and the CsI(Tl) scintillator has a thickness of 0.7 mm or 1 mm. The dependency of the energy and spatial resolution on the pixel size, electronic noise, data acquisition threshold, scintillator light yield, scintillator thickness and the reflector are presented to define the best parameter values.

In Chap. 8 the results of this work are summarized and conclusions are drawn.

2. Physical background of solid state radiation detectors

2.1. Interaction of photons with matter

The main interaction processes of photons with matter are the photoelectric effect, Compton scattering and pair production. The photoeffect is dominant for photon energies, E, where the ratio E_{K-edge}/E cannot be neglected. E_{K-edge} is the binding energy of the K-shell electron. For energies $E >> E_{K-edge}$, where the binding energy of the K-shell electron is negligible to the incident photon energy and the electron can be regarded as quasi free, Compton scattering becomes the dominant process. Photons with $E > 2m_e c^2 = 1022$ keV, with m_e the electron mass and c the velocity of light, interact additionally via pair production, which is the process with the largest cross section for photon energies of several MeV.

In this thesis, we are examining the direct detection of X- and γ-rays with the SDD / pnCCD and the indirect detection with a detector consisting of a SDD / pnCCD coupled to a scintillator. In case of the direct detection, X- or γ-ray photons interact with the SDD / pnCCD via the processes described above, by depositing the full or a part of their energy inside the SDD / pnCCD, generating signal electrons. In case of the indirect detector, the X- or γ-ray photons deposit their energy inside the scintillator, generating electron hole pairs, which have a certain probability to recombine radiatively, producing scintillation photons, which are transferred with a certain efficiency into the SDD / pnCCD. Scintillators generally produce scintillation photon spectra in the near ultra violet (UV) and visible (Vis) energy range [14]. The scintillation photons generate electron hole pairs via photo effect inside the SDD / pnCCD. The generated and collected electrons are the signal charge carriers.

The difference between the photo effect triggered by X- and γ-ray or scintillation photons is that in the first case the electron is ejected from a core shell into the continuum with a certain distance to the ionized atom. Whereas in the second case the electron is excited from the valence into the conduction band.

In the following we investigate the material and energy dependence of the absorption coefficient for X-, γ-ray photons, due to the photo effect, Compton scattering and pair production in Si, CsI and $LaBr_3$. We also investigate the absorption coefficient of photons from the Vis and near UV range in Si. Furthermore the number of electron hole pairs produced by one photon is examined in the energy range 1.24-8.2 eV. In the X- and γ-ray range the mean energy to create one electron hole pair and the Fano factor are analyzed.

2.1.1. Interaction of X- and γ-rays with Si, CsI and $LaBr_3$

At first we turn our attention towards the cross sections of the photo effect, Compton scattering and pair production and calculate the absorption coefficient of X- and γ-rays in Si, CsI and $LaBr_3$.

The photoelectric effect occurs only to bound electrons, due to simultaneous energy and momentum conservation. The total photon energy is absorbed by the electron, which is ejected from the atom with the kinetic energy E_{kin} = E - E_b, with E the photon energy and E_b the electron binding energy.

For photon energies larger than the K-edge energy of the material, E >> E_K, but for non-relativistic energies, E << $m_e c^2$ = 511 keV, the photoelectric cross section of the K-shell per atom, Φ_p, can be expressed in the Born approximation by

$$\Phi_{p-K} = 4\sqrt{2}\widetilde{\alpha}^4 Z^5 \Phi_0 \left(\frac{m_e c^2}{E}\right)^{\frac{7}{2}} \tag{2.1}$$

where m_e is the electron mass, c the velocity of light, Z the atomic number, $\Phi_0 = 8\pi r_e^2/3$ = 6.651 x 10^{-25} cm^2, $\widetilde{\alpha}$ = 1/137 the fine structure constant and r_e the electron radius [15, 16]. The deviation of Eq. 2.1 is small for photon energies E < $0.5 m_e c^2$ = 255.5 keV [15]. For relativistic energies, E $\geq$ $m_e c^2$, Sauter [17] derived in the Born approximation the formula:

$$\Phi_{p-K,rel} = \\ \frac{3}{2}\widetilde{\alpha}^4 Z^5 \Phi_0 \frac{(\gamma+1)^{3/2}}{(\gamma-1)^{7/2}} \left[\frac{4}{3} + \frac{\gamma(\gamma-2)}{\gamma+1}\left(1 - \frac{1}{2\gamma\sqrt{\gamma^2-1}} ln\left(\frac{\gamma+\sqrt{\gamma^2-1}}{\gamma-\sqrt{\gamma^2-1}}\right)\right)\right] \tag{2.2}$$

where

$$\gamma = \frac{1}{\sqrt{1-\frac{v_e^2}{c^2}}} = \frac{E + m_e c^2}{m_e c^2}. \tag{2.3}$$

v_e is the velocity of the photo electron. In the Born approximation the kinetic energy of the scattered particle is small compared to that of the incident particle and large compared to the ionization energy [15]. In this case the wave function of the scattered particle can be approximated by plane waves. The Born approximation is not valid for photon energies close to the ionization energy (K-edge) and for heavy elements [15]. These disturb the wave functions of the scattered particles by their stronger potential energy in such a way, that the plane wave approximation does not hold anymore. In this case the exact wave functions of the continuous spectrum must be used instead of the plane waves. Eq. 2.1 must be multiplied by a correction factor [15, 18]:

$$f(\xi) = \frac{\sqrt{2}\pi Z}{137}\sqrt{\frac{m_e c^2}{E}}\frac{exp(-4\xi arccot(\xi))}{1-exp(-2\pi\xi)} \tag{2.4}$$

where $\xi = \sqrt{\frac{\widetilde{I}}{E-\widetilde{I}}}$ and $\widetilde{I} = 0.5\frac{Z^2}{137^2} m_e c^2$, which yields the exact non-relativistic total cross section of the K-shell photo effect [15]

$$\Phi_{p-K,exact} = 8\pi\widetilde{\alpha}^5 Z^6 \Phi_0 \left(\frac{m_e c^2}{E}\right)^8 \frac{exp(-4\xi arccot(\xi))}{1-exp(-2\pi\xi)}. \tag{2.5}$$

The correction factor in Eq. 2.4 has also been used to correct the photoelectric cross section for heavier elements in the relativistic regime given by Eq. 2.2 [19].

The scattering of X- and γ-ray photons on quasi free electrons is called Compton scattering. The electrons in the inner atomic shells, the valence and the conduction band of a solid are quasi free, if their binding energy is negligible compared to the photon energy. The cross section for the Compton scattering per atom is described by the formula:

$$\Phi_c = 2\pi r_e^2 Z \left\{ \frac{1+\kappa}{\kappa^2} \left[\frac{2(1+\kappa)}{1+2\kappa} - \frac{1}{\kappa} ln(1+2\kappa) \right] + \frac{1}{2\kappa} ln(1+2\kappa) - \frac{1+3\kappa}{(1+2\kappa)^2} \right\} \tag{2.6}$$

where $\kappa = \mathrm{E}/\mathrm{m}_e\mathrm{c}^2$ [16].

The third process is called pair production and occurs only close to a third particle, due to energy and momentum conservation. The minimum energy necessary for this process to happen is $\mathrm{E}_{min} = 2\mathrm{m}_e\mathrm{c}^2(1 + \mathrm{m}_e/\mathrm{M})$, where M is the mass of the third particle. The cross section for pair production in the vicinity of a nucleus is proportional to

$$\Phi_{pair,nucl} \propto \widetilde{\alpha} r_e^2 Z^2. \tag{2.7}$$

In this work we investigate the interaction of photons with an energy below 1 MeV with CsI(Tl) and $LaBr_3$(Ce). Pair production does not occur in this energy range and therefore it is discussed in App. A.1.1 for the interested reader.

The total cross section for a photon interacting with matter is

$$\Phi = \Phi_p + \Phi_c + \Phi_{pair} \tag{2.8}$$

and the mass absorption coefficient

$$\frac{\mu}{\rho} = \frac{N[1/cm^3]\Phi[cm^2]}{\rho[g/cm^3]} = \frac{nN_A\Phi[cm^2]}{nM[g]} = \frac{N_A\Phi}{M}[cm^2/g] \tag{2.9}$$

with N the density of atoms, N_A the Avogadro number, n the number of mole and M the molar weight. For compounds and mixtures

$$\frac{\mu}{\rho} = \sum_i W_i \left(\frac{\mu}{\rho}\right)_i \tag{2.10}$$

where W_i is the weight fraction and $(\mu/\rho)_i$ the mass absorption coefficient of each element in the compound [20]. The absorption coefficient is then $\mu = (\mu/\rho) \cdot \rho$. To exhibit a large absorption coefficient, hence a high stopping power, for X- and γ-rays, scintillators should have a high atomic number, Z, and density, ρ, but a low molar weight, M. A high Z number increases the cross section for photo effect, so that the energy, where the Compton process becomes important is shifted to higher energies. Thus detectors of materials with a high Z number are favoured, because the background from Compton events is lower.

Fig. 2.1 shows the absorption coefficient of CsI, $LaBr_3$ and Si, calculated with the formulas 2.2 - 2.10 and A.2. The absorption coefficients for the photo effect, Compton scattering and pair production in CsI and Si are also presented (Fig. 2.1 black lines). In case of the photo effect the used cross sections are $\Phi_{p-K,exact}$ (Eq.

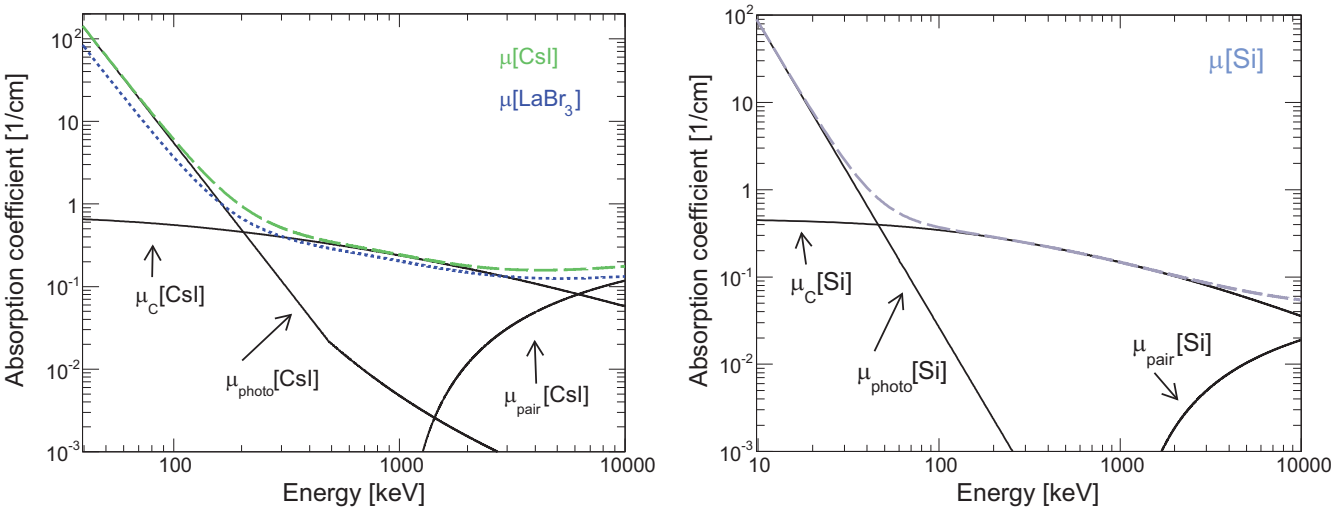

Figure 2.1.: *left Fig.: Calculated overall absorption coefficient for CsI (green) and $LaBr_3$ (blue) with the cross sections given in Eq. 2.5, 2.2 times 2.4, 2.6 and A.2; Absorption coefficients of the photo effect, Compton scattering and pair production for CsI (black curves); right Fig.: Calculated total absorption coefficient for Si (purple), composed of the absorption coefficients for the photo effect, Compton scattering and pair production for Si (black curves).*

2.5) and $\Phi_{p-K,rel} \cdot f(\xi)$ (Eq. 2.2 and 2.4) in the range 40 keV $\leq$ E $<$ 475 keV and E $\geq$ 475 keV. $\Phi_{p-K,exact}$ is not accurate in the energy range $0.5 m_e c^2 <$ E $< m_e c^2$. There is no analytical formula for the photoelectric cross section in this energy range. The curve of $\mu_p[CsI]$ has a discontinuity at E = 475 keV (Fig. 2.1 on the left), because the formula $\Phi_{p-K,exact}$ is substituted by $\Phi_{p-K,rel} \cdot f(\xi)$ from the discontinuity to higher energies.

The total absorption coefficient for the photo effect decreases with increasing energy and has the same magnitude as the absorption coefficient for Compton scattering around 200 keV in CsI and $LaBr_3$ and around 50 keV in Si. The difference in energy is due to the higher atomic number and density of CsI and $LaBr_3$ compared to Si. For photons with energies of about 50 keV the absorption coefficient is about 60 cm^{-1} and 40 cm^{-1} for CsI and $LaBr_3$ and about 1 cm^{-1} for Si (Fig. 2.1). In Fig. 2.2 the absorption coefficients of γ-rays in Si, Ge, $LaBr_3$ and CsI are plotted in the energy range from 1 keV to 10 MeV. In the energy range from 10 keV to 100 keV the absorption coefficients of Ge, $LaBr_3$ and CsI are 1 to 2 orders of magnitude larger compared to Si. For higher γ-energies 100 keV $<$ E $<$ 1022 keV the difference decreases below one order of magnitude, because the absorption coefficient is determined in this energy range mainly by the Compton effect, which depends linearly on the atomic number Z. On the one hand the overall absorption of the system can be increased by increasing the thickness of the scintillators. On the other hand, increasing the thickness of the semiconductor detector has a lot of technological challenges. The leakage current and the bias voltage of thicker semiconductor detectors are larger, thus its thickness is limited. In Fig. 2.3 the energy

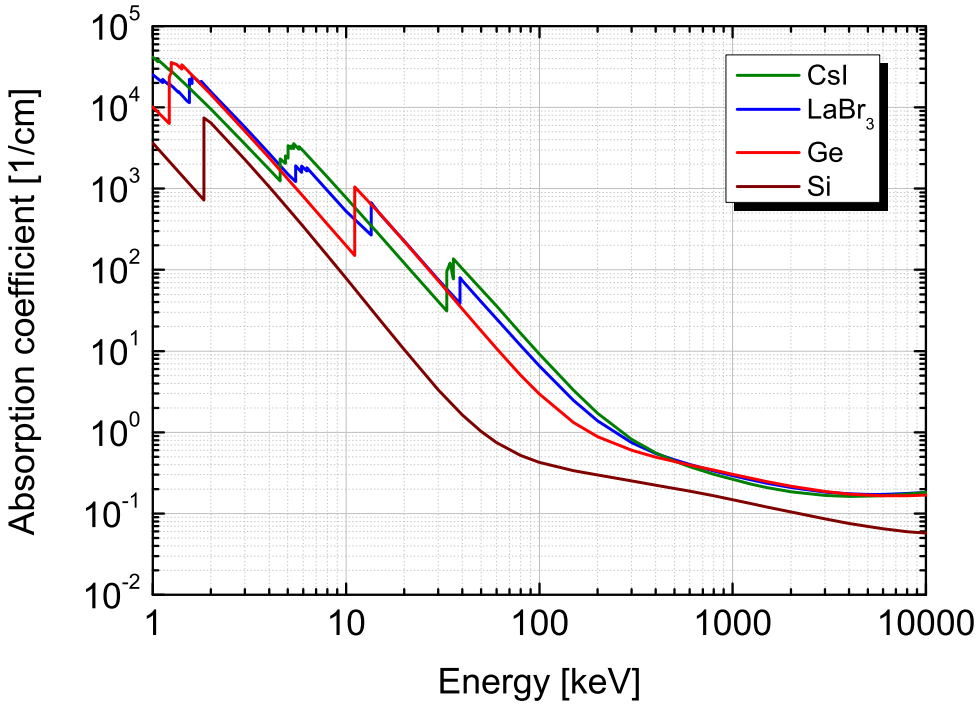

Figure 2.2.: *Absorption coefficients of Si, Ge, $LaBr_3$ and CsI are taken from [21] and [22].*

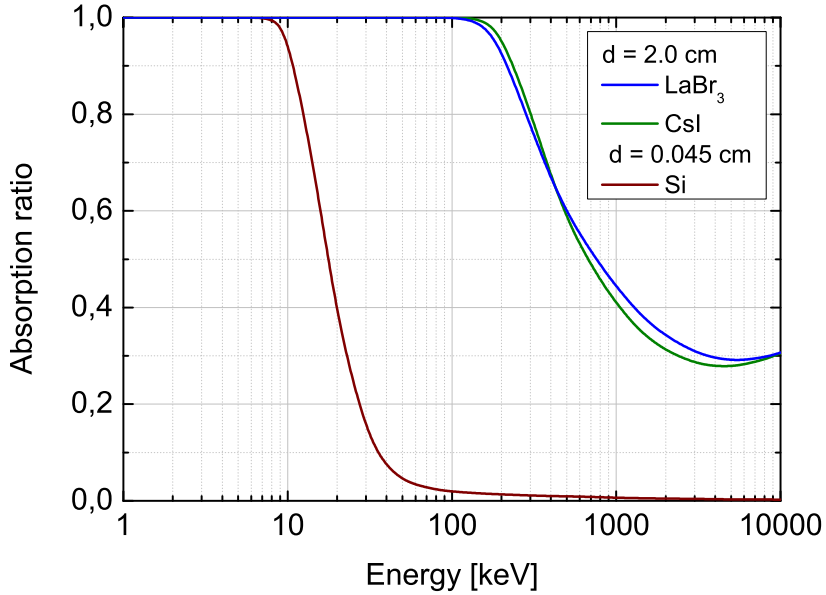

Figure 2.3.: *Calculated ratio of absorbed to incident photons in a 450 µm thick Si, 2 cm thick $LaBr_3$ and CsI with values from Fig. 2.2.*

dependent absorption of γ-rays in a 2 cm thick $LaBr_3$ and CsI and 450 μm thick Si is shown. The energy threshold for 100 % absorption in 2 cm thick $LaBr_3$ and CsI is more than one order of magnitude higher (E < 100 keV) compared to a 450 μm thick Si (E < 10 keV).

Interaction of electrons with matter

The photo effect and Compton scattering generate free electrons with a certain kinetic energy and holes in valence bands and atomic shells. The excited atoms relax via generation of Auger electrons and/or fluorescence photons, which again generate free electrons and/or fluorescence photons. The photo, Compton and Auger electrons can generate secondary electrons by inelastic collisions with atomic electrons, leading to the ionization of the atom. For the investigated γ-energies, E < 1 MeV, the energy loss of electrons by bremsstrahlung can be neglected. Below 1 MeV the differential energy loss of an electron per unit path length in matter can be approximated by the equation developed by Bethe [19]

$$-\frac{dE}{dx} = \frac{e^4 N_A \rho Z}{4\pi\epsilon_0^2 A m_e v^2} ln\left(1.166\frac{m_e v^2}{2I}\right) = \frac{e^4 N_A \rho Z}{4\pi\epsilon_0^2 A m_e c^2 \beta^2} ln\left(1.166\frac{E_e}{I}\right) \tag{2.11}$$

where e is the electron charge, N_A the Avogadro number, A the atomic weight, v the relativistic velocity of the incident electron, $\beta = v/c$, I the mean excitation energy of the atoms inside the medium and E_e the kinetic energy of the incident electron. For compound materials the effective values of Z, A and I have to be used instead [16]:

$$\begin{aligned} Z &= \sum a_i Z_i \\ A &= \sum a_i A_i \\ I &= exp\left(\sum \frac{a_i Z_i ln\,(I_i)}{Z_{tot}}\right), \end{aligned} \tag{2.12}$$

where a_i is the number of atoms of the i-th element in the compound molecule. The effective values for CsI and $LaBr_3$ are Z(CsI) = 108, A(CsI) = 259.8, I(CsI) = 553 eV and Z($LaBr_3$) = 162, A($LaBr_3$) = 378.6, I($LaBr_3$) = 455 eV. For E_e close to I formula 2.11 becomes inaccurate and for $E_e = I/1.166$ it is zero. The mean excitation energy, which is about several hundreds of eV is determined from fits to experimental data for E_e of a few keV and larger in literature [24]. For E_e falling below the binding energy of electrons in a certain atomic shell, the mean excitation potential I decreases as well. It has been proposed to substitute the constant I in formula 2.11 by an energy dependent mean excitation energy $I^{'}$ given by [24]

$$I^{'} = \frac{I}{1 + k\frac{I}{E_e}}. \tag{2.13}$$

Inserting $I^{'}$ instead of I into formula 2.11 yields:

$$-\frac{dE}{dx} = \frac{e^4 N_A \rho Z}{4\pi\epsilon_0^2 A m_e c^2 \beta^2} ln\left(1.166\frac{E_e + kI}{I}\right) \tag{2.14}$$

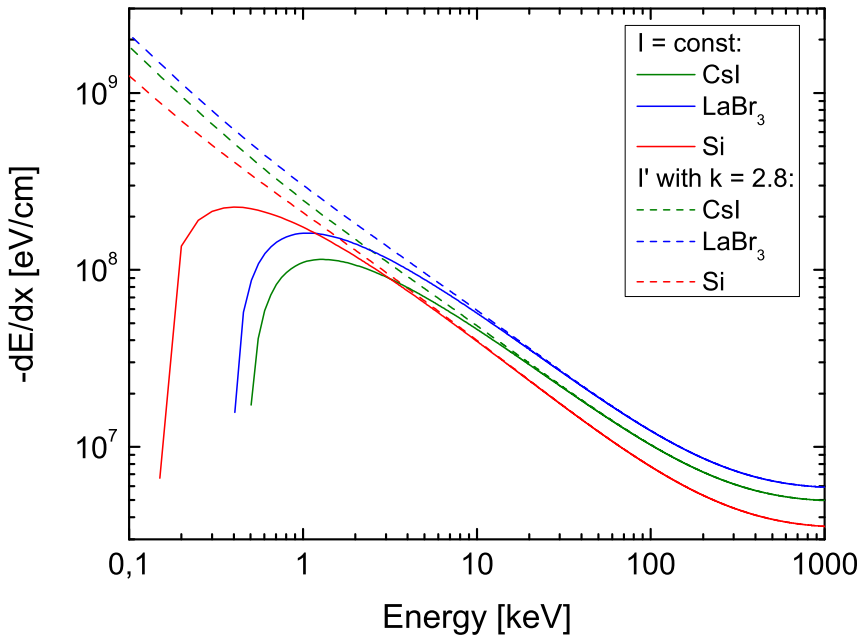

Figure 2.4.: *Mean energy loss of electrons depending on the electron energy in CsI, $LaBr_3$ and Si. The mean excitation energies are I_{CsI} = 553 eV, I_{LaBr_3} = 455 eV and I_{Si} = 173 eV [23].*

Fig. 2.4 shows the energy loss of electrons depending on their kinetic energy up to 1 MeV, described by Eq. 2.11 (solid lines) and Eq. 2.14 (dotted lines) where k = 2.8. A value of k = 2.8 has been proposed in [25] for scintillators down to electron energies equal to the mean excitation energy, E_e = I.

The path length of the electron inside the medium can be calculated by

$$s(E_e) = \int_{E_e}^{0} \frac{dE}{-dE/dx} = s_0 + \int_{E_e}^{E_{e,thr}} \frac{dE}{-dE/dx} \tag{2.15}$$

where s_0 is the path length of the electron with energies below the threshold energy, $E_{e,thr}$, at which formula 2.11 or 2.14 become inaccurate. In Fig. 2.5 the path lengths of electrons in CsI, $LaBr_3$ and Si are plotted against the energy of the incident electron, using the parameters k = 2.8, s_0 = 0 and $E_{e,thr}$ = 150 eV. The path length is not the penetration depth inside the medium, which is shorter, due to the angle dependent multiple scattering of the electron. The value of the deposited energy per path length for an incident electron decreases by about two orders of magnitude, if the kinetic energy of the electron increases from 1 to 1000 keV. Electrons with a lower kinetic energy generate a higher ionization density.

Another important fact is the change of -dE/dx along the track, due to the reduction of the kinetic energy of the electron. Fig. 2.6 shows the value of -dE/dx along the track inside CsI covered by an incident electron with a kinetic energy of E_e = 10 keV at the beginning of the track. It shows that -dE/dx increases slowly along the track and faster at the end of the electron track.

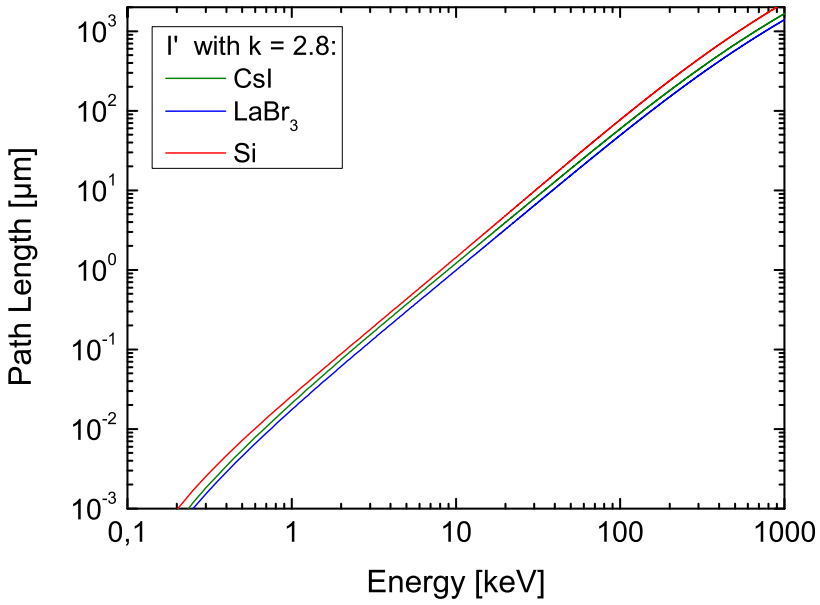

Figure 2.5.: *Path length of electrons in CsI, $LaBr_3$ and Si as a function of their energy.*

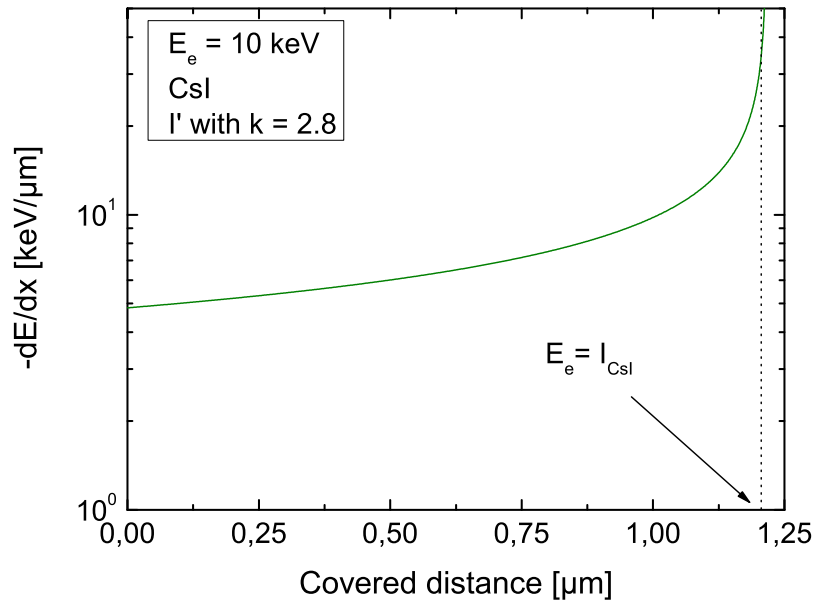

Figure 2.6.: *Deposited energy per track length for an incident electron with an energy of 10 keV along its track inside CsI. After a path length of about 1.2 µm, the electron has an energy of $E_e = I_{CsI}$ left. I_{CsI} is the mean excitation energy in CsI.*

Furthermore -dE/dx fluctuates at each position along the track for a constant kinetic energy of the incident electrons. These fluctuations can be described by Landau fluctuations [26]. The probability distribution of these fluctuations can be approximated by the Moyal distribution [27]:

$$Moyal(\zeta) = \frac{1}{\sqrt{2\pi}} exp\left[-\frac{1}{2}\left(\zeta + exp\left(-\zeta\right)\right)\right] \text{[27]} \tag{2.16}$$

where

$$\zeta = \frac{1}{B}\left(-\frac{dE}{dx} - \left(-\frac{dE}{dx}\right)_{max}\right) \tag{2.17}$$

and

$$B = \frac{e^4 N_A \rho Z}{4\pi\epsilon_0^2 A m_e v^2} = \frac{e^4 N_A \rho Z}{4\pi\epsilon_0^2 A 2 E_e} \tag{2.18}$$

the factor in front of the logarithm in Eq. 2.11. The advantage of the Moyal compared to the Landau distribution is, that the mean value and variance have an analytical form. The full width at half maximum of the Moyal distribution is $\text{FWHM}_{Moyal} = 3.58 \cdot \text{B}$.

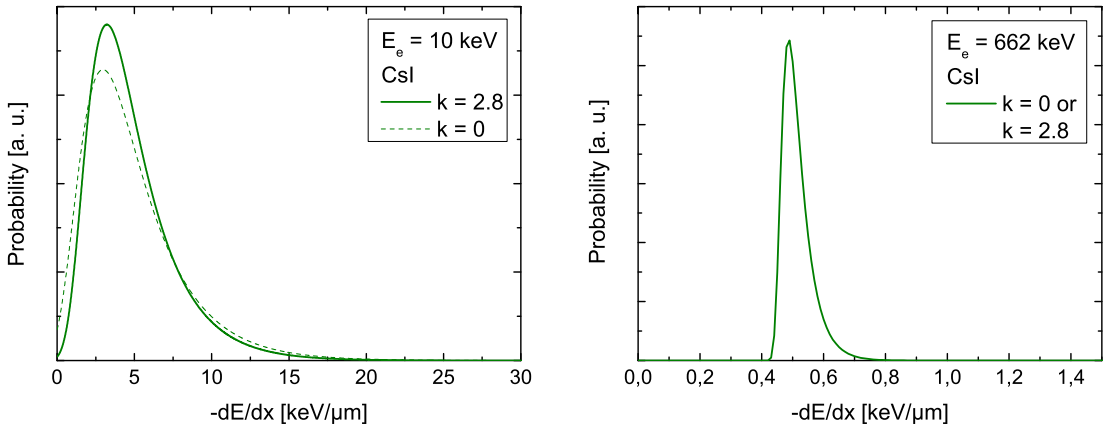

Figure 2.7.: *Fluctuations of -dE/dx described by the Moyal distribution for electrons with kinetic energies of 10 keV and 662 keV in CsI.*

Landau's theory states that the deposited energy of charged particles after their passage through thin layers is subjected to fluctuations [26, 27]. The electron path inside the scintillator can be divided into thin layers, in which the fluctuations of the energy deposited by electrons are described by Landau fluctuations. Fig. 2.7 shows the distribution of the fluctuations of -dE/dx, which are approximated by the Moyal distribution, for two different electron energies, 10 and 662 keV. The solid line describes the Moyal distribution, if E_e is substituted by $E_e = E_e + k \cdot I$, in equivalence to the correction of the Bethe formula at low electron energies.

Conversion of the deposited energy into eh-pairs

On its path through the medium the electron generates a number of electron hole (eh) pairs until it reaches a threshold energy below which its remaining kinetic

energy is deposited through other processes, such as the generation of plasmons and phonons. The mean number of generated eh-pairs after the deposition of a certain energy, E, inside the medium, can be determined, if the mean energy, $\overline{w}$, to create an eh-pair and the Fano factor, F, in the material is known:

$$\overline{N}_{eh} = \frac{E}{\overline{w}}. \tag{2.19}$$

An approximation for $\overline{w}$ in semiconductors and insulators (scintillators) is the formula

$$\overline{w} = a \cdot E_g + \overline{r} E_{ph} \tag{2.20}$$

where $\overline{r}$ is the mean number of excited phonons, E_{ph} the phonon energy and $\overline{r} \cdot E_{ph}$ the mean energy converted into phonon excitations. For wide band gap materials a = 2 and $\overline{r}E_{ph}$ = 1.43 eV [28]. The energy gap of silicon is E_g = 1.12 eV at 300 Kelvin [3]. Inserting this value into formula 2.20 yields $\overline{w}$ = 3.67 eV. For photon energies larger than 200 eV, mean energies to create an electron hole pair of $\overline{w}$ = 3.63 [29, 30] and 3.66 eV [31, 32] have been presented in literature. The energy gap of CsI and $LaBr_3$ are 6.1 eV [33] and 5.6 eV [34]. Formula 2.20 yields $\overline{w} \approx$ 13.6 eV for CsI in good agreement to $\overline{w}$ = 13.3 eV, which has been determined from measurements and is presented in [35]. For $LaBr_3$ it yields $\overline{w} \approx$ 12.6 eV. Results of $\overline{w}$ for CsI from Monte Carlo simulations presented in [36] show a decreasing value from 19 to 15.2 eV with an increasing energy from E = 100 eV to 10 keV. For E >10 keV $\overline{w}$ remains constant at 15.2 eV. In this work the mean energy to create an electron hole pair is set to 14 eV for CsI and 13 eV for $LaBr_3$.

The Fano factor introduced by Fano [37, 38] describes the deviation of the variance of the number of ionizations produced by charged particles in gas chambers from Poisson statistics. The Fano factor has also been adapted for semiconductor detectors [39] in order to describe the difference of the measured variance, V_{meas}, of the number of generated eh-pairs, N_{eh}, by charged particles from the variance described by Poisson statistics:

$$Var_{meas}\left(N_{eh}\right) = F \cdot Var_{pois}\left(N_{eh}\right) = F \cdot \overline{N}_{eh}. \tag{2.21}$$

In literature F has been calculated for different semiconductors with a value F = 0.115 for silicon [29]. Results of calculations for CsI presented in [36] show that F increases with increasing energy and remains constant at F = 0.28 for energies larger than 1 keV.

The physical reason for the variance of the number of generated eh-pairs around its mean value $\overline{N}_{eh}$ is the following. The deposited energy E by X- or γ-ray photons is distributed among Compton, photo and Auger electrons and core and valence band holes. These electrons generate further electrons by ionization (leaving holes in the valence band). Generation of secondary electrons by ionization continuous until the energy of all generated electrons reach an energy threshold E_{th}, below which no further electrons and holes can be generated by inelastic electron electron scattering [29, 30]. Due to the fact, that the generated electrons (holes) can occupy an energy range $E_g < E_e < E_{th}$, the deposited energy E can be distributed among a varying number of electrons (holes) from event to event. Furthermore the energy of the electrons (holes) is also dissipated into a number of phonons and plasmons,

which is also varying from event to event, increasing the variation of the number of generated electrons (holes) [29, 30]. The variation of $\overline{N}_{eh,j}$ from one event j to another results in the variance given by formula 2.21.

2.1.2. Interaction of UV−Vis photons with Si

The maximum intensity of the scintillation spectrum of most of the scintillators is in the near ultra violet and visible (UV−Vis) range. These photons interact with silicon mainly via the so called "inner" photo effect, where electrons from the valence band or impurity states are excited into higher available energy states, which can be higher impurity states or conduction bands. But there is also the probability for excitations within the same band [40].

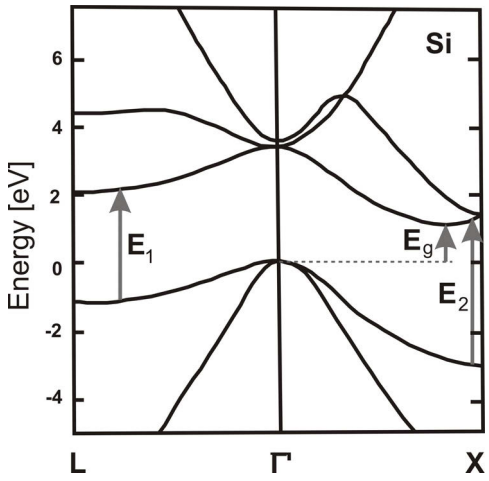

Figure 2.8.: *Bandscheme of silicon after [41]*

For certain photon energies the joint density of states of the conduction and valence band becomes maximum. This leads to the so called Van Hove singularities in the joint density of states (see A.1.2). In Fig. 2.8 the band structure of intrinsic silicon is illustrated [41]. Two regimes with an excitation energy E_1 and E_2, give rise to Van Hove singularities, hence to characteristic points of the absorption of silicon at $E = E_1$ and E_2 (Fig. 2.9).

For photon energies close to the energy gap, phonons have to participate in the absorption process, with the emission or absorption of at least one phonon, because silicon is an indirect semiconductor. Thus the excitation of an electron from the valence into the conduction band by photons with energies around the energy gap of silicon, E_g, is a second order process with a lower absorption coefficient compared to the first order direct transitions for photon energies ≥ 3.3 eV, which is explained in more detail in A.1.2. Fig. 2.9 shows the absorption coefficient of intrinsic silicon, which has been taken from [42].

If silicon is doped with impurities, the so called Mott transition occurs at doping concentrations of about 10^{18} cm^{-3} [40]. At higher doping concentrations electrons or holes localized on the donators or acceptors become free carriers.

For heavily doped semiconductors the absorption coefficient is larger, compared to lowly doped and intrinsic silicon. This is due to a narrower energy gap [43].

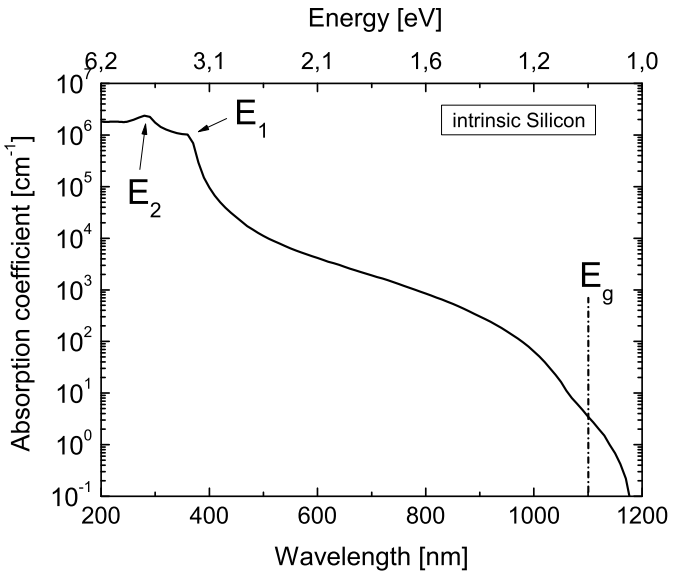

Figure 2.9.: *Absorption coefficient of intrinsic silicon at 300 Kelvin. Data are taken from [42].*

Furthermore, at high doping levels the high density of charge carriers enables an additional absorption process, where a charge carrier transfers the suitable momentum to the excited electron instead of a phonon. There is a third absorption process in heavily doped semiconductors. This is the free carrier absorption, where electrons or holes are excited within the same band. These three processes lead to an increase of the absorption coefficient in doped silicon compared to intrinsic silicon in the energy range below 3.3 eV. Fig. 2.10 shows the absorption coefficient of intrinsic

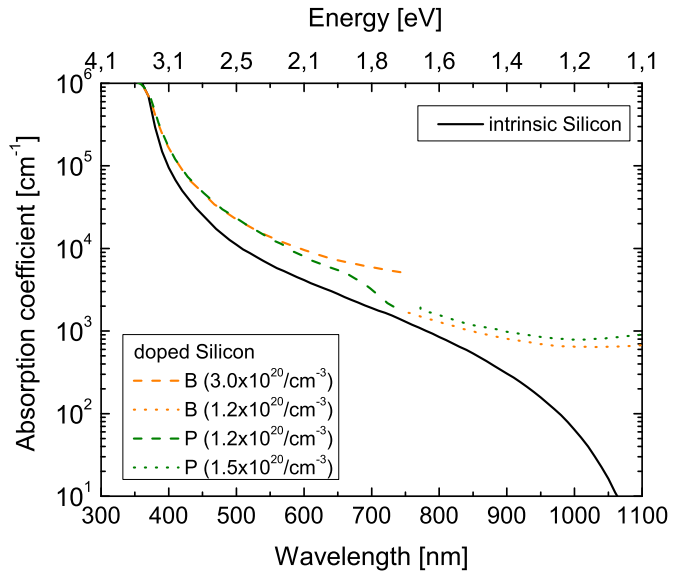

Figure 2.10.: *Absorption coefficient of intrinsic and phosphor or boron doped silicon at 300 Kelvin. Data are taken from [42, 43, 44, 45].*

and heavily doped silicon. Calculated absorption coefficients in the range 400 to

1200 nm are presented in App. A.1.2.

In Fig. 2.10 absorption coefficients of photons are shown for intrinsic and heavily phosphor or boron doped silicon in the range from 300 to 1100 nm. For photons with wavelengths in the range from 370 to 700 nm the absorption coefficient in heavily doped silicon is larger as in intrinsic silicon by a factor up to 3. To longer wavelengths this difference increases and reaches a value of more than 3 orders of magnitudes at 1150 nm. Due to the fact, that the maximal doping concentration of silicon inside the SDD / pnCCD entrance window is at least one order of magnitude lower than the doping concentration of silicon shown in Fig. 2.10, the absorption coefficient inside the p-doped part of the SDD / pnCCD entrance window is approximated by that of intrinsic silicon in the considered range from 300 to 1000 nm in this work. Intrinsic silicon becomes transparent for photon energies below $E = E_g - E_{ph} = 1.12 - 0.05$ eV $= 1.07$ eV ($\lambda = 1160$ nm), whereas for heavily doped silicon the absorption coefficient increases slowly to longer wavelengths, due to free carrier absorption.

Another important material parameter is the number of electron hole pairs, hence the number of signal electrons, generated by one absorbed photon from the UV - Vis range, which is denoted as the internal quantum efficiency (iQE). Fig. 2.11 presents the measured iQE for a silicon pn-detector. Coming from low energies or

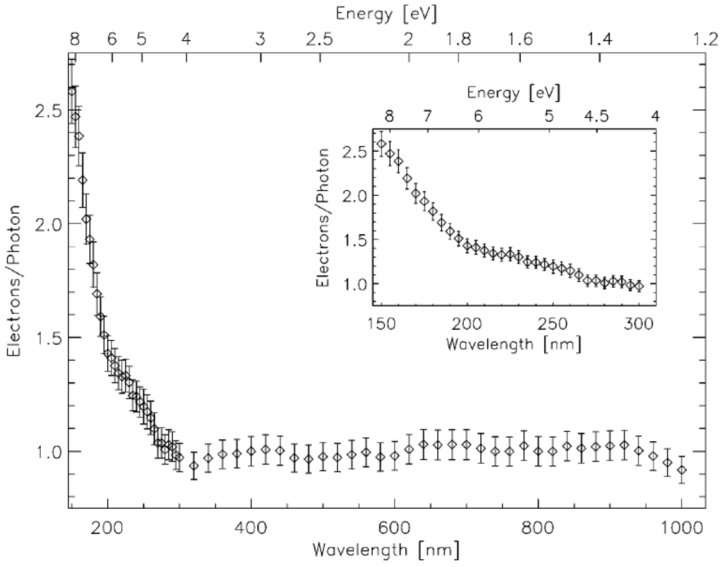

Figure 2.11.: *Internal quantum efficiency of a silicon pn-detector taken from [46].*

long wavelengths the iQE increases to 1 from 1000 to 950 nm [46]. In the wavelength rage from 950 to 300 nm the iQE remains constant at 1 [46]. To shorter wavelengths the iQE increases, so that there is the probability that one photon generates more than one electron hole pair.

2.2. Light generation in scintillators: CsI(Tl) and $LaBr_3$(Ce)

Scintillators are materials, which convert a part of the energy deposited by X-, γ-ray photons or ionizing particles into UV-Vis photons, which can be detected by a photodetector like PMTs, PDs, APDs, SiPMs and SDDs / pnCCDs.

The first scintillators have been produced in the late 1800s [47]. From the beginning of the 1900s until today many scintillators with different properties have been developed. Inorganic scintillators are often used in combination with photodetectors as γ-ray or particle detectors, because of their high stopping power, due to a high density, ρ, and atomic number, Z. The conversion of the deposited energy into

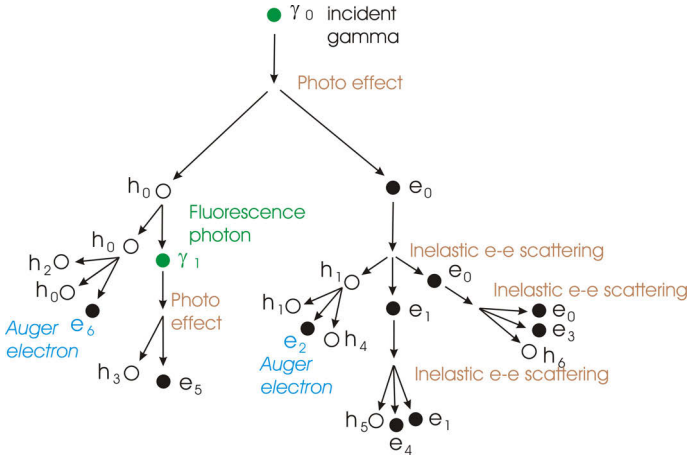

Figure 2.12.: *Beginning of one possible path of secondary particles generation after the interaction of a γ-ray with the scintillator.*

scintillation photons includes the following steps:

1. generation of electrons and holes by an incident high energetic photon (Fig. 2.12)
2. generation of secondary electrons, holes, photons (Fig. 2.12) and plasmons
3. thermalization of electrons and holes (Fig. 2.13)
4. energy and charge transfer to luminescence centers (Fig. 2.13)
5. radiative (generation of scintillation photons) or non-radiative decay of the excited luminescent centers (Fig. 2.13)

[14, 48].
The mean number of generated scintillation photons is

$$\overline{N}_{ph} = \overline{N}_{eh} \cdot \overline{S} \cdot \overline{Q} = \frac{E}{\overline{w}} \overline{S} \cdot \overline{Q}. \tag{2.22}$$

Eq. 2.22 is a phenomenological approach, which describes the mean number of generated scintillation photons, $\overline{N}_{ph}$, after an interaction of an incident photon,

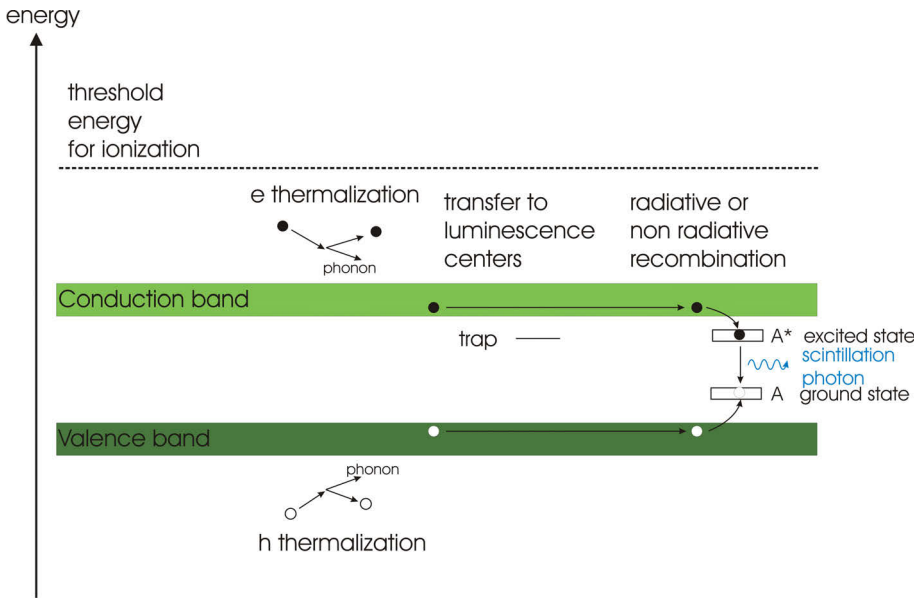

Figure 2.13.: *Processes following the thermal relaxation of the produced electrons and holes to their recombination via scintillation photon generation.*

which deposits the energy E inside the scintillator [14]. $\overline{N}_{ph}$ depends on the mean energy, $\overline{w}$, to create an electron hole pair, the mean transfer probability $\overline{S}$, of the energy of thermalized eh-pairs to the excited states of luminescence centers and the mean probability, $\overline{Q}$, for radiative relaxation of the excited luminescence centers, A^* (see Fig. 2.13).

Calculations for CsI presented in [36] indicate that $\overline{w}$ remains constant for energies above 10 keV. On the contrary $\overline{S}$ varies with the deposited energy over the whole energy range from several 100 eV to several 100 keV [49]. In this work it will be shown that the dependence of $\overline{S}$ on the deposited energy in combination with other particular scintillator properties and the ionization density lead to an energy dependent light yield and a degradation of the intrinsic energy resolution of the scintillator.

The light yield of scintillators is defined by equation

$$\overline{L}(E) = \frac{\overline{N}_{ph}}{E} = \frac{\overline{S} \cdot \overline{Q}}{\overline{w}}, \tag{2.23}$$

which is the mean number of generated scintillation photons $\overline{N}_{ph}$ divided by the deposited energy, E. Manufacturers of scintillators generally specify an energy independent light yield, which is often defined as the light yield at 662 keV.

The mean number of created eh−pairs, $\overline{N}_{eh}$, follows from $\overline{N}_{eh} = E/\overline{w}$. For a γ energy of E = 662 keV and $\overline{w} \approx 13$ eV (see Sec. 2.1.1) a value of $\overline{N}_{eh} \approx 51000$, which corresponds to about 77 eh-pairs/keV, is calculated. A light yield of $\overline{L} \approx 65$ photons/keV for an absorbed energy of 662 keV in CsI(Tl) and $LaBr_3$(Ce) have been presented in [50, 51]. Inserting $\overline{N}_{eh}$ and $\overline{L}$ for 662 keV into Eq. 2.23 yields the result $\overline{S} \cdot \overline{Q} \approx 0.84$, what means that only a fraction of 0.84 of the generated electrons and holes are captured and recombine radiatively.

From Eq. 2.22 and 2.20 it can be deduced that scintillators with small band gaps and $\overline{S}$, $\overline{Q}$ as close as possible to 1 reach a maximal light yield $\overline{L}$.

The transfer probability, $\overline{S}$, of thermalized electrons and holes to activators depends on the following processes:

1. limitation of charge carrier capture probability at luminescence centers
2. trapping due to unwanted impurities
3. * low ionization densities in combination with low and unequal mobilities for electrons and holes reducing the probability of finding each other before recombining non radiatively (Occurs at low ionization densities, mainly in alkali halide scintillators.)

[14, 48, 52, 53, 54]. Competing processes for non-radiative transitions from excited activator states are:

1. thermal quenching, caused by electron-phonon coupling and the emission of phonons instead of photons
2. concentration quenching for high concentrations of activators, caused by the migration of the energy from one activator to the next until a quenching site is reached
3. quenching due to energy levels of the excited activator states close to or inside the conduction band with a high probability for the electron to be excited into a free state again
4. * high ionization densities in combination with low mobilities, which lead to an Auger like quenching of excitations

[14, 48, 53, 54].
All these non-radiative transitions reduce the radiative recombination efficiency, $\overline{Q}$, which is further investigated in App. A.2 (Eq. A.28). The processes listed in the enumeration points 3* and 4* are proposed to be the cause of the so called non-proportionality in scintillators [52, 53, 54], which will be discussed in detail in Chap. 6.

The scintillators investigated in this work are Thallium (Tl) doped CsI and Cerium (Ce) doped $LaBr_3$. Tl is supposed to be substitutionally integrated onto Cs and Ce onto La sites of the host lattice. The electron configuration of free atoms and atoms bound inside these scintillator crystals are presented in Table 2.1. Due to spin-orbit coupling the ground and excited states of Tl^+ and Ce^{3+} are supposed to be split into multiplets (see Fig. 2.14), which are named $^{2S+1}L_J$, where S is the total spin, L the total angular momentum and J = L + S the total electronic momentum. The selection rules for an electric dipole transition are $\Delta J = 0, \pm 1$, $\Delta S = 0$ and $J = 0 \rightarrow J' = 0$ is forbidden. In case of spin-orbit coupling the selection rule $\Delta S = 0$ is not strong. Black and green arrows in Fig. 2.14 show allowed transitions, which have a fast decay time of several 10 ns, whereas partly allowed transitions with a slow decay time of several 100 ns are illustrated by the orange arrow. The position of the ground and excited states relative to the valence band maximum and conduction band minimum determines the capture probability of holes and electrons. The capture probability is 0, if the states reside inside the valence and conduction

free atom	**configuration**	**free atom**	**configuration**
Cs	[Xe]6s	**La**	$[Xe]5d6s^2$
I	$[Kr]4d^{10}5s^25p^5$	**Br**	$[Ar]3d^{10}4s^24p^5$
Tl	$[Xe]4f^{14}5d^{10}6s^26p$	**Ce**	$[Xe]4f^26s^2$
CsI(Tl)		**$LaBr_3$(Ce)**	
atom inside lattice	**configuration**	**atom inside lattice**	**configuration**
Cs^+	[Xe]	**La^{3+}**	[Xe]
I^-	[Xe]	**Br^-**	[Xe]
Tl^+	$[Xe]4f^{14}5d^{10}6s^2$	**Ce^{3+}**	$[Xe]4f^1$
$(Tl^+)^*$	$[Xe]4f^{14}5d^{10}6s6p$	**$(Ce^{3+})^*$**	[Xe]5d

Table 2.1.: *Electron configuration of free and bound atoms in the scintillators CsI(Tl) and $LaBr_3(Ce)$. * denotes the excited state. [48]*

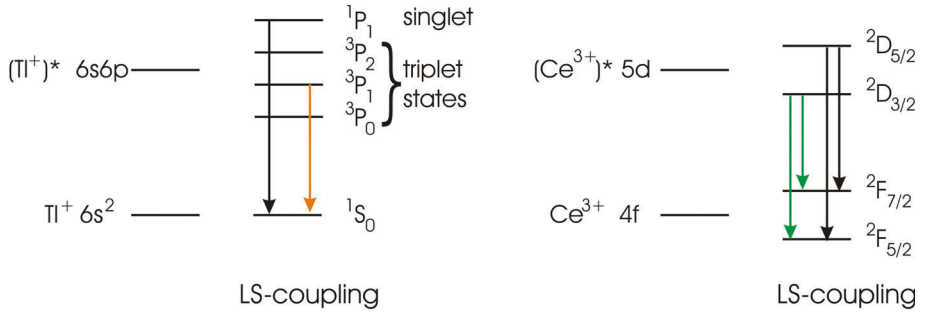

Figure 2.14.: *Multiplet, due to spin-orbit coupling, of the ground and excited state of Tl^+ and Ce^{3+} with allowed (black and green arrows) and partly allowed (orange arrows) electric dipole transitions. (from [48])*

band. If the ground or excited states are close to the valence or conduction band with an energy difference around $\Delta E = k_B T_{emp} \leq 25\ meV$ at room temperature, where k_B is the Boltzmann constant and T_{emp} the temperature, then the capture probability depends strongly on the temperature. A low capture probability of the Tl^+ and Ce^{3+} states increases the probability that electrons and holes are captured by shallow or deep traps with an increase of non-radiative recombination.

The energy of the Ce^{3+} ground state ($^2F_{5/2}$) is supposed to be about 0.9 eV above the valence band edge and the lowest excited state ($^2D_{3/2}$) 4 eV above the lowest ground state and 0.7-1 eV below the conduction band edge [55]. These energy states of Ce^{3+} are optimal for capturing electrons and holes without any quenching caused by temperature. The scintillation in $LaBr_3$(Ce) is claimed to originate from the allowed electric dipole transitions from the lowest excited $(Ce^{3+})^*$ 5d energy level, $^2D_{3/2}$, to the Ce^{3+} 4f ground states, $^2F_{7/2}$ and $^2F_{5/2}$ (Fig. 2.14 green arrows) [55].

In literature the position of the ground states of Tl^+ relative to the valence band maximum in CsI has been determined from calculations to be 0.73 eV and a value of 1.5 eV has been inferred from experiments [56]. The origin of the scintillation spectrum in CsI(Tl) is more complicated. The lowest excited Tl^+ state with a partially allowed electric dipole transition into the ground state $^1S_0$ is the triplet state $^3P_1$. It is claimed that the radiative transition $^3P_1 \rightarrow ^1 S_0$ contributes to the UV range of the scintillation spectrum [57]. The crystal environment around Tl leads to a splitting of the degenerate triplet state $^3P_1$ into two states, creating two weak emission bands in the ultra violet range at 3.09 and 3.31 eV of the transition $^3P_1 \rightarrow ^1 S_0$ [58]. This transition is assigned to the UV portion of the CsI(Tl) scintillation spectrum (see Fig. 2.15 left shoulder at about 400 nm of the green curve) and it has a low intensity compared to the visible portion [59]. The visible part of the scintillation spectrum is attributed to the recombination of two kinds of self trapped excitons (STEs) perturbed by a Tl^+ ion, the so called "weak off" and the "strong off" STE with emissions around 485 nm and 550 nm [60, 58, 61, 57], which can be described by

$$e + V_k Tl^+ = e + I_2^- Tl^+ \rightarrow (I_2^{2-})^* Tl^+ \rightarrow 2I^- Tl^+ + h\nu \tag{2.24}$$

[48], where V_k is a hole localized between the two anions, I^-, and STE $= (I_2^{2-})^*$. The STE is composed of a V_k center and a trapped electron. The STE is a system of two spins, which can couple in such a way to build triplet and singlet states. The singlet state is supposed to have a higher energy than the triplet states, so that the slower transition from the triplet state dominates the decay time at low temperatures [58, 60]. At room temperature the decay time is faster, due to a higher number of electrons in the singlet state [58].

Besides the number of transitions, which contribute to the radiative transitions, the width of the scintillation spectrum is also determined by the coupling of the excited states to phonons, which has an influence on the radiative decay time too. The spontaneous transition probability for the electric dipole transition without and with inclusion of lattice vibrations is discussed in more detail in App. A.2.

Observed decay times range from about 10 ns for allowed dipole transition (selection rules) on free atoms and molecules to values larger than 1 ms for triplet to singlet transitions in some molecules [62]. For a short scintillation decay time also the energy between the ground and excited state, $E_{ba} = hc/\lambda$, and the index of

refraction have to be as large as possible. One reason for the slow scintillation decay times in the range from several 0.1 to several 1 μs in CsI(Tl) [59] in contrast to about 30 ns in $LaBr_3$(Ce) [63] at room temperature is attributed to the fact, that triplet states are involved into the emission of scintillation light in CsI(Tl) with partially allowed transitions from the excited into the ground state of the luminescence center.

The effect of lattice vibrations is not to change the overall transition probability, but to alter and broaden the absorption and emission band shape (Fig. A.3), which can be determined from photoluminescence measurements, which excite the medium with photon energies smaller than the ionization energies of the atoms [14]. The luminescence caused by ionizing radiation is called radioluminescence and leads generally to several emission bands, because of the existence of several luminescence centers. Moreover the absorption and emission spectra are shifted in energy against each other (Fig. A.3), so that their overlap is minimized, reducing self-absorption, for an increasing coupling of the electronic states with lattice vibrations. This shift is called Stokes Shift (Fig. A.3), E_{Stokes}, which is specified as the energy difference between the absorption and emission band maximum and can be expressed by the Hyang-Rhys parameter, H [64]:

$$E_{Stokes} = (2H - 1)E_{ph} \tag{2.25}$$

where E_{ph} is the energy of the phonon. A stronger coupling between electronic states and lattice vibrations (phonons) leads to a larger Stokes Shift. The Stokes

	$LaBr_3$(Ce)		**CsI(Tl)**			
emission maximum [eV]	3.48[a]	3.21[a]	3.31[b]	3.09[b]	2.55[b]	2.25[b]
emission maximum [nm]	356	386	375	401	486	551
decay time [μs] at 300 K	0.03[f]		?	?	0.7-16 [e]	0.55-0.9 [e]
Stokes Shift[eV]	0.55[a]		1.01[b]	1.13[b]	1.74[b]	2.03[b]
optical phonon E_{ph}[meV]	15[c]		11[d]			
calculated Intensity	1	1.7	1	1.7	13	67.5
calculated H	19		46	52	80	93
calculated Γ[eV] at 300 K	21		0.28	0.3	0.37	0.4
calculated Γ[nm] at 300 K	23	26	32	39	71	99

Table 2.2.: *Summarization of the energy of the emission maximum, decay time, Stokes Shift, optical phonon energy, intensity, Hyang-Rhys parameter H and width Γ of the emission bands in $LaBr_3$(Ce) and CsI(Tl) [a]:[65], [b]:[58], [c]:[66, 67], [d]:[48], [e]:[59], [f]:[63].*

Shift and the energy of optical phonons in $LaBr_3$(Ce) and CsI(Tl) are listed in Tab. 2.2. Inserting E_{Stokes} and E_{ph} into Eq. 2.25 yields the Hyang-Rhys parameter (Tab. 2.2). The temperature dependent absorption and emission (luminescence) bandwidth can be described by

$$\Gamma(T_{emp}) = 2.35E_{ph}\sqrt{H \cdot coth\left(\frac{E_{ph}}{2k_B T_{emp}}\right)}. \tag{2.26}$$

where k_B is the Boltzmann constant and T_{emp} the temperature. In this special case the absorption and emission band are mirror images. From Eq. 2.26 the band widths for $LaBr_3$(Ce) and CsI(Tl) at 300 Kelvin are calculated and presented in Tab. 2.2. The decay time of $LaBr_3$(Ce) is much faster than that of CsI(Tl), so that it is suitable in detector applications, which have to resolve high count rates. The advantage of CsI(Tl) compared to $LaBr_3$(Ce) is that its emission spectrum peaks at longer wavelengths, around 550 nm compared to 355 nm. The challange to build a photodetector with a high quantum efficiency is larger for photons from the ultra violet range, because a large amount of photons is absorbed inside the entrance window, due to a shorter absorption length compared to photons from the visible range. Furthermore the self-absorption should be lower in CsI(Tl) compared to $LaBr_3$(Ce), because of a larger Stokes Shift. The intensities, which are the sum of several Gaussian peaks, used in the calculations in Fig. 2.15 (dotted lines) have been chosen to fit the measured scintillation emission spectra.

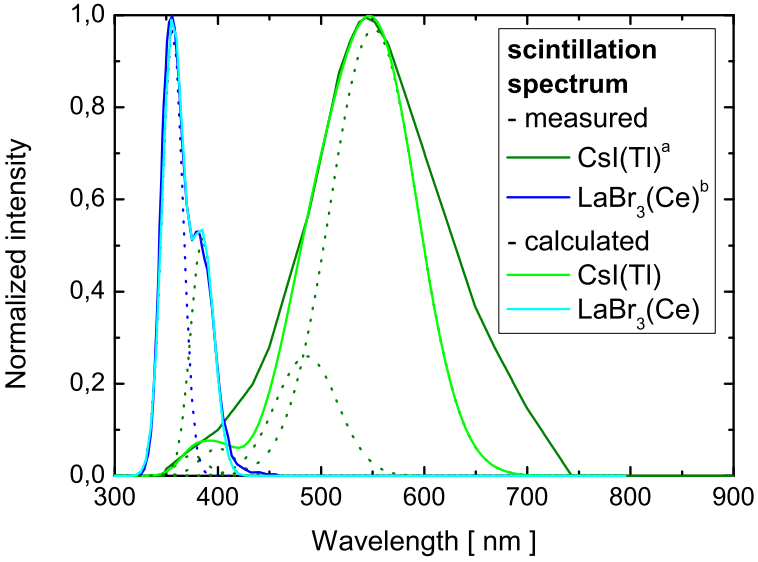

Figure 2.15.: *Normalized scintillation spectra of $LaBr_3$(Ce) [63, 68] and CsI(Tl) [69] with the maximum of the emission spectrum of $LaBr_3$(Ce) at about 355 nm in the ultra violet range, and of CsI(Tl) at 550 nm in the visible range with the following assignments [a]:[69] and [b]:[63, 68]. Dotted lines are the spectra of the calculated emission bands of the scintillators.*

Scintillation spectra of CsI(Tl) and $LaBr_3$(Ce) are plotted in Fig. 2.15. The calculated width of the emission spectrum of CsI(Tl) and $LaBr_3$(Ce) (Fig. 2.15 solid bright green and blue line) underestimates the measured emission spectrum (Fig. 2.15 solid dark green and blue line). This may be, due to a still not complete understanding of the complicated luminescence processes in CsI(Tl).

The photodetector, which is coupled to these scintillators, has to be optimized for the detection of scintillation photons. Two SDD / pnCCD entrance windows have been developed, which are optimized for scintillation light from $LaBr_3$(Ce) and CsI(Tl) (Chap. 5).

3. Principles of hard X- and γ-ray detection with Silicon Drift Detectors (SDDs)

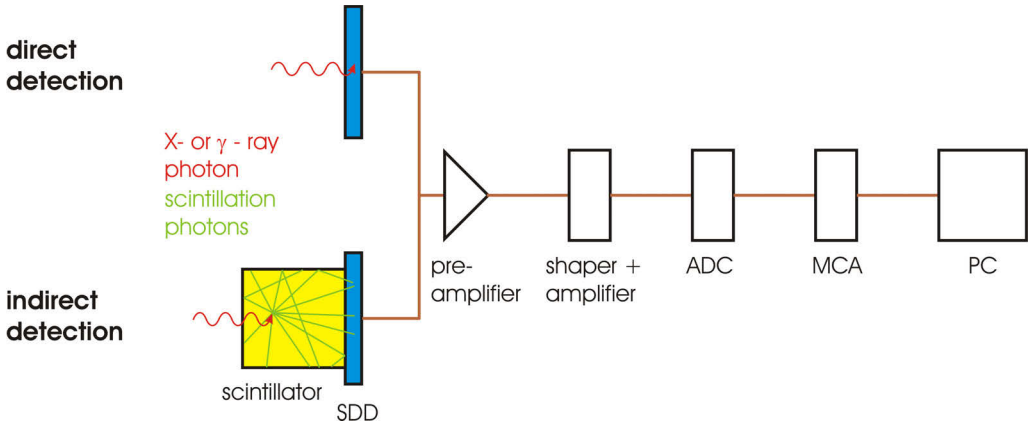

Figure 3.1.: *Drawing of the detector application consisting of a bare SDD in direct or SDD + scintillator indirect detection mode with the readout electronics.*

Fig. 3.1 shows a drawing of the SDD detector and its readout electronic for the direct and indirect detection of X- or γ-rays. In the direct detection mode X- or γ-rays deposit their whole or a part of their energy directly inside the SDD. A part of the deposited energy is then converted into a number of eh-pairs. In the indirect detection mode X- or γ-rays interact with the scintillator, where the deposited energy is converted into scintillation photons. A fraction of these photons reach the SDD and are transferred with a certain efficiency into the SDD. Each absorbed scintillation photon generates an eh-pair. In both modes the electrons are collected with a certain efficiency at the anode. The amount of charges is converted into an electrical signal, which is further filtered and amplified. The analog signal is then digitized by an analog to digital converter (ADC) and a multi channel analyzer (MCA) converts the digital signal into a number, the ADC channel number. Plotting the channel number into a histogram for a high number of incident photons yields the spectrum.

3.1. Direct detection of X-rays with a Silicon Drift Detector

Silicon Drift Detectors (SDDs) fabricated by PNSensor in Munich are widely used as sensors in high resolution X-ray spectroscopy. The state-of-the-art SDD shows energy resolution values, expressed as the full width at half maximum (FWHM), down to 123 eV of the Mn-K_α peak at moderate operation temperatures of T = -20°C and input count rates up to a few hundreds of kilo counts per second (kcps) with peak-to-background (P/B) values up to 20000. Investigations of the light element performance yielded energy resolution values of 38 eV for the Boron line (180 eV) or 42 eV for the Carbon line (277 eV) [9]. Different detector sizes and shapes have been developed from 5 mm^2 up to 50 cm^2.

3.1.1. Detector working principle

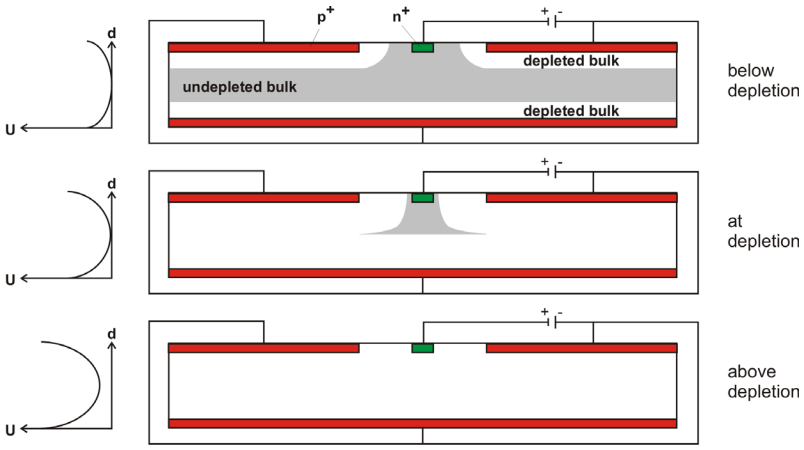

Figure 3.2.: *Concept of sideward depletion*

The working concept of a SDD is based on the principle of sideward depletion, which has been introduced by Gatti and Rehak in the year 1984 [70]. The basic idea is to deplete a n^--type silicon substrate from both sides of the wafer, which are reverse biased p^+-type contacts with respect to a small n^+-type contact (Fig. 3.2). The voltage necessary to reach the depletion is four times lower compared to a pn-diode of the same thickness, due to the relation $W \propto \sqrt{U_{dep}}$, where W is the width of the depletion layer and U_{dep} the depletion voltage.

Most SDDs consist of a low doped n^- silicon (Si) bulk with a thickness of typically 500 μm, a homogeneously boron doped p-type back contact, which represents the radiation entrance window (EW), p^+-type drift rings on the front side, a n^+-type anode and a monolithically integrated junction gate field effect transistor (JFET), which acts as an impedance converter. By applying a negative voltage of approximately -100 V on the back contact, increasing voltages from -10 V (R1) to -100 V (RX) on the drift rings, while setting the bulk contacts OS and IS to 0 V (Fig. 3.3), the Si bulk gets depleted. Fig. 3.3 (on the right) shows a drawing of the potential distribution for electrons with a maximum at RX and a minimum at the anode. Along the blue line there is a potential gradient from RX to the anode, pushing the

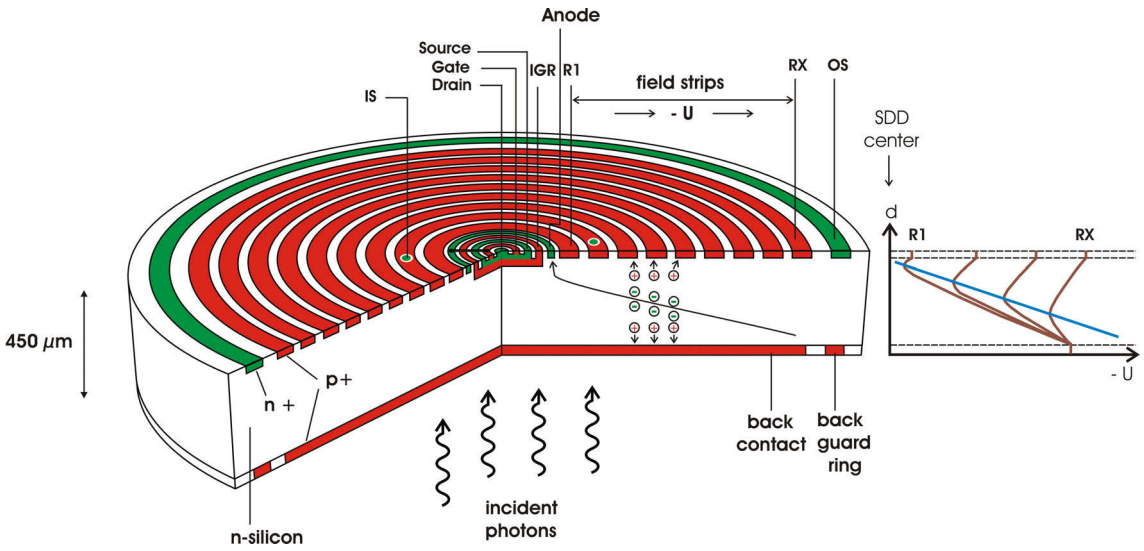

Figure 3.3.: *Drawing of the SDD layout with the entrance window on the side of the back contact (left Fig.); Drawing of the internal potential distribution (brown curves) generated by voltages applied on the drift rings (R1 ≈ -10 to RX ≈ -100 V), back contact (about -100 V) and substrate, OS and IS, (0 V). The inner guard ring, IGR, is needed to decouple the integrated JFET from the SDD bulk. The potential minimum for electrons with a negative gradient from RX to the anode is shown by the blue curve.*

generated electrons in the direction of the anode. The anode is connected to the gate of the JFET (see Fig. 3.4). Electrons reaching the anode change its potential,

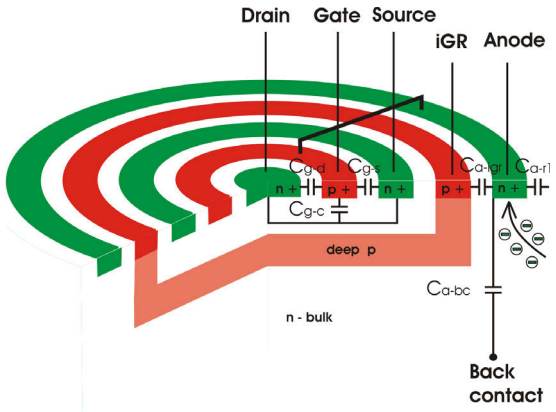

Figure 3.4.: *Zoom into the center of Fig. 3.3 illustrates the cross section of the monolithically integrated JFET and the capacitances seen by the anode.*

hence the potential of the gate by the negative electron charge: $\Delta Q = C \cdot \Delta U$. Due to the fact, that the JFET is biased by applying a positive voltage of about +9 V at the drain and a constant current between source and drain, a change of the anode potential leads to a change of the source potential. This value of the voltage change represents the SDD output. It is proportional to the deposited energy inside the SDD. The SDD output is further amplified, shaped and converted into a digital

channel number. The distribution of these channel numbers, plotted in a histogram yields the overall spectrum. This is a convolution of the X-ray source spectrum with noise contributions of the detector.

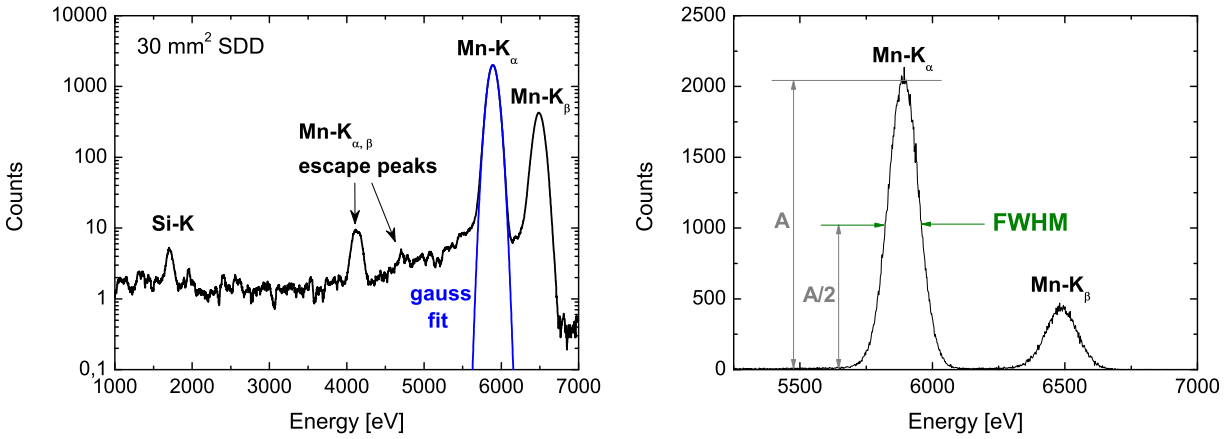

Figure 3.5.: *Left Fig. (logarithmic scale): Spectrum generated by the irradiation of a SDD with a ^{55}Fe source. The Mn-K$_\alpha$ full energy peak is fitted by a Gaussian function. Right Fig. (linear scale): Mn-K$_\alpha$ and Mn-K$_\beta$ peak and the definition of the full width at half maximum (FWHM).*

A spectrum generated by photons from a ^{55}Fe-source inside the SDD is plotted in Fig. 3.5 with a Gaussian fit (blue curve) over the Mn-K$_\alpha$ full energy peak. Peaks in the spectra are called full energy peaks, if the total X-ray energy is deposited inside the sensitive part of the detector. The shape of a peak in a X- or γ-ray spectrum can usually be approximated by a Gaussian distribution. If n processes contributing to the overall fluctuation are statistically independent and happen simultaneously, the square of the overall standard deviation, σ^2, can be expressed by

$$\sigma^2 = \sum_{i=0}^{n} \sigma_i^2, \tag{3.1}$$

where σ_i^2 is the variance of process i. The energy resolution of X- and γ-ray detectors is defined as the full width at half maximum (FWHM), which is illustrated on the example of the Mn-K$_\alpha$ peak in Fig. 3.5 (on the right). The FWHM of a Gaussian distribution is connected to σ in the following way:

$$FWHM = 2.35 \cdot \sigma = 2.35 \cdot \sqrt{\sum_{i=0}^{n} \sigma_i^2}. \tag{3.2}$$

For energy dispersive solid state X-ray detectors the main contributions to the FWHM (Eq. 3.3), is the so called Fano noise, σ_{Fano}(Eq. 3.4), caused by statistical fluctuations in the number of eh-pairs generated after a certain energy is deposited, and the electronic noise σ_{el} (Eq. 3.7):

$$FWHM[N_{eh}] = 2.35 \cdot \sqrt{\sigma_{Fano}^2 + \sigma_{el}^2}. \tag{3.3}$$

The Fano noise contribution (see Sec. 2.1.1) is defined by

$$\sigma^2_{Fano} = F \cdot \sigma^2_{Poisson} = F \cdot \overline{N}_{eh-SDD}. \tag{3.4}$$

The Fano noise sets the lowest limit for the detector energy resolution (continuous line in Fig. 3.6) assuming no electronic noise contribution. For silicon at room temperature F = 0.115 and $\overline{w}$ = 3.65 eV [29, 32]. The electronic noise component (Eq. 3.5) of the FWHM is described by

$$\sigma^2_{el} = \left(\frac{ENC}{e}\right)^2 = (ENC_{el})^2 \tag{3.5}$$

where ENC is the equivalent noise charge, e the electron charge and ENC_{el} the equivalent noise charge expressed in number of electrons. To convert the number of eh-pairs into energy units the FWHM has to be multiplied with $\overline{w}$, the mean energy to create an eh-pair:

$$FWHM(E)[eV] = \overline{w}[eV] \cdot FWHM[N_{eh}] \tag{3.6}$$

The electronic noise (see Eq. 3.7) is composed of three terms. They describe the contributions of the serial white noise, the "1/f" noise of the integrated JFET and the shot noise associated to the leakage current I_l of the detector [71]. Additional noise sources from other electronic components are neglected in the formula, respectively hidden in the factors A_1-A_3. The electronic noise is given by [71]

$$ENC^2 = \frac{4k_BT_{emp}}{3g_m}C^2_{tot}A_1\frac{1}{t_S} + 2\pi a_f C^2_{tot}A_2 + qI_lA_3t_S, \tag{3.7}$$

where k_B is the Boltzmann constant, T_{emp} the temperature, g_m the transconductance of the JFET, a_f the constant parameterizing the JFET "1/f" noise, q the elementary charge, t_S the shaping time, A_1 , A_2 , A_3 the constants depending on the filter functions of the shaper. The first noise component, the white noise, originates from thermal fluctuations of the number of charge carriers at the anode and cathode, which induces a time dependent voltage difference, between the anode and cathode [72]. The white noise decreases with increasing shaping time, due to the fact, that the integration of this time dependent noise component over an increasing period of time approaches a value in a decreasing range around its mean value, which is zero. The second noise component is the 1/f noise, mainly related to trapping processes of charge carriers [71]. This noise component is independent on the shaping time. The third noise component, the shot noise, is generated by a current, which is described by the net statistical flow of charge carriers between two terminals. The collected charge after a time Δt is $\Delta Q = I_l\Delta t$. It is connected to the number of charge carriers by $\Delta N = I_l\Delta t/q$. The standard deviation is approximated by $\sigma(\Delta N) = \sqrt{\Delta N}$ [72], which increases with increasing integration time Δt, hence increasing shaping time, t_S.

The serial white and 1/f noise strongly depend on the total capacitance, C_{tot}, seen by the detector anode (Fig. 3.4). It is a sum of the gate-source capacitance, C_{g-s}, the gate-JFET channel capacitance, C_{g-c}, the gate-drain capacitance, C_{g-d}, and the capacitances between the anode and the neighboring regions, C_{a-igr}, C_{a-r1} and

C_{a-bc} [73] and other parasitic contributions (see Fig. 3.4). The parallel shot noise is mainly determined by the value of the temperature dependent leakage current I_l [3]:

$$I_l(T) \propto T_{emp}^{\frac{3}{2}} exp\left(-\frac{E_g}{2k_B T_{emp}}\right), \tag{3.8}$$

where E_g is the energy gap of silicon.

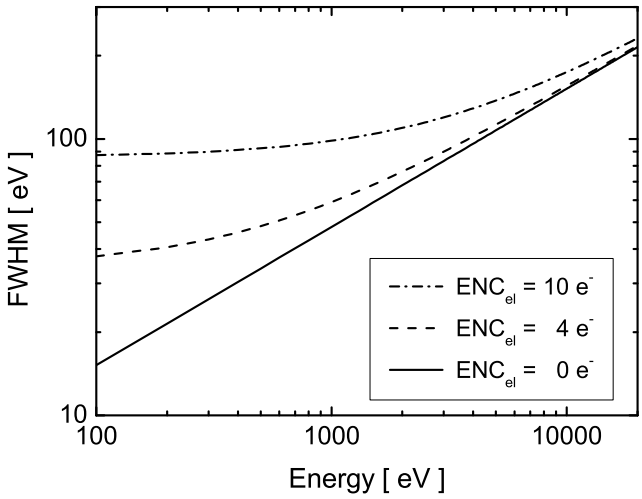

Figure 3.6.: *Energy resolution, FWHM, of silicon radiation detectors plotted against photon energy for different contributions of the electronic noise. The solid line shows the best achievable resolution, which is limited by the Fano noise. The dashed and dash-dotted lines show the energy resolution, if the electronic noise is increased to a value of ENC_{el} = 4 or 10 electrons.*

Fig. 3.6 shows the FWHM[eV], calculated according to Eq. 3.6, in dependence on the incident X-ray energy, E, for two values of the electronic noise, given in units of equivalent noise charge divided by the electron charge (ENC_{el}). If $ENC_{el} = 0$ electrons, the lower limit of the FWHM is determined by the Fano noise (Eq. 3.4), which is the physical limit of the energy resolution. An increase of ENC_{el} to 4, 10 electrons leads to a relative increase of the FWHM especially at lower X-ray energies. At low energies the electronic noise dominates the energy resolution, whereat at higher energies it has a minor contribution.

Additionally, for very low energies only a fraction of the charges generated in the SDD entrance window, which consists of partially sensitive layers and a doped p layer with a high concentration of impurities, are collected at the anode. This partial charge collection can degrade the energy resolution as well.

Methods to improve the energy resolution are the reduction of the total detector capacitance, the leakage current and improving the 1/f perfomance of the JFET. The SDD geometry enables a low anode capacitance independent of the detector size and the monolithic integration of the first JFET. This reduces additionally stray capacitances and avoids pick-up noise or microphony. The capacitance is in

the range C_{tot} = 120 fF to 150 fF for a circular SDD [74, 75]. For dedicated detector designs the total capacitance can be reduced to 50 fF. The leakage current of the SDD is decreased to a stable level down to 100 pA/cm^2 at room temperature, through a new fabrication technology using polysilicone. This further improves the energy resolution. The effect of partial charge collection, not included into the FWHM shown in Fig. 3.6, can also be reduced by an optimized entrance window.

The charge sensitive amplifier (CSA) readout configuration in combination with the pulsed reset operation mode ensures a nearly constant energy resolution up to a few hundred kcps [73], independent of the count rate. The small signal capacitance guarantees a high throughput.

The listed properties of SDDs make them to optimal detectors for X-rays with an excellent energy resolution and high count rate capability. These advantages still hold, if the SDD is used as a photodetector in combination with a scintillator in the following. Before that, results of the direct detection of hard X-rays with the SDD are presented.

3.1.2. Direct hard X- and γ-ray detection

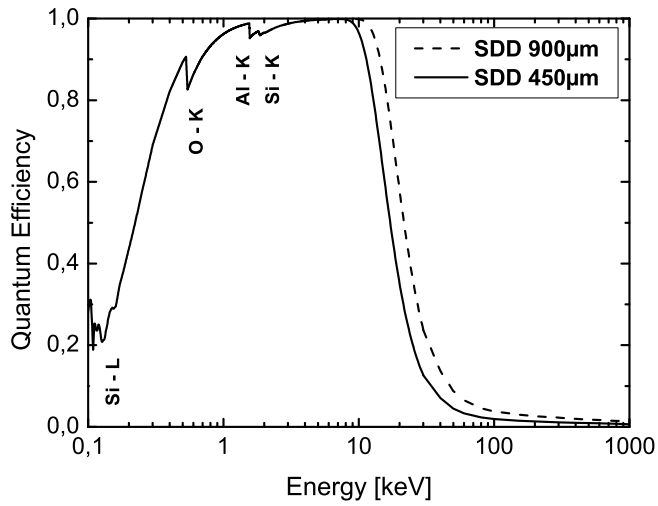

Figure 3.7.: *Calculated energy dependent quantum efficiency for hard X- and γ-rays in a 450 (solid line) and 900 μm (dashed line) thick SDD. Data of the absorption coefficient used in the calculations are taken from [21, 76].*

SDDs can be used as direct detectors in the hard X- and low γ-ray range, where an excellent energy resolution is required. The quantum efficiency of a 450 and 900 μm thick SDD is plotted in Fig. 3.7. Below 10 keV both quantum efficiencies are equal, with a decreasing value to low energies. The quantum efficiency (QE) decreases, because an increasing number of X-ray photons is absorbed inside the partially sensitive layers of the entrance window. Doubling the SDD thickness leads to a QE $>$ 0.6 for energies up to 20 keV. At E = 60 keV the quantum efficiency is still 0.065. The probability of Compton scattering in Si becomes dominant for energies larger than 50 keV (Fig. 2.1 on the left).

Spectra, which have been measured during irradiation of a 450 μm SDD with ^{57}Co and ^{241}Am sources are shown in Fig. 3.8. The measured values of the relative energy resolution, R = FWHM/E are R(24.9 keV) = 1.1 % and R(59.5 keV) = 0.67 %. The energy resolutions of SDDs belong also in the hard X- and γ-ray range to the best measured values. The relative energy resolution decreases with increasing photon energy. The quantum efficiencies at these energies are QE(24.9 keV) = 0.2 (0.36 for the 900 μm thick SDD) and QE(59.5 keV) = 0.033 (0.065 for the 900 μm thick SDD).

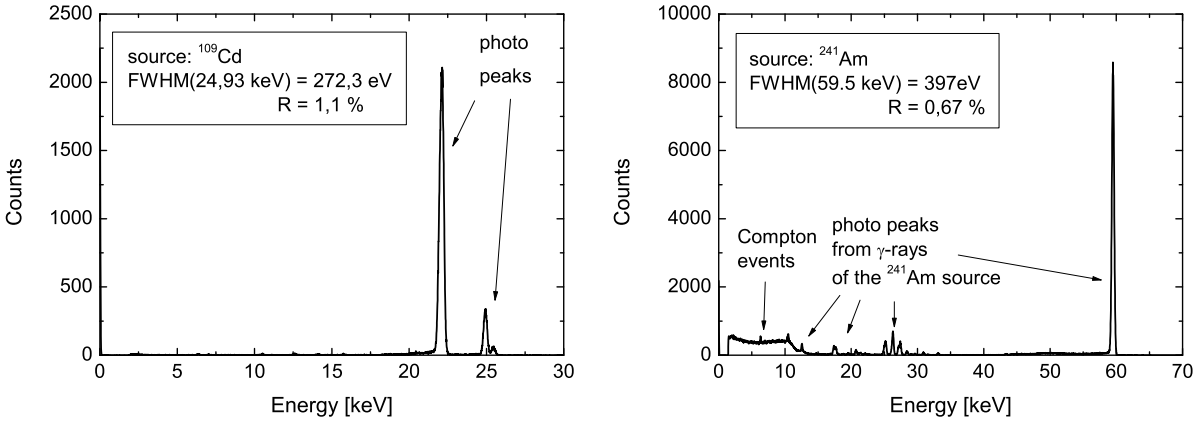

Figure 3.8.: *Spectrum of ^{109}Cd (21.99, 22.16, 24.91, 24.94 and 25.1 keV) and ^{241}Am (59.5 keV) measured with a SDD, having an active area of 30 mm^2, at - 20° C and a shaping time of 1 μs.*

The energy resolution values of a SDD coupled to CsI(Tl) (diameter 5 mm and thickness 10 mm) are R(22.1 keV) $\approx$ 6 % and R(59.5 keV) $\approx$ 10 % and to $LaBr_3$(Ce) (diameter 5 mm and thickness 10 mm) R(22.1 keV) $\approx$ 10 % and R(59.5 keV) $\approx$ 18 %.

3.2. Indirect detection of X- and γ-rays with a SDD coupled to a scintillator

The principles of γ-ray detectors consisting of a scintillator coupled to a SDD are illustrated in (Fig. 3.9). The energy of incident γ-rays is partially or fully converted into scintillation photons, depending on the type of interaction of the γ-rays with the scintillator. The mean number of generated scintillation photons, $\overline{N}_{ph}$, depends on the scintillator light yield, $\overline{L}$, and the magnitude of the deposited energy. The photons propagate isotropically into all directions from the generation point. All sides and faces of the scintillator but one are covered by a reflector (Fig. 3.9). The face with no reflector is in contact with the optical coupler and the photodetector (Fig. 3.9). The scintillation photons are reflected or transmitted on the scintillator interfaces, reflected or absorbed on the reflector surface until being absorbed inside the scintillator or reaching the SDD entrance window (Fig. 3.9). There the photons are reflected, absorbed or transmitted into the SDD. The entrance window of the SDD should be optimized, to ensure a high transmission probability for incident

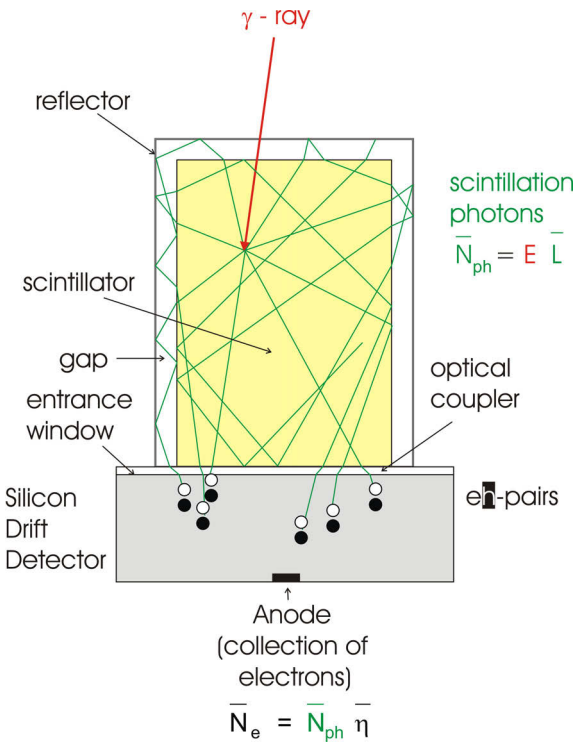

Figure 3.9.: *Drawing of a γ-detector consisting of a scintillator coupled to a Silicon Drift Detector (SDD) with the illustration of the conversion of the deposited energy into a number of electron hole pairs.*

scintillation photons. After the absorption inside the SDD, eh-pairs are generated. The electrons are collected at the SDD anode and the amount of collected charges is converted into a voltage pulse and further processed by the electronics. The mean number of collected electrons is an indicator for the amount of deposited energy inside the detector:

$$\overline{N}_e = \overline{N}_{ph}\overline{\eta} = E\overline{L}\overline{\eta} \tag{3.9}$$

where $\overline{\eta}$ is the mean system quantum efficiency for scintillation light. $\overline{\eta}$ is composed of the transfer efficiency of photons into the SDD times the conversion efficiency into eh-pairs times the collection efficiency of the generated electrons at the anode.

Fig. 3.10 shows spectra measured with a detector consisting of a SDD + $LaBr_3$(Ce) (blue) or SDD + CsI(Tl) (green) during irradiation with a ^{137}Cs source, which emits γ-rays with an energy of E = 662 keV. The scintillators are cylindrically shaped with a diameter of approximately 5 mm and a thickness of 10 mm. The relative energy resolution, R = FWHM/E, of the photo peak at E = 662 keV is about 3 % for SDD + $LaBr_3$(Ce) and 4.5 % for SDD + CsI(Tl). The energy resolution of the SDD + $LaBr_3$(Ce) detector is better at 662 keV compared to the SDD + CsI(Tl) detector, because of different energy dependent non-proportionality contributions to the energy resolutions of the two scintillators, $LaBr_3$(Ce) and CsI(Tl) (see Chap. 6).

The quantum efficiency of an SDD at 662 keV is lower than 1%, so that it is almost transparent and not suitable as detector material for such high energies.

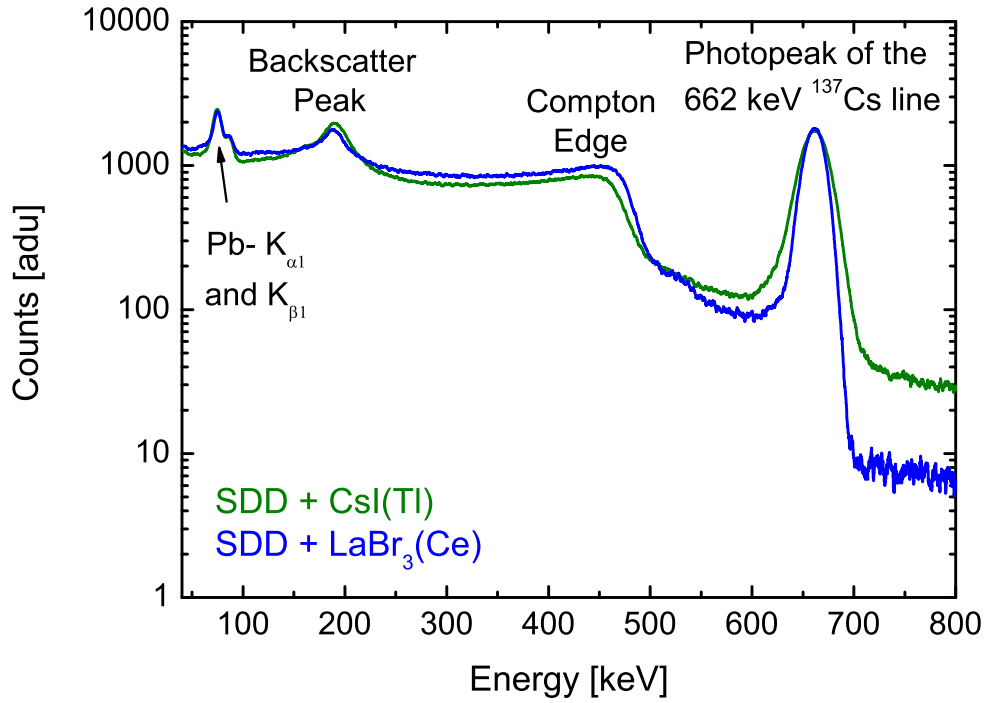

Figure 3.10.: *Spectra measured with a SDD with an active area of 30 mm^2 coupled to a cylindrical, 1 cm thick $LaBr_3(Ce)$ (blue) and CsI(Tl) (green) for γ-rays with an energy of E = 662 keV. The fluorescence peaks Pb-$K_{\alpha 1}$ and Pb-$K_{\beta 1}$ originate from the lead collimator.*

4. The relevant contributions to the energy resolution

Inside X- or γ-ray detectors the deposited energy is converted by several processes into an output signal (compare Fig. 3.9). These processes are of statistical nature and can happen simultaneously or after each other, forming a cascade. Furthermore, in some cases processes have to be taken into account, which are of composite nature. This means for example that the mean probability $\overline{p}_i$ for a process to occur can change from one event to another. The magnitude and resolution of the output signal are described by the mean value and variance of the overall process. The statistical background for its calculation is presented in App. B.

4.1. Derivation of the formula for the relative energy resolution

Based on the general considerations outlined in App. B a formula for the energy resolution will be derived in this section. The mean number of signal electrons,

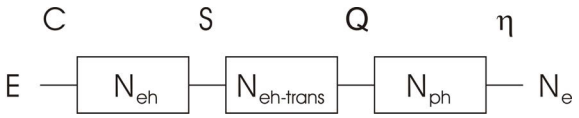

Figure 4.1.: *Scheme of the conversion of the deposited energy, E, into signal electrons, N_e, at the SDD anode, with the efficiencies $\overline{C}$, $\overline{S}$, $\overline{Q}$ and $\overline{\eta}$.*

$\overline{N}_{e,j}$, reaching the SDD anode (Fig. 4.1), after an interaction, j, of a γ-ray with the scintillator and the deposited energy, E, can be described by the formula

$$\overline{N}_{e,j} = E\overline{C}_j\overline{S}_j\overline{Q}_j\overline{\eta}_j = \overline{N}_{eh,j}\overline{S}_j\overline{Q}_j\overline{\eta}_j, \tag{4.1}$$

where $\overline{C}_j = 1/\overline{w}_{scint,j}$ is the conversion efficiency of the deposited energy into eh-pairs, $\overline{N}_{eh,j}$, inside the scintillator. Inserting Eq. 2.22 into 3.9 results into Eq. 4.1. In the following, the two processes, the transfer of thermalized electrons and holes to luminescence centers with the efficiency, $\overline{S}_j$, and the radiative recombination of eh-pairs, $\overline{N}_{eh-trans}$, at the excited luminescence centers with the efficiency, $\overline{Q}_j$, are summarized to one process with the efficiency $\overline{T}_j = \overline{S}_j \cdot \overline{Q}_j$. It describes the conversion of eh-pairs into scintillation photons, $\overline{N}_{ph}$. In the new notation Eq. 4.1 changes to

$$\overline{N}_{e,j} = \overline{N}_{eh,j}\overline{T}_j\overline{\eta}_j. \tag{4.2}$$

The overall process leading to the generation of signal electrons and their collection at the SDD anode is denoted as G, which is sub-divided into three processes: the

conversion of the deposited energy into eh-pairs, the conversion of eh-pairs into scintillation photons and the conversion of scintillation photons into signal electrons. These processes are denoted as A, B and D.

The probability distribution of N_{eh} is approximated in semiconductors by a Gaussian distribution, which has a mean value of $\overline{N}_{eh}$ and a variance of $Var(N_{eh}) = F \cdot \overline{N}_{eh}$. F is the Fano factor of the semiconductor material (compare Sec. 3.1). The relative variance is $v(N_{eh}) = F/\overline{N}_{eh}$. We are adapting this approximation also for materials with a larger band gap, such as scintillators, where F_{scint} is the Fano factor of the scintillator. A second approximation is made by assuming that the processes denoted by A, B and D are statistically independent. All three processes happen after each other, forming a cascade. Furthermore, the mean values $\overline{T}_j$ and $\overline{\eta}_j$ change frequently from one event, j, to another, because the processes denoted as B and D consist of several competing processes. Process B can be described by an energy dependent conversion efficiency, $\overline{T}(E)$, of eh-pairs into scintillation photons, (Sec. 4.2), which results in an energy dependent light yield $\overline{L}(E)$ (Eq. 2.23). Due to the fact, that $\overline{L}(E) \neq constant$, the light yield is said to be "non-proportional". The efficiency, $\overline{\eta}_j$, of process D depends on the position, where the scintillation photons are generated inside the scintillator (Sec. 4.3). This changes from one event, j, to another, because the source emits γ-ray photons into a certain solid angle, which interact in a certain depth range. The relative variance of the overall process can be determined in analogy to Eq. B.28 and B.29 with the result

$$v(N_e) = v(N_{eh}) - \frac{1}{\overline{N}_{eh}} + v(T \cdot \eta)\left(1 + v(N_{eh}) - \frac{1}{\overline{N}_{eh}}\right) + \frac{1}{\overline{N}_{eh}\overline{T}\overline{\eta}}. \tag{4.3}$$

The relative variance, $v(T \cdot \eta)$, of the product of the efficiencies T and η can be written as

$$v(T \cdot \eta) = v(T) + v(\eta) + v(T) \cdot v(\eta) \tag{4.4}$$

[77]. Inserting Eq. 4.4 into 4.3 yields

$$\begin{aligned} &v(N_e) \\ &\quad = v(N_{eh}) - \frac{1}{\overline{N}_{eh}} + (v(T) + v(\eta) + v(T) \cdot v(\eta))\left(1 + v(N_{eh}) - \frac{1}{\overline{N}_{eh}}\right) + \frac{1}{\overline{N}_{eh}\overline{T}\overline{\eta}} \end{aligned} \tag{4.5}$$

The relative variance, $v(N_{eh})$, is the Fano noise contribution of the scintillator

$$v(N_{eh}) = \frac{F_{scint}}{\overline{N}_{eh}}. \tag{4.6}$$

F_{scint} is the Fano factor of the scintillator. $v(N_{eh})$ is replaced by the right hand side of Eq. 4.6 in the following. The relative variance of the signal electrons specified in Eq. 4.5 can be approximated by

$$\begin{aligned} v(N_e) &\approx \frac{F_{scint}}{\overline{N}_{eh}} - \frac{1}{\overline{N}_{eh}} + v(T) + v(\eta) + \frac{1}{\overline{N}_{eh}\overline{T}\overline{\eta}} \\ &= \frac{F_{scint}}{\overline{N}_{eh}} + v(T) + v(\eta) + \frac{1 - \overline{T}\overline{\eta}}{\overline{N}_e}, \end{aligned} \tag{4.7}$$

where $\overline{N}_e = \overline{N}_{eh}\overline{T}\overline{\eta}$. The terms resulting from the multiplication of two or more relative variances, including the term $1/\overline{N}_{eh}$, which is the definition of the relative Poisson variance, are neglected. The value of $v(T)$, which is determined in Chap. 6 is the largest compared to the other contributions in Eq. 4.7. For γ-energies around E = 10 keV $v(T)$ has a value of about 0.007. $v(T)^2$ can be neglected compared to $v(T)$.

The relative variance of signal electrons in Eq. 4.7 is composed of four terms, which could be interpreted in the following way: The first term is the relative variance of the Fano noise contribution, $F_{scint}/\overline{N}_{eh}$, originating from the conversion process of the deposited γ-energy inside the scintillator into eh-pairs. $v(T)$, is the relative variance, originating from the conversion process of generated electron hole pairs into scintillation photons. $v(\eta)$ is the relative variance, originating from the transfer process of scintillation photons into the SDD, the conversion into electron hole pairs and the collection of signal electrons at the anode. The last term can be interpreted as the relative variance of the number of signal electrons, which is given by the variance of a binomial probability distribution with the conversion efficiency, $\overline{T}\cdot\overline{\eta}$, of the generated electrons and holes inside the scintillator into signal electrons inside the SDD.

Breitenberger derived the following formula for the relative signal variance for a detector consisting of a scintillator coupled to a photomultiplier (PMT) [78]:

$$\begin{aligned} v(N_{e,M}) &= v(N_{ph}) - \frac{1}{\overline{N}_{ph}} + v(\eta)\left(1 + v(N_{ph}) - \frac{1}{\overline{N}_{ph}}\right) + \frac{1+v(M)}{\overline{N}_{ph}\overline{\eta}} \\ &\approx v(N_{ph}) - \frac{1}{\overline{N}_{ph}} + v(\eta) + \frac{1+v(M)}{\overline{N}_{ph}\overline{\eta}}. \end{aligned} \tag{4.8}$$

$N_{e,M}$ is the number of electrons after the multiplication process inside the PMT. $v(M)$ considers the relative variance of the PMT gain, M. In a detector consisting of a scintillator coupled to a SDD, with an SDD gain of 1, the gain variation is negligible. Breitenberger has not included statistical processes contributing to the generation of scintillation photons, N_{ph}, into the derivation of formula 4.8.

The contribution of the electronic noise to the variance of the number of signal electrons, calculated by Eq. 4.7, has not been included yet. The process for the generation of signal electrons inside the SDD can be described by two main processes. One process generates signal electrons, due to electronic noise sources. The other process generates signal electrons, due to the conversion of photons into electron hole pairs and the collection of the electrons at the SDD anode. Both processes occur simultaneously and are assumed to be independent of each other. The variance including the electronic noise can be calculated by (comp. Sec. B.1.1)

$$Var(N_{e-el}) = Var(N_e) + Var(N_{el}). \tag{4.9}$$

The total "relative" variance, V_{tot}, including the electronic noise, is defined by

$$V_{tot} = \frac{Var(N_{e-el})}{\overline{N}_e^2} = \frac{Var(N_e) + Var(N_{el})}{\overline{N}_e^2} = v(N_e) + \frac{ENC_{el}^2}{\overline{N}_e^2}. \tag{4.10}$$

In this definition the relative variance of the signal electrons, including the electronic

noise, is

$$V_{tot} \approx \frac{F_{scint}}{\overline{N}_{eh}} + v(T) + v(\eta) + \frac{1-\overline{T}\overline{\eta}}{\overline{N}_e} + \frac{ENC_{el}^2}{\overline{N}_e^2}. \tag{4.11}$$

The pulse height distribution of the detector output signal is usually approximated by a Gaussian distribution (comp. Sec. 3.1) with the relative energy resolution defined as the relative full width at half maximum of a Gaussian peak, $\mathrm{R} = \mathrm{FWHM}_{rel} = 2.35\sqrt{V_{tot}}$. The total energy resolution of the γ-detector system, SDD coupled to a scintillator, can be expressed as

$$R \approx 2.35\sqrt{\frac{F_{scint}}{\overline{N}_{eh}} + v(T) + v(\eta) + \frac{1-\overline{T}\overline{\eta}}{\overline{N}_e} + \frac{ENC_{el}^2}{\overline{N}_e^2}}. \tag{4.12}$$

Eq. 4.12 shows that the energy resolution can be improved, if the following criteria are fulfilled:

1. a low electronic noise ENC_{el}
2. scintillators, which produce a high number of eh-pairs, $\overline{N}_{eh}$, and scintillation photons, $\overline{N}_{ph}$
3. a high transfer efficiency, $\overline{T}$, and system quantum efficiency, $\overline{\eta}$, for scintillation photons
4. scintillators with a small non-proportionality contribution, $v(T)$
5. a low contribution of the light collection non-uniformity, $v(\eta)$

In literature the contributions to the relative energy resolution in the γ-ray range are generally expressed by $R_i = 2.35\sqrt{v_i}$. In this notation Eq. 4.12 has the form:

$$R^2 = R_{Fano-Scint}^2 + R_T^2 + R_\eta^2 + R_{Bino}^2 + R_{el}^2. \tag{4.13}$$

In literature the Fano noise of the scintillator is generally not investigated and instead of the binomial variance, the Poisson variance is usually used to describe the statistical fluctuation of the number of signal charge carriers (see e.g. [48, 14]). This approximation cannot be applied to modern scintillation detectors, due to a large conversion efficiency of electrons and holes inside the scintillator into signal electrons inside the photodetector. In literature the energy resolution is usually expressed by

$$R^2 = R_T^2 + R_\eta^2 + R_{stat}^2 + R_{el}^2 \tag{4.14}$$

where $\mathrm{R}_{stat} = 2.35\sqrt{1/\overline{N}_e}$.

Contributions to the magnitude of R_T are originating from the transfer process, S, of the energy of thermalized electrons and holes to the luminescence centers and the process of radiative relaxation of the luminescence centers, Q. Additionally inhomogeneity in the doping concentration of luminescence centers inside the scintillator

can lead to a further variation in the number of generated scintillation photons from one event to another. This could increase the value of R_T furthermore. The doping concentration in small scintillators, which are investigated in this work, are to a high degree homogeneous. In these scintillators the local light yield variation is about $\pm 0.25\%$ [79], so that the noise contribution, due to inhomogeneity of the doping concentration, can be neglected.

Contributions to R_η are originating from the variance of η, which is determined by the collection efficiency, K, of scintillation photons at the SDD entrance window, the transfer efficiency, T_{ew}, of the scintillation photons through the SDD entrance window, the absorption efficiency, A_{sv}, inside the sensitive SDD volume, the conversion efficiency of scintillation photons into eh-pairs inside the SDD, which is $C_{SDD} = 1$, and the charge collection efficiency, CCE, of signal electrons at the SDD anode:

$$\overline{\eta} = \overline{K} \cdot \overline{T}_{ew} \cdot \overline{A}_{sv} \cdot \overline{CCE} = \overline{K} \cdot \overline{QE} \tag{4.15}$$

where $\overline{QE}$ the mean quantum efficiency of the SDD for the scintillation light.

In order to get an imagination of the magnitude of the different noise contributions, in Fig. 4.2 the energy resolution

$$R = \sqrt{R^2_{Fano-Scint} + R^2_{Bino} + R^2_{el}} \tag{4.16}$$

is plotted against the deposited energy inside the scintillator for three electronic noise values: $ENC_{el} = 0$ (black solid line), $ENC_{el} = 8$ (blue dotted line) and $ENC_{el} = 40$ (blue dashed line) electrons. The Fano factor of the scintillator is set to $F_{scint} = 0.28$ and the light yield to a constant value of $\overline{L} = 65$ photons/keV for all energies. The red solid line shows the value of R (Eq. 4.16) for $F_{Scint} = 1$. The contribution of the electronic noise, R_{el}, with an equivalent noise charge of $ENC_{el} = 40$ electrons becomes important for energies $E < 100$ keV. The contribution of R_{el} for $ENC_{el} = 8$ can be neglected for energies $E > 100$ keV and has a small contribution for $E < 100$ keV.

In Fig. 4.2 the difference in the energy resolution is recognizable for the two values of the Fano factor, $F_{Scint} = 1$ (red line) or $F_{Scint} = 0.28$ (black line). The energy resolution improves with a decreasing Fano factor of the scintillator.

In this work we put our focus on the investigation of the light yield non-proportionality contribution, R_T, and the contribution R_η, originating from the light transfer into the SDD, eh-pair generation inside the SDD and signal electrons collection at the SDD anode with the overall associated efficiency $\overline{\eta}$.

4.2. Scintillator non-proportional light yield

In the following section the physical reasons leading to the statistical variance, $v(T)$, of T will be explained. In the year 1961 it has been pointed out that the unknown contribution to the energy resolution of NaI(Tl) can be attributed to the non-proportional light yield of NaI(Tl) [80, 81]. It has been calculated that the non-proportional light yield of NaI(Tl) leads to a broadening of the energy resolution [80, 81].

After an interaction of a γ-photon with an atom of the scintillator via photo effect, an electron is ejected from an inner shell, so that the atom remains in an excited

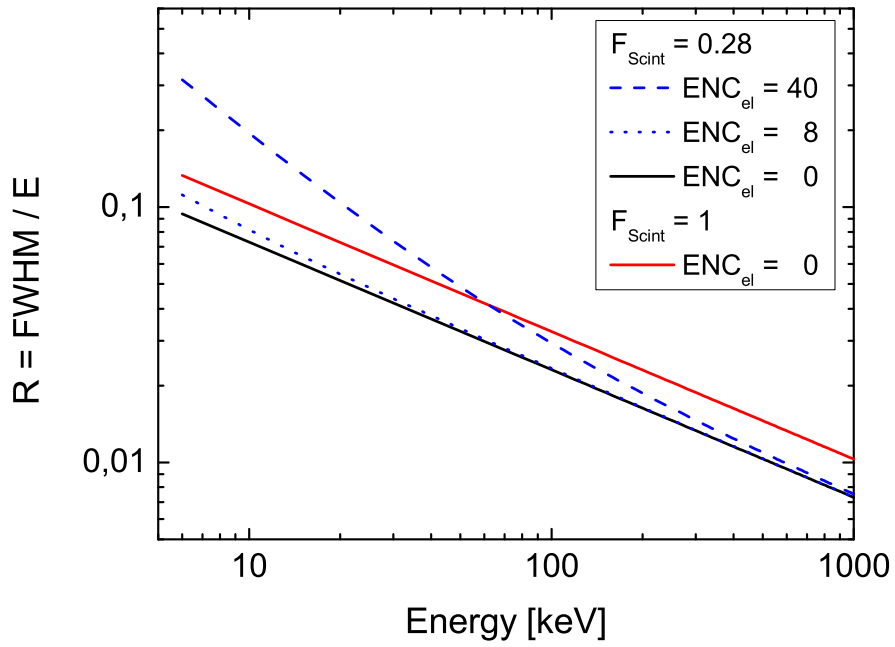

Figure 4.2.: *Energy resolution R described by Eq. 4.16 with the parameters* $\overline{w}_{Scint} = 13.3$ *eV,* $\overline{L} = 65$ *photons/keV for all energies and* $\overline{\eta} = 0.8$ *of CsI(Tl) (comp. Sec. 2.2 and Sec. 6.2.2).*

state. The atom relaxes by filling the hole with electrons from upper shells, producing fluorescence photons and Auger electrons. After a Compton interaction a bound electron is ejected into a free state and the Compton scattered photon escapes the scintillator or interacts again via photo effect or Compton scattering. The generated Compton, photo and Auger electrons lose their energy by generating secondary electrons through ionization scattering and bremsstrahlung. Considering mono energetic γ-rays with an energy E, which is fully deposited inside the scintillator, the number, M_j, and the energy distribution among the generated Compton, photo and Auger electrons differs for each event, j, due to the fact, that Compton, photo and Auger processes occur with certain probabilities inside the scintillator.

In order to calculate the mean number of generated scintillation photons, $\overline{N}_{ph,j}$, after a γ-event j, the number of photons generated by Compton, photo and Auger electrons have to be summed up. Therefore, the energy dependent mean light yield for electrons is

$$\overline{L}_e(E_e) = \frac{\overline{N}_{ph}}{E_e} = \frac{\overline{T}_e}{\overline{w}_{scint}} \tag{4.17}$$

where E_e is the electron energy, which has to be known.

The light yield of electrons can be measured by the so called Compton Coincidence Technique (CCT). The coincidence technique measures only the pulse height of the energy deposited by electrons, which are produced by γ-rays that are Compton scattered through a specific angle inside the scintillator and measured in coincidence with the Compton scattered photon, which is detected by a high resolution

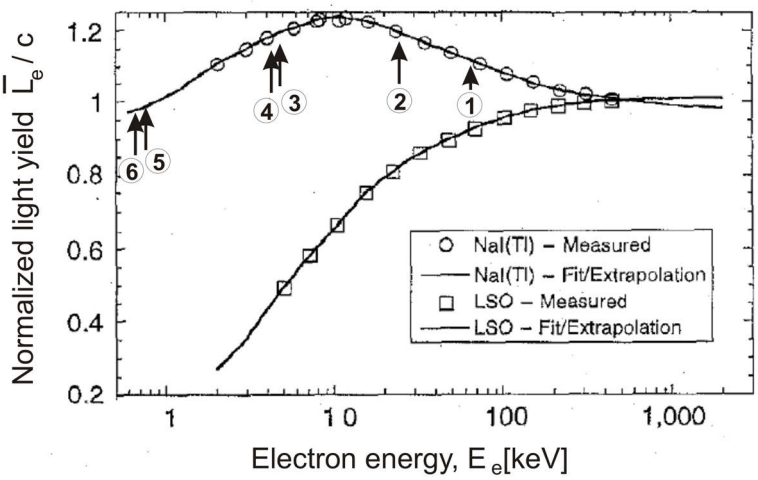

Figure 4.3.: *Measured normalized light yield of NaI(Tl) (circles) and LSO (squares) for electrons [82]. In addition one possibility of how the deposited energy inside the scintillator can be distributed among photo and Auger electrons.*

Germanium detector [83].

Fig. 4.3 shows the normalized mean light yield, $\overline{L}_e/c$, for electrons in NaI(Tl) and LSO [82]. The non-proportional behavior, which means $\overline{L}_e/c \neq constant$, is clearly visible. The normalized light yield of both scintillators rises from low electron energies up to an energy of 10 keV. It decreases for NaI(Tl) for increasing electron energies from 10 keV to 450 keV, which is characteristic for alkali halide scintillators, whereas for LSO it increases further in that range and saturates, which is characteristic for non-alkali halide scintillators.

The energy dependence of the light yield can be explained as follows. The decrease of the light yield from 10 keV to lower electron energies in NaI(Tl) is due to an increase of the deposited energy density, which originates from the increase of the differential energy loss, -dE/dx, with decreasing particle energies (see Sec. 2.1.1). An increase of the deposited energy density leads to an increasing density of eh-pairs, which again leads to a reduction of the radiative recombination efficiency, due to an Auger-like quenching [84, 52, 53, 54]. In such a case the scintillation photon generated by the recombination of an eh-pair excites an exciton and separates the electron from the hole. For these electrons, there is again a certain probability to recombine non-radiatively. This circumstance increases the probability of non-radiative recombination.

The decrease of the light yield from 100 keV to higher energies occurs, due to a reduction of the density of the generated electrons and holes. A lower density is equivalent to a larger distance of electrons and holes, which reduces their recombination probability, due to Coulomb attraction [85, 86], especially if the electron and hole mobilities are low (cm^2/Vs) and have a larger difference. Different mobilities of electrons and holes cause a separation of the electrons from the holes to a certain fraction, due to the diffusion of electrons and holes from the track, where they have been generated, with different velocities [54, 87]. Low mobilities increase the

probability that electrons and holes do not find each other to recombine radiatively. The mobilities ($\mu \propto 1/m^*$ where μ is the mobility and m^* the effective mass) of electrons and holes have a larger difference in alkali halide, than in non-alkali halide scintillators [52], so that the decrease of the light yield at low ionization densities is more pronounced in alkali halide scintillators.

A short example should illustrate the distribution of the deposited energy among photo, Compton and Auger electrons. A γ-photon with an energy of 100 keV can interact via photo effect with NaI by ejecting an electron from the K-shell of the Iodine atom. This photo electron has the kinetik energy E_{kin1} = 100 keV-$E_b(I_K)$ = 66.8 keV (Light yield of the first photo electron is denoted as 1 in Fig. 4.3), where $E_b(I_K)$ = 33.2 keV is the binding energy of the K-shell electron. The hole created in the Iodine K-shell can be filled by an electron from the L-shell, generating a fluorescence photon with an energy of 32.3 keV. This fluorescence photon can generate a second photo electron by ejecting an electron from the L-shell of another Iodine atom. The second photo electron has the kinetic energy E_{kin2} = 32.3 keV-$E_b(I_L)$ = 27.2 keV (Light yield of the second photo electron is denoted as 2 in Fig. 4.3), with $E_b(I_L)$ = 5.1 keV. The remaining holes in the L-shells of both atoms can be filled with electrons from upper shells. This process can lead to the generation of four Auger electrons (Light yields of the four Auger electrons are denoted as 3, 4, 5 and 6 in Fig. 4.3). The energy deposited by the γ-ray is distributed among 6 electrons in this example. In a second energy deposition the described interaction can occur with a Natrium atom, which has different K- and L-shell binding energies compared to the Iodine atom, so that the energy distribution of the generated electrons will differ, just as the number of scintillation photons, if the mean light yield $\overline{L}_e$ of the generated electrons depends on their energy.

The mean number of scintillation photons, $\overline{N}_{ph,j}$, determined by the energy dependent non-proportional mean light yield for electrons, $\overline{L}_e(E_e)$ (Fig. 4.3), and the energy distribution among the Compton, photo and Auger electrons with a total energy E, deposited by a γ-ray inside the scintillator in the event j, can be calculated by

$$\overline{N}_{ph,j} = \sum_{i=1}^{M_j} E_{e,i}\overline{L}_e\left(E_{e,i}\right) = \sum_{i=1}^{M_j} E_{e,i}\frac{\overline{T}_e(E_{e,i})}{\overline{w}_{scint}} = \sum_{i=1}^{M_j} \overline{N}_{eh,i}\overline{T}_e(E_{e,i}) = \overline{N}_{eh}\overline{T}_j. \quad (4.18)$$

M_j is the number of generated Compton, photo and Auger electrons generated by the j-th $\gamma-$ray interaction and $E_{e,i}$ is the energy of the i-th electron. The mean number of generated scintillation photons $\overline{N}_{ph}$ is

$$\overline{N}_{ph} = \frac{\sum_{j=1}^{m}\overline{N}_{ph,j}}{m} = \frac{\sum_{j=1}^{m}\overline{N}_{eh}\cdot\overline{T}_j}{m} = \overline{N}_{eh}\frac{\sum_{j=1}^{m}\overline{T}_j}{m} = \overline{N}_{eh}\overline{T} \quad (4.19)$$

where m is the number of mono energetic γ-rays. The relative variance of $\overline{N}_{ph,j}$ can be calculated by

$$v(\overline{N}_{ph,j}) = \frac{\sum_{j=1}^{m}(\overline{N}_{ph,j}-\overline{N}_{ph})^2}{m\cdot\overline{N}_{ph}^2} = \frac{\sum_{j=1}^{m}\overline{N}_{eh}^2(\overline{T}_j-\overline{T})^2}{m\cdot(\overline{N}_{eh}\cdot\overline{T})^2} = \frac{\sum_{j=1}^{m}(\overline{T}_j-\overline{T})^2}{m\cdot\overline{T}^2} = v(\overline{T}_j). \quad (4.20)$$

If the light yield would not depend on the energy, Eq. 4.18 changes to

$$\overline{N}_{ph,j} = \sum_{i=1}^{M_j} E_{e,i}\overline{L}_e = \overline{L}_e \sum_{i=1}^{M_j} E_{e,i} = \overline{N}_{ph} \tag{4.21}$$

where $v(\overline{N}_{ph,j}) = v(\overline{T}_j) = 0$.

The energy dependent light yield, $\overline{L}_e(E_e) = \overline{T}_e(E_e)/\overline{w}_{scint}$, for electrons in combination with the variation of the number and energy distribution of Compton, photo and Auger electrons, leads to a frequently changing mean conversion efficiency, $\overline{T}_j$ (Eq. 4.18), and to a contribution to $v(T)$. This contribution to $v(T)$ is investigated for $LaBr_3$(Ce) and CsI(Tl) in Subsec. 6.1.1 and 6.2.1 respectively. Furthermore, the energy dependent light yield, $\overline{L}_e(E_e)$, for electrons leads to an energy dependent light yield, $\overline{L}(E)$, for $\gamma-$rays, which is also investigated for $LaBr_3$(Ce) and CsI(Tl) in Subsec. 6.1.1 and 6.2.1 respectively.

In Fig. 4.4 the normalized light yield, $\overline{L}_n$, of NaI(Tl) is plotted against the incident γ-energy. $\overline{L}_n$ is defined as

$$\overline{L}_n = \frac{\overline{L}}{c} = \frac{\overline{N}_{ph}}{E \cdot c} = \frac{\overline{N}_{eh} \cdot \overline{T}}{E \cdot c} = \frac{E \cdot \overline{T}}{\overline{w}_{scint} \cdot E \cdot c} = \frac{\overline{T}}{\overline{w}_{scint} \cdot c} \tag{4.22}$$

where c is the normalization constant. c is set to a value, so that $\overline{L}_n$(E) = 1 for incident γ-rays with an energy of E = 662 keV. A proportional light yield would be a constant, if plotted against E. This is not the case as shown in Fig. 4.4. $\overline{L}_n$ increases from low γ-energies to 20 keV, has two maxima in the energy range between 10 and 60 keV and decreases again towards higher energies. The minimum around 33 keV occurs, due to the K-absorption edge of Iodine. For γ-energies above this edge, there is the probability to generate a photo electron from the K-shell. Before and after the edge the deposited energy inside the NaI(Tl) scintillator is distributed among a different set of electrons with different energies. The decrease of the light

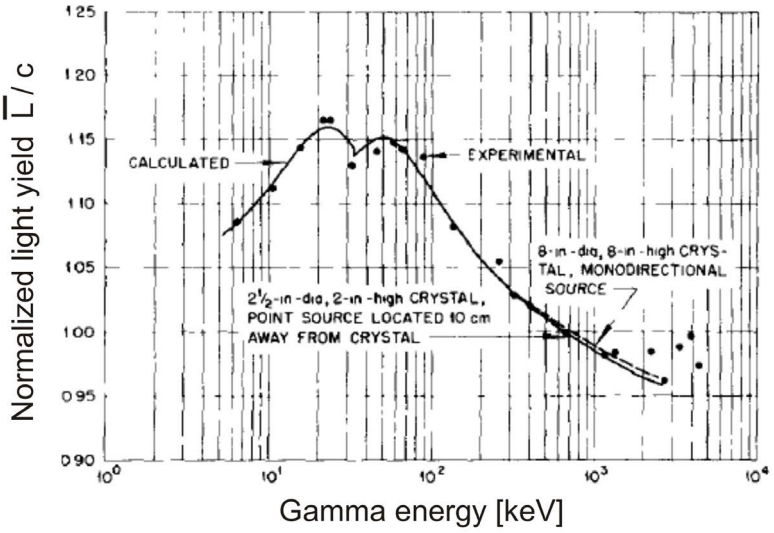

Figure 4.4.: *Normalized light yield of NaI(Tl) for incident γ-rays taken from [80]*

yield from 20 keV to lower γ-energies is due to an increase of the ionization density

in combination with the low mobilities of electrons and holes. The decrease of $\overline{L}_n$ above 50 keV is due to a decreasing ionization density in combination with a low mobility of electrons and holes and a larger difference between their value [54, 87].

The calculations in Eq. 4.18 - 4.21 are only taking the mean value of the electron light yield, $\overline{L}_e(E_e)$, into account. The variation of $\overline{L}_{e,j}(E_e)$, which results also from the variation of $\overline{T}_{e,j}(E_e)$ from one event, j, to another for a certain electron energy, E_e, has been neglected so far. Taking its variation into account does not change the mean values $\overline{N}_{ph,j}$ and $\overline{N}_{ph}$, but increases the relative variance $v(\overline{N}_{ph,j}) = v(\overline{T}_j)$.

A contribution to the variance $v(T_e(E_e))$ originates also from the energy dependence of its mean value $\overline{T}_e(E_e)$. Each of the electrons resulting from Compton, photo and Auger effect loses its energy by ionization. The ionization density is proportional to the deposited energy per track length -dE/dx, which can be parameterized by the Bethe formula presented in Sec. 2.1.1. -dE/dx depends on the electron energy, hence on its path through the scintillator. Fluctuations in the ionization density (Landau fluctuations) in combination with the energy dependent light yield for electrons lead to a degradation of the energy resolution [49] by increasing the value of $v(T_e)$.

4.3. Light and charge collection in the system SDD + scintillator

Besides the contribution of a non-proportional light yield of the scintillator to the energy resolution, it depends also on the transfer of scintillation photons into the SDD and the charge collection of the generated signal electrons inside the SDD. Optical properties of the scintillator, reflector and SDD entrance window determine the detection efficiency of scintillation photons. Important parameters are the refraction index, n, and the absorption coefficient for scintillation light, α. Moreover the shape and surface roughness of the scintillator, the reflectivity and surface roughness of the reflector, the coupling between scintillator and SDD, the quantum efficiency, QE, of the SDD entrance window and the charge collection efficiency, CCE, inside the SDD determine the system quantum efficiency, η, for scintillation photons and alter the energy resolution. The mean number of signal electrons reaching the anode inside the SDD is given by

$$\overline{N}_e = \overline{N}_{ph} \cdot \overline{K} \cdot \overline{T}_{ew} \cdot \overline{A}_{sv} \cdot \overline{CCE} = \overline{N}_{ph} \cdot \overline{K} \cdot \overline{QE} = \overline{N}_{ph} \cdot \overline{\eta}, \tag{4.23}$$

where $\overline{K}$ is the transfer efficiency of the scintillation photons to the SDD entrance window and $\overline{T}_{ew}$ the transmission efficiency through the SDD entrance window, $\overline{A}_{sv}$ the absorption efficiency of scintillation photons inside the SDD and CCE the collection efficiency of signal electrons at the SDD anode. $\overline{K}$, $\overline{T}_{ew}$ and $\overline{A}_{sv}$ depend on the parameters n and α. In addition $\overline{K}$ is also determined by the surface roughness of the scintillator, the absorption length of scintillation photons inside the scintillator, the reflectivity and reflector type of the reflector.

η depends also on the position, where the deposited energy is converted into scintillation photons inside the scintillator. The system quantum efficiency, η, varies with the position, where the scintillation photons are generated inside the scintillator. This is illustrated in Fig. 4.5. It shows a γ-detector, consisting of a scintillator

coupled to a SDD. Let us assume two γ-events, which generate the same number of scintillation photons at different positions inside the scintillator. The number of signal electrons, N_e, is varying, due to the fact, that the photons generated at these two positions have to cover different distances and undergo a different number of reflections under different angles with a certain probability of being absorbed inside the scintillator ($\alpha > 0$) or lost, due to imperfect reflectors with a reflectivity < 1, before being absorbed inside the SDD. A high quantum efficiency of the SDD entrance

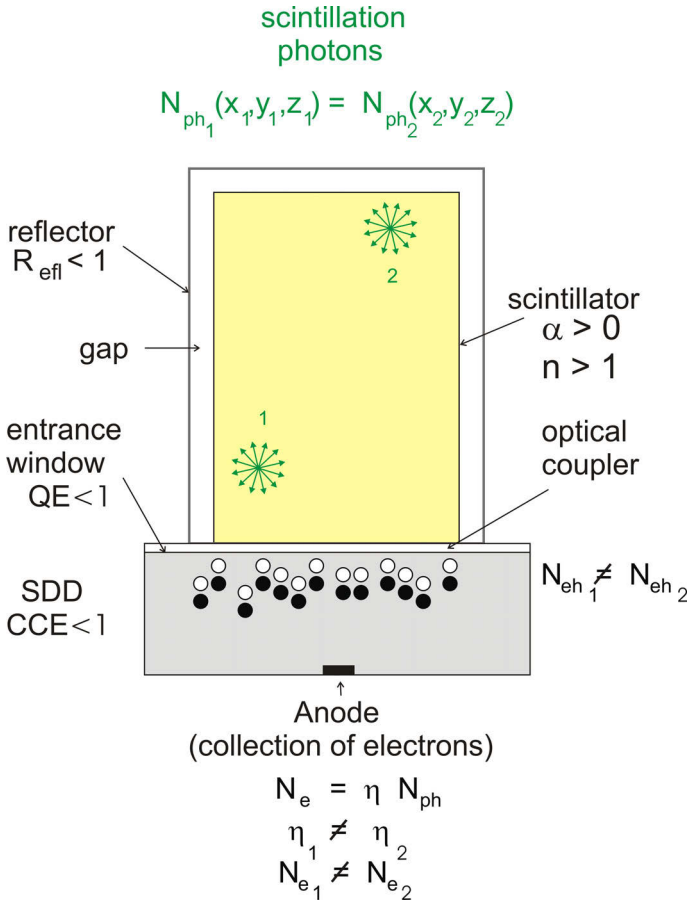

Figure 4.5.: *Light collection non-uniformity in the system scintillator coupled to a SDD, caused by different distances, which scintillation photons have to cover before being absorbed inside the SDD; The quantum efficiency of the system η depends on the generation point, the absorption coefficient of the scintillator α, the reflectivity, R_{efl}, of the reflector, the quantum efficiency, QE, of the SDD entrance window and the charge collection efficiency, CCE, of the electrons at the SDD anode.*

window for the scintillation photons, guaranteed by an appropriate anti reflection coating (ARC), reduces the number of reflected photons back into the scintillator, thus reducing the probability of being absorbed outside of the SDD or escaping the system. A radioactive source emits γ-rays into a certain solid angle and the absorption depth of a γ-ray inside the scintillator follows the exponential absorption law, so that the position, where mono energetic γ-rays interact with the scintillator differs for each event. This leads to a variation of the mean system quantum efficiency, $\overline{\eta}$,

from event to event, hence to an increase of the variance of the number of generated signal electrons and to a degradation of the energy resolution. The values of R_{η}, R_{Bino} and R_{el} depend on the system quantum efficiency for scintillation photons, $\overline{\eta}$.

There have been a few publications in which the contribution of the light collection efficiency in γ-detectors, consisting of scintillators coupled to PMTs, on the resulting pulse height spectra have been investigated [88, 89, 90, 91]. Analytical calculations of the contribution of the light collection non-uniformity onto the energy resolution are presented in [92] for CsI(Tl) and CsI(Na), but without taking the PMT entrance window into account. Analytical calculations of complex detector systems can only be performed with a lot of approximations. Monte Carlo simulations can overcome these difficulties, because the detector can be modeled more precisely.

The influence of the efficiencies T_{ew}, A_{sv} and CCE onto the QE of the SDD is investigated in Chap. 5. Additionally, in Subsec. 6.1.2 and 6.2.2 of this work, the effect of the collection efficiency of scintillation photons inside the SDD + scintillator system and the influence of the system quantum efficiency, η, onto the energy resolution contributions, given by R_{η} and R_{Bino} will be analyzed. Results from investigations of cubical (4 x 4 mm^2) and cylindrical ($\oslash$ = 4.5 mm) CsI(Tl) scintillators with three different thicknesses (5 mm, 10 mm and 20 mm), and one cylindrical ($\oslash$ = 5) $LaBr_3$(Ce) scintillator with a thickness of 10 mm coupled to a SDD, will be presented.

5. The quantum efficiency of Silicon Drift Detectors

The quantum efficiency of a SDD is a measure of the detector efficiency with regard to the transmission efficiency, T_{ew}, of photons through the partially sensitive detector parts, the so called dead layers (DL) of the entrance window (EW), the absorption efficiency, A_{sv}, of incident photons inside the sensitive volume of the detector, the conversion efficiency, G, of the deposited energy into eh-pairs inside the SDD and the charge collection efficiency, CCE, of the generated electrons at the anode.

In the system SDD + scintillator the detector efficiency is determined additionally by the absorption efficiency, A_{scint}, of γ-rays inside the scintillator, the conversion efficiency, C, of the deposited energy by γ-rays inside the scintillator into eh-pairs, the conversion efficiency, T, of the eh-pairs into scintillation photons and the collection efficiency K of scintillation photons at the SDD entrance window. The efficiencies T_{ew}, A_{sv} and CCE are properties of the SDD and determine its QE. The so called system quantum efficiency, η (comp. Sec. 4.1), for scintillation photons is determined by the parameters K, T_{ew}, A_{sv}, G and CCE:

$$\eta = K \cdot QE \tag{5.1}$$

where

$$QE = T_{ew} \cdot A_{sv} \cdot G \cdot CCE. \tag{5.2}$$

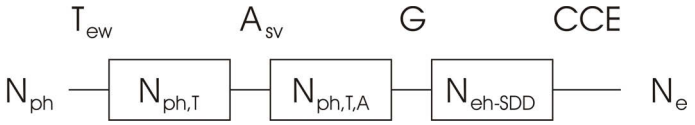

Figure 5.1.: *Scheme of the conversion of incident photons, N_{ph}, into signal electrons, N_e, with an overall efficiency, consisting of the efficiencies K, T_{ew}, A_{sv}, G and CCE. $N_{ph,T}$ is the number of transmitted photons, $N_{ph,T,A}$ is the number of transmitted and absorbed photons and N_{eh-SDD} is the number of generated eh-pairs inside the SDD.*

In this chapter we are comparing the measured and calculated QEs of SDDs in the X-, γ-ray and near UV-Vis range.

The quantum efficiency can be defined through

$$QE(E) = \frac{N_e}{N_{ph} \cdot G} \tag{5.3}$$

where N_{ph} is the number and E the energy of the incident photons (Fig 5.1). In this definition also partial events, where only a fraction of the photon energy is

deposited inside the sensitive volume, contribute to the quantum efficiency. For X- or γ-rays the conversion efficiency of photons with an energy E can be described by $G(E) = E/\overline{w}$, where $\overline{w}$ is the mean energy to create an eh-pair. In the UV-Vis range 300 - 800 nm one photon generates one eh-pair, G = 1 (see Sec. 2.1.2). The definition of the QE in Eq. 5.3 is usually used, if the QE is determined from the value of the measured current, I, between cathode and anode, which is generated by an incident photon flux of the power $P = \Delta N_{ph} E/\Delta t$, where Δt is the time unit in seconds.

In this work the QE is determined from the value of the measured current, $I = \Delta N_e \cdot e/\Delta t$, where e is the electron charge.

5.1. Entrance window

For X-ray detection various SDD entrance windows have been developed. In this section only the pn-Window, which consists of a SiO_2- and Al-layer on top of the p-layer will be discussed. The pn-Window allows a good energy resolution for low X-ray energies down to several 100 eV and a high peak to background and peak to valley ratio [9].

For the detection of near UV-Vis photons antireflection coatings (ARC) have been developed. The ARCs consist of SiO_2 and Si_3N_4 layers on top of the p-layer. The QE can be tuned by changing the layer thicknesses of SiO_2 and Si_3N_4.

Decreasing the thickness and increasing the quality of the p-layer also leads to a better charge collection efficiency and higher quantum efficiency.

The interface SiO_2-p-layer or Al-p-layer and the p-layer itself exhibit a reduced mobility and lifetime for charge carriers compared to the n^--type Si substrate. Interfaces are often a source of an increased number of defects, if the lattice structures of the two materials are not similar. Furthermore, the p-doping with Boron is done by ion implantation. Although the Si sample is annealed afterwards, this technique generates additional defects inside the doped layer. Defects and interface states act as trapping centers for electrons [93].

After the generation of eh-pairs by photons, the probability of signal electrons, which are generated close to the interface, to reach the anode is less than 1. The reduction of signal electrons is evaluated by the so-called charge collection efficiency (CCE). Fig. 5.2 illustrates the configuration of the entrance window (EW). Charge carriers generated in different depths inside the p^+-layer are collected at the anode or cathode with different efficiencies described by a depth dependent CCE(z). The CCE has been set to 0 inside the insensitive part (DL) of the EW. This applies for near UV-Vis photons, because the energy of the generated charge carriers inside the DL does not suffice to penetrate into the p-layer. Incident X- or γ-ray photons can generate fluorescence photons or hot electrons inside the DL, which have a certain probability to reach the p-layer or Si bulk, where they can generate charge carriers. There is also the possibility that fluorescence photons generated inside the p-layer escape the sensitive volume. In both cases only a part of the incident photon energy is deposited inside the sensitive part of the SDD, so that the number of generated charge carriers is lower compared to their number, if the full photon energy is deposited inside the sensitive detector volume. The contribution of this so

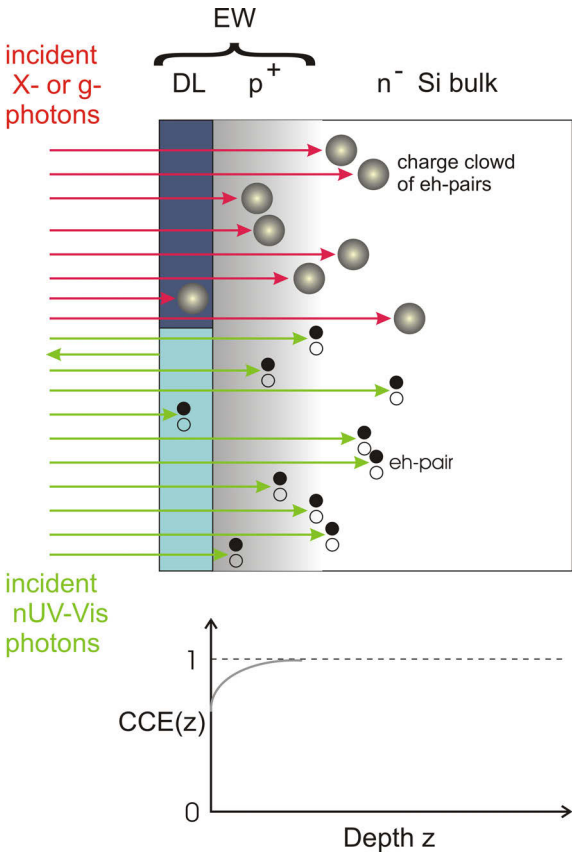

Figure 5.2.: *Generation of eh-pairs inside the SDD, after the absorption of photons in different regions of the entrance window (EW), consisting of partially sensitive dead layers (DL), the p-layer and the n^--silicon bulk. The charge collection efficiency, CCE(z), depends on the depth, z, at which the charge carriers have been generated. Inside the DL the CCE is set to 0. Events with partial energy deposition in the X-ray range are neglected and not illustrated.*

called "partial events" is neglected in the calculation of the QE in this work.

In [94] the depth dependent CCE has been firstly described by an exponential function with an increasing CCE for larger distances, z, from the dead layers of the EW (Fig. 5.2). In this work we use the following expression for the CCE(z):

$$CCE(z) = 1 - q \cdot exp(-\frac{z}{\tau}), \tag{5.4}$$

where q is the amount of charges trapped at the dead layer and p-layer interface at z = 0, τ the distance at which the CCE has increased from CCE(0) = 1 - q to CCE(τ) = 1 - q/e. e is Euler's number.

Fig. 5.3 shows the CCE(z) functions of the pn-Window (red) and the ARC-Window (brown), which have been determined from QE measurements in the near UV-Vis range presented in Sec. 5.5. The values of the parameters in the CCE(z) function are q = 0.04 and τ = 30 nm for the pn-Window and q = 0.23 and τ = 65 nm for the ARC-Window. The difference in the CCE originates from the Boron implantation through oxide layers with different thicknesses. The implantation through a

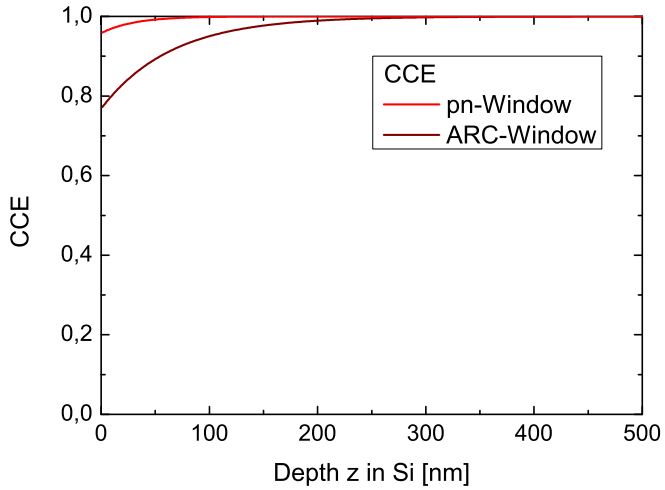

Figure 5.3.: *CCE function determined for the pn-Window (red) and the ARC-Window (brown) (comp. Sec. 5.5.1).*

thinner oxide layer leads to a deeper implantation depth and to a better robustness of the window (e.g. for the coupling with the scintillator) but also to a higher defect density within the p-layer, if the ion dose and ion energy remain constant.

5.2. Derivation of the formula for the quantum efficiency

The number of transmitted photons, N_T(E,z), through a medium of thickness z can be described by Lambert-Beers law

$$N_T(E,z) = N_0 exp\left(-\frac{z}{l(E)}\right), \tag{5.5}$$

where N_0 is the number of incident photons and l(E) the absorption length of photons in the considered media. The number of absorbed photons, N_A(E,z), can be calculated as follows

$$N_A(E,z) = N_0 - N_T(E,z) = N_0\left(1 - exp\left(-\frac{z}{l(E)}\right)\right). \tag{5.6}$$

The ratio of absorbed to incident photons $dN_A(E,z)/N_0$ in the range [z,z+dz] follows from

$$dA(E,z) = \frac{dN_A(E,z)}{N_0} = \frac{1}{l(E)} exp\left(-\frac{z}{l(E)}\right) dz. \tag{5.7}$$

Equation 5.7 can also be interpreted as the probability, P(E,z), for an individual photon to be absorbed in a depth range [z,z+dz].

Due to the fact, that the CCE(z) depends on the depth, z, inside the SDD, where electrons and holes have been generated, the number of signal electrons, dN_e(E,z),

originating from a certain depth range [z,z+dz], can be calculated by

$$dN_e(E,z) = N_{ph} T_{ew}(E, \theta_i = 0°) dA_{sv}(E,z) G(E) CCE(z). \quad (5.8)$$

where θ_i is the angle of the incident photons relative to the detector surface normal and dA_{sv}(E,z) the energy dependent ratio of absorbed photons inside the sensitive detector volume in the depth range [z,z+dz]. The total number of detected signal electrons results from the integration over the sensitive volume thickness, d, of the SDD:

$$N_e(E) = \int_0^d dN_e(E,z) = N_{ph} T_{ew}(E, \theta_i = 0°) G(E) \int_0^d CCE(z) dA_{sv}(E,z). \quad (5.9)$$

Inserting Eq. 5.9 into Eq. 5.3 yields the electron quantum efficiency

$$QE(E) = T_{ew}(E, \theta_i = 0°) \int_0^d CCE(z) dA_{sv}(E,z). \quad (5.10)$$

Partial events are neglected in the formula of the QE(E) in Eq. 5.10. Inserting Eq. 5.4 and 5.7 into 5.10 gives

$$QE(E) = T_{ew}(E, \theta_i = 0°) \int_0^d \left(1 - q \cdot exp\left(-\frac{z}{\tau}\right)\right) \cdot \frac{1}{l_{Si}(E)} exp\left(-\frac{z}{l_{Si}(E)}\right) dz \quad (5.11)$$

where l_{Si} is the absorption length in silicon. Is the radiation incident under a certain angle, θ_i, to the SDD surface normal, the photons are penetrating the p-layer and Si-bulk under an angle θ_t. For X-rays holds $\theta_i = \theta_t$. For near UV-Vis photons $\theta_t = \theta_t(\theta_i)$ has to be calculated with the equations described by Snell's law. Eq. 5.12 changes for photons incident under an angle to

$$QE(E, \theta_i) = T_{ew}(E, \theta_i) \int_0^{d'} \left(1 - q \cdot exp\left(-\frac{s \cdot cos(\theta_t(\theta_i))}{\tau}\right)\right) \cdot \frac{1}{l_{Si}(E)} exp\left(-\frac{s}{l_{Si}(E)}\right) ds, \quad (5.12)$$

where $z = s \cdot cos(\theta_t(\theta_i))$ and $d' = d/cos(\theta_t(\theta_i))$.

The CCE is included for the first time into the calculation of the quantum efficiency of a SDD, in this work. In order to calculate the QE an expression for T_{ew}(E,θ_i) has to be derived for photons from the X-ray and near UV-Vis range respectively.

In the following, results of the QE in the X-ray and the near UV-Vis range from calculations are compared to results determined from measurements.

5.3. Setup for photocurrent measurements

Applying bias voltages to the SDD as described in Sec. 3.1.1, is suitable for single photon (X- or γ-ray) detection, where the detector is sensitive to charge collection at the anode. To measure the photocurrent the SDD has to be biased in a different

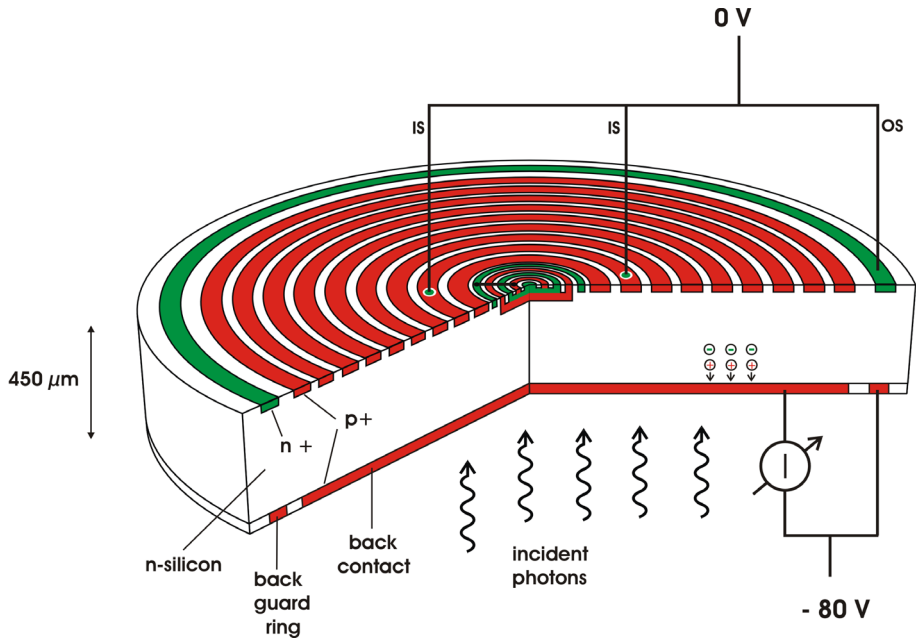

Figure 5.4.: *Setup for photocurrent measurements*

way, which is described in Fig. 5.4. The back contact is set to - 80 V and the inner and outer substrates, which act now as the collecting anodes for the electrons, are set to 0 V. The drift rings and the JFET are floating. With this biasing the SDD is operated in the same way as a simple pn-diode. The electrical current, generated by an incident photon flux, is given by

$$I = \frac{\Delta N_{ch} \cdot e}{\Delta t} \tag{5.13}$$

where ΔN_{ch} is the detected charge carriers, which are either electrons or holes. In the setup illustrated in Fig. 5.4 we measure the hole current, I_{h^+}, which has the same magnitude as the electron current, I_{e^-}, within the detector bulk (steady state condition applies $I = I_{e^-} = - I_{h^+}$). The power, P, of the incident photon flux is

$$P = \frac{\Delta N_{ph} E}{\Delta t}. \tag{5.14}$$

Solving Eq. 5.13 of the photocurrent for ΔN_{ch} and Eq. 5.14 of the incident power for ΔN_{ph} and inserting the results into Eq. 5.3 yields the quantum efficiency

$$QE(E) = \frac{I \cdot E}{e \cdot P \cdot G(E)}. \tag{5.15}$$

The incident power is determined from the measured current, I_{dio}, generated by the photon flux in a calibrated diode with a known quantum efficiency, QE_{dio}, so that:

$$QE(E) = \frac{I \cdot G_{dio}(E)}{I_{dio} \cdot G(E)} \cdot QE_{dio}(E). \tag{5.16}$$

The calibrated reference diode used in the measurements of the photocurrent is a silicon diode, so that the conversion efficiencies of the deposited energy inside the

sensitive volume into electrons and holes are equal for the calibrated diode and the SDD: $G(E) = G_{dio}(E)$. In this case the quantum efficiency in Eq. 5.16 can be written as

$$QE(E) = \frac{I}{I_{dio}} \cdot QE_{dio}(E). \tag{5.17}$$

5.4. Quantum efficiency in the X-ray range

The absorption length of X-rays in materials of the entrance window of SDDs is pictured in Fig. 5.5. The SDD consists of a 450 μm thick n$^-$-type Si bulk with an

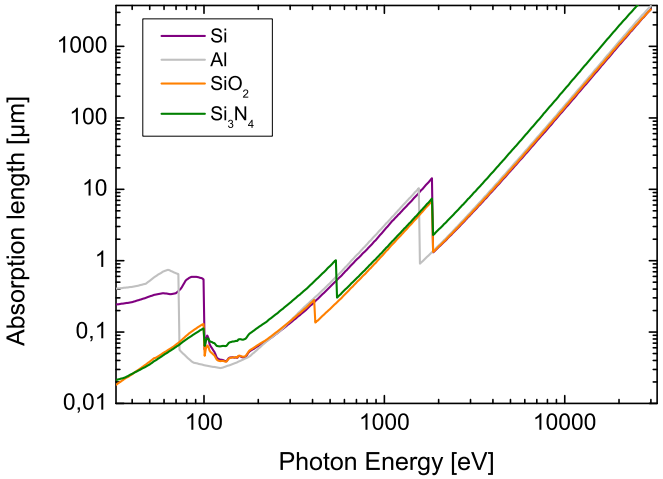

Figure 5.5.: *Absorption length of materials the SDD entrance window. Data are taken from [21].*

entrance window composed of a p-layer, SiO_2 and Si_3N_4 or Al or a combination on top. The absorption length in Si and the window materials (Fig. 5.5) ranges from about 100 nm for E = 200 eV to 1000 μm for E = 20000 eV. X-rays, with energies above 10 keV, are transmitted through the SDD with an increasing probability to higher energies. The ratio of X-ray photons absorbed inside the SDD entrance window increases with decreasing photon energy. The photons absorbed in the EW are either generating none or a fraction of the number of signal electrons compared to a X-ray photon absorbed inside the Si-bulk.

To calculate the QE given by Eq. 5.12 for X-ray photons, the transmission efficiency, T_{ew}, of X-rays through the entrance window has to be determined. With Eq. 5.5 the ratio of transmitted photons, $T_{ew,i}$, through a material with thickness z_i, can be determined by

$$T_{ew,i}(z_i, l_i(E)) = \frac{N_T(z_i, l_i(E))}{N_0} = exp\left(-\frac{z_i}{l_i(E)}\right). \tag{5.18}$$

The insensitive part of the entrance window consists of several layers, n, each layer, i, with a thickness z_i. The transmission efficiency through all layers can be calculated

by

$$T_{ew}(E) = \prod_i^n T_{ew,i} = exp\left(-\sum_i^n \frac{z_i}{l_i(E)}\right). \tag{5.19}$$

If the photons are incident under an angle θ onto the SDD, Eq. 5.19 changes to

$$T_{ew}(E,\theta) = \prod_i^n T_{ew,i} = exp\left(-\sum_i^n \frac{z_i}{cos(\theta)\cdot l_i(E)}\right). \tag{5.20}$$

Inserting Eq. 5.20 into Eq. 5.12 yields the SDD quantum efficiency for X-rays.

Fig. 5.6 shows the calculated QE($E, \theta = 0°$) for the pn-Window (red dashed line) and the change of the QE($E, \theta = 0°$), if the CCE(z) function of the pn-Window is substituted by the CCE(z) = 1 (black solid line) or if the CCE function of an ARC-Window (dashed brown line) is used. The CCE functions of the pn-Window

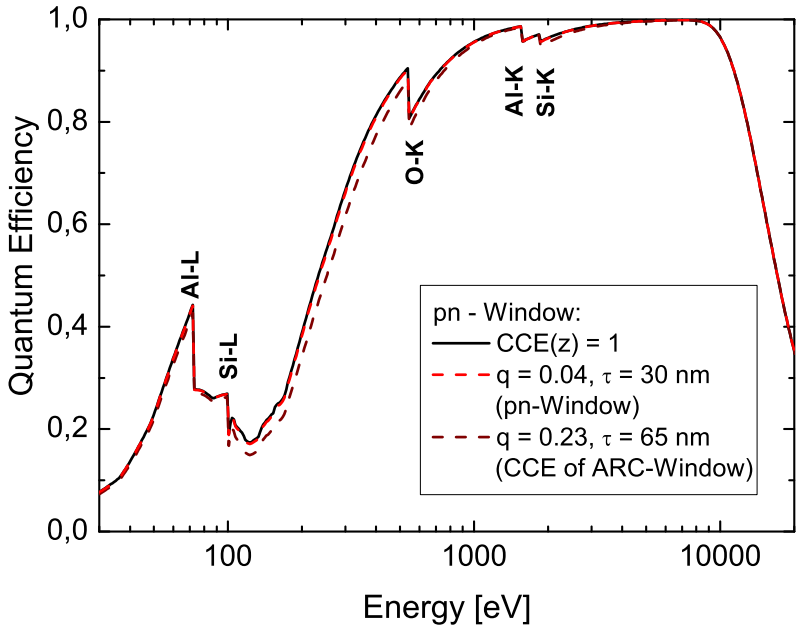

Figure 5.6.: *Calculated QE($E, \theta = 0°$) for a pn-Window and two similar entrance windows, where only the parameter of the CCE function differs from that of the pn-Window. Absorption lengths of the materials of the entrance window are from [21]. The values of the thicknesses z_i, are in the range of several 10 nm. The CCE is shown in Fig. 5.3.*

and ARC-Window have been presented in Fig. 5.3, red and brown dashed line. The charge collection efficiency of the pn-Window is close to 1, so that the QE($E, \theta = 0°$) has almost the same value, as if the CCE(z) is set to 1. The CCE function of this kind of ARC-Window leads to a decrease of the QE($E, \theta = 0°$). This is largest in the energy range 100 eV < E < 700 eV, due to the fact, that the absorption length, $l_{Si}(E)$, in silicon is minimal (30 nm < l_{Si} < 600 nm) in this energy range, regarding the energy range from 30 eV to 30000 eV. A smaller absorption length increases the

ratio of absorbed photons close to the entrance window, where the defect density of the p-type back contact has its maximum.

The measurement of the QE($E, \theta = 0°$) has been performed at the synchrotron radiation source facility Bessy II of the Helmholtz-Zentrum Berlin. Certain photon energies can be filtered from the X-ray spectrum, generated by the accelerated electrons, with a grating and crystal monochromator in the energy range 30 to 1800 eV and 1750 to 10000 eV.

The measurement setup for the photocurrent has been introduced in Sec. 5.3. In order to determine the electron quantum efficiency, QE($E, \theta = 0°$), the photocurrent $I = I_{irrad} - I_{dark}$ of the SDD and the calibrated silicon diode has to be inserted into Eq. 5.17, where I_{irrad} is the current during irradiation and I_{dark} the dark current. Furthermore, the ratio of the electron currents inside the synchrotron ring at the times when the photocurrent has been measured with the calibrated diode, $I_{ring}(t_{dio})$, and the SDD, $I_{ring}(t_{SDD})$, has to be multiplied to Eq. 5.17 as a correction, because the electron current inside the synchrotron ring changes with time. Thereby the following expression results for the quantum efficiency:

$$QE(E,\theta) = \frac{I_{irrad} - I_{dark}}{I_{dio,irrad} - I_{dio,dark}} \cdot QE_{dio}(E,\theta) \cdot \frac{I_{ring}(t_{dio})}{I_{ring}(t_{SDD})}. \tag{5.21}$$

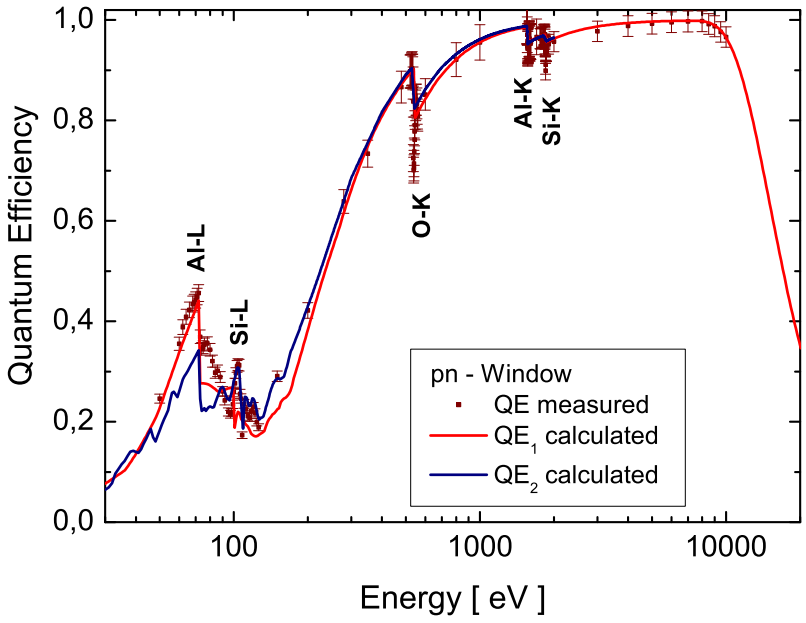

Figure 5.7.: *Measured and calculated QE($E, \theta = 0°$), for a SDD with pn-Window. The absorption lengths used in the calculations are from [76] (blue curve) and [21] (red curve).*

Fig. 5.7 shows the measured and calculated QE($E, \theta = 0°$) for a SDD with pn-Window. Down to an energy of E = 300 eV the measured and calculated QEs are in good agreement within the error bars of the measured values. In the energy range 100

to 200 eV the calculated blue QE($E, \theta = 0°$) curve in Fig. 5.7 is in good agreement with the measured values within the error bars. In the energy range 70 to 95 eV the measured values are in no agreement with the calculated values within the error bars of the measured values. The errors of the absorption lengths from literature are not known. It is thus not possible to state whether the measured QE($E, \theta = 0°$) values are in agreement with the calculated values inside the measured and calculated error bars or not. In the energy range below 70 eV the measured QE($E, \theta = 0°$) values are in agreement with the calculated QE($E, \theta = 0°$) (red curve) within the error bars of the measured values.

In total, the model for the calculation of the QE(E, θ) is accurate and can be used as a prediction tool. The CCE has a non-negligible effect on the QE($E, \theta = 0°$) of the ARC-Window in the range 100 - 600 eV and a negligible effect on the QE($E, \theta = 0°$) of the pn-Window in the X-ray range above 50 eV.

5.5. Quantum efficiency in the near ultra violet and visible range

The SDD entrance window, developed for the detection of scintillation photons, consists of a Si_3N_4, SiO_2 and a p-type silicon layer. All these layers have certain thicknesses. The EW can be optimized for scintillation photons in the near ultra violet and visible range to allow a high QE. The thicknesses and the complex index of refraction, n, of the layers of the SDD entrance window determine the wavelength dependent QE. The calculation of the reflection, r, and transmission coefficient, t, of the SDD entrance window in dependence of the layer thicknesses and the refraction index, is described in the App. C.

The reflectance R_{efl} and transmittance T_{ARC} are defined by the ratios of the time averaged power of the reflected, P_r, and the transmitted, P_t, to the incident plane wave, P_i, [95].

$$R_{efl} = \frac{P_r}{P_i} = \frac{I_r \cdot A_r}{I_i \cdot A_i} = \frac{Re(n_r)\frac{\epsilon_0 c_0}{2}\left|E_r\right|^2}{Re(n_i)\frac{\epsilon_0 c_0}{2}\left|E_i\right|^2} = \left|\frac{E_r}{E_i}\right|^2 = |r|^2 \tag{5.22}$$

$$T_{ARC} = \frac{P_t}{P_i} = \frac{I_t \cdot A_t}{I_i \cdot A_i} = \frac{Re(n_t)\frac{\epsilon_0 c_0}{2}\left|E_t\right|^2}{Re(n_i)\frac{\epsilon_0 c_0}{2}\left|E_i\right|^2} = \frac{Re(n_t)cos\theta_t}{Re(n_i)cos\theta_i}\left|\frac{E_t}{E_i}\right|^2 = \frac{Re(n_t)cos\theta_t}{Re(n_i)cos\theta_i}\left|t\right|^2 \tag{5.23}$$

where I is the intensity, A the irradiated area, Re(n) the real part of the complex index of refraction, E the electric field amplitude, ϵ_0 the dielectric constant and c the velocity of light. The reflectance, $R_{efl}(E, \theta_i)$, and the transmittance, $T_{ARC}(E, \theta_i)$, are dependent on the photon energy, E, and its angle of incidence, θ_i.

The formulas 5.22, 5.23 and C.16 are used to calculate the reflection and transmission of UV-Vis photons through thin films.

5.5.1. Measured and calculated quantum efficiency

In order to calculate the quantum efficiency for near UV-Vis photons, first the transmission, $T_{ARC}(E,\theta_i)$ (see Eq. 5.23), of optical photons through the SDD entrance

window, which has an anti-reflection-coating (ARC), has to be evaluated by inserting the results of Eq. C.16 into Eq. 5.23. Substituting T_{ARC} for T_{ew} in the Eq. 5.12 yields the QE for near UV-Vis photons:

$$QE(E,\theta_i) = T_{ARC}(E,\theta_i) \int_0^{d'} CCE(s \cdot cos(\theta_t(\theta_i))) \cdot dA_{sv}(E,s). \tag{5.24}$$

The QE in the near UV-Vis range is usually expressed in dependence on the wavelength of the incident photons. The conversion of the photon energy, E, into the photon wavelength, λ, is described by

$$\lambda = \frac{hc}{E}, \tag{5.25}$$

[96] where h is the Planck's constant and c the velocity of light. The antireflection coating (ARC) of the SDD entrance window (EW) consists of a Si_3N_4-layer on top of a SiO_2-layer, which is on top of p-type silicon. Fig. 5.8 shows the calculated

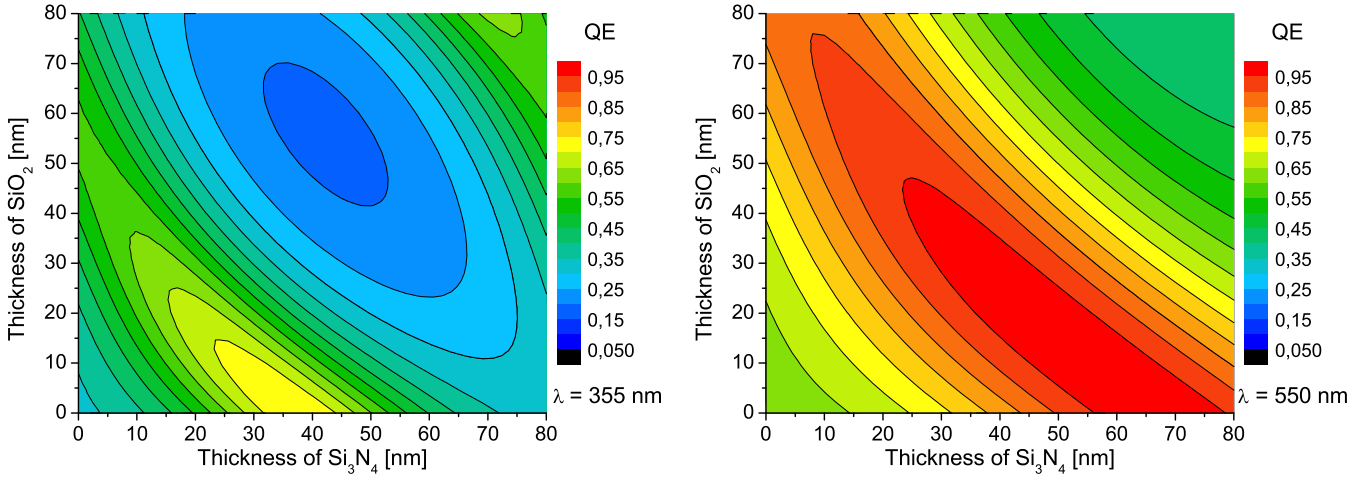

Figure 5.8.: *Calculated $QE_e(\theta_i = 0°)$ for an ARC consisting of a stack of layers, Si_3N_4 + SiO_2 + silicon, with varying Si_3N_4- and SiO_2-layer thicknesses for photons with a wavelength of λ = 355 nm or 550 nm. The charge collection efficiency is set to CCE = 1. Photons are penetrating from the air.*

$QE(\lambda, \theta_i = 0°)$ for photons, incident perpendicular onto the SDD EW, with wavelengths of λ = 355 nm and 550 nm, in dependence of the thicknesses of the Si_3N_4- and SiO_2-layer. These λ are the wavelengths of the emission maximum of the scintillation spectra of $LaBr_3$(Ce) and CsI(Tl). The CCE is set to 1. The maximum $QE(\lambda, \theta_i = 0°)$ for photons with a wavelength of λ = 355 nm is reached for an ARC with SiO_2- and Si_3N_4-layer thicknesses of about 0 nm and 38 nm respectively. A negative effect of this EW is that the Si_3N_4-Si interface exhibits more defects than the SiO_2-Si interface, so that the leakage current from the interface increases and the CCE at the interface decrease. For a better electrical performance a homogeneous SiO_2-layer should be between the p-type silicon and the Si_3N_4-layer. To assure a

homogeneous SiO_2-layer, its thickness is set to 20 nm. A homogeneous SiO_2-layer with a thickness of less than 20 nm is difficult to manufacture and the probability for pin holes increases with decreasing thickness. An ARC with a SiO_2-layer thickness of 20 nm has a maximal QE(λ = 355 nm,θ_i = 0°) for a Si_3N_4-layer thickness of about 20 nm. The maximum QE for photons with a wavelength of λ = 550 nm is for an ARC with a SiO_2-layer thickness of about 20 nm and a Si_3N_4-layer thickness of about 40 nm.

In the following calculated and measured results of the QE($\lambda, \theta_i = 0°$) for photons in the wavelength range from 300 to 1100 nm are compared and discussed.

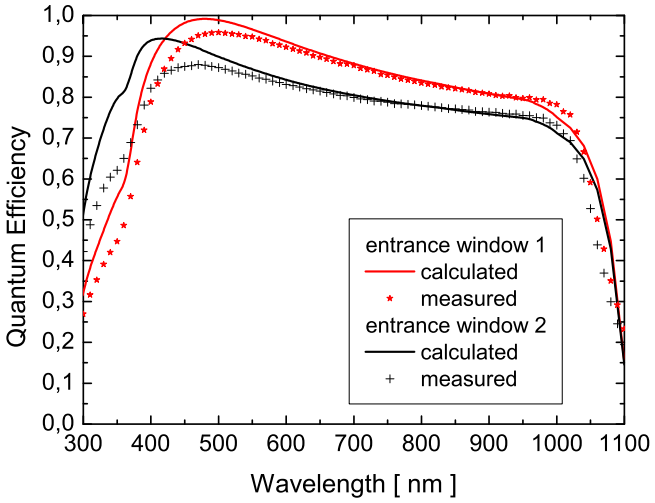

Figure 5.9.: *Calculated and measured QE($\lambda, \theta_i = 0°$) for two entrance windows, optimized for scintillation photons from CsI(Tl) (red curve) and $LaBr_3$(Ce) (black curve). For the calculations, the CCE is set to 1 in both cases. Maximum of the scintillation spectrum of CsI(Tl) is at 550 nm and of $LaBr_3$(Ce) at 355 nm. The measurements have been performed by Gigaherz Optik GmbH.*

Fig. 5.9 shows the measured (stars and crosses) and calculated (solid lines) QE($\lambda, \theta_i = 0°$) for two Anti reflection coatings (ARCs). One ARC is optimized for the scintillation spectrum of CsI(Tl) (red) and the other for $LaBr_3$(Ce) (black). The charge collection efficiency has been set to CCE = 1 in the calculated QE($\lambda, \theta_i = 0°$). In the wavelength range 300 to 600 nm the measured QE($\lambda, \theta_i = 0°$) values lie below the calculated ones.

To investigate the origin of the difference between the measured and calculated values, three entrance windows have been built with different Boron implantation depths. This has been achieved by implanting with the same ion dose and energy through SiO_2-layers of three different thicknesses. An increasing implantation depth leads to an increase of the defect density in the p-layer, which results in different CCE functions for the three entrance windows. These entrance windows have a lower transmittivity and QE, due to the fact, that there is no antireflection coating on top of the p-layer. Fig. 5.10 (left picture) shows the measured (dots) and calculated (dashed and solid lines) QE($\lambda, \theta_i = 0°$). In the UV range the CCE reduces the QE

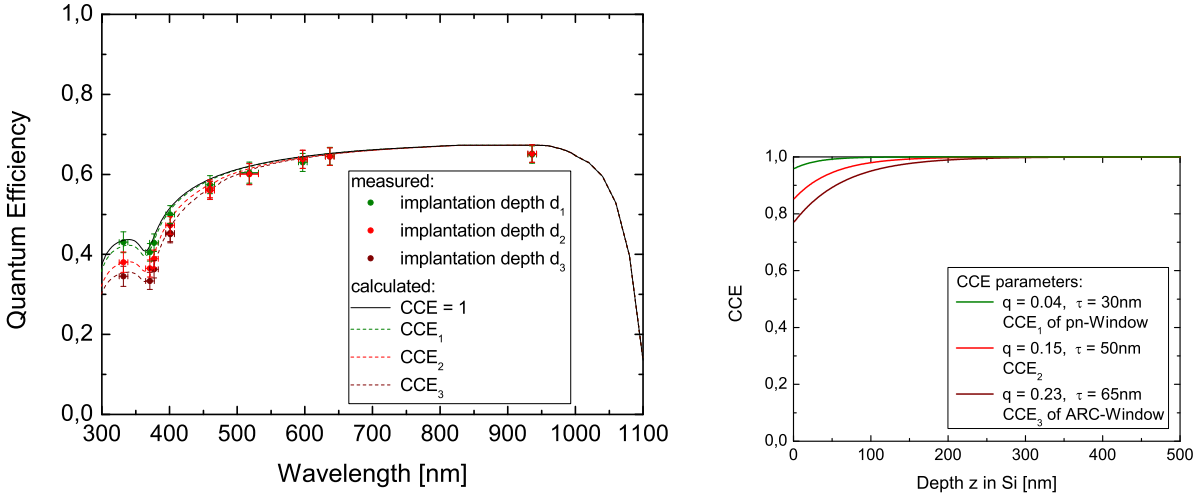

Figure 5.10.: *Calculated and measured QE($\lambda, \theta_i = 0°$) at room temperature for three different implantation depths and no ARC layers on top of the p-layer. The influence of the CCE is included in the calculations. The CCE functions resulting from the three implantation procedures are plotted on the right hand side.*

at the interface SiO_2-p-layer by about 4 % for the most shallow implantation depth compared to about 23 % for the deepest implantation depth. The CCE functions for these 3 implantation depths are shown in Fig. 5.10 in the graph on the right hand side.

Calculations of the QE($\lambda, \theta_i = 0°$) with the CCE(z) (see Fig. 5.10 brown solid line) function

$$CCE(z) = 1 - q \cdot exp(-\frac{z}{\tau}) = 1 - 0.23 \cdot exp\left(-\frac{z[nm]}{65nm}\right) \tag{5.26}$$

are illustrated in Fig. 5.11 (red and black solid lines), which can be compared to the measured QE($\lambda, \theta_i = 0°$) (red stars and black crosses). Including the CCE into the calculation leads to a good agreement between the measured and calculated QE($\lambda, \theta_i = 0°$).

To verify the validity of the calculated QE values for incident photons with an angle not equal to 0° to the SDD surface normal, measured and calculated values of the QE for the two entrance windows, introduced in Fig. 5.11 (angle of incidence: 0°), have been performed for an angle of incidence of 65°. The results are shown in Fig. 5.12. The measured and calculated QE($\lambda, \theta_i = 65°$) are in agreement within the error bars. The QE is smaller than for photons with an angle of incidence of 0°.

The knowledge of the angle dependent QE is necessary for the determination of the overall quantum efficiency, η, for scintillation photons, which are incident with angles in the range from 0 to 90° onto the SDD entrance window.

In this section it has been shown that the experimentally determined QE(λ, θ_i) can be fully described by the theory of the angle dependent transmission through

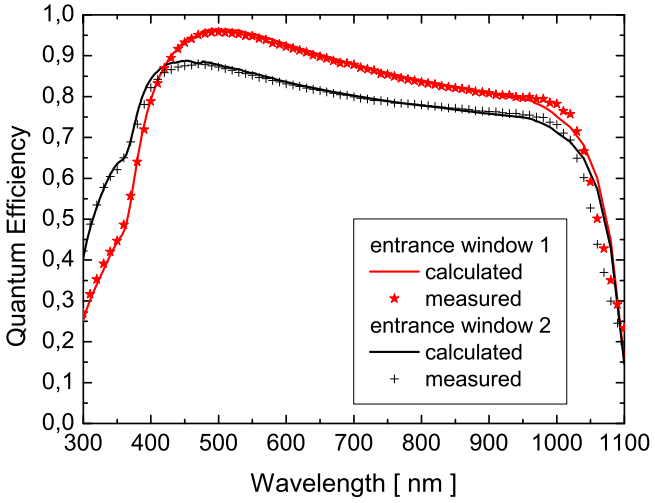

Figure 5.11.: *Calculated and measured QE for the two entrance windows. The CCE function used for the calculation is plotted in Fig. 5.10 on the right (brown line). Integration of the CCE in the QE improves the coincidence between measurement and calculation significantly. Measurements have been performed by Gigaherz Optik GmbH.*

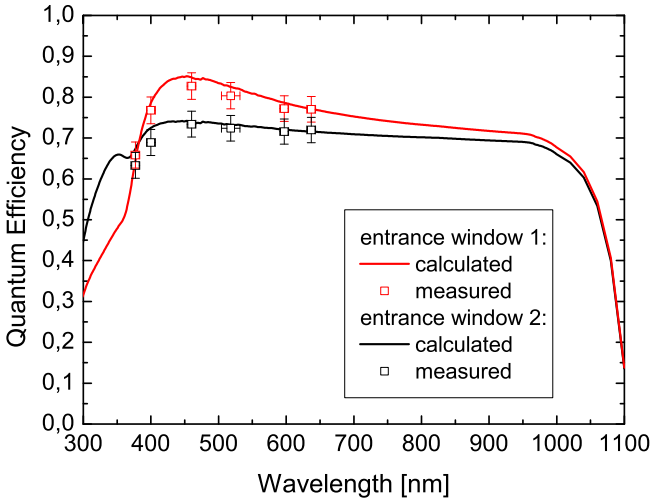

Figure 5.12.: *Calculated and measured QE($\lambda, \theta_i = 65°$) for the two entrance windows for an incident photon angle of 65°. The influence of the CCE is included into the calculations.*

the materials of the SDD entrance window and the introduced CCE function of the ARC-Window in dependence of wavelength and the angle of incidence.

5.5.2. Quantum efficiency for photons from CsI(Tl) or $LaBr_3$(Ce)

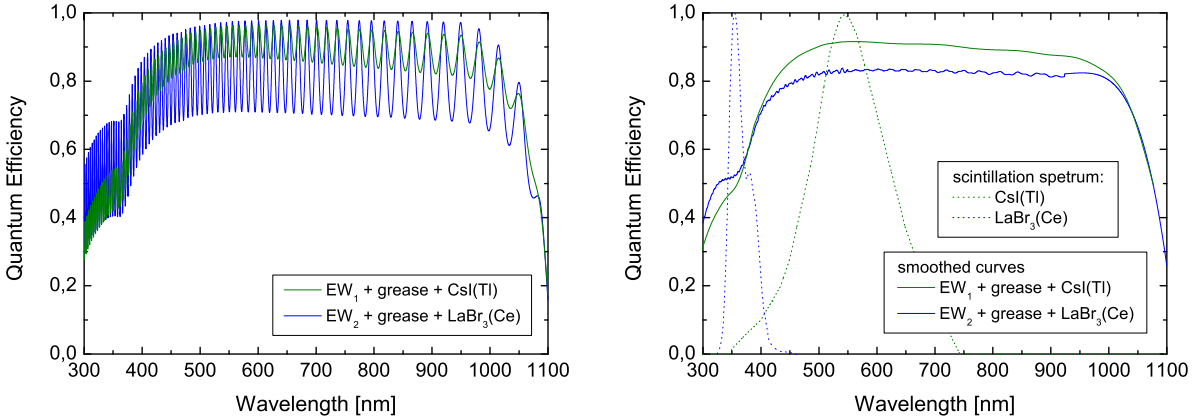

Figure 5.13.: *Calculated QEs of the two entrance windows introduced in Fig. 5.11 for incident photons from CsI(Tl) and $LaBr_3$(Ce) passing an optical coupler (on the left). The corresponding smoothed QE is in the Fig. on the right.*

The QE of the two introduced entrance windows for photons incident from air as shown in Fig. 5.11 is higher in the wavelength range between 300 nm to 600 nm, compared to photons, which are generated inside the scintillators, CsI(Tl) and $LaBr_3$(Ce), passing an optical coupler, with an index of refraction of n = 1.46 (Optical couplers have usually a refractive index around 1.5), before penetrating into the ARC (see Fig. 5.13). The oscillations in the left picture (Fig. 5.13) originate from interference of the electromagnetic waves, due to multiple reflections on the front and back interface of the optical coupler. In the right picture (Fig. 5.13) the oscillating curves have been smoothed to compare their mean value, whereby the dashed lines are the scintillation spectra of CsI(Tl) (green dotted line) and $LaBr_3$(Ce) (blue dotted line). The difference of the QEs between the two entrance windows is smaller compared to photons incident from the air (see Fig. 5.11). There is an improvement of the QE for long wavelengths above 800 nm, but the optimization in the range 300 to 400 nm is almost lost.

Fig. 5.14 shows the calculated QE (including the CCE of the ARC-Window) for 355 and 550 nm photons incident perpendicular from $LaBr_3$(Ce) and CsI(Tl) onto the optical coupler and SDD entrance window in dependence on the thicknesses of SiO_2 and Si_3N_4. The developed SDD entrance windows for scintillation photons from the scintillators $LaBr_3$(Ce) and CsI(Tl) cannot be optimized further by changing the layer thicknesses, if the SiO_2 layer thickness is not reduced below 20 nm.

For photons incident from a medium with a refraction index, n_i, onto an interface with another medium with a lower refractive index value, n_t, there exists an angle between the direction of propagation of the incident photons and the surface normal, ϑ_T, above which photons are totally reflected at the interface. The angle of total

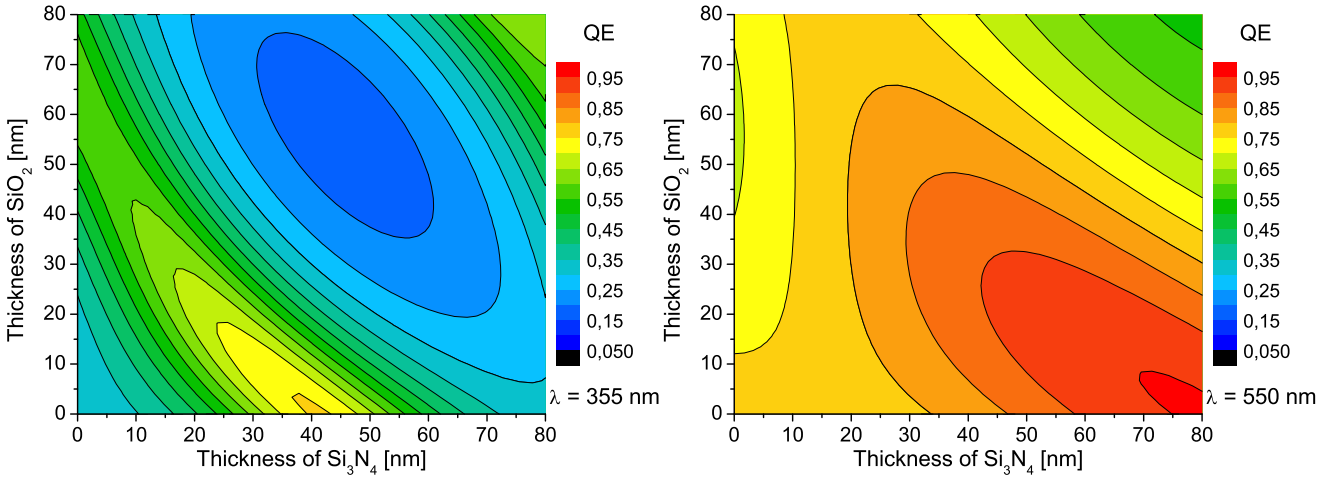

Figure 5.14.: *Calculated QE for photons with wavelengths of 355 and 550 nm, generated inside $LaBr_3(Ce)$ and CsI(Tl), incident perpendicular into the SDD after passing the optical coupler.*

reflectance is given by

$$\vartheta_T = arcsin\left(\frac{n_t}{n_i}\right). \tag{5.27}$$

Photons generated inside a scintillator are reaching the SDD entrance window with angles with respect to the surface normal in the range from 0 to 90°. Thus it is important to know the angle dependence of the quantum efficiency.

The angle dependent QE for photons, which are generated inside the CsI(Tl) or $LaBr_3$(Ce) crystal and passing through an optical coupler before reaching the SDD, where they are absorbed, is illustrated in Fig. 5.15. The QE decreases slightly with

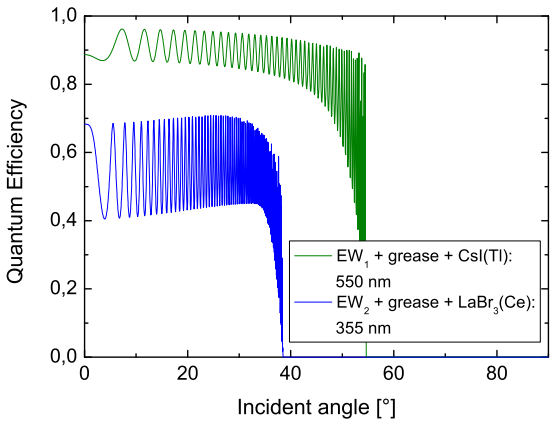

Figure 5.15.: *Angle dependent QE for photons with wavelengths of 355 nm (blue) and 550 nm (green) generated inside $LaBr_3(Ce)$ and CsI(Tl), passing the optical coupler before reaching the SDD EW with an angle of incidence perpendicular to the SDD entrance window.*

an increasing angle of the incident photons with respect to the surface normal of

the entrance window. Approaching the angle of total reflection, ϑ_T, leads to a faster decrease of the QE, until it becomes 0 for incident angles equal or greater than ϑ_T. The existence of an angle of total reflection could lead to a reduction of the system quantum efficiency, η.

ϑ_T is 54° (41°) for photons with a wavelength of 550 nm (355 nm), because the SiO_2 layer of the EW has an index of refraction of n $\approx$ 1.5, which is smaller than that of CsI(Tl) ($LaBr_3$(Ce)) scintillator, $n_{CsI(Tl)} = 1.8$ ($n_{LaBr_3(Ce)} = 2.3$). The second layer of the EW, Si_3N_4, has a refraction index of about $n_{Si_3N_4} = 2$ and silicon is in the range of $n_{Si} = 3.7$ to 6.8.

Subsequently some methods to increase the QE, which have not been implemented into ARC-Windows yet, are presented. To avoid total reflection the refraction index of the scintillator has to be smaller than the refractive indexes of the entrance window materials and silicon. This can be achieved by using a scintillator with a refraction index smaller than n < 1.5 or by constructing an entrance window without a SiO_2-layer, but a Si_3N_4-layer (see Fig. 5.16), if the SDD is coupled to a CsI(Tl) scintillator. The disadvantages of such a window is the higher defect density of the

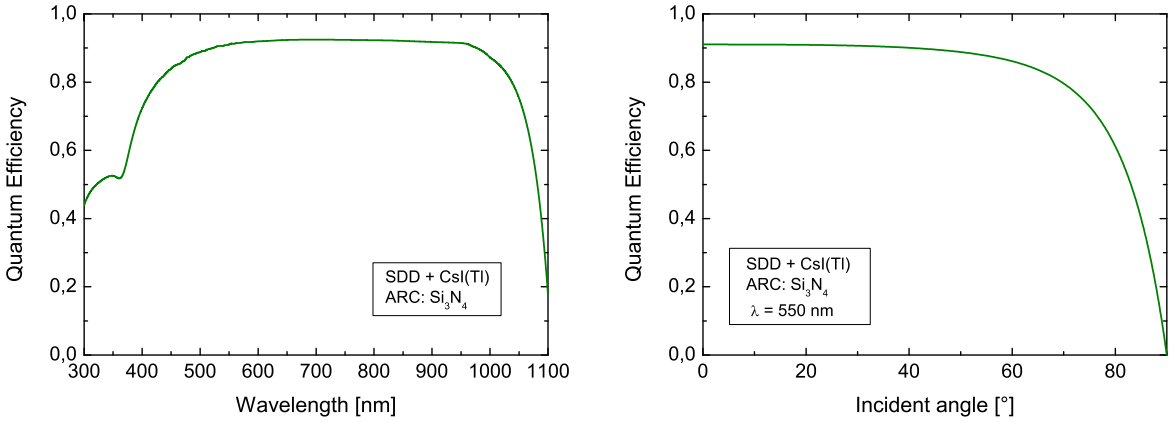

Figure 5.16.: *QE of an entrance window with an ARC, which consists only of a Si_3N_4 layer, for photons generated inside the CsI(Tl) scintillator, which is directly coupled to the SDD. On the left: QE plotted against the wavelength. On the right: QE for photons with a wavelength of $\lambda = 550$ nm plotted against the incident angle.*

Si_3N_4-silicon interface compared to the SiO_2-silicon interface (see Sec. 5.5.1) and the fact that an optical coupler with a refraction index of at least the refraction index of the used scintillator has to be used, in order to avoid an angle of total reflection. The common optical couplers with the physical condition of a gel, rubber or adhesive, have a refraction index around 1.5 (Wacker Silicones, Precision Converting, Cargille Labs, Norland Products, Polytec PT GmbH, leuna harze). Fluids with a refraction index of 1.8 and higher are available, but they have a higher absorption ratio than couplers with a lower refraction index and are corrosive and hazardous. Moreover fluids cannot be used as permanent couplers.

There is still room for improvements of the QE for scintillation photons generated in $LaBr_3$(Ce). First a narrower p-layer improves the CCE (see Fig. 5.10: right

hand side, green line), which results into an increase of the quantum efficiency to $QE_a \approx 0.70$ (Fig. 5.17 bright blue line). Secondly a smaller thickness of the SiO_2-layer of the ARC leads to a further increase of the quantum efficiency to a value of $QE_b \approx 0.76$ (Fig. 5.17 brown line). As the homogeneity of the SiO_2-layer cannot be guaranteed, investigations for the deposition of very thin and homogeneous SiO_2-layers (< 20 nm) are needed, before the realization of such an entrance window is possible. Thirdly an ARC consisting of a SiO_2-Si_3N_4-SiO_2 layer sequence with an optical coupler having a refractive index equal to that of $LaBr_3(Ce)$, produces a $QE_c \approx 0.87$ (Fig. 5.17 blue line). This option is also difficult to realize, because optical couplers with high refractive index, which is close to that of $LaBr_3(Ce)$ are needed.

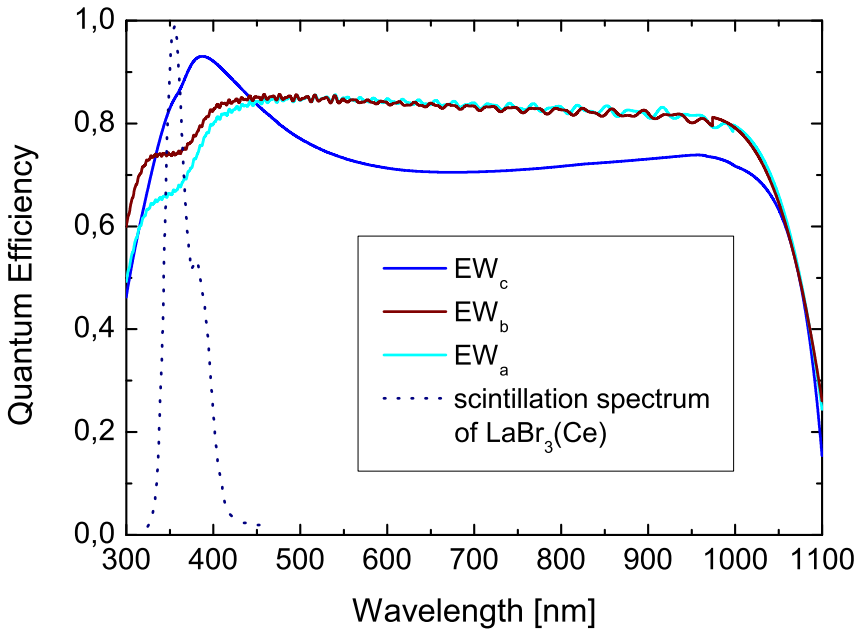

Figure 5.17.: *Calculated QE for photons penetrating from $LaBr_3(Ce)$ for three EWs, which have a larger QE around 355 nm, compared to the EWs presented in Fig. 5.13.*

Due to the coupling of the scintillator to the SDD with an optical coupler and the angle dependence of the QE, the maximum achievable QE especially for scintillation light from $LaBr_3(Ce)$ is limited. Entrance windows have been developed with QEs of 0.9 and 0.5 for scintillation photons from CsI(Tl) and $LaBr_3(Ce)$ respectively.

To conclude, we investigated in this chapter the quantum efficiency of SDDs for incident X-rays and ultra violet to visible photons generated inside the scintillator. Over the whole energy range the measured values of the QE can be reproduced by the presented models. Possibilities to improve the entrance window, especially in the UV-Vis range have been presented.

6. Detector response of a single SDD + CsI(Tl) or $LaBr_3$(Ce)

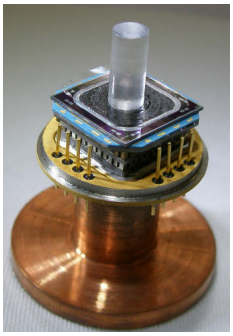

Figure 6.1.: *Photo of a 100 mm^2 SDD coupled to a cylindrical scintillator.*

As photodetectors, SDDs have been used with a circular or square shaped active area of 30 mm^2 and 100 mm^2. The entrance windows of these SDDs consist of an anti reflection coating (ARC) optimized for the near UV - Vis range. The SDDs are coupled with an optical pad and/or silicon grease to the scintillators CsI(Tl) or $LaBr_3$(Ce), which have been manufactured by Hilger Crystals and Saint Gobain Crystals. Millipore filter paper with a pore size of 25 nm [97] and a multilayer film, VM2002, have been used as diffuse and specular reflectors. The reflectivity of VM2002, which is labeled today as enhanced specular reflector (ESR), is larger than 0.98 [98]. Results from spectroscopic measurements indicate that the reflectivity of 5 to 6 layers Millipore paper is supposed to have a similar reflectivity as the VM2002 reflector.

The dimensions of the used scintillators are listed in Tab. 6.1. Parameters of

scintillator	**CsI(Tl)**			**$LaBr_3$(Ce)**
doping	0.1 - 0.13 mole % Tl			5 % Ce
shape	cylindrical		cubic	cylindrical
	⌀ 4.5 mm	⌀ 9.0 mm	4 x 4 mm^2	⌀ 5 mm
thickness [mm]	5	5	5	5
	10		10	10
	20		20	

Table 6.1.: *CsI(Tl) and $LaBr_3$(Ce) scintillator dimensions and concentrations of Tl and Ce used in our measurements.*

CsI(Tl) and $LaBr_3$(Ce) are specified in Table 6.2.

The long scintillation decay times of CsI(Tl) are the reason for the ballistic deficit, if shaping times, t_S, shorter than 12 μs are used. Even at t_S =12 μs, there is

scintillator	**CsI(Tl)**	**$LaBr_3$(Ce)**
emission maximum [nm]	$550^{a,b}$, 565^{c}	355^{e}
light yield [photons/keV] at 662 keV	65^{g}	65^{h}
decay time [μs] at 20°C at - 20°C	τ_1=0.5 - 0.9^{f}, τ_2=1 - 16^{f} τ_1=1.1^{f}, τ_2=9.5^{f}	0.03^{k}
refraction index at λ_{max}	$1.8^{a,b,c}$	2.3^{d}
density [g/cm^3]	$4.51^{a,b,c}$	5.08^{a}
Z_{eff}	54^{l}	47^{l}
absorption coefficient [cm^{-1}] at 500 keV	0.44	0.44
hygroscopic	slightly^{a,b}, no^{c}	yes^{a}
after glow [%]	0.5 - 5 (6 ms)^{l}	very low
radiation background	no	yes

Table 6.2.: *Properties of CsI(Tl) and $LaBr_3$(Ce) given by [a]S. Gobain, [b]Scionix, [c]Hilger Crystals and [d][99], [e][63, 68], [f][59], [g][100, 59], [h][51], [k][101, 63], [l][14].*

ballistic deficit, so that about 94 % of the generated electrons are collected at the anode (Fig. 6.2 graph on the right). For $LaBr_3$(Ce) + SDD only the drift time of the electrons inside the SDD to the anode determines their collection time after a gamma event, because of the short decay time of 30 ns of scintillation photons in $LaBr_3$(Ce). Fig. 6.2 (on the right) shows the amplitude of the preamplifier output plotted against the time for two temperatures, 10°C and - 20°C for the system SDD + $LaBr_3$(Ce) scintillator. The dimensions of cylindrical $LaBr_3$(Ce) scintillator are: 5 mm diameter and 10 mm thickness. The output signal is proportional to the number of the collected signal electrons. The drift path length is in the range from 0 to 2.5 mm. The rise time of the preamplifier output signal is about 300 ns at - 20°C and 420 ns at 10°C, which is in agreement to the drift time of electrons for a distance of 2.5 mm inside silicon and for an applied field of 520 V/cm convolved with the rise time of the preamplifier, which is about 50 ns. The electron drift time inside the SDD is in this case the reason for a ballistic deficit towards very short shaping times below 500 ns and it sets the limitation for the maximal possible count rate capability.

For CsI(Tl) + SDD the scintillation decay time exceeds the drift time of the electrons to the anode. The time dependent amount of the collected signal charge at 10°C and - 20°C for the detector CsI(Tl) + SDD is shown in Fig. 6.2 (on the right). The total amount of generated scintillation photons, $J_{int}(t)$, for a time, t, after a γ-event, can be described by formula [48]

$$J_{int}(t) = \left[\int_0^t \sum_{i=1}^{2} J_i \cdot \left(exp\left(-\frac{t}{\tau_i}\right) - exp\left(-\frac{t}{\tau_{r,i}}\right) \right) dt \right] \cdot \frac{1}{C_n} \qquad (6.1)$$

where J_i is the amplitude, τ_i and $\tau_{r,i}$ the scintillation decay and rise times of the i-th decay channel. C_n is a normalization constant. Neglecting the contribution of the drift time of the electrons inside the SDD and the rise time of the preamplifier, we fitted formula 6.1 to the measured output signals shown in Fig. 6.2 on the right. The obtained fitting parameters are $\tau_1 \approx 1500$ ns, $\tau_2 \approx 15000$ ns with the scintillation

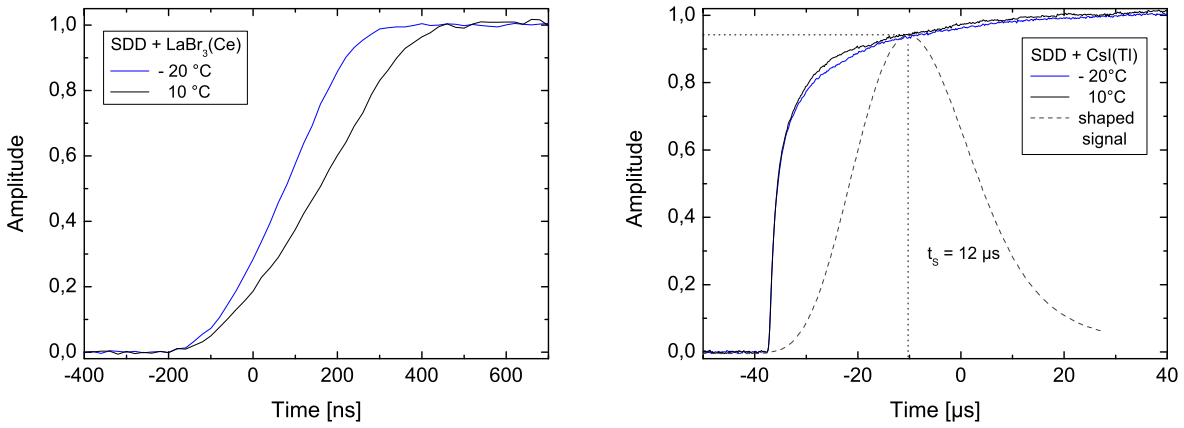

Figure 6.2.: *Measured rise time of the preamplifier output of SDD + $LaBr_3$(Ce) (left figure) and SDD + CsI(Tl) (right figure) at 10° C and - 20° C.*

rise times $\tau_{r,1} = \tau_{r,2} = 20$ ns (τ_r, which have been adapted from [59]). The intensity amplitudes are $J_1 \approx 0.73$ and $J_2 \approx 0.04$ for 10°C and - 20°C. τ_1 and τ_2, without the contribution of the SDD, are shorter than deduced from the fit, because the drift time of the electrons (300 - 400 ns) and the rise time of the preamplifier (50 ns) have not been included into the formula used to fit the measured data. Our deduced decay times at - 20°C and 10°C for the CsI(Tl) scintillator are slightly longer compared to values determined by [59].

The light yield of CsI(Tl) reported in literature is about 65 photons/keV [50, 100] for incident γ-rays with an energy of E = 662 keV. For Tl concentrations in the range 0.1 to 0.3 mole % the light yield is almost constant [102, 103, 104]. For $LaBr_3$(Ce) it is about 60-65 photons/keV for E = 662 keV [51, 100, 105]. In literature a slight increase of the light yield of $LaBr_3$(Ce) with an increasing Ce concentration from 0.5 to 5 % and a drop to higher concentrations has been measured [106, 107].

6.1. Results from spectroscopic measurements in the range 6 to 662 keV

In this section results from spectroscopic measurements with single cell SDDs coupled to CsI(Tl) or LaBr3(Ce) are discussed. First the ENC_{el} of the used SDDs for three temperatures are shown in Fig. 6.3. Measurements have been performed with shaping times in the range from 0.5 to 12 μs. For temperatures equal or larger than 0°C the ENC_{el} decreases to shorter t_S. This is due to a reduced number of collected electrons, originating from the leakage current. For -20 °C the ENC_{el} changes only slightly with t_S and has a minimum at $t_S = 1$ μs or $t_S = 2$ μs. The value of ENC_{el} has been calculated from the photo and noise peak of the directly detected spectrum generated after irradiation of the SDD with the ^{109}Cd (E = 22.1 keV) source:

$$ENC_{el} = \frac{\sigma_{noise}}{X_{Cd} - X_{noise}} \cdot \frac{E_{Cd}}{\overline{w}} \tag{6.2}$$

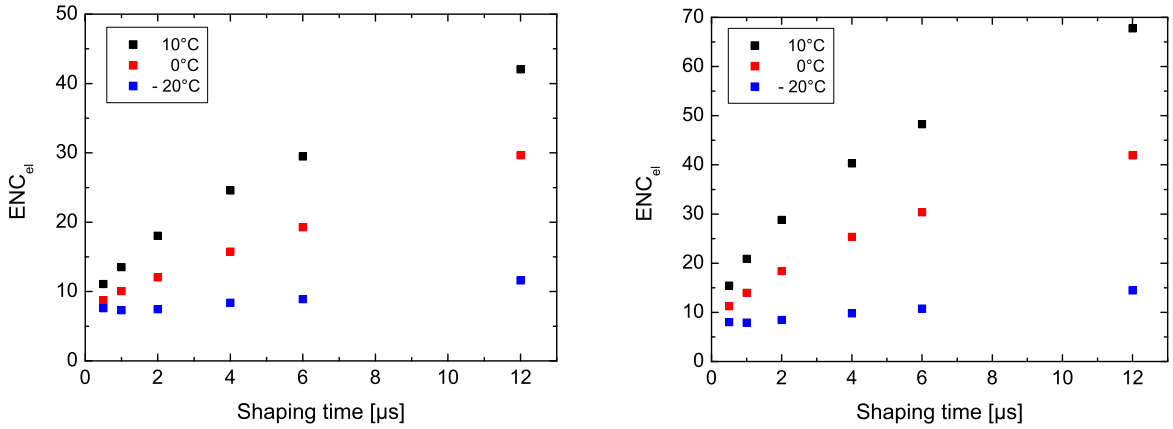

Figure 6.3.: *Equivalent noise charge if the electronic noise (ENC_{el}) dependent on the shaping time and temperature. Results for a 30 mm ^{2} (left graph) and 100 mm ^{2} (right graph) SDD.*

where X_{Cd} and X_{noise} are the channel numbers of the photo and noise peak positions at E_{Cd} = 22.1 keV and E = 0 keV. The relative energy resolution, R, is calculated by

$$R(E) = 2.35\frac{\sigma(E)}{X(E) - X_{noise}} \tag{6.3}$$

where $\sigma(E)$ is the standard deviation of the photo peak and $X(E)$ its position determined in indirect detection mode. The number of signal electrons per keV is given by

$$\frac{\overline{N}_e(E)}{E} = \frac{X(E) - X_{noise}}{X_{Cd} - X_{noise}} \cdot \frac{E_{Cd}}{\overline{w}} \cdot \frac{1}{E}. \tag{6.4}$$

Measured results of R and $\overline{N}_e/E$, with a 30 mm ^{2} and 100 mm ^{2} SDD coupled to a cylindrical CsI(Tl) with a diameter of $\oslash$ = 4.5 mm or 9.0 mm and a thickness of 5 mm, at 0°C are shown in Fig. 6.4 and 6.5. The detectors have been irradiated with ^{55}Fe (5.9 keV), ^{109}Cd (22.1 and 24.9 keV), ^{241}Am (59.5 keV), ^{57}Co (122 and 136.5 keV) and ^{137}Cs (662 keV) sources. The energy resolution has its minimum at a shaping time of t_S = 12 μs for energies E $\geq$ 60 keV. For photons with an energy of 22 keV and 6 keV the minimum of R is at t_S = 6 μs and t_S = 2 μs, due to the smaller number of generated signal electrons, the energy resolution is more sensitive with respect to the electronic noise contribution, which increases with increasing shaping time, t_S. The long decay time of the scintillation light in CsI(Tl) leads to ballistic deficit for $t_S \leq$ 12 μs. The value of $\overline{N}_e/E$ increases from 6 keV to 22 keV and decreases to higher γ-energies, such as 60 keV, 122 keV and 662 keV (Fig. 6.5).

Measurements of R and $\overline{N}_e/E$ for the γ-detector consisting of a 30 mm^2 SDD coupled to a cylindrical $LaBr_3$(Ce) scintillator with a diameter of $\oslash$ = 5 mm and a thickness of 5 mm are shown in Fig. 6.6 and 6.7. The detector temperature is 0°C and it is irradiated with ^{241}Am, ^{57}Co and ^{137}Cs sources. There is no dependency of R and $\overline{N}_e/E$ on the shaping time in the range t_S = 0.25 to 4 μs, because of an almost constant electronic noise and due to the fact that there is only a small

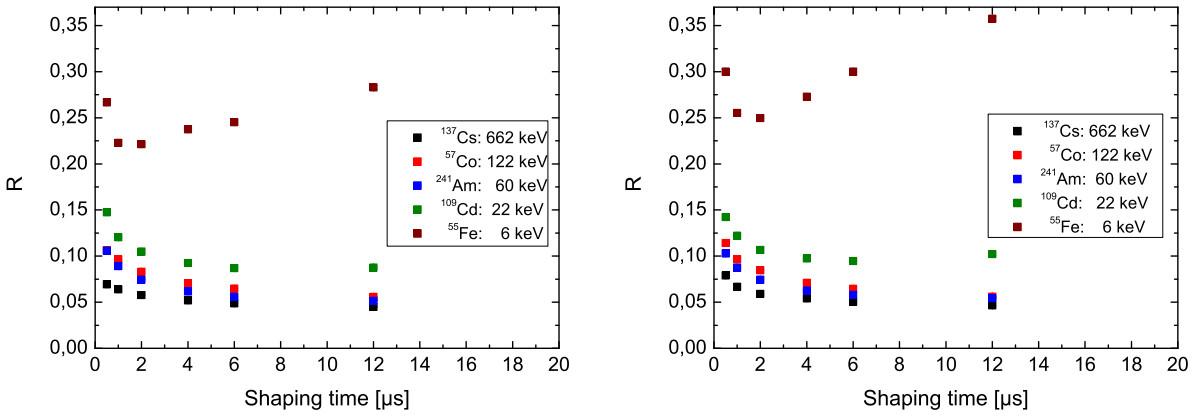

Figure 6.4.: *Relative energy resolution, R, of 30 mm² (on the left) and 100 mm² (on the right) SDDs coupled to cylindrical CsI(Tl) with the dimensions ⌀ = 4.5 (on the left) and 9 mm (on the right) and 5 mm thickness dependent on shaping time and γ-energy at 0° C.*

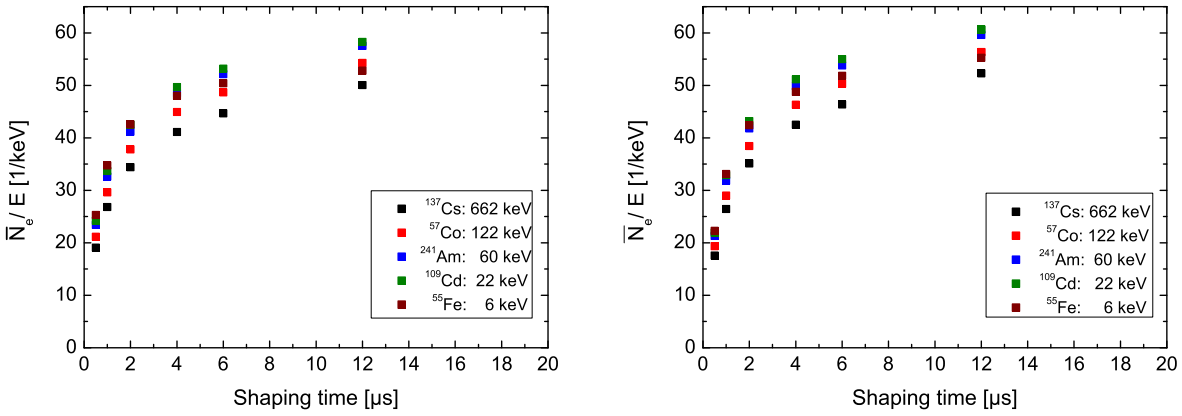

Figure 6.5.: *Measured number of signal electrons per keV, N_e/E, for the systems consisting of a SDD with an active area of 30 mm² (on the left) and 100 mm² (on the right) coupled to cylindrical CsI(Tl) with the dimensions ⌀ = 4.5 (on the left) and 9 mm (on the right), and 5 mm thickness, plotted against shaping time for different γ-energies at 0° C. The used reflector is Millipore paper.*

ballistic deficit for the shaping time $t_S = 0.25\ \mu s$. Compared to the γ-detector SDD + CsI(Tl) the value of $\overline{N}_e/E$ is 2.5 times lower for the system SDD + $LaBr_3$(Ce). The reason for a lower value of $\overline{N}_e/E$ is the lower quantum efficiency of the SDD for photons from the near ultra violet range compared to the visible range. The better energy resolution of $LaBr_3$(Ce) at 662 keV is due to the fact, that its light yield is more proportional compared to the light yield of CsI(Tl) in the energy range 60 to 662 keV. This will be discussed in the next sections.

Some spectra measured with the γ−detectors SDD + CsI(Tl) and SDD + $LaBr_3$(Ce)

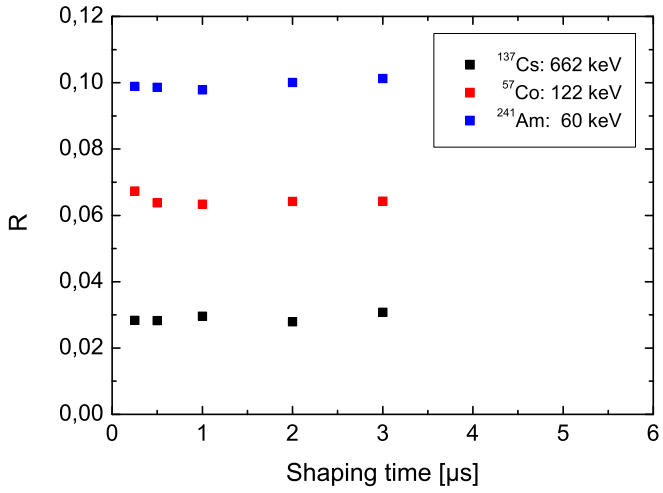

Figure 6.6.: *Measured relative energy resolution, R, of a 30 mm² SDD coupled to a cylindrical $LaBr_3(Ce)$ with the dimensions ⌀ = 5 mm and a thickness of 5 mm, plotted against shaping time and dependent on the γ-energy at 0° C.*

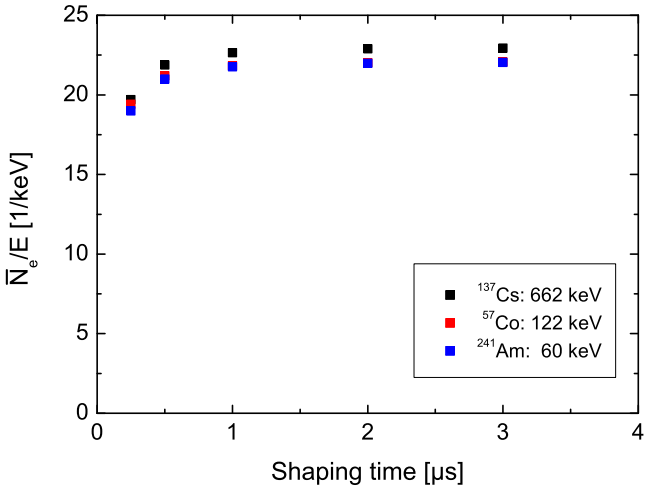

Figure 6.7.: *Measured mean number of signal electrons per keV, $\overline{N}_e/E$, with a 30 mm² SDD coupled to the cylindrical $LaBr_3(Ce)$ with the dimensions ⌀ = 5 mm and a thickness of 5 mm, plotted against shaping time and dependent on the γ-energy at 0° C.*

are illustrated in Fig. 6.8 and 6.9. The spectra show the photo, escape, Pb fluorescence peaks from the collimator and for higher energies also events generated by Compton scattering of the incident γ-rays. The shoulder of the photo peak at 59.5 keV is originating from the non-proportionality contribution of CsI(Tl) and will be explained in Sec. 6.2.1.

Due to the aluminium housing of the $LaBr_3(Ce)$ scintillator, X-rays from the

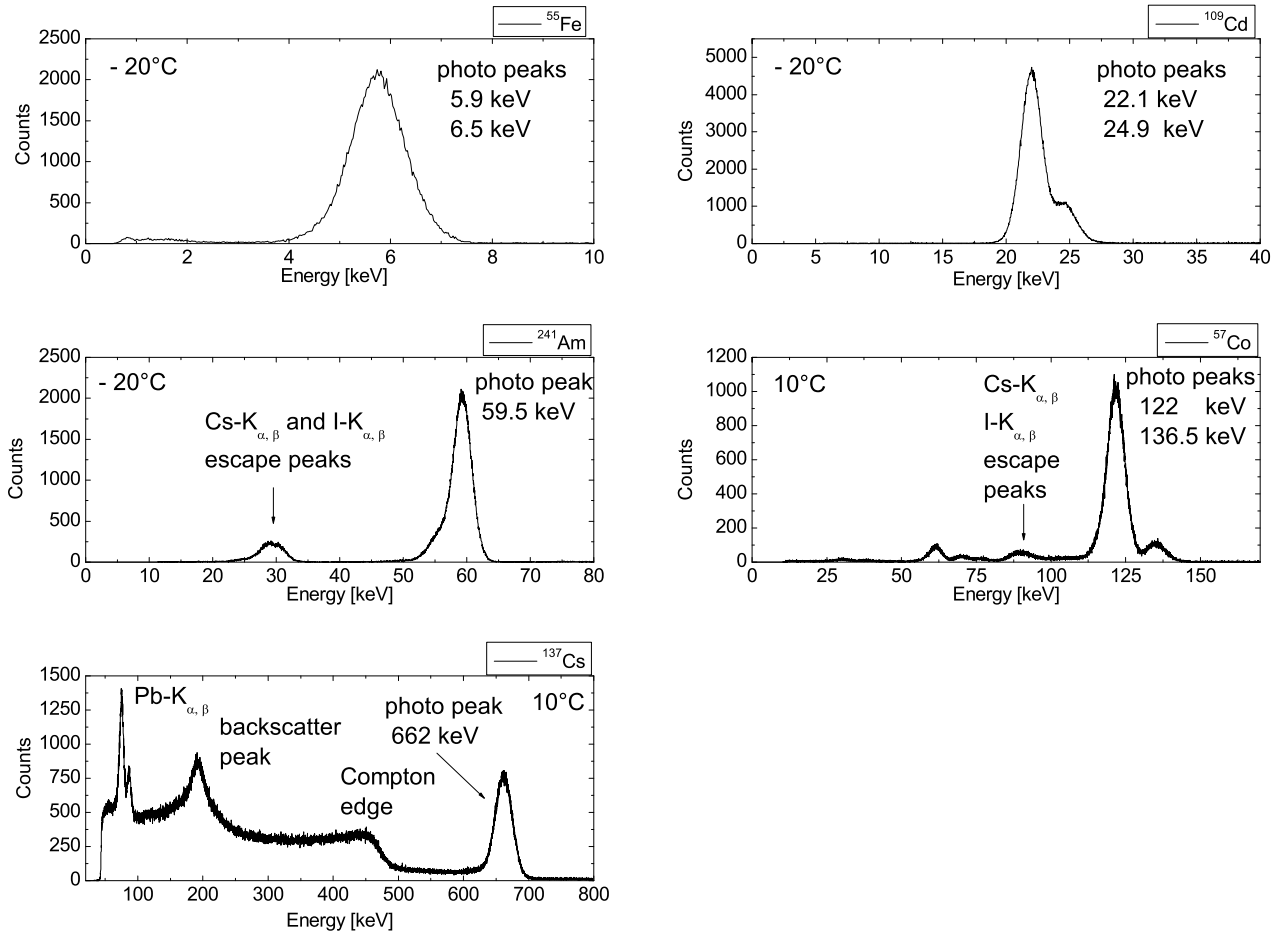

Figure 6.8.: *Spectra of a 100 mm^2 SDD coupled to CsI(Tl) measured with a shaping time of 12 μs during irradiation with different sources.*

^{55}Fe source are absorbed inside the Aluminum, so that photons with the energies E = 5.9 keV and 6.5 keV could not be detected in the system SDD + $LaBr_3$(Ce).

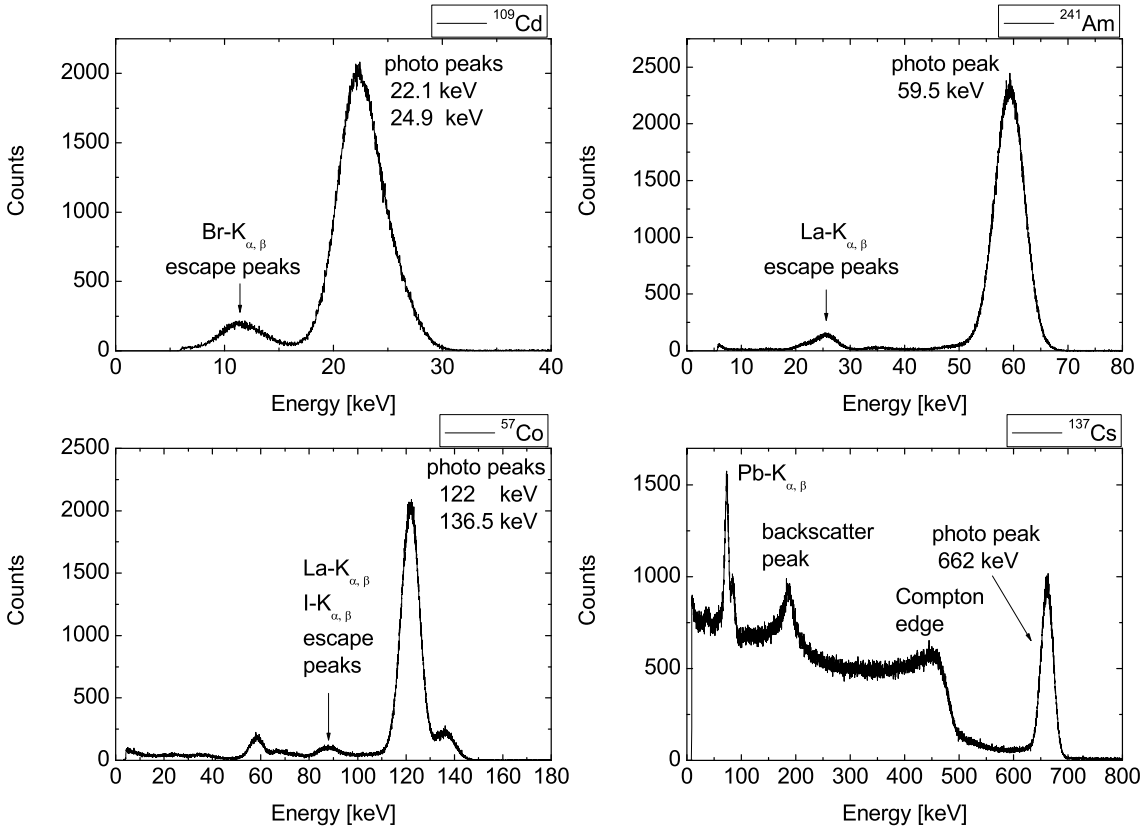

Figure 6.9.: *Spectra of a 30 mm^2 SDD coupled to $LaBr_3(Ce)$ measured at - 20° C with a shaping time of 2 μs during irradiation with different sources.*

6.1.1. Energy resolution and light yield dependence on the photon energy

In the following the results from measurements of the temperature and energy dependent energy resolution, R, and number of generated signal electrons per keV $\overline{N}_e/E$ will be discussed. The analytical formula for the total relative energy resolution has been derived in Chap. 4:

$$\begin{aligned} R &\approx \sqrt{R^2_{Fano-Scint} + R^2_T + R^2_\eta + R^2_{Bino} + R^2_{el}} \\ &= \sqrt{R^2_T + R^2_\eta + R^2_{stat} + R^2_{el}} \end{aligned} \tag{6.5}$$

where

$$R_{stat} = \sqrt{R^2_{Fano-Scint} + R^2_{Bino}}. \tag{6.6}$$

The statistical noise, R_{stat}, is the sum of the Fano and binomial noise contributions.

Fig. 6.10 shows for the detector system consisting of a SDD coupled to CsI(Tl) the measured energy resolution (squares) and the contributions to the energy resolution of the electronic (broken lines), statistical noise (dotted lines) and their sum. The values in between the discrete energies of the measured values are guides to the eye. It is recognizable that the contributions of R_T and R_η have to be significant,

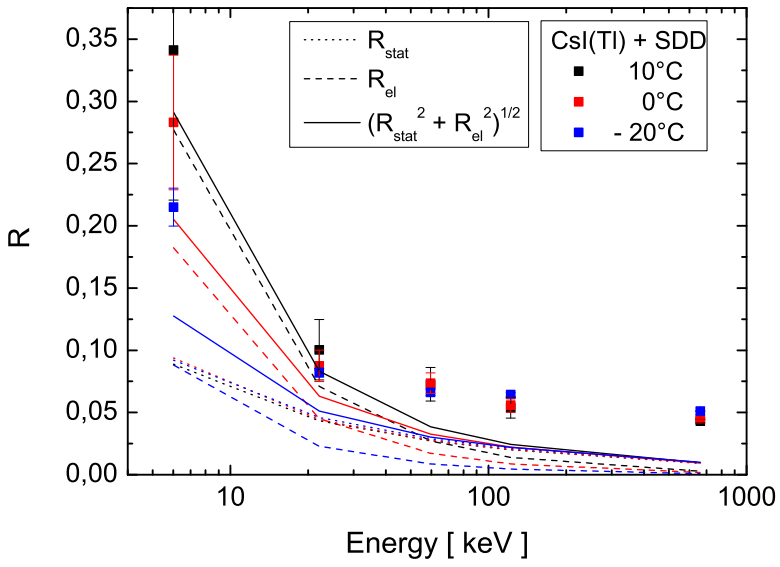

Figure 6.10.: *Energy and temperature dependent energy resolution, R, measured at 12 µs shaping time with a 30 mm² SDD coupled to a cylindrical CsI(Tl) with ⌀ = 4.5 mm and d = 5 mm, wrapped into Millipore paper. F_{CsI} = 0.28 and $\overline{w}_{CsI}$ = 14 eV.*

especially in the energy range above 22 keV. Due to an increase of the absolute number of scintillation photons for higher photon energies, the electronic and statistical noise contributions decrease with increasing energies. Their values become

important for energies lower than 60 keV. $R_T > 0$ results from the non-proportional light yield of the scintillator.

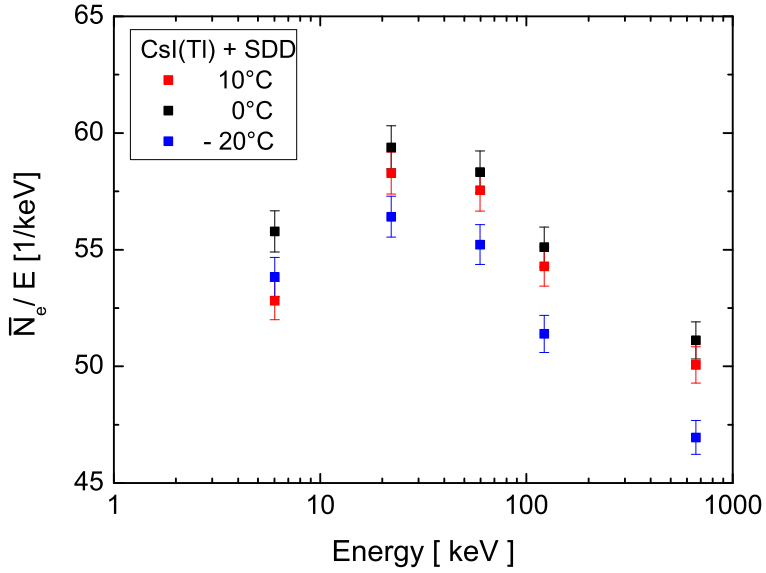

Figure 6.11.: *Energy and temperature dependent number of generated signal electrons per keV, $\overline{N}_e/E$, measured at 12 µs shaping time with a 30 mm² SDD coupled to a cylindrical CsI(Tl) with ⌀ = 4.5 mm and d = 5 mm, wrapped into Millipore paper.*

Fig. 6.11 shows the temperature and energy dependent mean number of the measured signal electrons per keV, $\overline{N}_e/E$, for the detector system consisting of SDD + CsI(Tl). $\overline{N}_e/E$ increases from 6 keV to 22 keV and decreases to higher energies. $\overline{N}_e/E$ is lower at lower temperatures. If the CsI(Tl) scintillator is cooled from 10 °C to - 20 °C $\overline{N}_e/E$ decreases by about 3 and 4 photons per keV.

Fig. 6.12 shows the temperature and energy dependent energy resolution, R, of the detector system consisting of a single SDD cell coupled to $LaBr_3$(Ce). The Fano factor of $LaBr_3$(Ce) is not known yet. It is set to the maximum possible value, $F_{LaBr_3} = 1$, which leads to an estimation of the energy resolution, which is poorer compared to the real case. It is clearly visible that also for this detector type the contribution of the two terms R_T and R_η have to be significant, as is illustrated by the gap between the measured resolution and the contributions of the electronic and statistical noise. The statistical noise contribution of the detector SDD + $LaBr_3$(Ce) is higher compared to that of the detector SDD + CsI(Tl), due to the lower number of scintillation photons reaching the SDD, because of its lower QE for scintillation photons from $LaBr_3$(Ce). The electronic noise has only a minor contribution to the peak broadening compared to the detector SDD + CsI(Tl). A shorter shaping time can be used in the measurements with $LaBr_3$(Ce) without a ballistic deficit in contrast to measurements with CsI(Tl), due to a much faster decay time of the scintillation light in $LaBr_3$(Ce).

In Fig. 6.13 the temperature and energy dependent number of signal electrons per keV, $\overline{N}_e/E$, are plotted for the detector SDD + $LaBr_3$(Ce). The value of $\overline{N}_e/E$

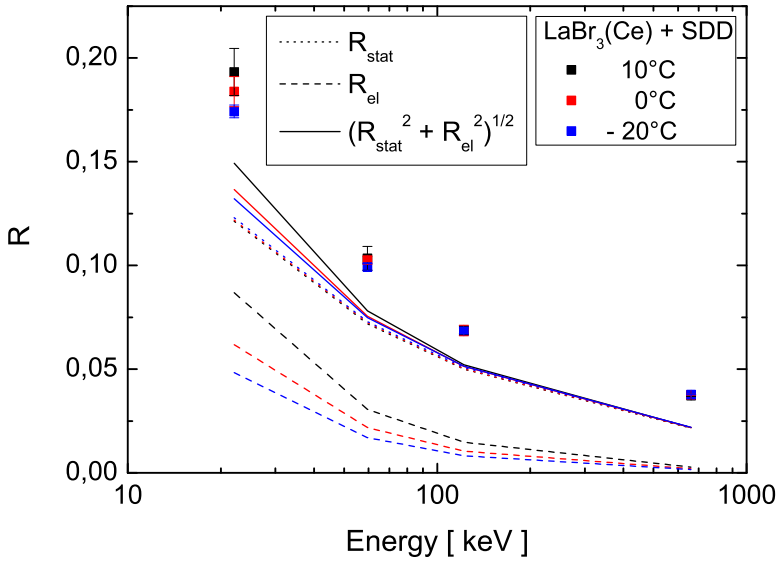

Figure 6.12.: *Energy and temperature dependent energy resolution of a 30 mm² SDD coupled to a cylindrical $LaBr_3(Ce)$ with ⊘ = 5 mm and d = 10 mm, enclosed into a vacuum sealed aluminum housing with a glass window, measured at 1 µs shaping time. $F_{LaBr_3} = 1$ and $\overline{w}_{LaBr_3} = 13$ eV.*

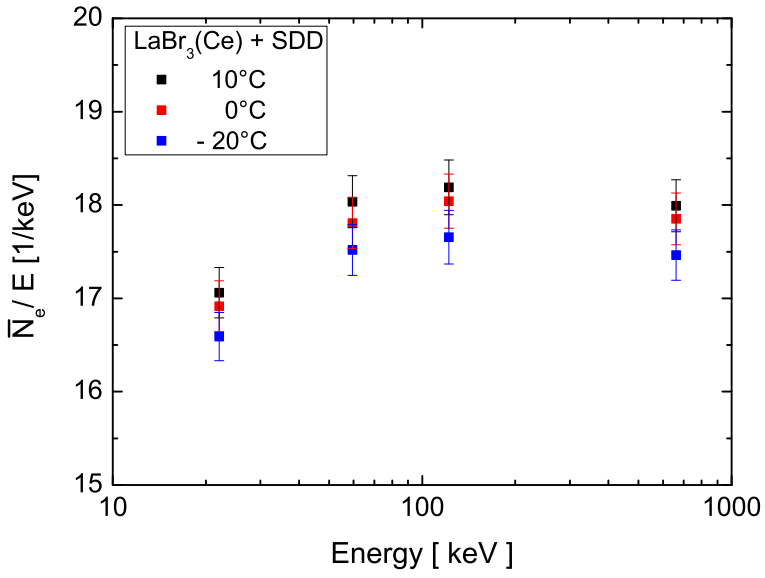

Figure 6.13.: *Energy and temperature dependent number of signal electrons, $\overline{N}_e/E$, of a 30 mm² SDD coupled to a cylindrical $LaBr_3(Ce)$ with ⊘ = 5 mm and d = 10 mm, enclosed into a vacuum sealed aluminum housing with a glass window, measured at 1 µs shaping time.*

for $LaBr_3$(Ce) is much lower than for CsI(Tl), because of a lower quantum efficiency of the SDD entrance window and losses, due to the crystal packaging. Above 60 keV the light yield is nearly constant. There is also a small decrease of the value $\overline{N}_e/E$ to lower temperatures. In Fig. 6.14 the normalized values of the number of signal electrons per keV, which is proportional to the light yields of the two crystals are presented. The variation of the normalized values of $\overline{N}_e/E$ with energy is much lower for the system SDD + $LaBr_3$(Ce) than for the system SDD + CsI(Tl) for energies equal or larger than 60 keV.

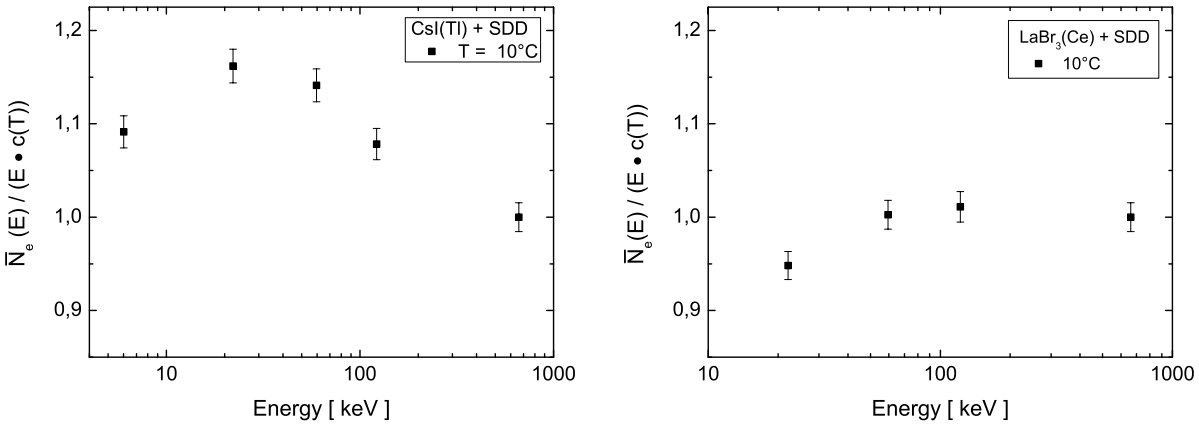

Figure 6.14.: *Measured energy dependent normalized values of $\overline{N}_e/E$ at 10°C. The data are taken from Fig. 6.11 and 6.13 and are normalized to 1 at 662 keV.*

6.1.2. Effect of the light and charge collection efficiency

In Fig. 6.15 two spectra are illustrated, which are measured with a detector consisting of a bare cylindrical CsI(Tl) scintillator with a diameter of $\oslash = 5$ mm and a thickness of d = 10 mm, wrapped into a reflector and coupled with optical grease to a SDD. Wrapping the scintillator into a reflector is very important to improve the collection efficiency and uniformity of scintillation photons. The use of a reflector improves the energy resolution and increases the number of detected photons.

Results from spectroscopic measurements with cylindrically and cubically shaped scintillators with a diameter of 4.5 mm or a face with an area of 4 x 4 mm^2 and thicknesses of 5, 10 and 20 mm are presented in the following. Measurements have been performed with CsI(Tl) wrapped into a diffuse, Millipore paper [97], and a specular reflector, VM2002 [98].

Fig. 6.16 shows the measured relative energy resolution, R, and the mean number of detected signal electrons per keV, $\overline{N}_e/E$, at the SDD anode after irradiation of the CsI(Tl) scintillator with a ^{57}Co (122 keV) source. For cylindrically and cubically shaped CsI(Tl), the enery resolution increases from 0.057 to 0.062 (Fig. 6.16), if the scintillator thickness increases from 5 mm to 20 mm. The detector with the cubical CsI(Tl) scintillator has a slightly better energy resolution. Comparing R of

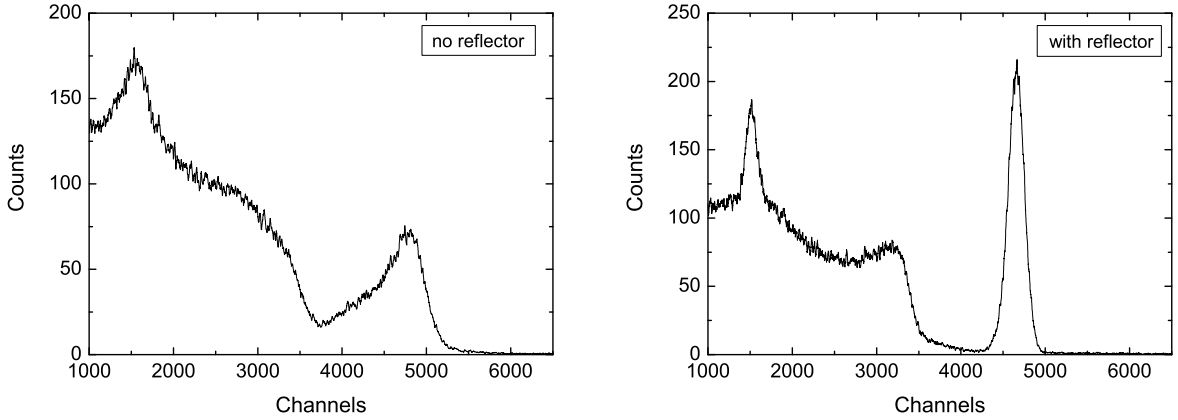

Figure 6.15.: *Measured spectrum with CsI(Tl) + SDD with a shaping time of 10 µs, at room temperature after irradiation with a ^{137}Cs source without (on the left) and with reflector (on the right). The cylindrical CsI(Tl) has a diameter of 5 mm and a thickness of 10 mm. The amplifier gain of the left spectrum is by a factor 2.2 larger than for the right spectrum.*

CsI(Tl) wrapped into the Millipore paper or the VM2002 reflector, shows that the wrapping into the diffuse Millipore paper reflector leads predominantly to a slightly better energy resolution. In Fig. 6.16 it can also be observed that the measured

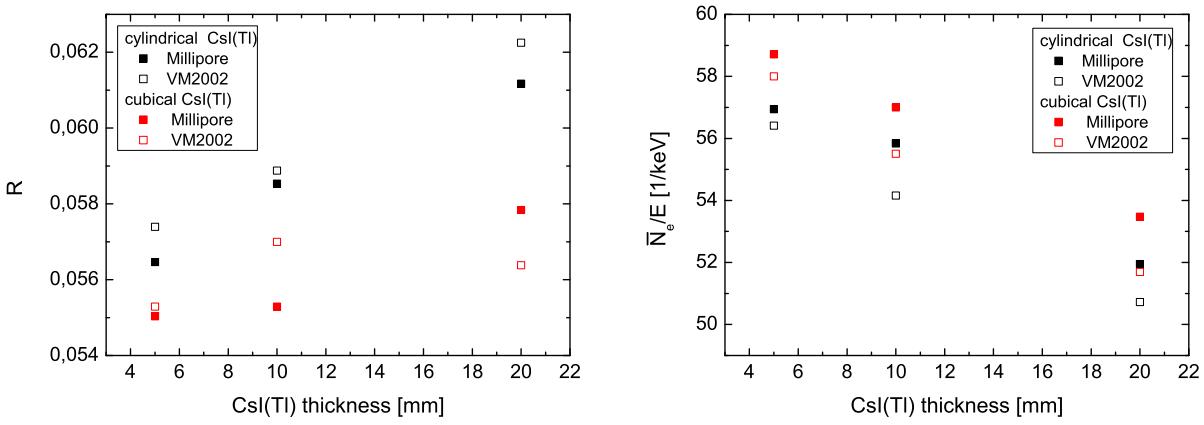

Figure 6.16.: *Measured energy resolution and number of signal electrons per keV at 10° C with a shaping time of t_s = 12 µs for cylindrical (black) and cubical (red) CsI(Tl) scintillators of different thicknesses with a diameter of 4.5 mm or a face of 4 x 4 mm^2. The energy of the incident photons is 122 keV.*

mean number of signal electrons per keV, $\overline{N}_e/E$, decreases from about 58 for 5 mm to 52 for 20 mm thick CsI(Tl). Cubically shaped CsI(Tl) scintillators have a larger value of $\overline{N}_e/E$ than cylindrically shaped CsI(Tl) scintillators. The difference is about 2 photons/keV. The light collection efficiency of the diffuse Millipore reflector

is slightly better compared to the specular VM2002 reflector, which results into a higher value of $\overline{N}_e/E$.

We can conclude that R increases by about 9 % and $\overline{N}_e/E$ decreases by about 10 % for an increasing CsI(Tl) thickness from 5 mm to 20 mm for incident γ-rays of 122 keV. These values change only slightly for different energies. The scintillator thickness, shape and wrapping have a small effect on the energy resolution for the used detector system. In Sec. 6.2.2 results of the energy resolution and the mean number of signal electrons from Monte Carlo simulations with the Geant4 toolkit show the same behavior as the measured values in Fig. 6.16 as a function of CsI(Tl) thickness and specular or diffuse reflectivity.

6.2. Results from calculations and simulations

In the previous chapter we have presented and analyzed the measured energy resolution and light yield. In the following sections we will investigate the energy dependence of the light yield and determine its the contribution and the contribution of the light collection efficiency to the energy resolution for the detector systems SDD + CsI(Tl) and SDD + $LaBr_3$(Ce) by calculations and Monte Carlo simulations.

The Monte Carlo simulations, including the passage of X-, γ-rays and optical photons through matter, are performed with the Geant4 simulation toolkit [108]. Detector geometry and material properties can be defined in the code. The cross sections for the interaction of X- and γ-rays are already included in the kernel. Optical properties, refraction index and absorption length, of the involved materials, the light yield and scintillation spectrum of the scintillator have to be inserted into the code. The values of the reflectivity and transmittivity of UV-Vis photons at the SDD entrance window, which are calculated with Eq. 5.22, 5.23 and C.16, had to be included into the kernel as a look-up table.

6.2.1. Non-proportional light yield and energy resolution

Several groups determined the contribution of the non-proportional light yield of NaI(Tl), has been discovered in the 1950s, to the energy resolution for γ-rays [80, 81]. In the last 10 - 20 years the interest for the scintillator performance has increased again, because the performance of photodetectors has improved. In literature Monte Carlo simulations have been carried out to determine the contribution of the non-proportional light yield to the energy resolution of NaI(Tl) and LSO [82]. Also the energy dependent light yields of NaI(Tl), LSO and CaF_2(Ce) for incident γ-rays have been calculated from the measured energy dependent light yield of electrons inside these scintillators [109]. In the following years additional publications appeared discussing the contribution of the light yield non-proportionality of NaI(Tl) to the energy resolution [110, 111].

Recently groups have approached the scintillator light yield non-proportionality by different models and deduced analytical expressions to describe the non-proportional light yield for electrons [49, 112]. Formulas for the energy resolution for incident electrons, including the non-proportional light yield convolved with the energy dependent ionization density for electrons and fluctuations of the energy deposition by

electron along their track have been presented in [25, 49, 100].

In this work the scintillators $LaBr_3$(Ce) and CsI(Tl) are investigated. $LaBr_3$(Ce) is a relatively new scintillator invented in the year 2001 [101] and experimentally examined by different groups [113, 114], because of its high light yield of 60 - 65 photons/keV [51, 100, 105] and very good energy resolution of 2.8 % for an incident γ-energy of 662 keV [9]. CsI(Tl) is a scintillator with excellent properties like workability, non hygroscopicity, scintillation spectrum matching the maximum quantum efficiency of photo diodes, a high light yield of about 65 photons/keV [59, 100] and a good energy resolution of about 4.3 % at 662 keV [9].

In the following a short overview will be given of the processes following the interaction of γ-photons with the scintillator and the consequences of a non-proportional light yield of scintillators. Then the method is presented by which the light yield for γ-photons and the energy resolution for electrons and γ-photons is calculated. Afterwards results of the calculated light yield and energy resolution for electrons are presented. Next the simulated spectra for incident γ-rays caused by the non-proportionality are discussed. At the end of this section the results from simulations of the energy dependent light yield and energy resolution for γ-rays arising from a non-proportional light yield are shown and compared to results from measurements.

Processes following the interaction of γ-photons with the scintillator

A γ-photon can deposit energy in the scintillator via photo effect, Compton scattering or pair production. We are considering γ-energies up to 662 keV, where pair production does not occur. After an interaction of a γ-photon with an atom

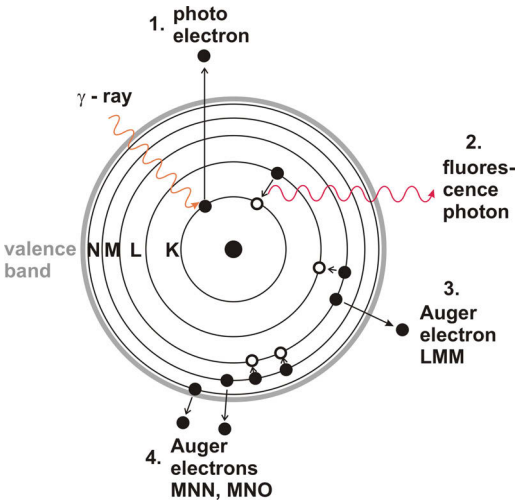

Figure 6.17.: *Schematic showing one possibility for the relaxation of the excited atom after the ejection of a K-shell electron (photo effect) by a γ-ray.*

of the scintillator via photo effect, an electron is ejected from an inner shell, so that the atom remains in an excited state. The atom relaxes by filling the hole with electrons from upper shells, producing fluorescence photons and Auger electrons. After a Compton interaction, an electron is ejected from the valence band, whereas the Compton scattered photon escapes the scintillator or interacts again via photo or Compton effect with another atom. Most of the electrons resulting

from Compton events and atomic relaxation are very energetic and generate via ionization and bremsstrahlung other electrons in the conduction bands, holes in the valence band and X, γ-rays. For electron energies below 1 MeV the energy loss by bremsstrahlung is very small compared to the loss by ionization scattering, so that the bremsstrahlung process is neglected in our simulations. The ionization scattering process continues until the generated electrons reach an energy level below which no additional eh-pairs can be created, so that the electrons and holes loose their remaining kinetic energy by phonon scattering. After thermalization, the energy of the electrons and holes is transferred to luminescence centers, where relaxation occurs radiatively or non-radiatively.

Consequence of a non-proportional light yield of scintillators

The non-proportional light yield leads to two contributions to the energy resolution for γ-rays. Considering a constant γ-energy and the absorption of the full energy inside the scintillator, an interaction generates a number of first electrons with an energy distribution, which varies for each γ-event, due to the fact, that the involved processes occur with a certain probability. The variation of the electron number and energy distribution among these first electrons, convolved with a non-proportional light yield for electrons leads to a degradation of the energy resolution.

The second contribution results from the fact, that the electrons generated by Compton scattering, photo and Auger effect produce further electrons by ionization. The ionization density of an electron depends on its energy, hence on its path through the scintillator. The deposited energy per path length can be described by the Bethe formula 2.11. Variations in the ionization density for electrons with a certain energy, due to variations in δ-ray production and Landau fluctuations, lead to a degradation of the energy resolution, if the generation of scintillation photons depends on the ionization density. The variations resulting from δ-rays are not considered in this work.

These two contributions to the energy resolution are investigated in the following.

Methodology

The γ-photon interacts with the scintillator via photo effect or Compton scattering. After the photo effect the whole energy of the incident photon is transferred to the photo electron and the recoil atom. The excited atom with a hole in an inner shell relaxes through the generation of fluorescence photons and Auger electrons [108, 115]. K, L, M, N and O shells are included into the relaxation process in Geant4 [115]. Fluorescence photons interact again with the scintillator by photo effect or Compton scattering, if they do not escape the scintillator. If a Compton scattering process occurs, a part of the energy of the incident photon is transferred to the Compton scattered electron. The Compton scattered photon interacts again with the scintillator by photo effect or Compton scattering, if it does not escape the scintillator.

The deposited energy of the incident γ-photon is distributed among Compton, photo and Auger electrons. Due to the fact, that Geant4 does not implement the energy bands of solids and the energy loss of electrons and holes to plasmons and

phonons, the relaxation process is not completely simulated, so that a residual energy in the range from several 10 to several 100 eV remains at the excited atom. This energy is deposited by Geant4 inside the crystal at the position of the relaxed atom. We attribute this energy to one electron in our calculations.

From the number, M_j, and energy distribution of the j-th energy deposition among the generated Compton, photo and Auger electrons, the number of scintillation photons, $\overline{N}_{ph,j}$, can be determined with Eq. 6.7, if the light yield, $\overline{L}_e(E_e)$, produced by electrons inside the scintillator is known.

$$\overline{N}_{ph,j}(E) = \sum_{i=1}^{M_j} E_{e,i}\overline{L}_e\left(E_{e,i}\right) \tag{6.7}$$

$E_{e,i}$ is the energy of the i-th electron from the relaxation process. For a non-proportional light yield for electrons, $\overline{L}_e(E_e) \neq constant$, the number of scintillation photons, $\overline{N}_{ph,j}(E)$, varies from event to event. The mean number of generated scintillation photons, $\overline{N}_{ph}$, is

$$\overline{N}_{ph}(E) = \frac{\sum_{j=1}^{m}\overline{N}_{ph,j}(E)}{m} \tag{6.8}$$

where m is the number of mono-energetic γ-rays. The light yield for a certain γ-energy is the average of $\overline{N}_{ph,j}(E)$ for m γ-photons:

$$\overline{L}(E) = \frac{\sum_{j=0}^{m}\overline{N}_{ph,j}(E)}{m \cdot E}. \tag{6.9}$$

It applies that, if $\overline{L}_e(E_e) \neq constant$ also the light yield for γ-rays is not proportional, $\overline{L}(E) \neq constant$. The energy resolution, due to the varying number of $\overline{N}_{ph,j}(E)$ from event to event, is calculated by formula

$$R_{\gamma,T}(E) = \frac{2.35}{\overline{L}(E)\cdot E}\cdot\sqrt{\frac{1}{(m-1)}\sum_{j=0}^{m}(\overline{N}_{ph,j}(E) - \overline{N}_{ph}(E))^2}. \tag{6.10}$$

$R_{\gamma,T}(E)$ does not account for the fluctuation of L_e for a certain electron energy E_e. To include these fluctuations, an approximation is made. The distribution of the number of scintillation photons, $N_{ph}(E_e)$, around its mean value, $\overline{N}_{ph}(E_e) = \overline{L}_e(E_e)\cdot E_e$, generated by an electron with a certain energy E_e, is defined in this work by a Gaussian distribution with the probability density function

$$P(N_{ph}(E_e)) = \frac{1}{\sqrt{2\pi}\sigma(E_e)} exp\left(-\frac{1}{2}\left(\frac{N_{ph}(E_e) - \overline{N}_{ph}(E_e)}{\sigma(E_e)}\right)^2\right), \tag{6.11}$$

where $\sigma(E_e) = \overline{N}_{ph}(E_e)\cdot R_{e,T}(E_e)/2.35$ and $R_{e,T}(E_e)$ is the relative energy resolution for (incident) electrons defined in Eq. 6.28. For this case Eq. 6.7 and 6.8 have to be changed into

$$N_{ph,j}(E) = \sum_{i=1}^{M_j} E_{e,i}L_e\left(E_{e,i}\right) = \sum_{i=1}^{M_j} N_{ph,i}(E_e). \tag{6.12}$$

and

$$\overline{N}_{ph}(E) = \frac{\sum_{j=1}^{m} N_{ph,j}(E)}{m}. \tag{6.13}$$

Then the total contribution of the non-proportional light yield to the energy resolution is given by

$$R_T(E) = \frac{2.35}{\overline{L}(E) \cdot E} \cdot \sqrt{\frac{1}{(m-1)} \sum_{j=0}^{m} (N_{ph,j}(E) - \overline{N}_{ph}(E))^2}. \tag{6.14}$$

$R_T(E)$ of Eq. 6.14 is larger than the value from Eq. 6.10, due to the additional noise component.

Light yield and energy resolution for electrons: phenomenological approach

The light yield of scintillators increases for increasing energies of the incident particles up to a certain energy (see Fig. 6.11, 6.13, 6.19). For $LaBr_3$(Ce) it remains almost constant and for CsI(Tl) it decreases, if the particle energy is increased further (see Fig. 6.11, 6.13, 6.19). Particles with a low kinetic energy have a high and particles with a high kinetic energy a low ionization density. The deposited energy per track length, -dE/dx, which is proportional to the ionization density, is defined by the Bethe formula introduced in Sec. 2.1.1. Birks presented an analytical formula, which describes the unimolecular quenching of the light yield at high ionization densities for organic scintillators [84, 116]. The light yield is proportional to the radiative recombination efficiency of the generated electrons and holes:

$$T_{Birks}(-dE/dx) = \frac{1}{1 + \frac{-dE/dx}{(dE/dx)_{Birks}}} \tag{6.15}$$

where $(dE/dx)_{Birks}$ is a fitting parameter, which depends on material properties, such as the mobilities of electrons and holes [84]. Higher order quenching is neglected in this formula. High ionization densities in combination with low mobilities for electrons and holes lead to a quenching of the radiative recombination [53, 54]. Higher mobilities would decrease the high ionization densities faster, reducing the probability of Auger like quenching to occur [54].

At low ionization densities the Onsager model describes the recombination probability of an electron and a hole in dependence on their separation distance, $r_{e/h}$, [85, 86]. The recombination probability follows

$$P_{Ons} = 1 - exp\left(-\frac{r_{Ons}}{r_{e/h}}\right) \tag{6.16}$$

where r_{Ons} is the Onsager radius, which is defined as the radius, where the Coulomb and thermal energy are equal [86]:

$$r_{Ons} = \frac{e^2}{4\pi\epsilon_0\epsilon k_B T_{emp}} \tag{6.17}$$

where e is the elemental electron charge, k_B the Boltzmann constant, T_{emp} the temperature, ϵ_0 and ϵ the vacuum and the relative permittivity. For $r_{e/h} << r_{Ons}$

the recombination probability of an electron and a hole approaches $P_{Ons} = 1$ and for $r_{e/h} >> r_{Ons}$ the recombination efficiency approaches $P_{Ons} = 0$. The relation between the deposited energy per unit track length, -dE/dx, and the mean electron hole separation distance, $r_{e/h}$, can be defined as [49]

$$\frac{dE}{dx} = \frac{\overline{w}}{r_{e/h}} \tag{6.18}$$

and

$$\left(\frac{dE}{dx}\right)_{Ons} = \frac{\overline{w}}{r_{Ons}} \tag{6.19}$$

where $\overline{w}$ is the mean energy to create an eh-pair inside the scintillator. A small value of dE/dx leads to a large distance of electrons and holes, hence to a small recombination probability. Solving Eq. 6.18 for $r_{e/h}$ and Eq. 6.19 for r_{Ons} and inserting the results into Eq. 6.16 yields the probability for the recombination of an electron and a hole in dependence on -dE/dx:

$$P_{Ons}(-dE/dx) = 1 - exp\left(-\frac{-dE/dx}{(dE/dx)_{Ons}}\right). \tag{6.20}$$

The diffusion model presented in [54] states that a part of the generated electrons and holes along the primary electron track are separated, due to a drift from the track. The ratio of separated to unseparated electrons and holes depends on the magnitude of the mobility difference between them. In alkali halide scintillators, such as CsI, the difference of the mobilities of electrons, μ_e, and holes, μ_h, is supposed to be larger ($\mu_h \approx 0\ cm^2/Vs$ and μ_e is several cm^2/Vs with $\mu_h/\mu_e << 1$) than in other scintillators, in which $\mu_h/\mu_e \leq 1$ applies, as in $LaBr_3$ [52, 87]. The larger the difference of the mobilities is, the larger is the fraction of separated electrons and holes at low -dE/dx [54]. In this model the unseparated electrons and holes recombine radiatively. To include the fact, that there is always a fraction of unseparated electrons and holes, which recombine radiatively, into the Onsager model, a new parameter, $n_{e/h}$, is introduced into Eq. 6.20, yielding the recombination efficiency of electrons and holes [100, 49]:

$$T_{Ons}(-dE/dx) = 1 - n_{e/h}exp\left(-\frac{-dE/dx}{(dE/dx)_{Ons}}\right). \tag{6.21}$$

$n_{e/h}$ is the ratio of electrons and holes, which are separated shortly after their generation and $(dE/dx)_{Ons}$ a fitting parameter, which depends on the dielectric constant and the temperature of the material. The Onsager model neglects time dependent processes, which lead to a radiative recombination of electrons and holes, which have not recombined, due to a not sufficient Coulomb attraction, because of a large initial distance. Fig. 6.18 shows $T_{Birks}(-dE/dx)$ and $T_{Ons}(-dE/dx)$ plotted against the electron energy E_e. The deposited energy density increases with decreasing electron energy (see Fig. 2.4). The combination of these two efficiencies yields the overall transfer and radiative recombination efficiency [25, 49, 100]:

$$T_e(-dE/dx) = T_e^0 T_{Ons} T_{Birks} = T_e^0 \frac{1 - n_{e/h}exp\left(-\frac{-dE/dx}{(dE/dx)_{Ons}}\right)}{1 + \frac{-dE/dx}{(dE/dx)_{Birks}}} \tag{6.22}$$

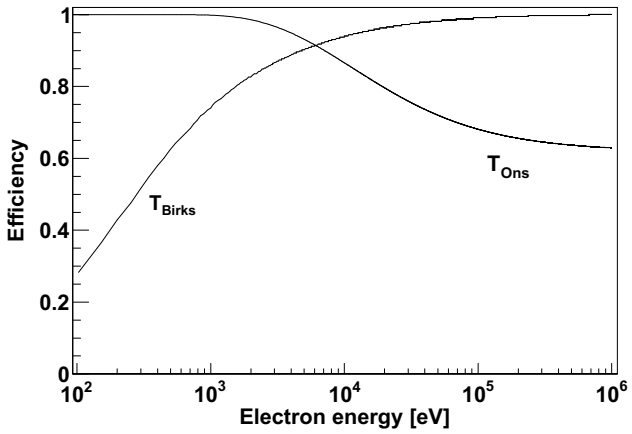

Figure 6.18.: *Energy dependent efficiencies, calculated with the models developed by Birks and Onsager [84, 86], for CsI(Tl).*

where T_e^0 is the normalization factor. The energy deposited by an electron per track length, -dE/dx, can be described by the modified Bethe formula [117]

$$-\frac{dE}{dx}(E_e) = \frac{e^4 N_A Z \rho}{8\pi\epsilon_0^2 A} \cdot \frac{1}{E_e} \cdot ln\left(\frac{1.166(E_e + kI)}{I}\right) \tag{6.23}$$

where e is the electron charge, N_A the Avogadro number, A the number of nucleons, I the mean excitation energy of the atoms inside the medium and k a parameter to correct the value of -dE/dx for electron energies, E_e, close to I. A changing value of -dE/dx along the electron track results into a changing transfer and radiative recombination efficiency $T_e(-dE/dx)$ along the electron track. The mean transfer and radiative recombination efficiency, $\overline{T}_e$, for a certain electron energy E_e can be calculated by the integration of $T_e(E_e)$ from the initial electron energy down to an electron energy equal to the mean excitation energy, I,

$$\overline{T}_e(E_e) = \frac{\int_{E_e}^{I} T_e(-dE/dx)dE}{\int_{E_e}^{I} dE} = \frac{1}{E_e - I}\int_{I}^{E_e} T_e(-dE/dx)dE. \tag{6.24}$$

The reason for the low energy integration limit is that the modified Bethe formula, which is presented in Eq. 6.23, is valid down to electron energies equal to the mean excitation energy, I. $\overline{T}_e(E_e)$ is set to 0 for $E_e < I$. The relation between $\overline{T}_e$ and $\overline{L}_e$ is given by $\overline{L}_e = \overline{T}_e/\overline{w}$ (see Eq. 4.17). Fig. 6.19 shows the fits of the numerically calculated efficiency $\overline{T}_e$ (Eq. 6.24) to the measured [100, 118] normalized light yields for incident electrons, $\overline{L}_e/c$, for $LaBr_3$(Ce) and CsI(Tl). The parameters of the calculated $\overline{T}_e$ values are listed in Tab. 6.3. The values of the mean energy to create an electron hole pair, $\overline{w}$, are in the range 13 to 19 eV (comp. Sec. 2.2). $(dE/dx)_{Ons}$ can be calculated by Eq. 6.19, if Eq. 6.17 is inserted into it. With a dielectric constant of 5.65 for CsI(Tl) Eq. 6.19 yields a value of $(dE/dx)_{Ons}$ in the range from 13 MeV/cm to 19 MeV/cm. For $LaBr_3$(Ce) $(dE/dx)_{Ons}$ has about the same value. There is a difference by a factor of about 2 to 3 compared to the values of $(dE/dx)_{Ons}$ from the fit in Tab. 6.3, but they have the same magnitude. The origin of this difference results most probably from the fact, that the model does not

scintillator	$n_{e/h}$	$(dE/dx)_{Ons}$**[MeV/cm]**	$(dE/dx)_{Birks}$**[MeV/cm]**	**I[keV]**	**k**
$LaBr_3$(Ce)	0.18	36.4	500	0.455	2.8
CsI(Tl)	0.38	45	700	0.553	2.8

Table 6.3.: *Parameters in the formula of $\overline{T}_e$ (6.24), which have been used to fit the normalized light yield, $\overline{L}_e/c$, of $LaBr_3$(Ce) and CsI(Tl) for incident electrons. The mean excitation energy I has been taken from [23].*

include all processes leading to the radiative recombination of electrons and holes. The calculated values of $\overline{T}_e$, which have been fitted to the measured data points of

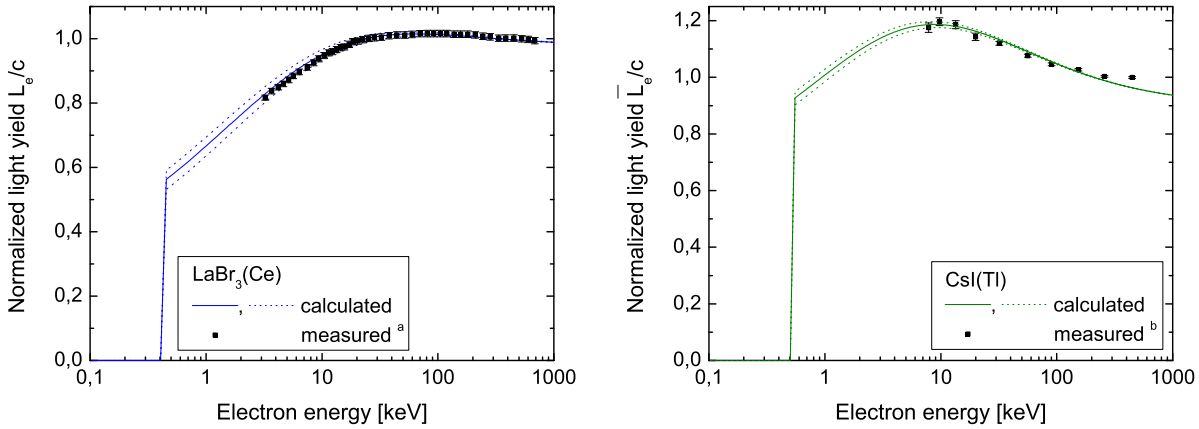

Figure 6.19.: *Calculated $\overline{T}_e$ and measured normalized light yield, $\overline{L}_e/c$, of $LaBr_3$(Ce) and CsI(Tl) for incident electrons. $\overline{T}_e(E_e)$ is set to 0 for $E_e < I$. [a]:[100], [b]:[118]*

$\overline{L}_e/c$ in Fig. 6.19 are in good agreement with the measured values for $LaBr_3$(Ce) and have a small discrepancy in the enery range $E > 100$ keV for CsI(Tl).

The deposited energy per track length, -dE/dx, fluctuates at each position of the track. These fluctuations are called Landau fluctuations and have a FWHM value of [27, 25]

$$FWHM\left(-\frac{dE}{dx}\right) = 3.58 \cdot \sigma\left(-\frac{dE}{dx}\right) = 3.58 \cdot \frac{e^4 N_A Z \rho}{8\pi\epsilon_0^2 A} \cdot \frac{1}{E_e + kI}. \tag{6.25}$$

The value 3.58 has to be multiplied to the standard deviation of Landau distributions to receive its FWHM and the factor kI is included as a correction for electron energies close and below the mean excitation energy, I (compare Sec. 2.1.1). Landau fluctuations $d\left(-\frac{dE}{dx}\right)$ in combination with the change of -dE/dx along the track lead to fluctuations of the transfer and radiative recombination efficiency, $\overline{T}_e(-dE/dx)$, hence to fluctuations of the number of generated scintillation photons, from one event to another. This generates a broadening of the energy resolution for electrons and γ-rays. The standard deviation, $\sigma(T_e(-dE/dx))$, along the electron track in

dependence of -dE/dx follows from the total derivative of $d(T_e(-dE/dx))$ [49, 100]

$$\begin{aligned} d(T_e(-dE/dx)) &= \frac{\partial T_e(-dE/dx)}{\partial\left(-\frac{dE}{dx}\right)} d\left(-\frac{dE}{dx}\right) \\ \Rightarrow \sigma(T_e(-dE/dx)) &= \frac{\partial T_e(-dE/dx)}{\partial\left(-\frac{dE}{dx}\right)} \sigma\left(-\frac{dE}{dx}\right), \end{aligned} \tag{6.26}$$

with the approximation $d() \approx \sigma()$ as described by the Gaussian error propagation [119]. Assuming that the processes of energy deposition of the electron inside the scintillator along its track are independent, the mean value of the standard deviation for a certain electron energy, E_e, arises from

$$\begin{aligned} \overline{\sigma}(T_e(E_e)) = \left[\frac{\int_{E_e}^{I} (\sigma(T_e(-dE/dx)))^2 dE}{\int_{E_e}^{I} dE}\right]^{\frac{1}{2}} = \\ \frac{1}{\sqrt{E_e - I}} \cdot \left[\int_{I}^{E_e} (\sigma(T_e(-dE/dx)))^2 dE\right]^{\frac{1}{2}}. \end{aligned} \tag{6.27}$$

The contribution $R_{e,T}(E_e)$ to the relative energy resolution can be calculated by

$$R_{e,T}(E_e) = 3.58 \cdot \frac{\overline{\sigma}(T_e(E_e))}{\overline{T}_e(E_e)}. \tag{6.28}$$

Due to the fact, that $\overline{T}_e(E_e)$ is not defined for $E_e < I$ in Eq. 6.24, also $R_{e,T}(E_e)$ is not defined for energies lower than I. In Fig. 6.20 the energy dependent values of

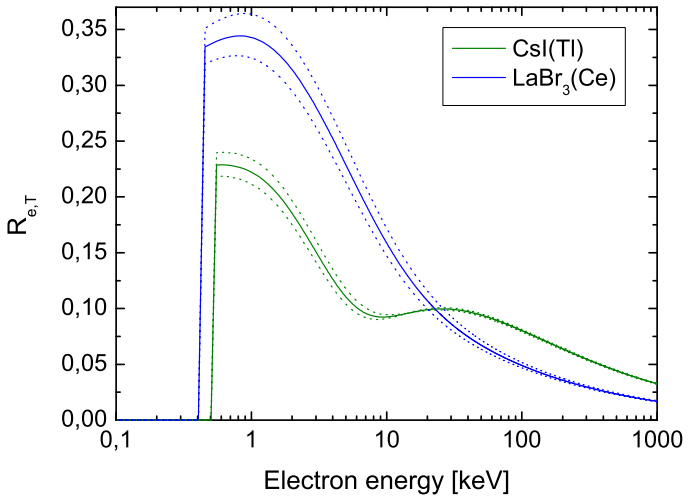

Figure 6.20.: *Calculated electron energy resolution, $R_{e,T}$ (Eq. 6.28), of $LaBr_3(Ce)$ (blue) and CsI(Tl) (green) with the parameters given in Tab. 6.3.*

$R_{e,T}$ of $LaBr_3(Ce)$ (blue) and CsI(Tl) (green) are plotted against the electron energy. It shows that the electron energy resolution, $R_{e,T}$, is poorer for $LaBr_3(Ce)$ than for CsI(Tl) for electron energies $E_e < 23$ keV and it is better for $E_e > 23$ keV. The

error of the calculated $R_{e,T}$ increases for electron energies approaching I, because the contributions from $E_e < I$ are neglected in Eq. 6.28.

In the publications [25, 100] the value of $R_{e,T}$ is only presented for an electron energy of $E_e = 662$ keV.

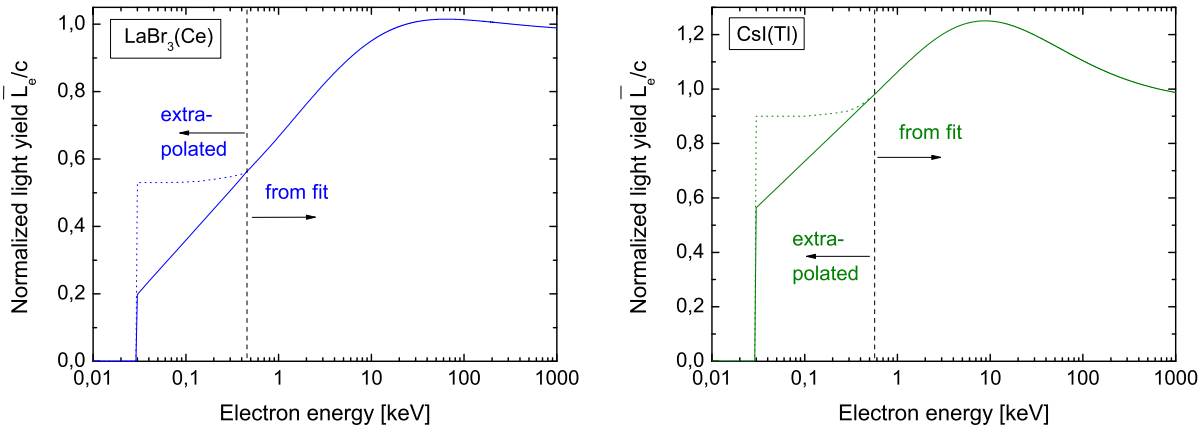

Figure 6.21.: *Normalized light yield, $\overline{L}_e/c = \overline{T}_e$, from the fit to the measured values for $LaBr_3(Ce)$ and CsI(Tl), in the range from I to 1000 keV as already presented in Fig. 6.19. Values below the mean excitation energy, I, of $LaBr_3(Ce)$ and CsI(Tl) have been extrapolated in two ways (dotted and solid lines) for a sensitivity analysis. These data have been used to simulate the energy resolution, $R_T(E)$, and the light yield, $\overline{L}(E)$, for incident γ-rays.*

Fig. 6.21 shows the calculated values of $\overline{T}_e$ down to the mean excitation energy, I, as presented in Fig. 6.19 and the extrapolated values from I down to 30 eV. Two extrapolations have been chosen in order to do a sensitivity analyses on the simulated light yield and energy resolution for incident γ-rays. One describes a flattening of $\overline{L}_e/c$ (dotted line) and the other a logarithmic decrease of $\overline{L}_e/c$ (solid line) below I. Measurements presented in [114, 120] indicate that the real values of the light yield for electrons lies between the two extrapolations. $\overline{L}_e/c$ values below 30 eV have been set to 0 because the energy to create an electron and a hole is about w $\approx$ 12..20 eV [28, 36] in scintillators with an efficiency smaller 1 for the creation of scintillation photons. The determined values of $\overline{L}_e(E_e)$ (Fig. 6.21) and $R_{e,T}(E_e)$ (Fig. 6.20) are used in the following to determine the light yield $L(E)$ and $R_T(E)$ for incident γ-rays by Monte Carlo simulations.

Relaxation after the photo effect

The relaxation processes of the excited atoms occur via generation of fluorescence photons plus Auger electrons or exclusively Auger electrons. The fluorescence yields for photons, which are generated by filling a vacancy in the K or L shell with an electron from a higher shell, are presented in Fig. 6.22. The probability for the generation of fluorescence photons increases for elements with a higher atomic

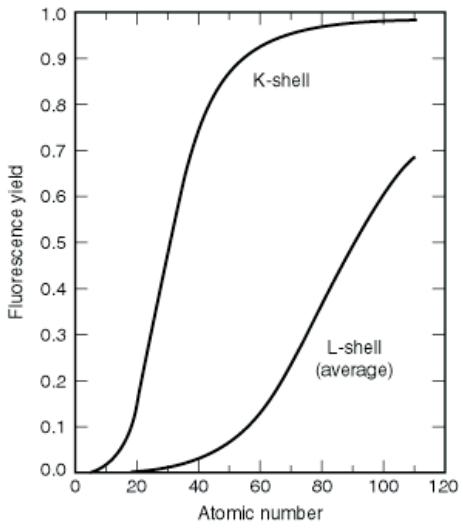

Figure 6.22.: *Fluorescence yields for K and L shells from [121].*

number Z ($Z_{Cs} = 55$, $Z_I = 53$, $Z_{La} = 57$, $Z_{Br} = 35$) and is much larger for K than L shell fluorescence photons. The overall probability for the relaxation via generation of fluorescence photons has a discontinuity for the γ-energy equal to the K shell electron binding energy. Lowering the γ-energy from energies above to energies below the K shell electron binding energy, the fluorescence yield decreases from 0.9 to 0.05 for Cs, I and La and from 0.6 to 0.02 for Br. The probabilities for the generation of fluorescence photons, P_{fluo}, and Auger electrons, P_{Auger}, add up to the probability $P_{relax} = 1$ for the relaxation of the excited atom [121]

$$P_{relax} = P_{fluo} + P_{Auger} = 1. \tag{6.29}$$

Therefore the probability is higher for an atom to relax via production of Auger electrons, if a photo electron from the L shell is ejected. The element Br with the lowest atomic number $Z_{Br} = 35$ of the elements in CsI(Tl) and $LaBr_3$(Ce) has a probability of about 0.4 to relax via the generation of Auger electrons, if a photo electron from the L shell is ejected.

Distribution of photo, Compton and Auger electrons and fluorescence photons in CsI

First a γ-photon generates a Compton or a photo electron after interaction with the scintillator. Then the excited atom relaxes via production of fluorescence photons and Auger electrons. The photo-, Compton and Auger electrons, which are denoted as first electrons, have a certain number and energy distribution after each γ-interaction. They generate a certain number of scintillation photons, depending on the light yield for incident electrons, after depositing their energy inside the scintillator.

The following simulations have been performed for a cylindrically shaped CsI(Tl) scintillator with a diameter of $\oslash = 4.5$ mm and a thickness of d = 10 mm or with a diameter of $\oslash = 25$ mm and a thickness of d = 25 mm. Fig. 6.23 shows the histograms of the number of first electrons (photo, Compton and Auger electrons)

and Fig. 6.24 shows the number of fluorescence and Compton scattered photons, which are generated after the interaction of a γ-ray photon with the CsI(Tl) scintillator. Maximum in the histograms of the number of first electrons are at 1 and

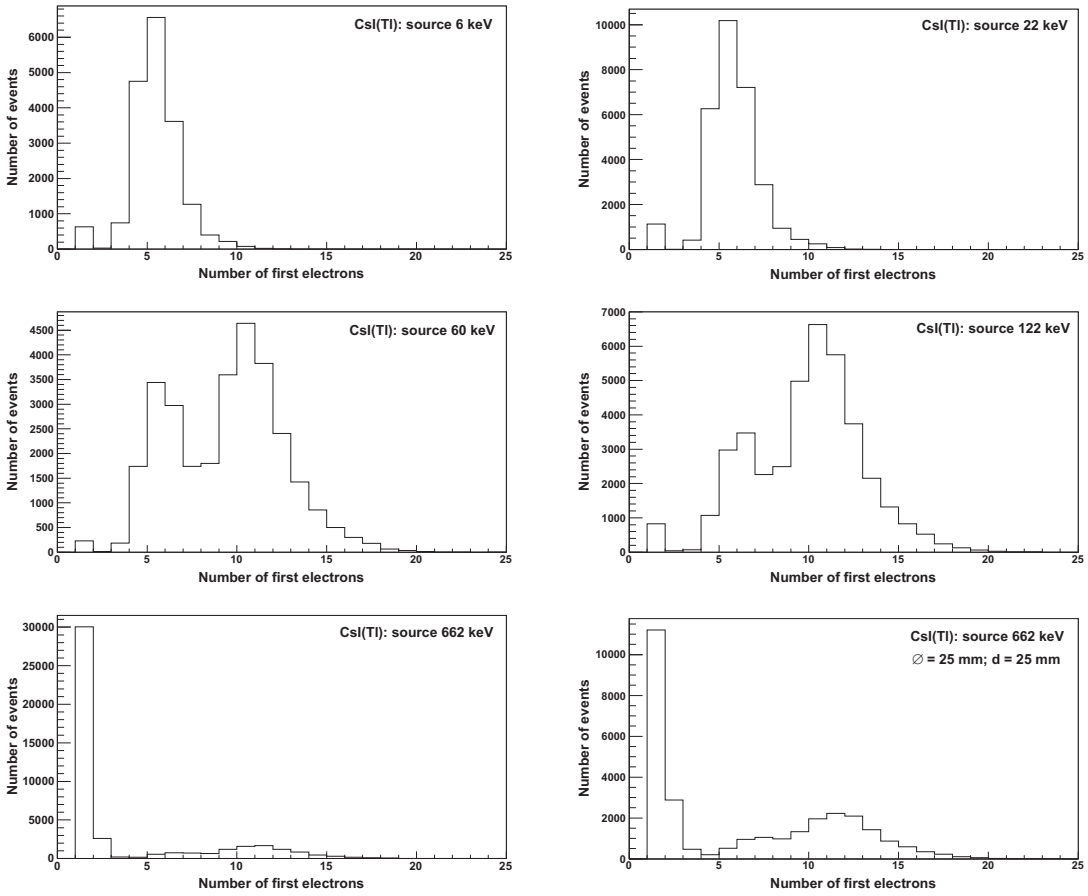

Figure 6.23.: *Number of first electrons generated by γ-rays incident into a cylindrically shaped CsI(Tl) scintillator with a diameter of $\oslash = 4.5$ mm and a thickness of $d = 10$ mm or with the dimensions: $\oslash = 25$ mm and $d = 25$ mm in the last picture.*

5 generated first electrons for incident γ-rays of 6 and 22 keV. 1 electron follows from the generation of 1 photo or 1 Compton electron from the valence band. The maximum around 5 electrons is originating from 1 photo electron from a deeper shell (L, M, N, O) and mainly 4 Auger electrons. The creation of one fluorescence photon and its interaction with a second atom includes the relaxation of two atoms and the production of a higher number than 6 first electrons. The generation probability of L fluorescence photons with an energy equivalent to the M→L electron transition in Cs or I, is very low compared to the relaxation of the Cs or I atom by the generation of Auger electrons only (Fig. 6.24 first picture).

The interaction of 60 and 122 keV γ-ray photons with CsI(Tl) generates an additional maximum at around 10 first electrons in the histogram (Fig. 6.23 second picture). The γ-energy is now high enough to eject an electron from the Cs and I K-shell. For these energies the probability for the atom to relax by filling the vacancy in the K-shell with an electron from the L-shell by producing a K fluorescence

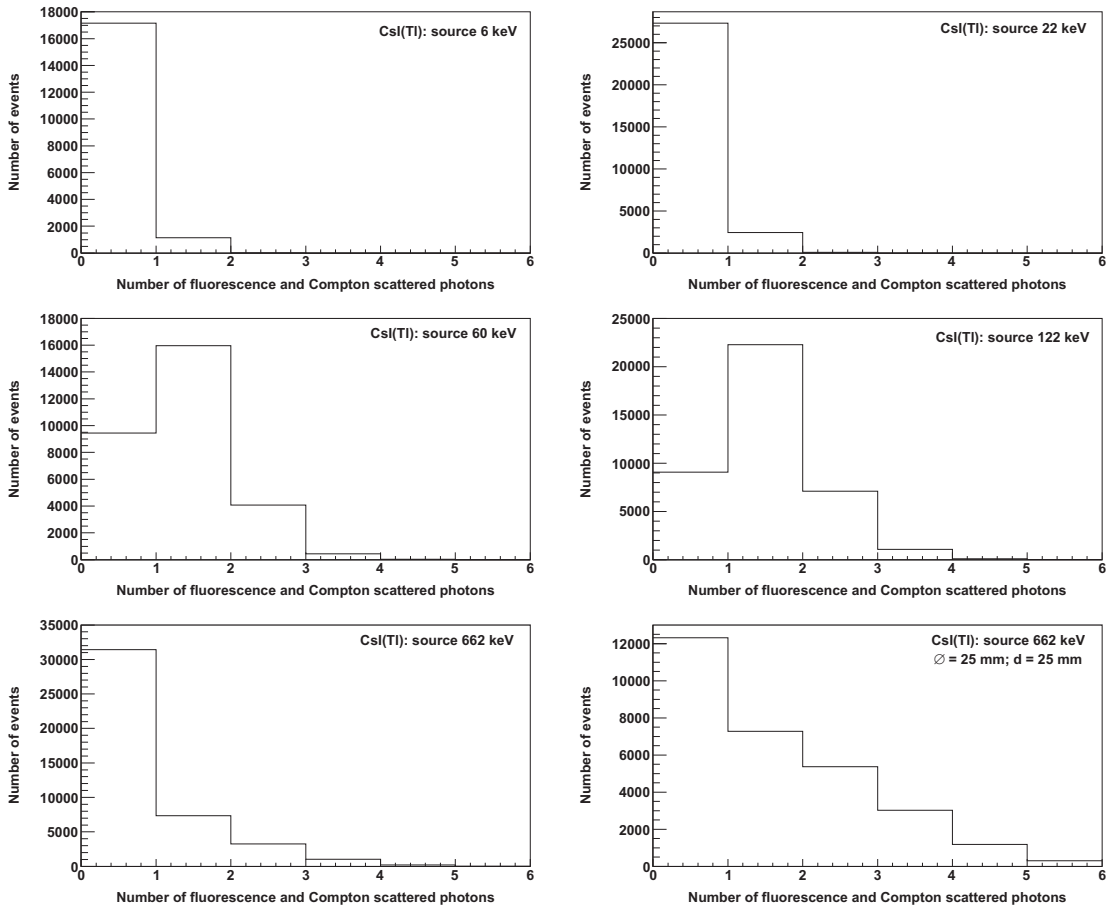

Figure 6.24.: *Number of fluorescence and Compton scattered photons generated by γ-rays incident into a cylindrically shaped CsI(Tl) scintillator with a diameter of $\oslash = 4.5$ mm and a thickness of $d = 10$ mm or with the dimensions: $\oslash = 25$ mm and $d = 25$ mm in the last picture.*

photon equivalent to the transition energy L→K and Auger electrons from L and higher shells is higher compared to the probability of producing exclusively Auger electrons (Fig. 6.22). The production of one photo electron after the interaction of the γ-ray photon with a Cs or I atom and its relaxation by producing mainly 4 Auger electrons, yields 5 electrons from one atom. The fluorescence photon interacts with another atom, if it does not escape, by producing 1 photo and mainly 4 Auger electrons. The total number of first electrons from both atoms is about 10. For 122 keV γ-ray photons the maximum at 1 and 10 first electrons have relatively more events than the maximum at 6 first electrons compared to the histogram for 60 keV γ-ray photons. This effect is caused by the generation of more Compton electrons and fluorescence photons (Fig. 6.24) after the interaction with higher energy photons.

662 keV γ-ray photons generate a much higher portion of only 1 and 2 first electrons per event (Fig. 6.23 last picture two pictures), because of a higher probability for Compton events. For the larger CsI(Tl) scintillator in Fig. 6.23 (last picture) the counts at 2, 3 and 4 Compton electrons have increased at the cost of the 1 Compton electron intensity, because of the larger probability for the Compton scattered photon to interact again in the larger CsI(Tl) volume. There is also a relative increase

of the number of first electrons above 4 first electrons for the larger scintillator, due to a lower number of escapes of Compton scattered photons, which can be seen by a relative increase of 2 and more detected photons in Fig. 6.24 (last picture).

Simulated spectra of CsI(Tl)

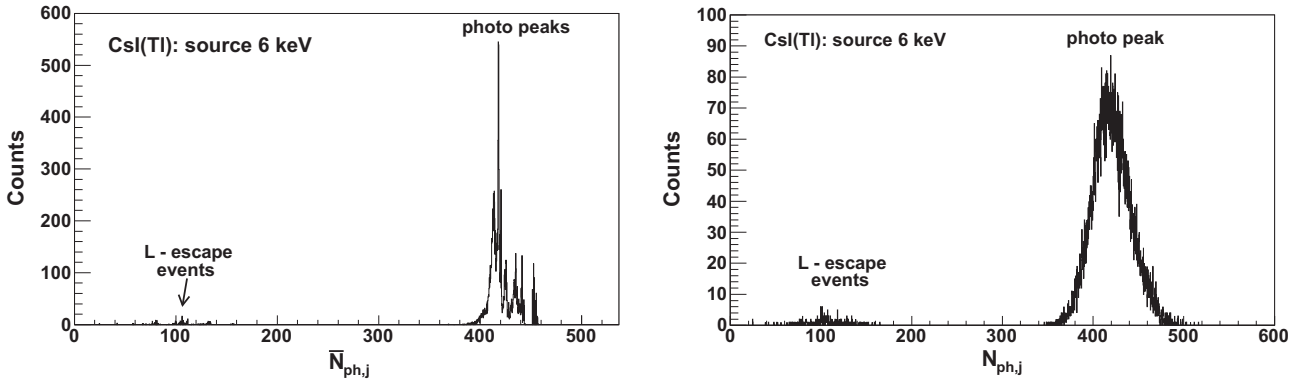

Figure 6.25.: *Simulated results of generated scintillation photons, $\overline{N}_{ph,j}$ and $N_{ph,j}$, produced by 6 keV γ-rays incident into a cylindrically shaped CsI(Tl) scintillator (diameter $\oslash$ = 4.5 mm, thickness d = 10 mm). $N_{ph,j}$ includes an additional noise component, which originates from Landau fluctuations in the energy deposition of the first electrons.*

Two kind of scintillation photon spectra, $\overline{N}_{ph,j}(E_e)$ and $N_{ph,j}(E_e)$, where j is the γ-event number, are presented. One kind is simulated by using Eq. 6.8, where the number of scintillation photons generated by an electron (photo, Compton and Auger) with a certain energy is constant for each event. The other kind is simulated by using Eq. 6.12, which includes an additional noise component, resulting from Landau fluctuations of the deposited energy by photo, Compton and Auger electrons along their track through the scintillator. In this case the number of scintillation photons, $N_{ph}(E_e)$, generated by an electron with a certain energy, E_e, fluctuates around its mean value, $\overline{N}_{ph}(E_e)$, for each event. These fluctuations are described by Gaussian distributions with energy dependent standard deviations given by $\sigma(E_e) = \overline{N}_{ph}(E_e) \cdot R_{e,T}(E_e)/2.35$ (comp. Eq. 6.11).

In the following the simulated spectra, generated by incident γ-rays with energies of 6, 22, 60, 122 and 662 keV are discussed in detail. The simulations have been performed for a cylindrically shaped CsI(Tl) scintillator with a diameter of $\oslash$ = 4.5 mm and a thickness of d = 10 mm or with a diameter of $\oslash$ = 25 mm and a thickness of d = 25 mm. $\overline{L}_e$ has been set to $\overline{L}_e/c \cdot 61.5$ photons/keV for CsI(Tl). $\overline{L}_e/c$ is shown in Fig. 6.21 on the right (solid line).

Fig. 6.25 and 6.26 show the spectra for incident γ-rays with energies of $E = 6$ keV and 22 keV. Histograms of $\overline{N}_{ph,j}(E)$ and $N_{ph,j}(E)$ are plotted on the left and right hand side. The shape of the photo peaks for these two energies is similar, except of their width, because the distribution of the first electrons and the number of fluorescence photons are almost equal (Fig. 6.23 and 6.24). The width of the photo peak at 22 keV is narrower, due to a different energy distribution of E = 22 keV

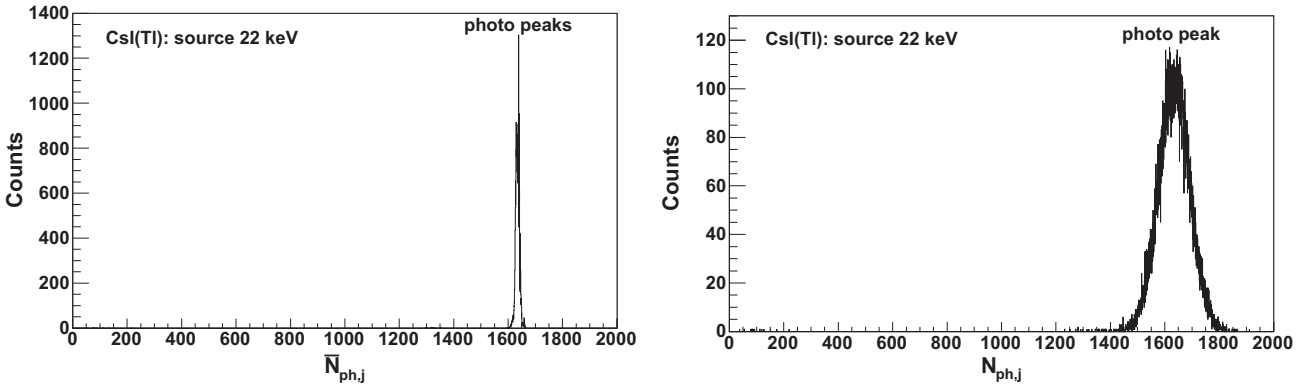

Figure 6.26.: *Simulated results of generated scintillation photons, $\overline{N}_{ph,j}$ and $N_{ph,j}$, produced by 22 keV γ-rays incident into a cylindrically shaped CsI(Tl) scintillator (diameter $\oslash$ = 4.5 mm, thickness d = 10 mm). $N_{ph,j}$ includes an additional noise component, which originates from Landau fluctuations in the energy deposition of the first electrons.*

compared to $E = 6$ keV among the first electrons in combination with the energy dependent mean light yield for electrons, $\overline{L}_e(E_e)$ (Fig. 6.21 on the right solid line).

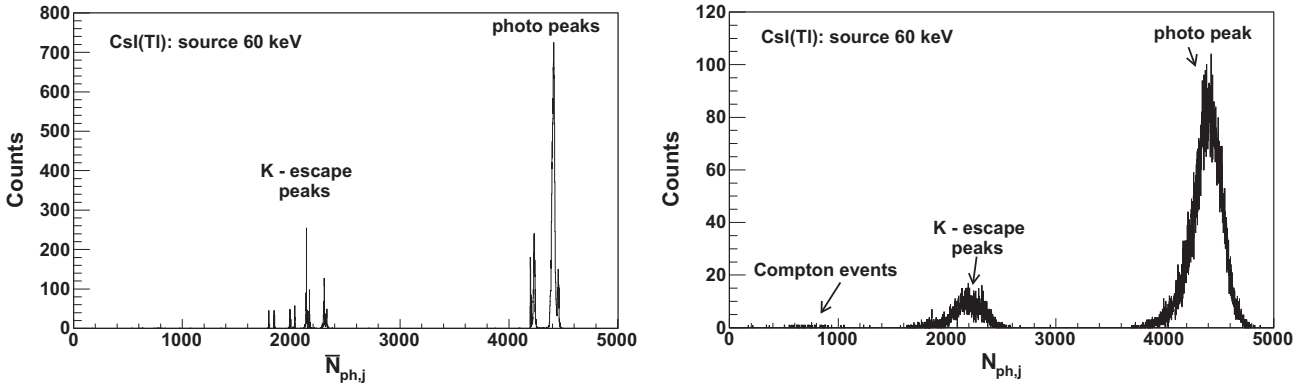

Figure 6.27.: *Simulated results of generated scintillation photons, $\overline{N}_{ph,j}$ and $N_{ph,j}$, produced by 60 keV γ-rays incident into a cylindrically shaped CsI(Tl) scintillator (diameter $\oslash$ = 4.5 mm, thickness d = 10 mm). $N_{ph,j}$ includes an additional noise component, which originates from Landau fluctuations in the energy deposition of the first electrons.*

Fig. 6.27 and 6.28 show the spectra of CsI(Tl) for incident γ-rays with energies of $E = 60$ keV and 122 keV. The histogram of $\overline{N}_{ph,j}(E)$ shows that the photo peak in the range of $\overline{N}_{ph,j} = 4000$ to 4600 for 60 keV and $\overline{N}_{ph,j} = 8000$ to 9000 for 122 keV consists of several peaks, which accumulate on two positions. The peaks around 2200 photons (60 keV) and 6000 photons (122 keV) are the escape peaks. The peaks attributed to the photo peak with a lower number of photons around $\overline{N}_{ph,j} \approx 4200$ for 60 keV and 8200 for 122 keV, have a lower intensity compared to the peaks with a higher number of photons, around $\overline{N}_{ph,j} \approx 4400$ for 60 keV and 8500 for 122 keV. These peaks originate from events, where the number of

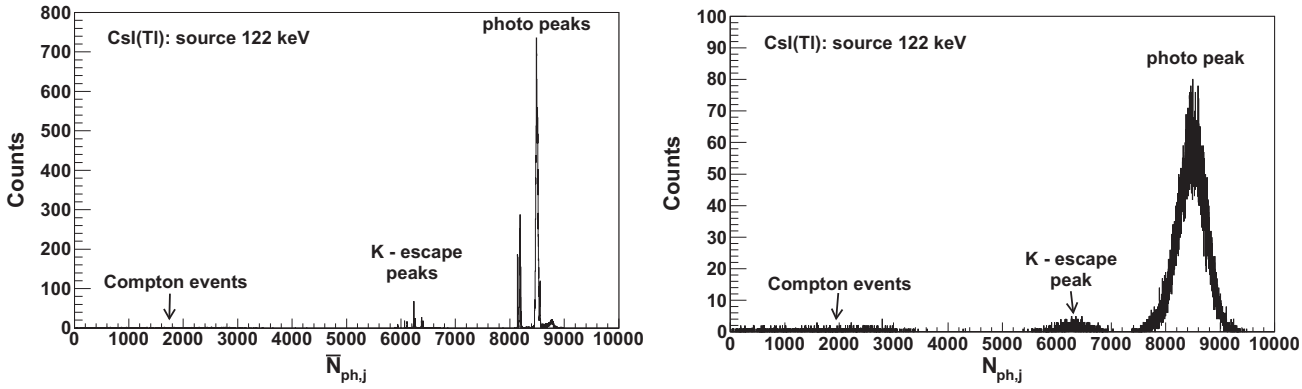

Figure 6.28.: *Simulated results of generated scintillation photons, $\overline{N}_{ph,j}$ and $N_{ph,j}$, produced by 6 keV γ-rays incident into a cylindrically shaped CsI(Tl) scintillator (diameter $\oslash$ = 4.5 mm, thickness d = 10 mm). $N_{ph,j}$ includes an additional noise component, which originates from Landau fluctuations in the energy deposition of the first electrons.*

first electrons is smaller or equal to 6 (Fig. 6.23 and 6.24). The peaks with the higher number of photons $\overline{N}_{ph,j}(E)$ are generated by events with a number of first electrons larger than 6 (Fig. 6.23 and 6.24). This accumulation of $\overline{N}_{ph,j}(E)$ on two positions with two very different intensities produces in the histogram of $N_{ph,j}(E)$ a shoulder on the left hand side of the photo peak, which is also resolved in the measured CsI(Tl) spectra in this energy range (Fig. 6.8). The exsistence and the origin of a shoulder on the low energy side of the photo peak of measured spectra, generated by γ-rays in the energy range 40 keV-122 keV in a detector system SDD + CsI(Tl), have not been mentioned and explained in literature yet, although it is clearly visible in measured spectra of other publications [10]. Simulations presented in this work indicate, that its origin may be attributed to the non-proportional light yield of CsI(Tl). Additionally for 122 keV photons, there appears a third peak with a very low intensity at even higher numbers of $\overline{N}_{ph,j}(E)$ around 8750, which can be attributed to first electrons resulting from events, where the incident γ-photon has been Compton scattered before interacting via photo effect with CsI(Tl).

Fig. 6.29 shows the histograms of $\overline{N}_{ph,j}(E)$ and $N_{ph,j}(E)$ for incident γ-photons with an energy of 662 keV. Fig. 6.30 on the left shows a zoom of the photo peak of the spectrum in Fig. 6.29 on the left around $\overline{N}_{ph,j}$ = 41000. In Fig. 6.29 on the right the spectrum of the photo peak is presented in the same range for a larger cylindrical scintillator with a diameter of $\oslash$ = 25 mm and a thickness of d = 25 mm. The peaks below 41500 photons are generated in the same way as the photo peaks for incident γ-rays with energies of 60 keV and 122 keV. The peaks with a photon number above 41500 are produced by events, where Compton scattered electrons are generated beside photo and Auger electrons. The first two peaks above 41500 photons originate from processes where the incident photon is Compton scattered once and twice before interacting via photo effect with an atom of CsI(Tl). The peaks above 42400 are caused by an incident photon, which is Compton scattered 3 and 4 times before interacting via photo effect with the scintillator. The probability of processes, where the incident γ-ray is scattered 2, 3, 4 times or more is higher for

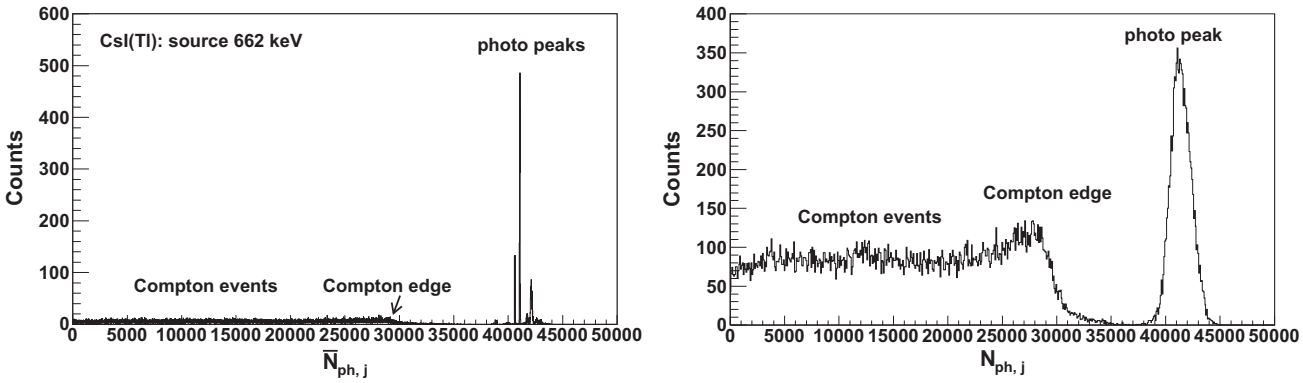

Figure 6.29.: *Simulated results of generated scintillation photons, $\overline{N}_{ph,j}$ and $N_{ph,j}$, produced by 6 keV γ-rays incident into a cylindrically shaped CsI(Tl) scintillator (diameter $\oslash$ = 4.5 mm, thickness d = 10 mm). $N_{ph,j}$ includes an additional noise component, which originates from Landau fluctuations in the energy deposition of the first electrons.*

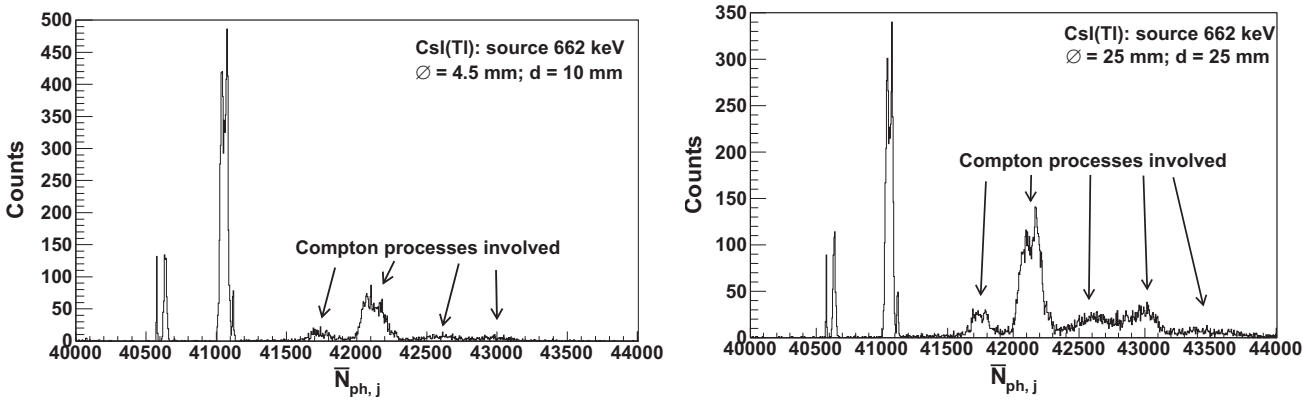

Figure 6.30.: *On the left: Zoom into the range of the photo peak around $\overline{N}_{ph,j}$ = 41000 of the spectrum shown in Fig. 6.29 on the left. On the right: Illustration of the same range but for a larger cylindrical scintillator also irradiated with 662 keV γ-rays.*

larger CsI(Tl) scintillators, which is revealed by the higher relative number of first electrons in the range 2 to 4 (escape of the Compton scattered photon) and above 11 electrons in Fig. 6.23 (last two pictures). Whereas the higher number of detected fluorescence photons for larger scintillators, due to a lower number of escapes, leads also to a relative increase of the number of first electrons in Fig. 6.23 (last picture).

Distribution of photo, Compton and Auger electrons and fluorescence photons in $LaBr_3$

In this section results from Geant4 simulations for $LaBr_3$(Ce) are presented. Before discussing the simulated spectra, histograms of the number of generated first electrons or Compton and fluorescence photons per event are investigated.

Fig. 6.31 shows the histograms of the number of generated first electrons per

incident γ-ray with energies of 6, 22, 60, 122 and 662 keV in $LaBr_3$(Ce). The $LaBr_3$(Ce) scintillator is cylindrically shaped with a diameter of $\oslash = 4.5$ mm and a thickness of d = 10 mm or with a diameter of $\oslash = 25$ mm and a thickness of d = 25 mm (last picture of Fig. 6.31 and 6.32).

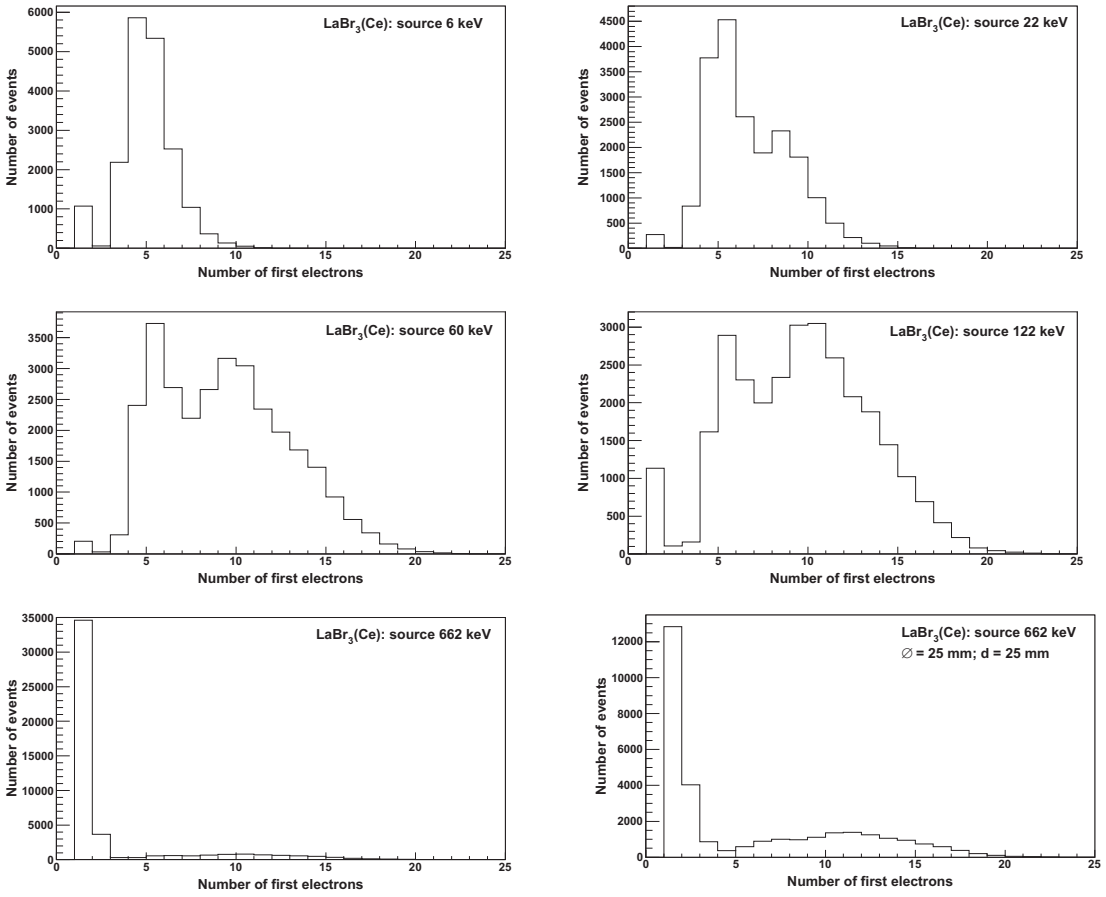

Figure 6.31.: *Histograms of the number of first electrons, which are generated per deposited energy by a γ-ray in a cylindrically shaped $LaBr_3$(Ce) scintillator with a diameter of $\oslash = 4.5$ mm and thickness of d = 10 mm or with the dimensions: $\oslash = 25$ mm and d = 25 mm in the last picture.*

6 keV γ-ray photons eject an electron from the K-shell, whereas the atom with the vacancy relaxes via generation of mainly 3 and 4 Auger electrons, resulting in a total number of 4 and 5 first electrons. Therefore the histogram for 6 keV photons has a maximum around 4 and 5 first electrons (Fig. 6.31 first picture). The maximum at 1 results from one Compton or one photo electron from the valence band, without the generation of further electrons.

A third maximum appears in the histogram around 8 first electrons for 22 keV γ-ray photons. This can be explained by the generation of one photo electron and one fluorescence photon (Fig. 6.32), with an energy equivalent to the L→K transition in Br, and the relaxation of the excited atom via the production of mainly 3 Auger electrons, resulting in 4 electrons from one atom. The fluorescence photon interacts, if it does not escape, with a second atom, generating again about 4 first electrons.

The total number of first electrons from both atoms are about 8 (Fig. 6.31 second picture).

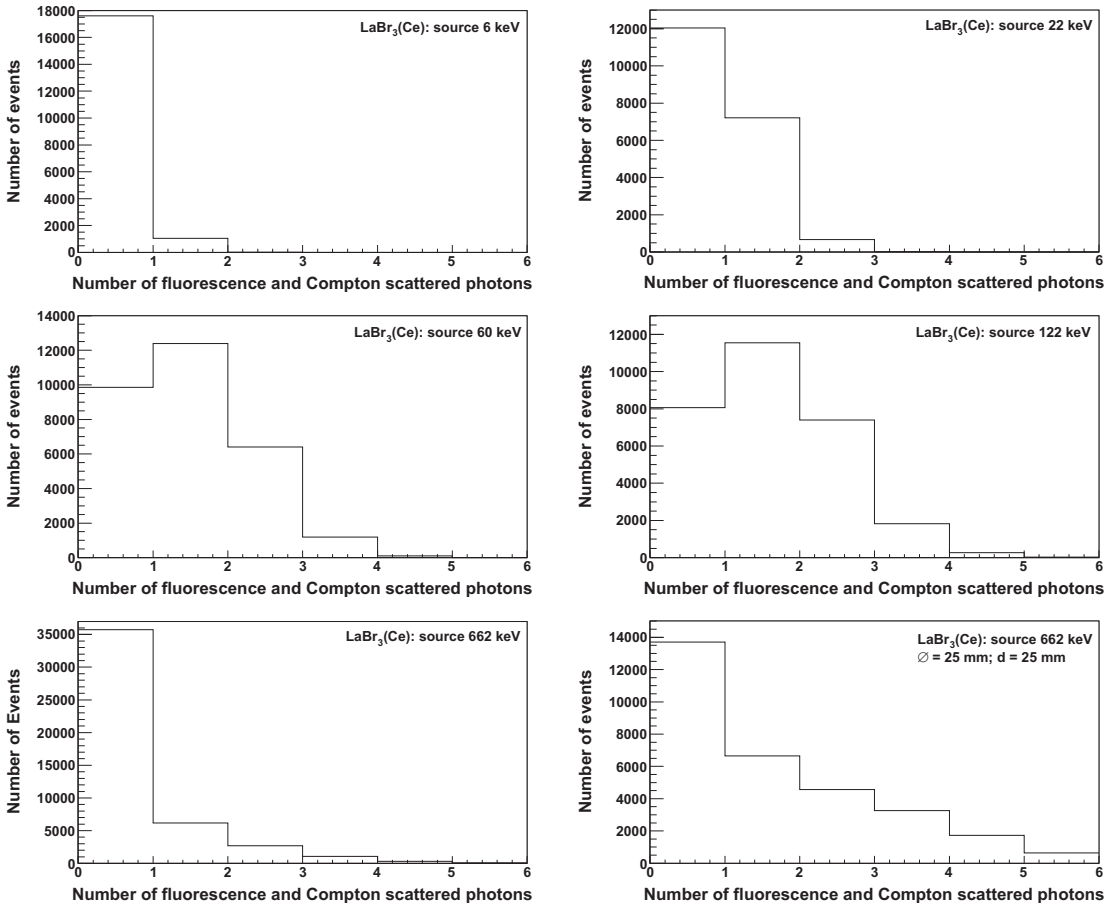

Figure 6.32.: *Histograms of the number of generated fluorescence and Compton scattered photons per deposited energy by a γ-ray in a cylindrically shaped $LaBr_3$(Ce) scintillator with a diameter of $\oslash = 4.5$ mm and thickness of $d = 10$ mm or with the dimensions: $\oslash = 25$ mm and $d = 25$ mm in the last picture.*

For 60 keV γ-ray photons the maximum around 8 has moved to 9 first electrons and has increased relatively to the maximum around 5, because the γ-energy is now high enough to eject photo electrons from the La K-shell. The relaxation process of La via production of K fluorescence photons with an energy equivalent to the L$\rightarrow$K transition in La is dominant compared to a relaxation exclusively via the production of Auger electrons. The increase of the maximum around 9 electrons is larger for incident 122 keV photons, due to the fact that a larger number of fluorescence photons are produced at higher γ-energies (Fig. 6.32). It is also recognizable that events, where 1 electron is generated, increase from 60 to 122 keV γ-ray photons, because a higher number of Compton events occur for 122 keV photons.

For 662 keV γ-ray photons the number of 1, 2 and 3 Compton electrons increases drastically. These numbers are higher for the larger $LaBr_3$(Ce) scintillator (Fig. 6.31 last picture). For the larger scintillator also the number of lost Compton scattered photons is lower, which is illustrated by a smaller difference of the intensities at 1,

2, 3 compared to the intensities for a number of first electrons larger than 5 (Fig. 6.31 last picture).

Simulated spectra of $LaBr_3(Ce)$

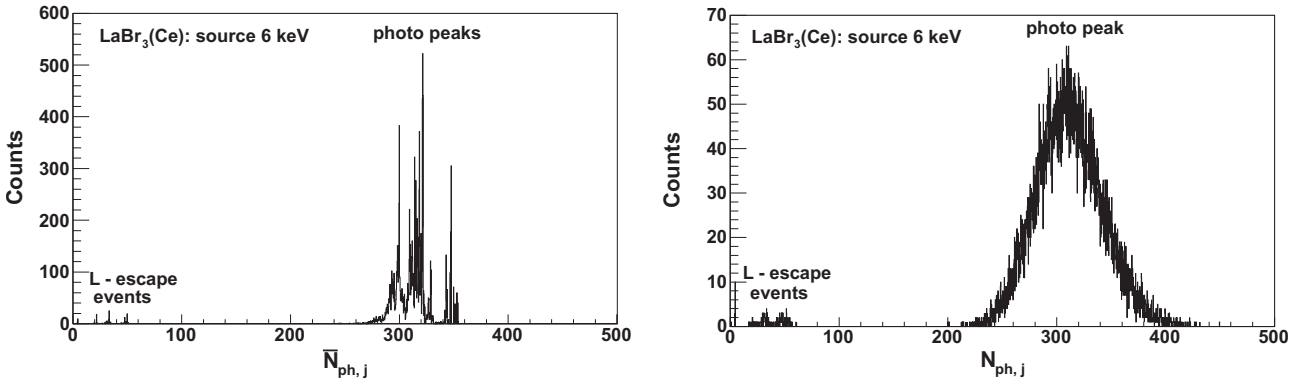

Figure 6.33.: *Simulated results of generated scintillation photons, $\overline{N}_{ph,j}$ and $N_{ph,j}$, produced by 6 keV γ-rays incident into a cylindrically shaped $LaBr_3(Ce)$ scintillator (diameter $\oslash$ = 4.5 mm, thickness d = 10 mm). $N_{ph,j}$ includes an additional noise component, which originates from Landau fluctuations in the energy deposition of the first electrons.*

Next the simulated spectra of a cylindrically shaped $LaBr_3(Ce)$ scintillator with a diameter of $\oslash$ = 4.5 mm and a thickness of d = 10 mm, if not otherwise stated, created by 6, 22, 60, 122 and 662 keV γ-ray photons are examined. $\overline{L}_e$ has been set to $\overline{L}_e = \overline{L}_e/c \cdot 65$ for $LaBr_3(Ce)$. $\overline{L}_e/c$ is illustrated in Fig. 6.21 on the left (solid line).

The histograms of $\overline{N}_{ph,j}$ and $N_{ph,j}$ in Fig. 6.33 show the distribution of generated photons. Whereas $N_{ph,j}$ includes an additional noise component compared to $\overline{N}_{ph,j}$, originating from Landau fluctuations of the energy deposition of the first electrons along their track through the scintillator. For 6 keV photons the first electrons are constituted mainly of one photo electron and several Auger electrons. The strong decrease of the mean electron light yield $\overline{L}_e(E_e)$ for electron energies $E_e < 6$ keV to lower energies in combination with the energy distribution of the deposited γ-energy among the first electrons leads to a relatively broad distribution of $\overline{N}_{ph,j}$(E = 6 keV) and $N_{ph,j}$(E = 6 keV) in this energy range (Fig. 6.33).

Incident γ-ray photons of 22 keV can eject an electron from the K-shell of Br. There is the probability for an excited Br atom with a vacancy in the K-shell to relax via generation of a K-shell fluorescence photon besides several Auger electrons, which leads to additional possibilities of the γ-energy E = 22 keV to be distributed among first electrons. These additional possibilities result in a larger number of first electrons than 6, so that the mean energy of the electrons is lower. Therefore the strong decrease of the electron light yield, $\overline{L}_e$, from E_e = 20 keV to lower energies (Fig. 6.21 on the left, solid line) leads to a broader distribution of $\overline{N}_{ph,j}$, compared to the case, where the energy is distributed among 6 or less first electrons (Fig. 6.34 on the left). This results, in combination with a large value of the energy resolution

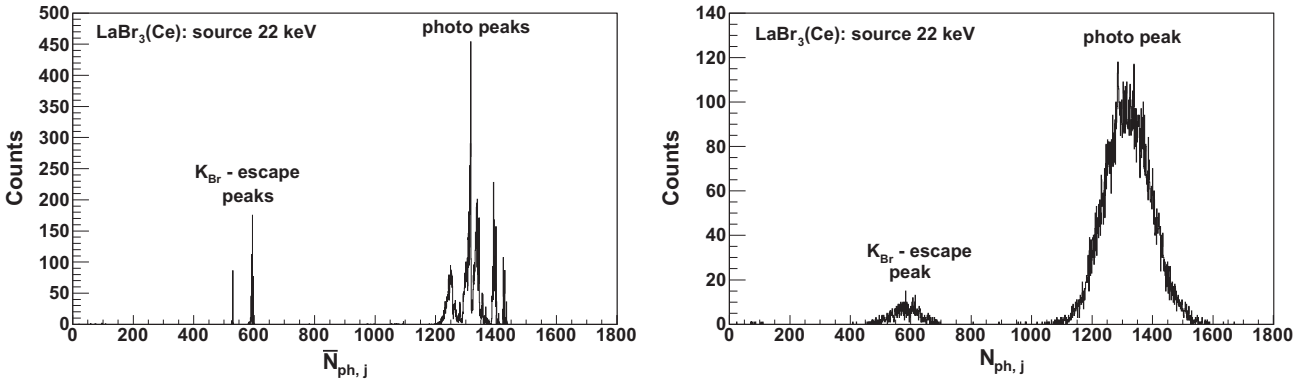

Figure 6.34.: *Simulated results of generated scintillation photons, $\overline{N}_{ph,j}$ and $N_{ph,j}$, produced by 22 keV γ-rays incident into a cylindrically shaped $LaBr_3(Ce)$ scintillator (diameter $\oslash = 4.5$ mm, thickness d = 10 mm). $N_{ph,j}$ includes an additional noise component, which originates from Landau fluctuations in the energy deposition of the first electrons.*

for electrons, $R_{e,T}(E_e)$, for energies $E_e < 22$ keV, into a broad width of the photo peak (Fig. 6.34 on the right).

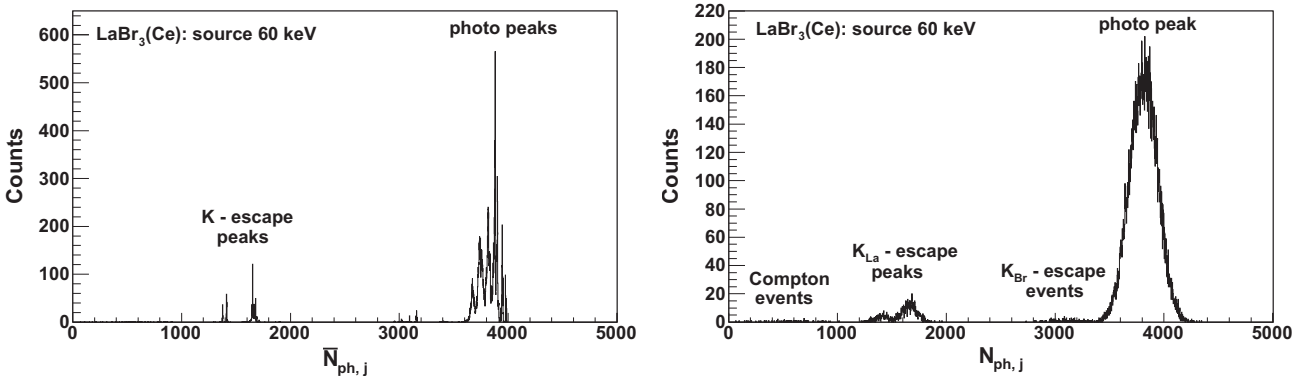

Figure 6.35.: *Simulated results of generated scintillation photons, $\overline{N}_{ph,j}$ and $N_{ph,j}$, produced by 60 keV γ-rays incident into a cylindrically shaped $LaBr_3(Ce)$ scintillator (diameter $\oslash = 4.5$ mm, thickness d = 10 mm). $N_{ph,j}$ includes an additional noise component, which originates from Landau fluctuations in the energy deposition of the first electrons.*

For 60 and 122 keV γ-ray photons, there is a relative increase of events, which are generated by a large number of first electrons, larger than 6 (Fig. 6.31). This is due to the additional possibility to eject an electron from the K-shell of the La atom and its relaxation by producing a K fluorescence photon (Fig. 6.32) plus several Auger electrons. If it does not escape, the fluorescence photon ejects a second photo electron from another atom, which relaxes again via the production of fluorescence and Auger electrons or exclusively Auger electrons. Thus a larger number of photo peak entries originate from events with a higher number of first electrons (> 6) for 60 and 122 keV compared to 22 keV γ-rays. The electron light yield, $\overline{L}_e$, changes

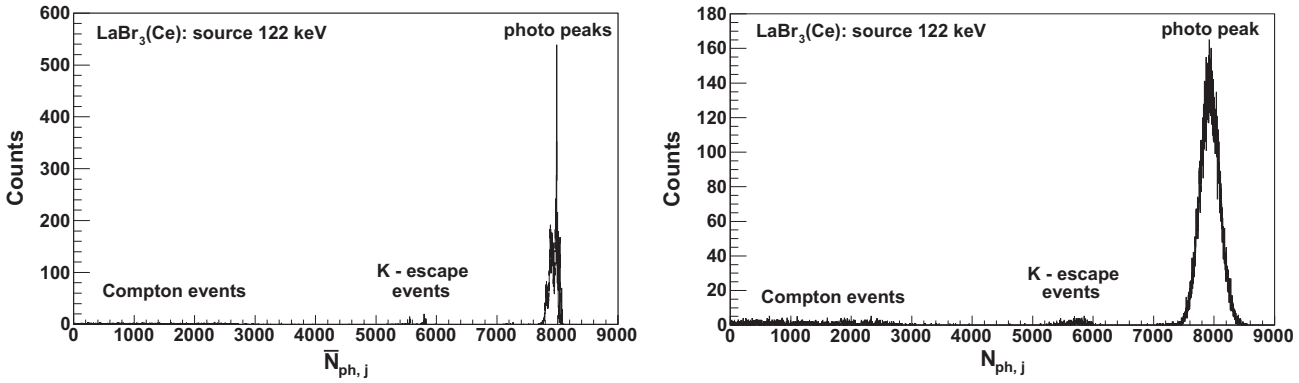

Figure 6.36.: *Simulated results of generated scintillation photons, $\overline{N}_{ph,j}$ and $N_{ph,j}$, produced by 122 keV γ-rays incident into a cylindrically shaped $LaBr_3(Ce)$ scintillator (diameter $\oslash = 4.5$ mm, thickness d = 10 mm). $N_{ph,j}$ includes an additional noise component, which originates from Landau fluctuations in the energy deposition of the first electrons.*

only slightly at higher energies (> 30 keV) (Fig. 6.21 on the left, solid line). Due to an improving energy resolution for electrons, $R_{e,T}(E_e)$, towards higher energies (> 30 keV), the relative width of the photo peak, especially for 122 keV, is narrower than for 22 keV γ-ray photons.

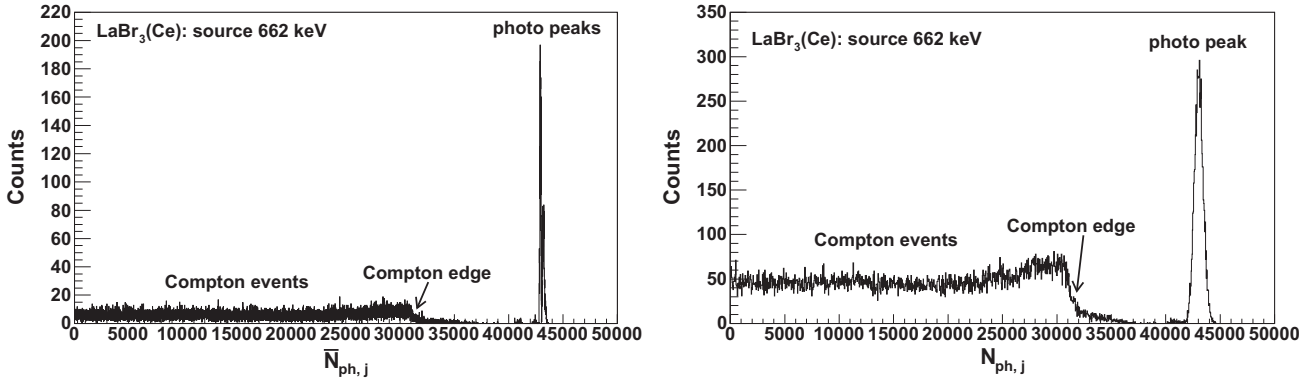

Figure 6.37.: *Simulated results of generated scintillation photons, $\overline{N}_{ph,j}$ and $N_{ph,j}$, produced by 662 keV γ-rays incident into a cylindrically shaped $LaBr_3(Ce)$ scintillator (diameter $\oslash = 4.5$ mm, thickness d = 10 mm). $N_{ph,j}$ includes an additional noise component, which originates from Landau fluctuations in the energy deposition of the first electrons.*

The histograms of $\overline{N}_{ph,j}(E)$ and $N_{ph,j}(E)$ generated by 662 keV γ-rays are presented in Fig. 6.37. A zoom into the region of the photo peak, is shown in Fig. 6.38 for the cylindrically shaped $LaBr_3$(Ce) scintillator with a diameter of $\oslash = 4.5$ mm and a thickness of d = 10 mm (left hand side) and with a diameter of $\oslash = 25$ mm and a thickness of d = 25 mm (right hand side). Events without participation of Compton scattered electrons in the range from $\overline{N}_{ph,j}(662keV) = 42750$ to 43050 scintillation photons have a lower number of first electrons than events where also

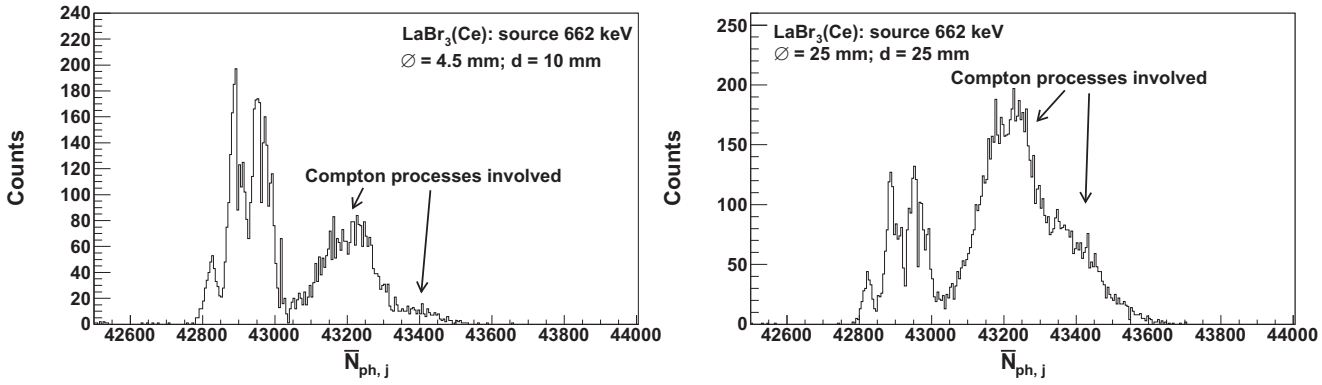

Figure 6.38.: *Histogram of the photo peak for 662 keV γ-rays incident into a cylindrically shaped $LaBr_3(Ce)$ scintillator.*

Compton scattered electrons are created. These events generate entries in the range $\overline{N}_{ph,j}(662keV) = 43050$ to 43700. Entries which originate from events without Compton scattered electrons have a lower number of scintillation photons, $\overline{N}_{ph,j}$, due to a lower number of first electrons in combination with the slowly decreasing slope of the light yield for electrons, $\overline{L}_e(E_e)$, for energies above 122 keV. The width of the photo peak is also narrower for 662 keV compared to lower γ-energies. This is, because the light yield for electrons, $\overline{L}_e(E_e)$, changes less for higher energies ($E_e > 122$ keV).

The light yield for electrons in $LaBr_3$(Ce) changes less compared to that in CsI(Tl) for electron energies $E_e > 30$ keV. This leads in combination with a lower energy resolution for electrons, $R_{e,T}(E_e)$, in $LaBr_3$(Ce) compared to that in CsI(Tl) for electron energies $E_e > 23$ keV, to a narrower width of the photo peak of 662 keV γ-ray photons in $LaBr_3$(Ce) than in CsI(Tl).

Light yield as a function of γ-ray energy

The energy dependent mean light yield, $\overline{L}(E)$ (see Eq. 6.9), and its contribution to the energy resolution, R_T (see Eq. 6.10), for incident γ-rays is investigated in the following. The light yield for electrons, $\overline{L}_e$, is set to $\overline{L}_e = (\overline{L}_e/c) \cdot 65$ and to 61.5 scintillation photons per keV for $LaBr_3$(Ce) and CsI(Tl) respectively.

Fig. 6.39 and 6.40 show the simulated light yield, $\overline{L}(E)$, of $LaBr_3(Ce)$ and CsI(Tl) for incident γ-rays. The shapes of the curves result from the non-proportional light yield, $\overline{L}_e(E_e)$, for electrons, which is shown in Fig. 6.21, in combination with the energy dependent distribution of the deposited energy among the Compton, photo and Auger electrons. The calculated light yield, $\overline{L}(E)$, of $LaBr_3(Ce)$ for incident γ-rays is presented for the first time in this work. Calculated values of $\overline{L}(E)$ of CsI(Tl) for incident γ-rays have already been presented in [118]. Values from literature show that the measured energy dependent light yield can vary especially for γ-energies below the K-shell electron binding energy, due to a changing quality and Tl doping concentration from one scintillator sample to another [122, 123, 124]. It is reasonable therefore to calculate $\overline{L}(E)$ for the scintillator samples used in this work. Clearly visible is the decreasing light yield to low energies for both scintilla-

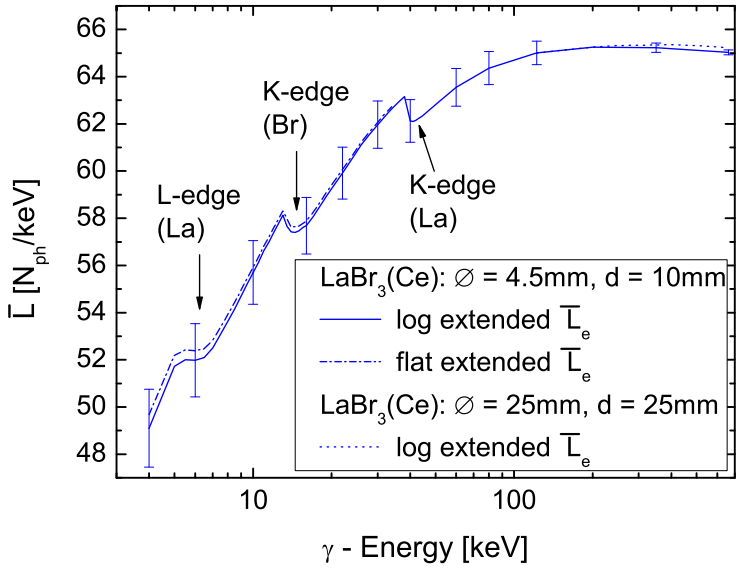

Figure 6.39.: *Simulated values of the energy dependent mean light yield, $\overline{L}(E)$, of $LaBr_3(Ce)$ for incident γ-rays.*

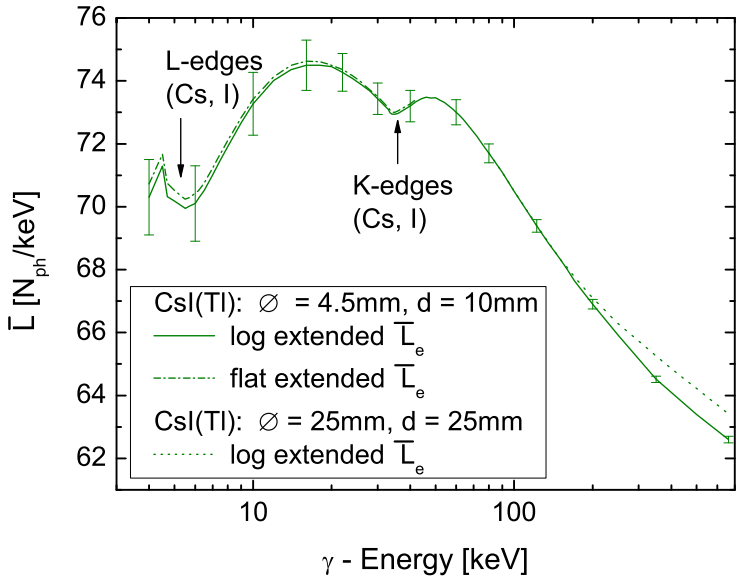

Figure 6.40.: *Simulated values of the energy dependent mean light yield, $\overline{L}(E)$, of CsI(Tl) for incident γ-rays.*

tors and the decreasing light yield to high energies for CsI(Tl). The curves of the light yield for γ-rays, $\overline{L}(E)$, have discontinuities at the K- and L-edges of Cs and I for CsI(Tl) and La and Br for $LaBr_3$(Ce). The two extrapolations of $\overline{L}_e(E_e)$ to lower energies than the mean excitation energy I ($\approx$ 500 eV) for CsI(Tl) and $LaBr_3(Ce)$,

which are shown in Fig. 6.21, have only a negligible effect on $\overline{L}(E)$. Increasing the dimensions of the cylindrically shaped scintillators from ⊘ = 4.5 mm, d = 10 mm to ⊘ = 25 mm, d = 25 mm leads only for CsI(Tl) to a higher light yield for energies above $E > 160$ keV. This increase is caused by a higher number of Compton scattered photons being absorbed and not escaping the scintillator, so that the deposited energy can be distributed among a higher number of first electrons. This results into a lower mean energy of the first electrons. The summation over the scintillation photons generated by the first electrons, leads to a higher total number of scintillation photons, $\overline{N}_{ph,j}$, for the larger compared to the smaller CsI(Tl) scintillator, because of the lower mean energy of the generated first electrons and the values of $\overline{L}_e(E_e)$, which is increasing for decreasing electron energies from 662 keV to 10 keV (Fig. 6.21). This circumstance shifts $\overline{L}(E)$ to higher values for the larger CsI(Tl) scintillator. Because of the small increase of $\overline{L}_e(E_e)$ for $LaBr_3(Ce)$ from 60 keV to 662 keV, the increase of $\overline{L}(E)$ for the larger compared to the smaller scintillator is also small for energies E > 100 keV.

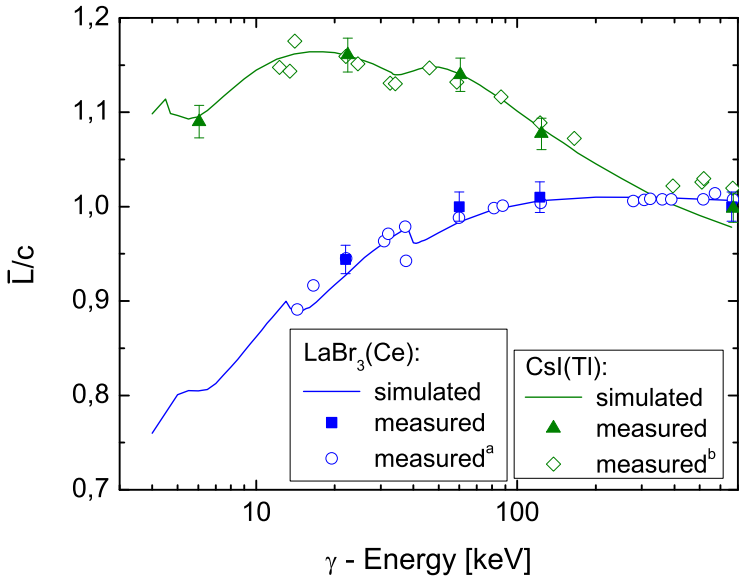

Figure 6.41.: *Simulated and measured normalized mean light yield of CsI(Tl) and $LaBr_3(Ce)$. Our simulations and measurements (solid curve and full symbols) have been performed for cylindrical CsI(Tl) and $LaBr_3(Ce)$ with the dimensions, ⊘ = 4.5 mm and d = 10 mm. Measured values from literature have open symbols [a][12] and [b][118].*

In Fig. 6.41 the normalized light yields, $\overline{L}(E)/c$, of CsI(Tl) and $LaBr_3(Ce)$ are compared with normalized values from measurements. The shape of $\overline{L}(E)/c$ of CsI(Tl) is in good agreement with the normalized measured values within the error bars below 122 keV. Above 122 keV the calculated light yield of CsI(Tl) decreases faster than the measured light yield. A larger change of the light yield in the energy range 122-662 keV compared to the measured values leads to a larger contribution of the non-proportional light yield to and an overestimation of the energy resolution.

The shape of the simulated normalized light yield, $\overline{L}(E)/c$, of $LaBr_3(Ce)$ is in good agreement with the normalized measured values within the error bars over the whole energy range.

Energy resolution as a function of γ-ray energy

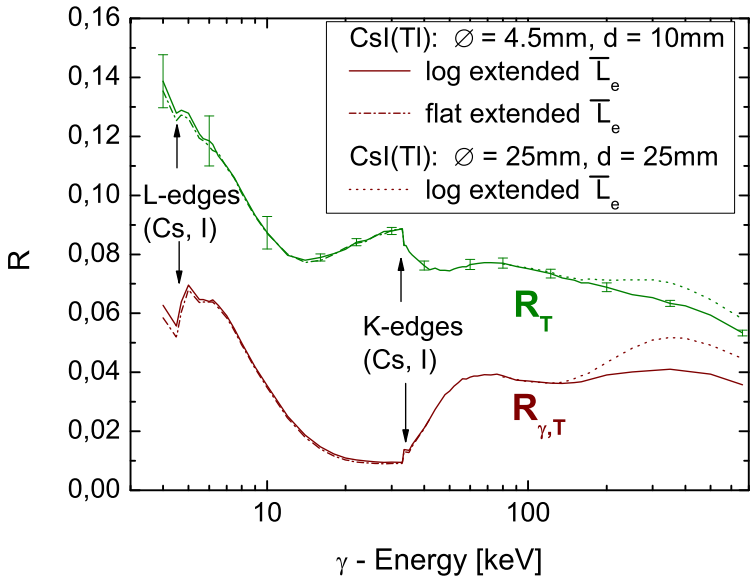

Figure 6.42.: *Simulated values of $R_{\gamma,T}(E)$ and $R_T(E)$ for CsI(Tl), dependent on the incident γ-energy. $R_T(E)$ in contrast to $R_{\gamma,T}(E)$ includes the noise component originating from Landau fluctuations in the energy deposition of the Compton, photo and Auger electrons.*

The values of the energy resolution, $R_{\gamma,T}$ and R_T, are determined by Eq. 6.10 and 6.14 from the simulated spectra of $\overline{N}_{ph,j}$ and $N_{ph,j}$. The results are plotted in Fig. 6.42 and 6.43. R_T includes the additional noise component from the Landau fluctuations in the energy depositions of the generated Compton, photo and Auger electrons (first electrons) along their track through the scintillator. A sensitivity test has shown that a change of $\overline{L}_e$ for $LaBr_3$(Ce) from $\overline{L}_e/c \cdot 65$ to $\overline{L}_e/c \cdot 55$ leads to a negligible change of $R_{\gamma,T}$ and R_T. This sensitivity test has been performed, because results of the mean number of signal electrons, $\overline{N}_e$, from measurements and simulations (see Sec. 6.2.2) indicate that the light yield of the used $LaBr_3$(Ce) scintillators is more likely to be $\overline{L} = 55\ N_{ph}/keV$ than $65\ N_{ph}/keV$ at 662 keV. The difference of the two extrapolations of $\overline{L}_e(E_e)$ (Fig. 6.21) to energies below the mean excitation energy I ($\approx$ 500 eV) of CsI(Tl) and $LaBr_3(Ce)$, has only a negligible effect on $R_{\gamma,T}(E)$ and $R_T(E)$. An increase of the cylindrical scintillator with the dimensions $\oslash$ = 4.5 mm, d = 10 mm to $\oslash$ = 25 mm, d = 25 mm degrades the energy resolution, $R_{\gamma,T}(E)$ and $R_T(E)$, of CsI(Tl) only for $E > 160$ keV, but not for $LaBr_3$(Ce). As explained before, in larger scintillators the probability of Compton scattered photons being absorbed is higher compared to smaller scintillators, so that

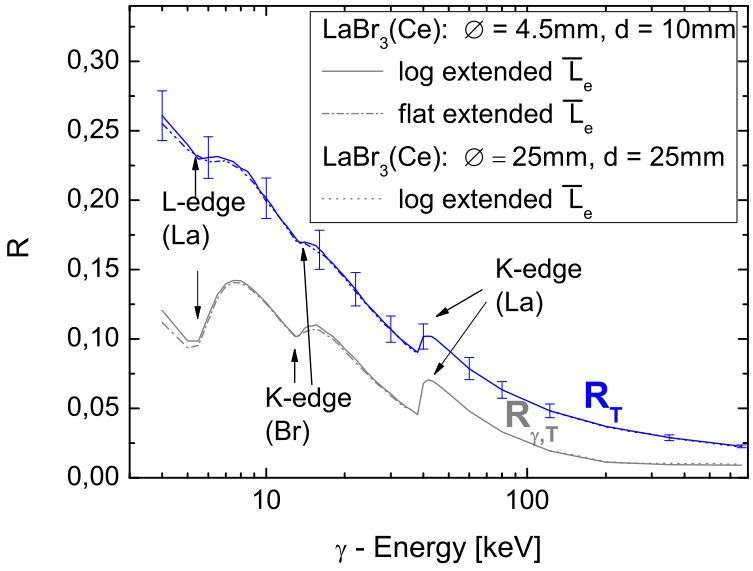

Figure 6.43.: *Simulated values of $R_{\gamma,T}(E)$ and $R_T(E)$ for $LaBr_3(Ce)$, dependent on the incident γ-energy. $R_T(E)$ in contrast to $R_{\gamma,T}(E)$ includes the noise component originating from Landau fluctuations in the energy deposition of the Compton, photo and Auger electrons.*

there are additional possibilities of distributing the deposited γ-energy among the first electrons. This leads to a larger spread of $\overline{N}_{ph,j}$ and $N_{ph,j}$, hence to a poorer energy resolution of the contributions $R_{\gamma,T}$ and R_T, if the change of $L_e(E_e)$ with electron energy is large. This is the case for CsI(Tl) (Fig. 6.21 right). For energies above 30 keV $L_e(E_e)$ of $LaBr_3(Ce)$ changes only slightly (Fig. 6.21 left). $R_T(E)$ of both scintillators shows discontinuities at their K- and L-edges. This is due to the fact, that for energies, E, above the edges, there are more possibilities to distribute the γ-energy among electrons, which leads to an increase of $R_{\gamma,T}(E)$. Also $R_T(E)$ of $LaBr_3$(Ce) shows this effect, caused by the monotonous decrease of $R_e(E_e)$ from low to high energies. Because of a local maximum of $R_e(E_e)$ of CsI(Tl) around $E_e \approx 25\ keV$, there is no increase of $R_T(E)$ above the K-edge. For γ-energies around $E \approx 70\ keV$ both scintillators have the same energy resolution, $R_T(E)$. CsI(Tl) has a better resolution for $E < 70\ keV$ and $LaBr_3$(Ce) for $E > 70\ keV$.

Fig. 6.44 shows the simulated values of $R_T(E)$ for CsI(Tl) and $LaBr_3$(Ce) and measured values of the total energy resolution, R, at -20°C and values from literature, which have also been determined from measurements. The total energy resolution, which is described by Eq. 6.5, consists of several noise components. It is expected that $R_T(E) < R(E)$, especially at lower energies. The moderate cooling to -20°C minimizes the effect of electronic noise. $R_T(E)$ of CsI(Tl) is also determined by the relative FWHM of a Gaussian fit to the photo peak of the simulated spectra (dotted green curve). In case of CsI(Tl) the photo peaks have a shoulder on the low energy side in the energy range from 40 to 122 keV. Its origin is explained in Sec. 6.2.1. Only the data points of the photo peak, which do not include the shoulder, are used

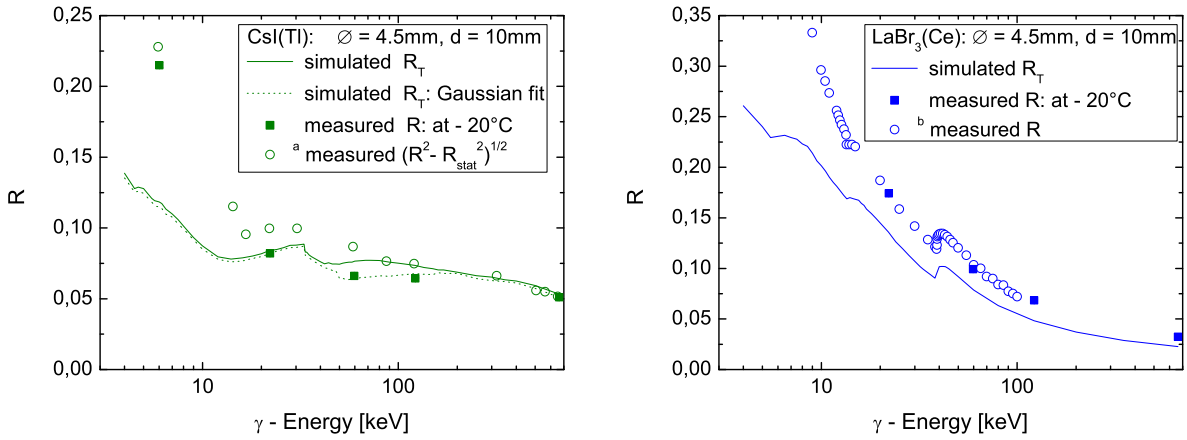

Figure 6.44.: *Values of R_T for CsI(Tl) and $LaBr_3$(Ce) compared to values of the energy resolution, determined from measurements. The values illustrated by the green and blue squares are values of the total energy resolution, R, measured at -20° C. The values illustrated by the green and blue circles are taken from literature ([a][123], [b][114]) and have been determined from the total energy resolution by subtracting the components originating from statistics including fluctuations of the PMT gain.*

for the Gaussian fit.

For the detector CsI(Tl) + SDD the simulated values of $R_T(E)$ (dotted line), is approximately equal to the measured values of the total energy resolution, $R(E)$, at -20 $°C$. This suggests that the other noise terms in Eq. 6.5 have smaller contributions to R for γ-energies $E \geq 22$ keV. The measured values of the energy resolution (full green squares) for γ-energies $E < 22$ keV are larger than $R_T(E)$, because the values of the electronic noise R_{el}, R_{Bino} and R_η increase, because of the decreasing absolute number of scintillation photons with decreasing γ-energy (compare Fig. 6.10). A more detailed presentation of the values of all contributions to the energy resolution will be given in Sec. 6.2.3. For energies $E > 122$ keV the simulation overestimates slightly the value of R_T, because the best possible fit of the calculated mean efficiency, $\overline{T}_e$, to the measured values of $\overline{L}_e/c$ from literature lead to a slightly larger change of its slope in the energy range 122 to 662 keV compared to that of the measured values. This circumstance increases the non-proportionality of T_e, thus also of $\overline{T}_e$, due to Eq. 6.26. The difference between our measured values R (full green squares) and the values $\sqrt{(R^2 - R_{stat}^2)}$ (R_{stat} includes for this detector system the contribution resulting from fluctuations in the multiplication process of the photomultiplier tube (PMT)), which are values from measurements presented in literature [123], can arise from the use of different CsI(Tl) scintillators, reflectors and readout detectors, such as PMTs. Scintillator properties, such as scintillator quality and Tl doping concentration (0.25 mole %) [123, 104] can change from one sample to another, even if the scintillators are from the same distributor.

The values of $R_T(E)$ of the detector system $LaBr_3$(Ce) + SDD are smaller than the measured values of the total energy resolution, R, as expected, but both curves

have the same slope. The contributions of R_{Bino} and R_η, are supposed to be larger compared to the detector CsI(Tl) + SDD, because of a lower number of detected signal electrons, due to a lower light collection and quantum efficiency of the SDD for scintillation photons from $LaBr_3$(Ce). The contribution of the light and charge collection efficiency, $\overline{\eta}$, and its contribution to R_η and R_{Bino} is investigated in Sec. 6.2.2.

To summarize, the model for incident electrons proposed in [49, 25, 100], which is based on the dependency of the conversion efficiency of the generated electrons and holes into scintillation photons on the deposited energy density, which is specified by a combined efficiency of the two efficiencies proposed by Birks [84, 116] and Onsager [85, 86], in combination with Landau fluctuations of the deposited energy by the electron on its path through the scintillator, reproduces quite well the mean light yield, $\overline{L}_e(E)$, of the scintillator and makes an estimation of the energy resolution, $R_{e,T}(E)$, for incident electrons. To determine the energy resolution, $R_T(E)$, and the mean light yield, $\overline{L}(E)$, for incident γ-rays, in a first step, their interaction with the scintillator and the generation of photo, Auger and Compton electrons is simulated by the Monte Carlo toolkit Geant4. In a second step each of these electrons generates a number of scintillation photons, which is calculated from the mean light yield, $\overline{L}_e(E)$, and fluctuations of $R_{e,T}(E) \cdot \overline{L}_e(E)/2.35$ around the mean light yield for incident electrons. The values of $R_T(E)$ and $\overline{L}(E)$ describe very well the slope and magnitude of the measured energy resolution and reproduce the mean light yield.

The calculated mean light yield, $\overline{L}(E)$, of $LaBr_3$(Ce) and the calculated values of $R_{\gamma,T}(E)$ and $R_T(E)$ in the energy range 6 keV - 662 keV for CsI(Tl) and $LaBr_3$(Ce) are presented for the first time in this work.

6.2.2. Effect of the light and charge collection efficiency on the energy resolution

In this section the contribution of the light and charge collection efficiency to the energy resolution is investigated.

Geant4 uses the Fresnel equations to calculate the probability for reflection, transmission and refraction between two media. The degree of surface roughness of the scintillator and reflector can also be modeled and the value of the reflector reflectivity and the absorption length of scintillation photons inside the scintillator can be defined in Geant4. The reflection, absorption and transmission at the interface between optical coupler and SDD entrance window is read from a look-up table. The values in the look-up table have been calculated with the equations presented in Sec. 5.5. The effect of the charge collection efficiency, CCE, inside the SDD entrance window, which is defined in Eq. 5.26 has been included into Geant4 by a short algorithm.

Parameters used in simulations of the light and charge collection

In Fig. 6.45 the layout of γ-detectors are illustrated consisting of a CsI(Tl) (on the left) or a $LaBr_3$(Ce) scintillator coupled to a SDD (on the right) generated by Geant4. The CsI(Tl) scintillator is wrapped into a reflector with an air gap between

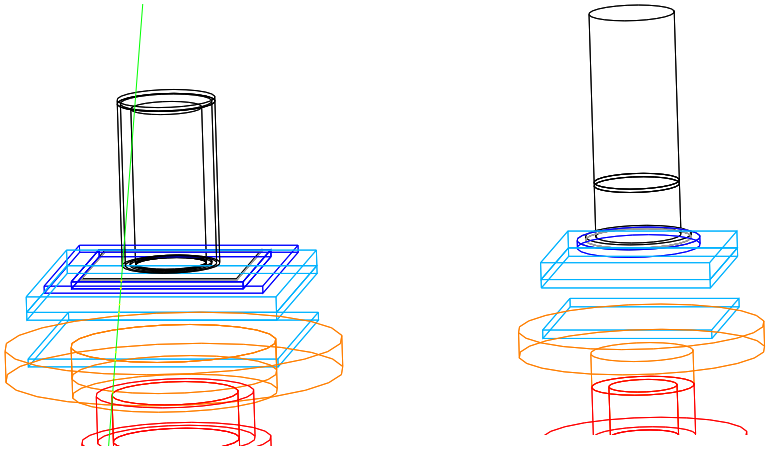

Figure 6.45.: *Detector geometry of a CsI(Tl) (on the left) and $LaBr_3$(Ce) (on the right) scintillator coupled with an optical coupler to the SDD, which is mounted onto a substrate, peltier cooler and socket. Between $LaBr_3$(Ce) and the SDD is the glass window of the $LaBr_3$(Ce) housing. The green line is an incident γ-ray. The layout is generated by Geant4.*

CsI(Tl) and reflector of several 100 μm thickness. CsI(Tl) is coupled directly with an optical coupler onto the SDD entrance window. The $LaBr_3$(Ce) scintillator is wrapped into a reflector with an infinitesimal thin air gap. There is an optical coupler between $LaBr_3$(Ce) and the 3 mm thick glass window. The glass window itself is also coupled to the SDD entrance window with an optical coupler. The surface roughness of the scintillator is modeled by micro facets. The orientation of the surface normals of the micro facets to the average surface normal of the scintillator faces is given by a Gaussian distribution, with the standard deviation, sa. For a 100 % polished surface the value of sa has to be set to 0 rad (1 rad = $180°/\pi$). In Fig. 6.46 the orientation distribution of the micro facets normals are plotted for two degrees of surface roughness, with a value of sa = 0.05 rad and 0.1 rad. From measured surface roughnesses of BGO crystals, values of sa = 0.02 rad for polished and sa $<$ 0.21 rad for ground surfaces have been determined in [91]. The surfaces of the cylindrical and cubical CsI(Tl) scintillators are shown in Fig. 6.47 and 6.48. The degree of surface roughness of the cylindrical scintillators is larger than for the cubical scintillators. The exact value of the surface roughness has not been determined experimentally, therefore we simulated the light collection for several values of surface roughness in the range from sa = 0.04 rad to 0.18 rad.
The reflectors used in the measurements are of specular or diffuse type. The used multilayer specular reflector has a reflectivity larger than 0.98 in the visible range [98]. In simulations, reflectivity values in the range 0.87 - 0.98 are investigated. The absorption length of CsI(Tl) is supposed to be several meters [50]. The effect of different values in the range from several 10 cm to several meters onto the detector response is examined. The values of the light yield of CsI(Tl) are taken from results presented in Sec. 6.2.1.

The degree of surface roughness of the used $LaBr_3$(Ce) scintillators is not specified by its distributor. Examination of the crystal and the reflector is not possible, because the $LaBr_3$(Ce) scintillator is vacuum sealed into an aluminum housing. In

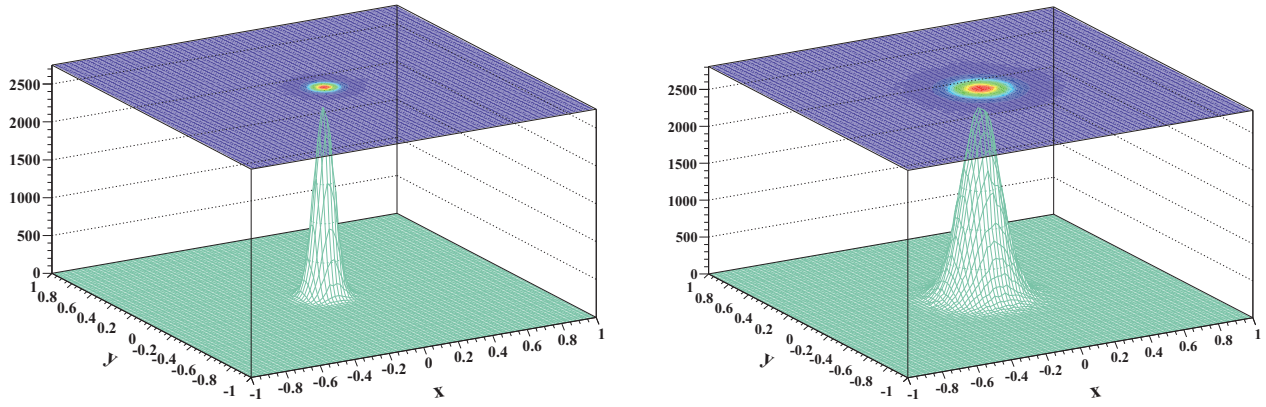

Figure 6.46.: *Gaussian orientation distribution of the surface normals of the micro facets relative to the average surface normal of the scintillator face, which is the normal of the xy-plane. Its standard deviation, sa, is set to sa = 0.05 rad (on the left) and sa = 0.1 rad (on the right).*

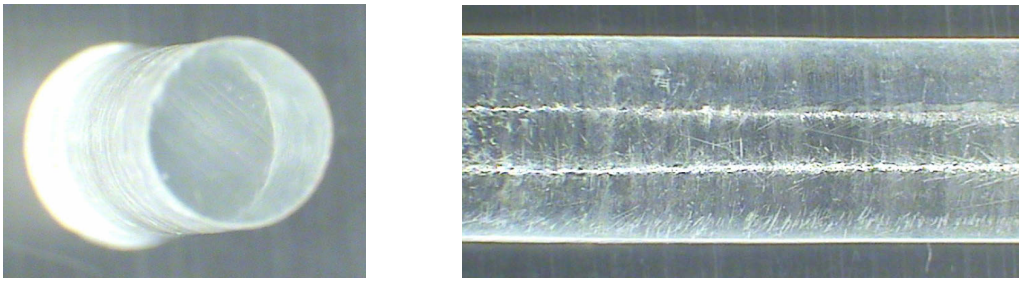

Figure 6.47.: *Pictures of the surface of a cylindrical CsI(Tl) scintillator used in the experiments.*

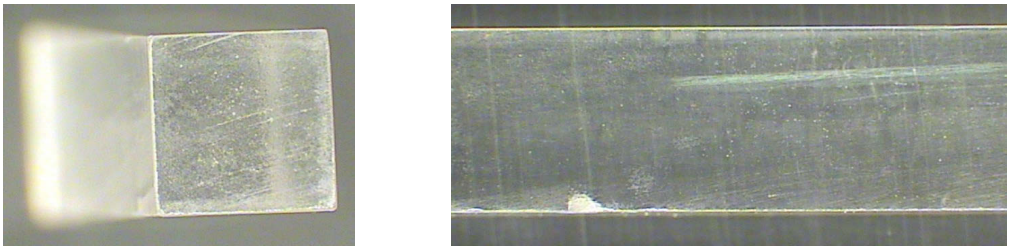

Figure 6.48.: *Pictures of the surface of a cubical CsI(Tl) scintillator used in the experiments.*

our simulations the influence of the surface roughness onto the number of signal electrons and the energy resolution is examined in the range sa = 0.06-0.14 rad. The reflector is made of 500 μm thick teflon. The diffuse reflectivity of a several millimeter thick teflon is specified by Ocean Optics to be larger than 0.98 in the near ultra violet range. In our simulations, the influence of a diffuse reflector with a reflectivity in the range of 0.87 - 0.98 onto the number of signal electrons and the energy resolution is investigated. The absorption length of $LaBr_3$(Ce) has been presented in [99]. It is in the range from some millimeters to some meters for photons in the wavelength range from 300 nm to 400 nm. The values of the scintillator light yield, $\overline{L}(E)$, of $LaBr_3$(Ce) are taken from results presented in Sec. 6.2.1.

Spatial and angular distribution of scintillation photons at the SDD EW

We are first studying the propagation of scintillation photons from their generation point, which is in this case the center of a cylindrically shaped CsI(Tl) scintillator with a polished surface. The photons reaching the CsI(Tl)-air interface with an

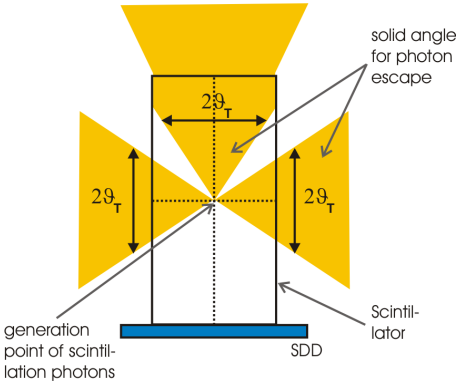

Figure 6.49.: *Escape of scintillation photons from the scintillator with polished surface and no reflector.*

angle, ϑ, relative to the surface normal, which is smaller than the angle of total reflection

$$\vartheta_T = arcsin\left(\frac{n_{air}}{n_{CsI(Tl)}}\right) = arcsin\left(\frac{1}{1.8}\right) = 33.7°, \tag{6.30}$$

where n_{air} and $n_{CsI(Tl)}$ are the refraction indexes of air and CsI(Tl), are reflected to a small extend, but mainly transmitted (Fig. 6.49 yellow areas). The reflectance and transmittance are about 0.1 and 0.9 for the CsI(Tl)-air interface and can be determined from the Fresnel equations. Scintillation photons incident onto the CsI(Tl)-air interface with a larger angle than ϑ_T relative to the surface normal are totally reflected. These photons (Fig. 6.49 white areas) remain within the scintillator. Reaching the CsI(Tl) - SDD interface after several reflections, they are transmitted into the SDD or totally reflected and trapped inside the scintillator, depending on their angle of incidence at the SDD entrance window.

The calculated angle dependent distribution of photons at the CsI(Tl) face, which is supposed to be coupled to the SDD entrance window, is illustrated in Fig. 6.50 (on the left) for a bare, polished and cylindrically shaped CsI(Tl) scintillator (solid line)

and a CsI(Tl) scintillator wrapped into a specular reflector with a reflectivity of 1 (dashed line). The right histogram in Fig. 6.50 shows the results from Monte Carlo simulations with Geant4 for the scintillator without reflector. It is assumed that the scintillation photons are generated in the center of the scintillator. In this case and also in the example shown in Fig. 6.51 every photon reaching the scintillator face, which is supposed to be coupled to the SDD, is detected and destroyed afterwards. No reflection and transmission at the SDD entrance window is taken into account in the results illustrated in Fig. 6.50 and 6.51. The analytical formula describing

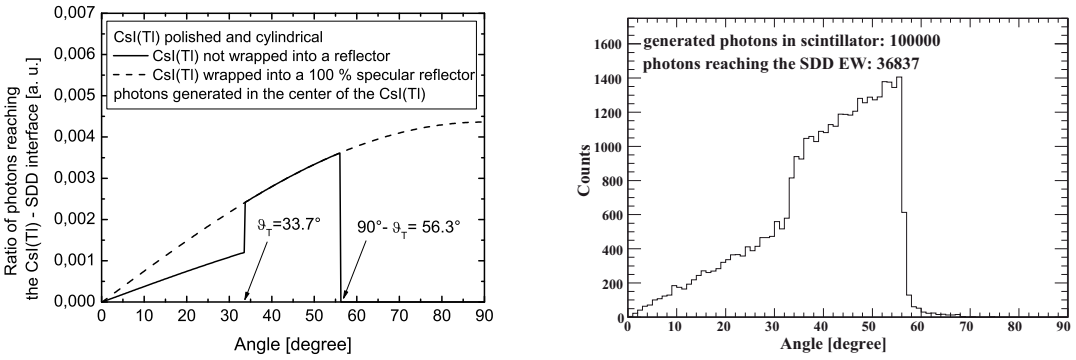

Figure 6.50.: *Angle distribution of the photons incident on one face of the CsI(Tl) scintillator, determined from calculations and Monte Carlo simulations for a bare CsI(Tl) scintillator. The generation point for scintillation photons is in the center of the cylindrically shaped CsI(Tl) crystal with the dimensions ⌀ = 5 mm and d = 10 mm.*

the angle dependent distribution, $D(\vartheta)$, of incident photons can be derived from the integral, which determines the surface of a spherical sector with radius one,

$$D(\vartheta) = \frac{1}{4\pi}\int_0^{2\pi}\int_{\vartheta}^{\vartheta+\Delta\vartheta} sin(\vartheta)d\vartheta d\varphi = \frac{1}{2}(cos(\vartheta) - cos(\vartheta + \Delta\vartheta)). \tag{6.31}$$

It is assumed that the generated photons are propagating isotropically into all directions. The broken line in Fig. 6.50 arises from $2 \cdot D(\vartheta)$, because photons with angles ϑ and $\vartheta + 180°$ of their momentum directions relative to the normal of the CsI(Tl) face, which is supposed to be coupled to the SDD, reach this face under the same angle of incidence. The solid line in Fig. 6.50 results from $D(\vartheta)$ in the range $[0, \vartheta_T]$ and $2D(\vartheta)$ in the range $[\vartheta_T, 90° - \vartheta_T]$. The results from calculation and Monte Carlo simulation of the bare crystal are in good agreement (Fig. 6.50). The drop of the number of photons with incident angles of $\vartheta < \vartheta_T$ is due to the loss of photons through the CsI(Tl)-air interface on the opposite side of the SDD (Fig. 6.49). The drop in the number of photons for incident angles $\vartheta > 90° - \vartheta_T$ results from the loss of photons at the interface between the air and the cylindrical CsI(Tl) shell (Fig. 6.49). The calculation in Fig. 6.50 on the left has been performed to verify the result from the Geant4 Monte Carlo simulation. In the following only results from simulations are presented.

If the position of the generation point of scintillation photons changes from the center to the position with the coordinates z = 5 mm, x = 0 mm and y = 2.45 mm

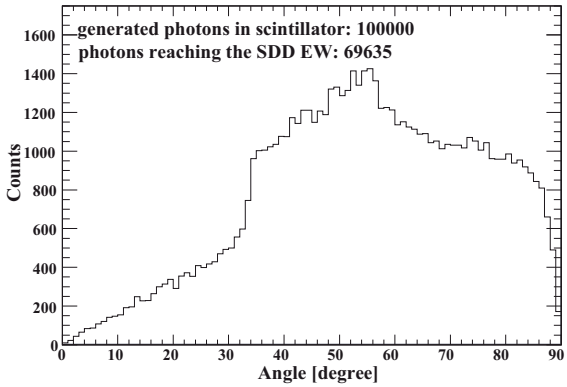

Figure 6.51.: *Angle distribution at one face of a cylindrically shaped CsI(Tl) scintillator for photons propagating isotropically from a generation point close to the border of the scintillator. The dimensions of the scintillator are* $\oslash = 5$ *mm and* $d = 10$ *mm.*

inside the scintillator, then the angular distribution of the incident photons onto the CsI(Tl) face, which is supposed to be coupled to the SDD entrance window, for a bare and polished scintillator, changes drastically. Now the reflectivity of the photons at the interface between the CsI(Tl) shell and air depends on the angle, φ. The angular distribution of the photons is shown in Fig. 6.51. In this case much more photons are totally reflected at the interface between the cylindrical CsI(Tl) shell and the air for incident angles $\vartheta > 90° - \vartheta_T$. Comparing the angular distribution of scintillation photons and the number of photons reaching one face of CsI(Tl) in Fig. 6.50 (on the right) and Fig. 6.51, it is recognizable that the light collection in a bare and polished scintillator strongly depends on the position, where the scintillation photons are generated.

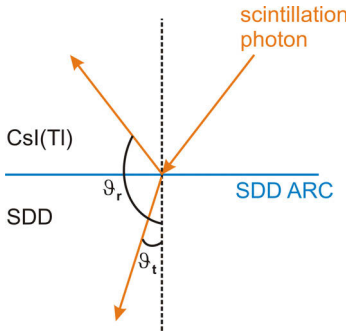

Figure 6.52.: *Illustration of the notation for the angles of the reflected and transmitted scintillation photon relative to the interface normal between CsI(Tl) and SDD.*

In the following results from simulations of the position distribution, where scintillation photons hit the CsI(Tl) - SDD interface, and distributions of the angles (Fig. 6.52) of the transmitted ($\vartheta_t \leq 90°$) and reflected photons ($\vartheta_r > 90°$) are presented.

The maximal angle of the transmitted photons can be calculated from Snells law by

$$\vartheta_{t,max} = arcsin\left(\frac{n_{CsI(Tl)}}{n_{Si}} \cdot sin\left(\vartheta_{T,(CsI(Tl)|SDD-EW)}\right)\right) = arcsin\left(\frac{n_{SiO_2}}{n_{Si}}\right) \approx 23^\circ \tag{6.32}$$

where n is the refraction index of the material and $\vartheta_{T,(CsI(Tl)|SDD-EW)} \approx 54^\circ$ the angle of total reflection for a photon incident on the SDD entrance window from the CsI(Tl) scintillator with a wavelength of 550 nm.

Next, results from simulations are presented, where an energy of $E = 122$ keV is deposited inside cylindrically and cubically shaped, polished CsI(Tl) scintillators close to the top face. The dimensions of the scintillators are $\oslash = 4.5$ mm and d = 10 mm or 4 x 4 x 10 mm^3, whereas the scintillators are surrounded by a specular reflector. The specular reflector, VM2002, used in the experiments, has a reflectivity larger than 0.98. In the following simulations it is set to 0.98. The transmission and reflection at the CsI(Tl)-SDD interface and the absorption inside the SDD entrance window is also included into these simulations. The energy is deposited at x = 0 mm and y = 2.23 mm in case of the cylindrical or at x = 0 mm and y = 1.98 mm in case of a cubical CsI(Tl) scintillator close to the top face. In each simulation 122 keV have been deposited 100 times inside the scintillator. Each deposition generates $E \cdot \overline{L}(E) = 122 \cdot 69 = 8418$ scintillation photons. There is an air gap of several 100 μm between the scintillator surface and the reflector.

Fig. 6.53 shows distribution of the hits of scintillation photons at the CsI(Tl)-SDD interface. If the generation point of the scintillation photons is in the center of CsI(Tl) at x = 0 mm and y = 0 mm, then most of them hit the CsI(Tl)-SDD interface in the center in case of the cylindrical CsI(Tl) (Fig. 6.53(a)) and homogeneously within the interface in case of the cubical CsI(Tl) scintillator (Fig. 6.53(c)). If the generation point is close to the CsI(Tl) side face at x = 0 mm and y = 2.23 mm or x = 0 mm and y = 1.98 mm, most of the scintillation photons hit the CsI(Tl)-SDD interface close to the cylindrical shell of the scintillator, in case of the cylindrical CsI(Tl) (Fig. 6.53(b)) or homogeneously within the interface for the cubical CsI(Tl) scintillator (Fig. 6.53(d)). A fraction of the scintillation photons hit the air - SDD interface between CsI(Tl) and reflector. The probability for scintillation photons to be transmitted is higher in this area (comp. Fig. 5.9). There is no angle of total reflection at the air - SDD interface.

Fig. 6.54 shows the angular distribution of the transmitted ($\vartheta \leq 90^\circ$) and reflected scintillation photons ($\vartheta > 90^\circ$). The fraction of transmitted photons increases with an increasing angle. Due to the air gap between scintillator and reflector an additional fraction of photons can be transmitted in this area. The maximal angle of transmittance from air into the SDD is

$$\vartheta_{t,max-air} = arcsin\left(\frac{n_{air}}{n_{Si}}\right) \approx arcsin\left(\frac{1}{3.6}\right) \approx 16^\circ, \tag{6.33}$$

which can be identified at the drop in the number of counts around 16° in the histogram of the angular distribution. For the cylindrical scintillator the fraction of transmitted scintillation photons is larger, if their generation point is on the scintillator axis (Fig. 6.54(a)) compared to positions close to its surface (Fig. 6.54(b)). This is due to a lower number of trapped photons, visible at the reduced number of reflections in the range $\vartheta > 90^\circ$ (Fig. 6.54(a)) compared to the

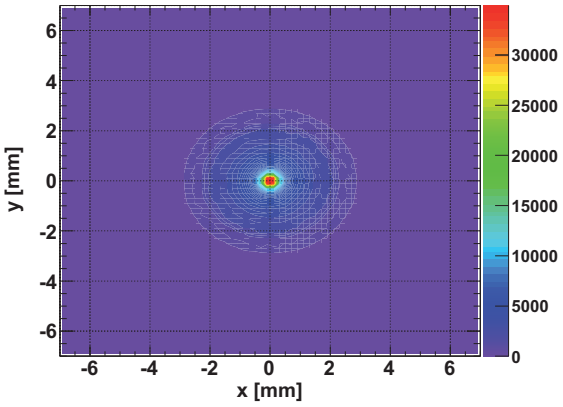

(a) *CsI(Tl): ⊘ = 4.5 mm and d = 10 mm, generation point inside CsI(Tl) at x = 0 mm and y = 0 mm, reflector: ⊘ = 5.8 mm and d = 10.4 mm*

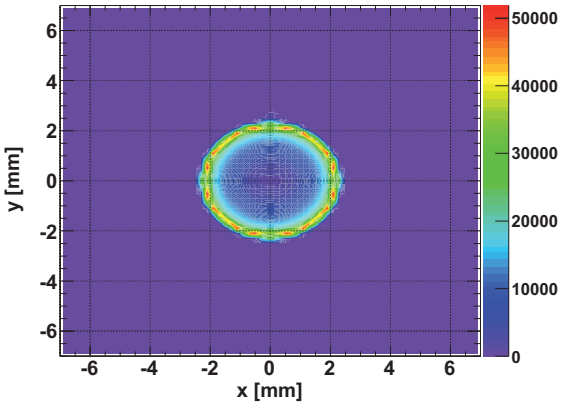

(b) *CsI(Tl): ⊘ = 4.5 mm and d = 10 mm, generation point of inside CsI(Tl) at x = 0 mm and y = 2.23 mm, reflector: ⊘ = 5.8 mm and d = 10.4 mm*

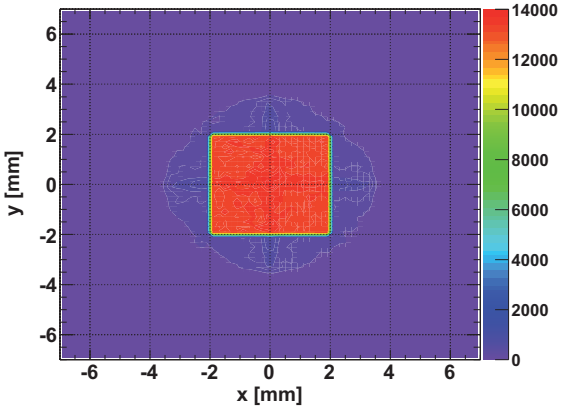

(c) *CsI(Tl): 4 x 4 x 10 mm³, generation point inside CsI(Tl) at x = 0 mm and y = 0 mm, reflector: ⊘ = 7.0 mm and d = 10.4 mm*

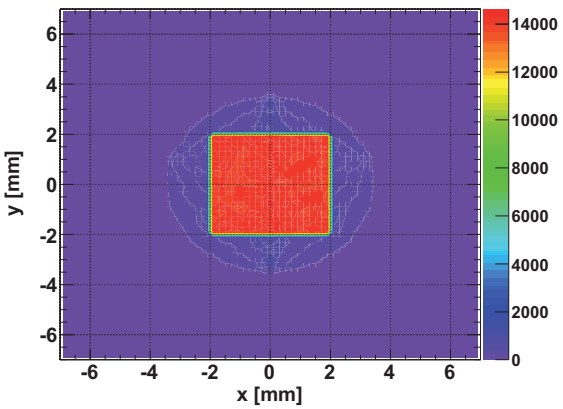

(d) *CsI(Tl): 4 x 4 x 10 mm³, generation point inside CsI(Tl) at x = 0 mm and y = 1.98 mm, reflector: ⊘ = 7.0 mm and d = 10.4 mm*

Figure 6.53.: *Distribution of the hits at the SDD entrance window for polished cylindrical ((a) and (b)) and cubical ((c) and (d)) CsI(Tl) scintillators. The photons are generated inside the CsI(Tl) scintillator with a surface roughness of sa = 0 rad, which is wrapped into a specular reflector with a reflectance of R = 0.98 and an air gap of several 100 µm between scintillator and reflector.*

case, where the generation point is close to the scintillator side face (Fig. 6.54(b)). For the cubical scintillator, there is almost no difference in the angular distribution for the two examined positions of generation (Fig. 6.54(c) and 6.54(d)). In all four histograms of Fig. 6.54 there is a drop in the number of reflections at $\vartheta_{T,2} = 180° - \vartheta_{T,(CsI(Tl)|SDD-EW)}$, which arouses from the total reflection of the scintillation photons at the CsI(Tl) - SDD interface. Only in Fig. 6.54(a) there is an additional large change at $\vartheta_{T,1} = 90° + \vartheta_{T,(CsI(Tl)|Air)}$, which originates from the existence of the angle of total reflection at the CsI(Tl) - air interface.

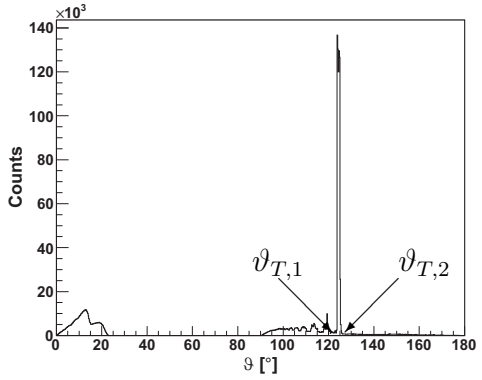

(a) *CsI(Tl): ⊘ = 4.5 mm and d = 10 mm, generation point inside CsI(Tl) at x = 0 mm and y = 0 mm, reflector: ⊘ = 5.8 mm and d = 10.4 mm*

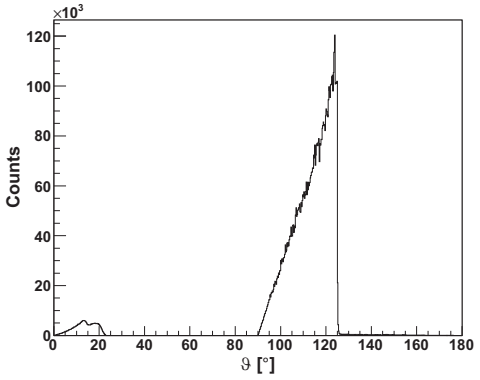

(b) *CsI(Tl): ⊘ = 4.5 mm and d = 10 mm, generation point inside CsI(Tl) at x = 0 and y = 2.23 mm, reflector: ⊘ = 5.8 mm and d = 10.4 mm*

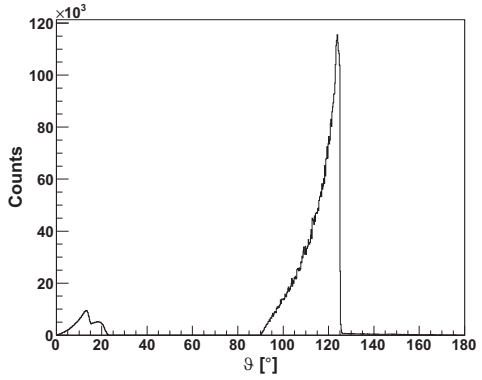

(c) *CsI(Tl): 4 x 4 x 10 mm³, generation point of γ-rays inside CsI(Tl) at x = 0 mm and y = 0 mm, reflector: ⊘ = 7.0 mm and d = 10.4 mm*

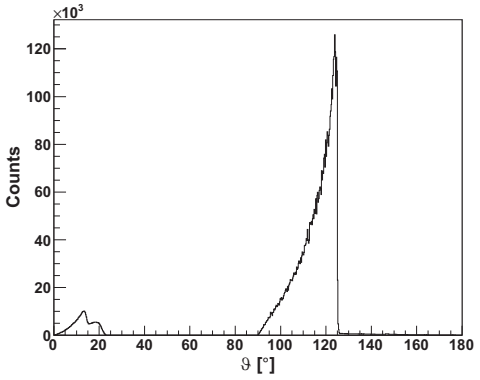

(d) *CsI(Tl): 4 x 4 x 10 mm³, generation point inside CsI(Tl) at x = 0 and y = 1.98 mm, reflector: ⊘ = 7.0 mm and d = 10.4 mm*

Figure 6.54.: *Angle distribution of transmitted scintillation photons ($\vartheta = 0° - 23°$) and number of reflections ($\vartheta = 90° - 180°$) at the SDD-CsI(Tl) interface with respect to the SDD surface normal. The photons are generated inside a cylindrical ((a) and (b)) or a cubical ((c) and (d)) CsI(Tl) scintillator with a roughness of sa = 0 rad, which is wrapped into a specular reflector with a reflectivity of 0.98 and an air gap of several 100 μm between scintillator and reflector.*

The system quantum efficiency, η, for the conversion of scintillation photons into signal electrons, N_e, for the four cases in Fig. 6.54 is about 0.74 (Fig. 6.54(a)), 0.51 (Fig. 6.54(b)), 0.63 (Fig. 6.54(c)) and 0.63 (Fig. 6.54(d)). For polished scintillators the light and charge collection defined by η is more uniform for cubically compared to cylindrically shaped CsI(Tl).

The system quantum efficiency can be increased and made more homogeneous by increasing the scintillator surface roughness. Thereby the number of trapped scintillation photons is reduced and the light collection uniformity enhanced, due to

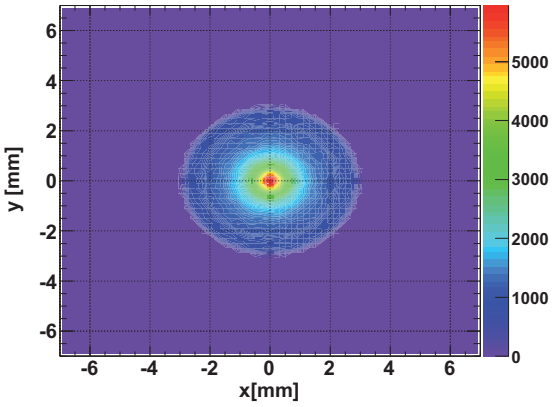

(a) *CsI(Tl):* $\oslash = 4.5$ *mm and* $d = 10$ *mm, generation point inside CsI(Tl) at* $x = 0$ *mm and* $y = 0$ *mm, reflector:* $\oslash = 5.8$ *mm and* $d = 10.4$ *mm*

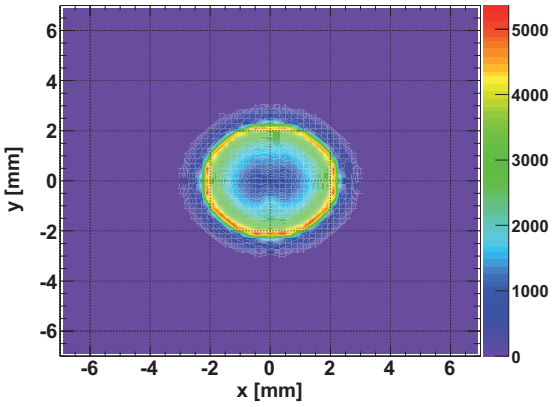

(b) *CsI(Tl):* $\oslash = 4.5$ *mm and* $d = 10$ *mm, generation point inside CsI(Tl) at* $x = 0$ *and* $y = 2.23$ *mm, reflector:* $\oslash = 5.8$ *mm and* $d = 10.4$ *mm*

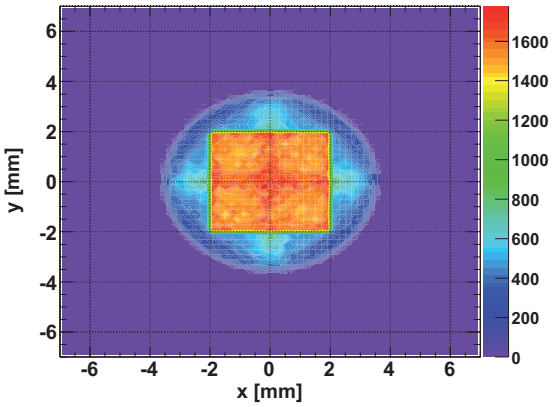

(c) *CsI(Tl): 4 x 4 x 10* mm^3*, generation point inside CsI(Tl) at* $x = 0$ *mm and* $y = 0$ *mm, reflector:* $\oslash = 7.0$ *mm and* $d = 10.4$ *mm*

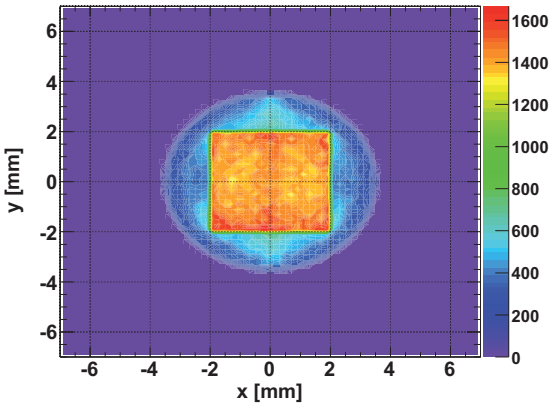

(d) *CsI(Tl): 4 x 4 x 10* mm^3*, generation point inside CsI(Tl) at* $x = 0$ *and* $y = 1.98$ *mm, reflector:* $\oslash = 7.0$ *mm and* $d = 10.4$ *mm*

Figure 6.55.: *Distribution of the hits at the SDD entrance window for cylindrical ((a) and (b)) and cubical ((c) and (d)) CsI(Tl) scintillators with a rough surface (sa = 0.06 rad). The photons are generated inside the CsI(Tl) scintillator, which is wrapped into a specular reflector with a reflectance of 0.98 and an air gap of several 100 µm between scintillator and reflector.*

the fact, that the scintillator symmetry is reduced.

Fig. 6.55 shows the hits distribution of scintillation photons at the SDD-scintillator interface for cylindrical and cubical shaped CsI(Tl) scintillators with a surface roughness of sa = 0.06 rad, wrapped into a specular reflector with a reflectivity of 0.98 and an air gap between scintillator and reflector. Compared to the histograms in Fig. 6.53 the hits are distributed more homogeneously in case of a rough scintillator surface. This is the case, especially for cylindrical scintillators.

The number of trapped scintillation photons is reduced to a large extent, which is shown by the reduction of the number of reflections in the range 90° - 124° and the

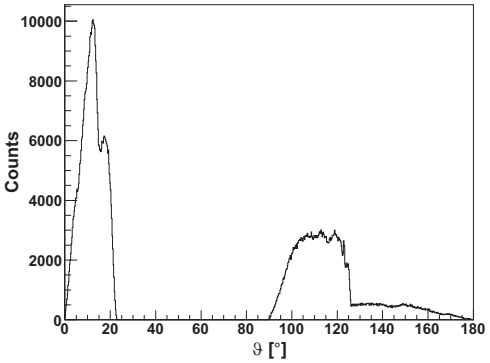

(a) *CsI(Tl): ⊘ = 4.5 mm and d = 10 mm, generation point inside CsI(Tl) at x = 0 mm and y = 0 mm, reflector: ⊘ = 5.8 mm and d = 10.4 mm*

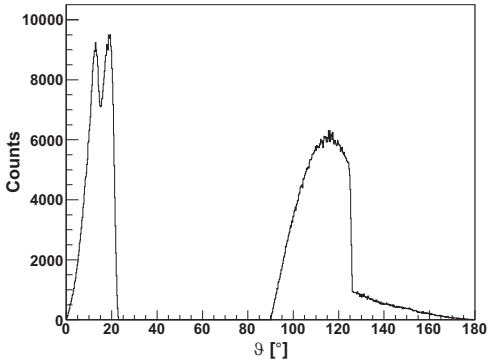

(b) *CsI(Tl): ⊘ = 4.5 mm and d = 10 mm, generation point inside CsI(Tl) at x = 0 and y = 2.23 mm, reflector: ⊘ = 5.8 mm and d = 10.4 mm*

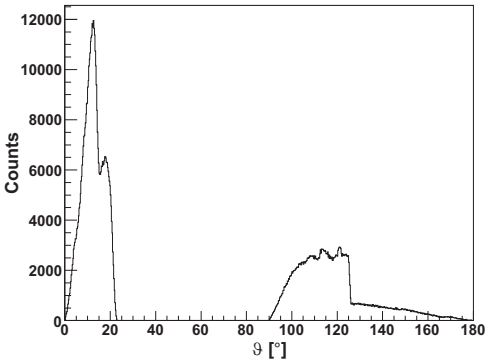

(c) *CsI(Tl): 4 x 4 x 10 mm^3, generation point inside CsI(Tl) at x = 0 mm and y = 0 mm, reflector: ⊘ = 7.0 mm and d = 10.4 mm*

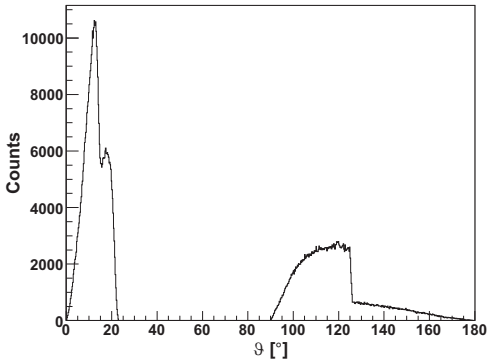

(d) *CsI(Tl): 4 x 4 x 10 mm^3, generation point inside CsI(Tl) at x = 0 and y = 1.98 mm, reflector: ⊘ = 7.0 mm and d = 10.4 mm*

Figure 6.56.: *Angle distribution of transmitted scintillation photons ($\vartheta = 0° - 23°$) and number of reflections ($\vartheta = 90° - 180°$) at the SDD-CsI(Tl) interface with respect to the SDD surface normal. The photons are generated inside a cylindrical ((a) and (b)) or a cubical ((c) and (d)) CsI(Tl) scintillator with a rough surface (sa = 0.6 rad), which is wrapped into a specular reflector with the reflectance 0.98 and an air gap of several 100 µm between scintillator and reflector.*

increase of the transmitted photons in Fig. 6.56 compared to the values in Fig. 6.54. The value of η changes from (a) to (d) in the Fig. 6.56 from 0.80, 0.82, 0.85 and 0.85 respectively. The relative improvement of the light collection efficiency and its homogeneity is larger for cylindrical CsI(Tl) scintillators with rough surfaces, but the absolute values are better for cubical CsI(Tl) scintillators with the same surface roughness.

Results from measurements, which are illustrated in Fig. 6.57, confirm the assumptions drawn from results of simulations, that an increasing surface roughness of the scintillator, increases the number of transmitted photons. Independent on

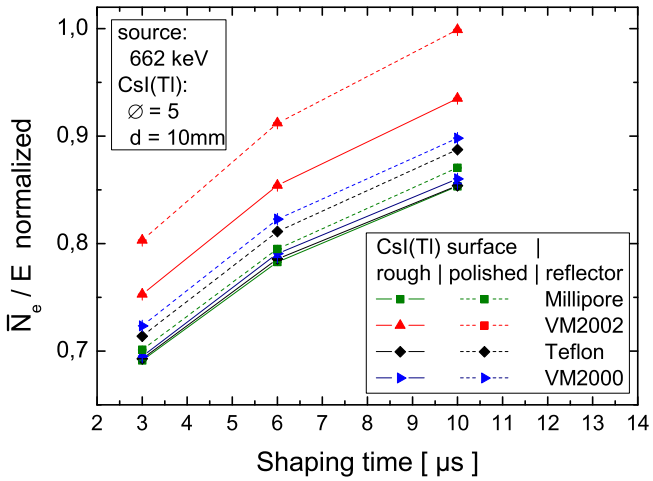

Figure 6.57.: *Normalized measured number of signal electrons, $\overline{N}_e/E$, for E = 662 keV with different reflectors and two kinds of surface roughness. VM2000, VM2002 and specular side of Millipore paper are specular reflectors, whereas Teflon is a diffuse reflector.*

the fact, whether the reflector is specular or diffuse, an increase of the scintillator surface roughness leads to an increase of the system quantum efficiency, hence to a larger number of signal electrons per keV, N_e/E.

The effect of the light and charge collection efficiency and homogeneity onto the spectrum generated by incident γ-rays with an energy of E = 662 keV onto a bare CsI(Tl) scintillator or wrapped into a reflector is illustrated in Fig. 6.58. The simulated spectra is similar to the measured spectra in Fig. 6.15. Also the measured and simulated ratios of the number of signal electrons from the detector system with and without a reflector are close to each other. The ratio determined from measurement is 2.2 and the ratios determined from simulations are 2.1 for sa = 0.04 rad and 2.6 for sa = 0.1 rad. Increasing the surface roughness by increasing the value sa, leads to a better resolution, but also to the loss of a larger fraction of scintillation photons, if the scintillator is not wrapped into a reflector. The differences between the measured (Fig. 6.15) and simulated (Fig. 6.58) spectra result from the fact, that only the contribution of the light and charge collection are included in the simulations. Other noise sources are disregarded here.

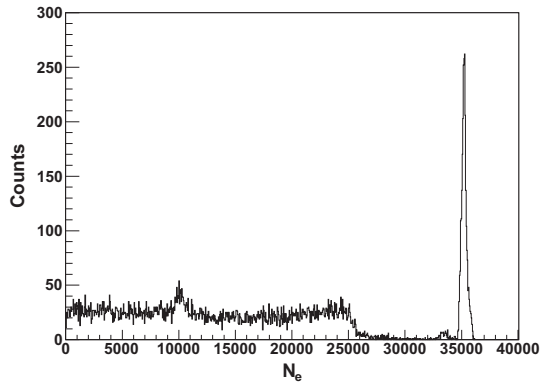

(a) *diffuse reflector, surface roughness sa = 0.04 rad*

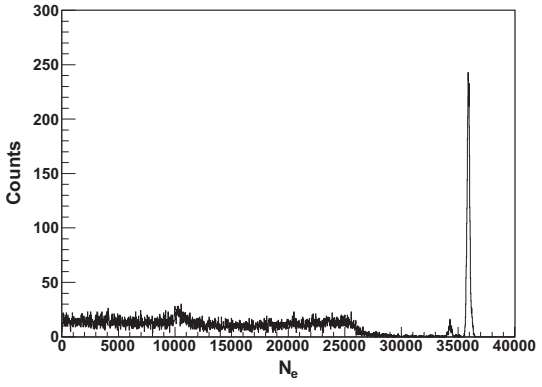

(b) *diffuse reflector, surface roughness sa = 0.1 rad*

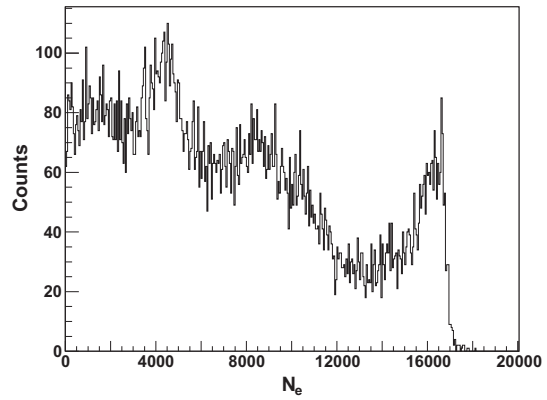

(c) *no reflector, surface roughness sa = 0.04 rad*

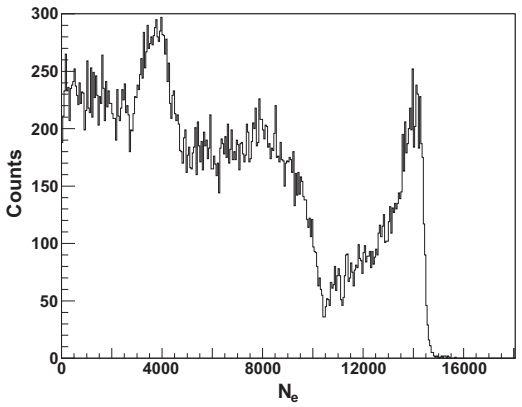

(d) *no reflector, surface roughness sa = 0.1 rad*

Figure 6.58.: *Simulated spectra in number of signal electrons after irradiation of a cylindrical CsI(Tl) scintillator, ⌀ = 4.5 mm and d = 10 mm, with 662 keV γ-rays. The scintillator is wrapped into a reflector with a reflectivity of 0.98.*

Effect of the light and charge collection

Detector parameters, which affect the contributions R_η and R_{Bino} to the energy resolution and the system quantum efficiency, η, for scintillation photons, are the surface roughness of the scintillator, the reflector type and reflectivity, the absorption length for scintillation photons inside the scintillator and the quantum efficiency of the SDD.

SDD + $LaBr_3$(Ce)

The $LaBr_3$(Ce) scintillator is wrapped into a teflon reflector and vacuum sealed inside an aluminum housing with a 3 mm thick glass window. The coupler is an optical grease (d = 100 μm) with a refraction coefficient of $n_{grease} = 1.46$. Between scintillator and reflector is an infinitesimal thin air gap. The dimensions of the

cylindrical scintillator are: a diameter of ⊘ = 5 mm and a thickness of 10 mm. The measured absorption length of UV-Vis photons in $LaBr_3$(Ce) up to 360 nm is

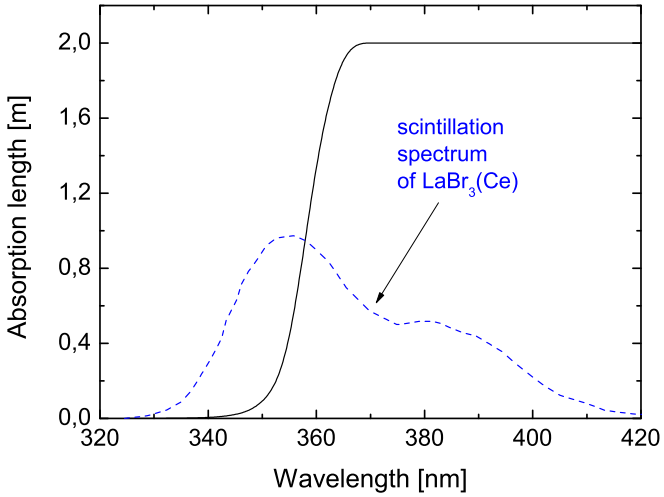

Figure 6.59.: *Measured absorption length of $LaBr_3$(Ce) up to photon wavelengths of 360 nm from [99]. The absorption length is set to 2 m for wavelengths larger than 370 nm. The dashed line is the normalized scintillation spectrum of $LaBr_3$(Ce) [68].*

presented in [99]. It is illustrated in Fig. 6.59. For wavelengths larger than 370 nm the values have been set to 2 m.

The light yield of $LaBr_3$(Ce) is set to 55 photons per keV for γ-rays with an energy of 122 keV in the following simulations to match the measured number of signal electrons. The scintillator distributor stated that the light output of our $LaBr_3$(Ce) sample is about 90 % of the nominal value.

Fig. 6.60 shows the simulated values of the energy resolution, R_η, and the number of signal electrons per keV, $\overline{N}_e/E[keV]$, in dependence of the degree of scintillator surface roughness, sa, and the reflectivity of the diffuse reflector, for the absorption length illustrated in Fig. 6.61. The value $\overline{N}_e/E[keV]$ has been measured for two cylindrical $LaBr_3$(Ce) scintillators. For incident γ-rays of 122 keV the mean number of measured signal electrons per keV is 21 or 23. Values with $\overline{N}_e/E(122\text{keV}) = 17$ to 23 N_{ph}/keV have an energy resolution in the range $R_\eta = 0.02$ to 0.06 for γ-rays with an energy of 122 keV. Reducing the $LaBr_3$(Ce) scintillator surface roughness from sa = 0.14 to 0.06 rad or the reflectivity of the reflector from 0.98 to 0.87 degrades the energy resolution and reduces the number of signal electrons drastically. R_η and $\overline{N}_e/E$ change only slightly, if the light yield is increased from $\overline{L} = 55$ to 60 N_{ph}/keV.

The energy dependent energy resolution, $R_\eta(E)$, and the mean number of signal electrons per keV, $\overline{N}_e/E[keV]$, are presented in Fig. 6.61 for a surface roughness of sa = 0.1, a diffuse reflectivity of 0.96 and 0.98 and an energy dependent mean light yield of $\overline{L}(662\text{keV}) = 55$ N_{ph}/keV. $R_\eta(E)$ decreases with increasing γ-energies up to 40 keV and remains almost constant, if the energy is increased above 40 keV. The decrease of the $R_\eta(E)$ up to 40 keV originates from the fact, that the absolute

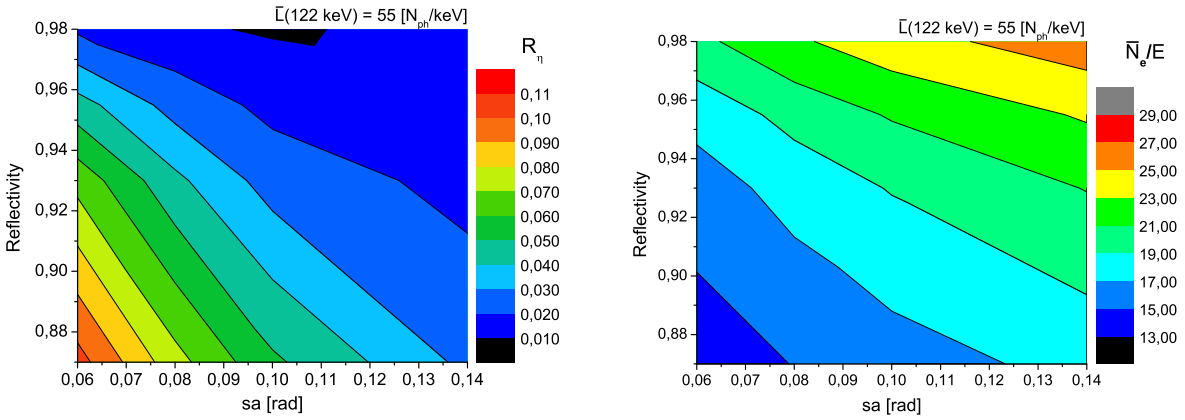

(a) *energy resolution* (b) *signal electrons per keV*

Figure 6.60.: *Results of the energy resolution, R_η, and the mean number of signal electrons per keV, $\overline{N}_e/E$, for the cylindrical $LaBr_3(Ce)$, $\oslash$ = 5 and d = 10 mm, plotted against the surface roughness, sa, and the reflectivity of the diffuse reflector. The light yield is $\overline{L}$ = 55 N_{ph}/keV for the incident 122 keV γ-rays. The absorption length is illustrated in Fig. 6.59.*

number of photons increases with an increasing γ-energy. For energies larger than 40 keV the absorption depth range of γ-rays inside the scintillator is larger. This leads to larger fluctuations of the collection efficiency of scintillation photons, so that $R_\eta(E)$ does not decrease further for energies larger than 40 keV. $R_{Bino}(E)$ decreases with increasing energy and approaches the value of $R_\eta(E)$ at 662 keV, but it remains for all energies larger. A reduction of the reflectivity from 0.98 to 0.96 leads to an

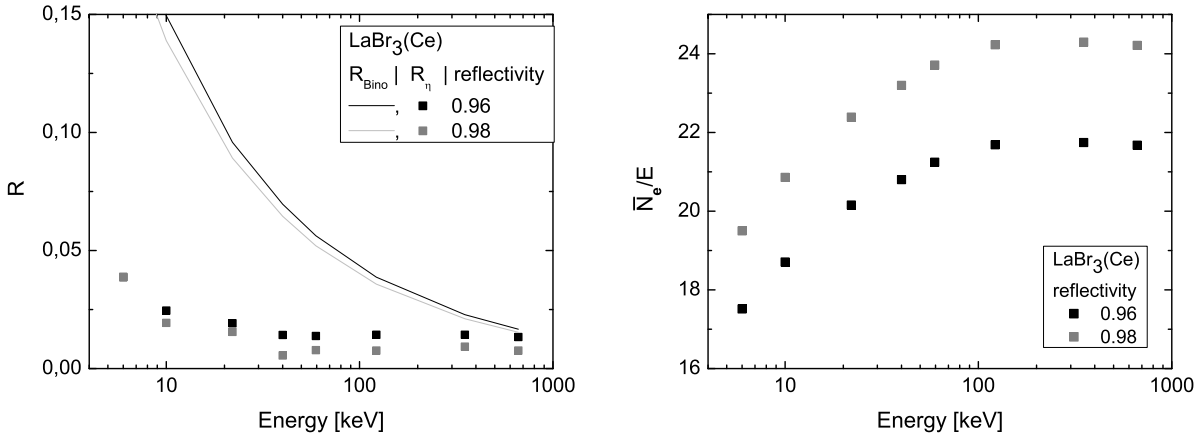

Figure 6.61.: *Simulated values of $R_\eta(E)$ and mean number of signal electrons per keV, $\overline{N}_e/E$, for the absorption length given in Fig. 6.59, a surface roughness of sa = 0.1 rad, a diffuse reflectivity of 0.96 and 0.98 and an energy dependent light yield with $\overline{L}$(662keV) = 55 photons/keV.*

increase of $R_\eta(E)$ by a factor up to two and to a reduction of the system quantum efficiency, $\overline{\eta}$, by about 12 %. $\overline{\eta}$ remains almost constant in the energy range 6 - 662

keV, due to the small scintillator thickness and the high reflectivity of the reflector.

Simulations show that, if $LaBr_3$(Ce) is directly coupled onto the SDD entrance window, without a 3 mm glass window in between, R_η and the system quantum efficiency, η, are improving slightly.

To further optimize the detector performance, the $LaBr_3$(Ce) scintillator has to be coupled directly onto the SDD and the SDD quantum efficiency has to be increased in the range between 300 nm to 400 nm as supposed in Sec. 5.5.2.

SDD + CsI(Tl)

In the following, the effect of the light and charge collection on the energy resolution and the mean number of signal electrons per keV, inside the detector system consisting of a SDD coupled to CsI(Tl) are investigated by Monte Carlo Simulations. The coupler is an optical pad (100 μm) and grease (40 μm) with refraction coefficients of $n_{pad} = 1.41$ and $n_{grease} = 1.46$. Between scintillator and reflector is an air gap of several 100 μm.

Fig. 6.62 shows R_η and $\overline{N}_e/E$ for the cylindrically and cubically shaped CsI(Tl), plotted against the surface roughness, sa, and reflectivity of the diffuse reflector. The absorption length of the scintillation light is set to 2 m inside CsI(Tl). The measured mean number of signal electrons per keV for γ-energies of $E = 122$ keV measured with the cylindrical CsI(Tl) and including the ballistic deficit, due to the long scintillation decay time in CsI(Tl), is about 56 $\overline{N}_e/E[keV]$. Removing the loss of signal electrons from ballistic deficit, which is about 5 %, results into a value of 59 $\overline{N}_e/E[keV]$. This value, in combination with a surface roughness of sa ≥ 0.1 and a reflectivity of about 0.98, corresponds to a R_η(122 keV) value of maximal 0.01 (Fig. 6.62(a)) in case of a cylindrical scintillator. The dependence of R_η(122 keV) and $\overline{N}_e/E$(122 keV) in Fig. 6.62(a) and 6.62(b) on the CsI(Tl) surface roughness is not as strong as for the γ-detector composed of the $LaBr_3$(Ce) scintillator and SDD shown in Fig. 6.60.

R_η(122 keV) and N_e/E(122 keV) for cubical CsI(Tl) scintillators with a face of 4 x 4 mm^2 and a thickness of d = 10 mm are better and higher (Fig. 6.62(c) and 6.62(d)) compared to the cylindrical scintillator for the same set of parameters. At 122 keV the measured value of 57 $\overline{N}_e/E[keV]$, which is about 60 without ballistic deficit, corresponds to a value of R_η(122 keV) of maximal 0.005. There is also almost no dependence of R_η(122 keV) and $\overline{N}_e/E[keV]$(122 keV) on the CsI(Tl) surface roughness for the cubical scintillator. R_η(122 keV) becomes actually slightly worse for reflectivity values below 0.94 and for an increasing CsI(Tl) surface roughness above sa = 0.06 rad.

R_η(122 keV) and $\overline{N}_e/E[keV]$(122 keV) depend stronger on a change of the reflectivity than on a change of the surface roughness in the illustrated range.

For incident γ-rays of 122 keV Fig. 6.63 and 6.64 show values of R_η and R_{Bino} and the system quantum efficiency, $\overline{\eta}$, as a function of the absorption length and scintillator surface roughness for a diffuse reflector with a reflectivity of 0.98. The scintillator thickness is 10 mm. R_η decreases strongly for cylindrically shaped CsI(Tl) scintillators for increasing values of the absorption length from 0.2 to 1 m and increases slightly up to 8 m (Fig. 6.63 on the left). R_η decreases slightly for cubically shaped CsI(Tl) scintillators for absorption lengths in the range from 0.2 to 1 m and remains

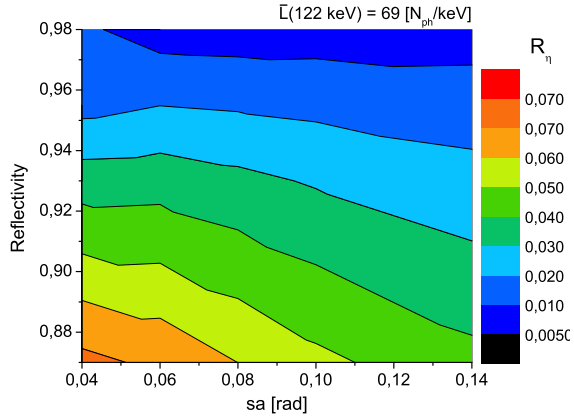

(a) *energy resolution, CsI(Tl): ⊘ = 4.5 and d = 10 mm*

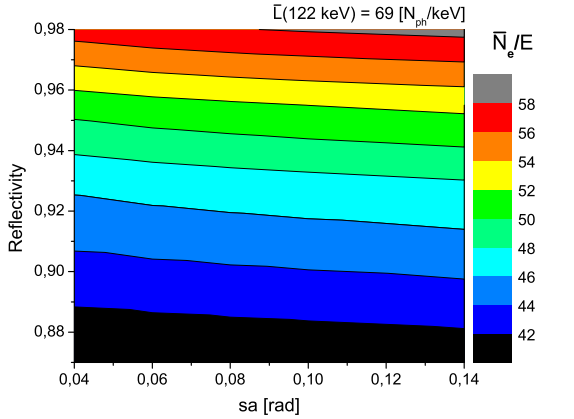

(b) *signal electrons per keV, CsI(Tl): ⊘ = 4.5 and d = 10 mm*

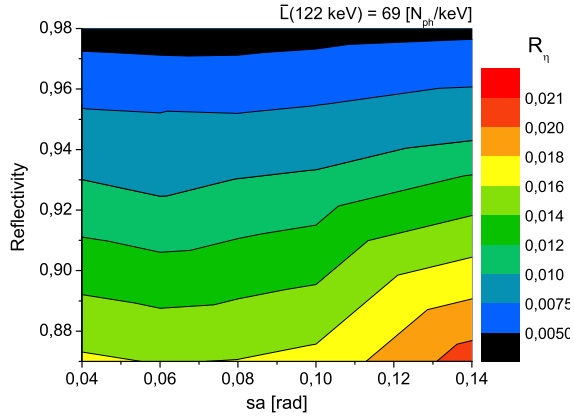

(c) *energy resolution, CsI(Tl): 4 x 4 x 10 mm^3*

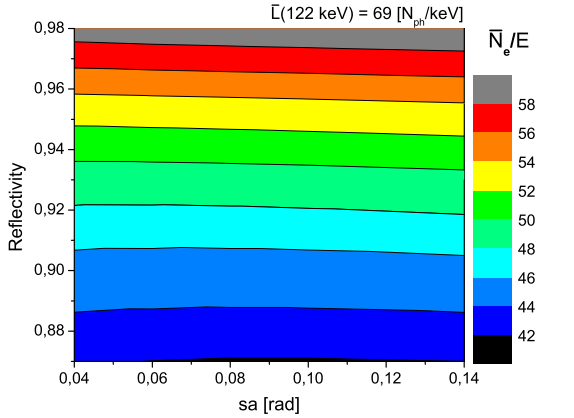

(d) *signal electrons per keV, CsI(Tl): 4 x 4 x 10 mm^3*

Figure 6.62.: *Results of R_η(122 keV) and $\overline{N}_e/E$(122 keV) from Monte Carlo simulations for cylindrical ((a) and (b)) and cubical ((c) and (d)) CsI(Tl) scintillators plotted against the surface roughness, sa, and reflectivity of the diffuse reflector. The absorption length is set to 2 m and the light yield for the incident photons to $\overline{L}$(122 keV) = 69 keV.*

constant up to 8 m. R_η of the cubically is smaller compared to the cylindrically shaped scintillator especially for absorption lengths smaller than 1 m, due to the fact, that scintillation photons have to travel longer distances inside the cylindrically shaped scintillator before being absorbed inside the SDD. This circumstance makes this system more sensitive on the position where scintillation photons are generated.

$\overline{\eta}$ increases up to an absorption length of 2 m and remains almost constant for higher values (Fig. 6.63 on the right). $\overline{\eta}$ is larger for the cubically compared to the cylindrically shaped CsI(Tl) scintillator. From an absorption length of 2 m to lower values, the difference of the system quantum efficiency between cubically and cylindrically shaped CsI(Tl) increases. This is because scintillation photons have to travel longer distances inside the cylindrically shaped scintillator before reaching the SDD.

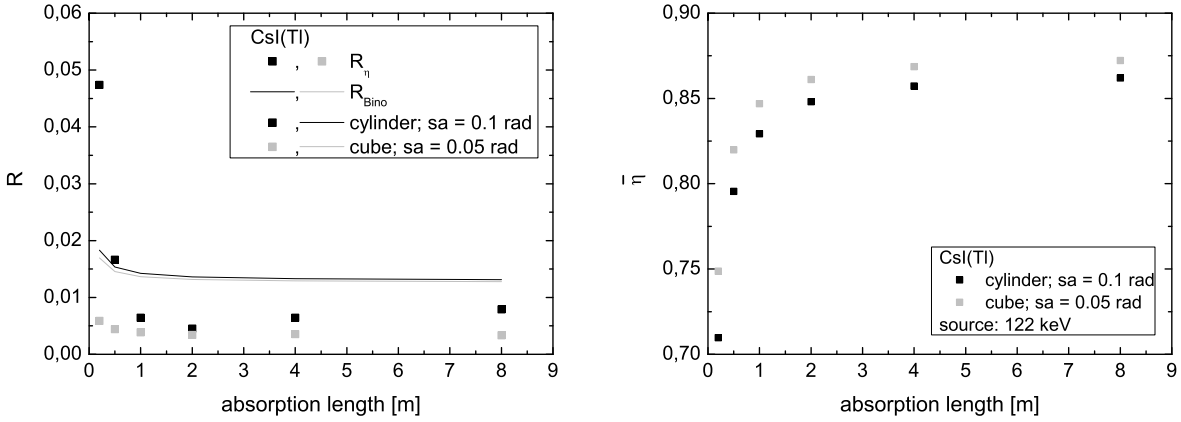

Figure 6.63.: *Effect of the absorption length of scintillation light in CsI(Tl) on the energy resolution, R_η, and quantum efficiency of the system, η, for incident γ-rays of E = 122 keV. The CsI(Tl) scintillator is cylindrical or cubical with the dimensions ⊘ = 4.5 mm and d = 10 mm or 4 x 4 x 10 mm^3. The reflector is diffuse with a reflectivity of 0.98.*

R_{Bino} is almost constant for absorption lengths in the range from 0.2 to 8 m and it is larger than R_η, except for the case, where the cylindrical CsI(Tl) scintillator has absorption lengths of 0.2 m and 0.5 m.

In Fig. 6.64 the parameter of the surface roughness, sa, of CsI(Tl) is varied and the absorption length is kept constant at 2 m. R_η for the cylindrically shaped

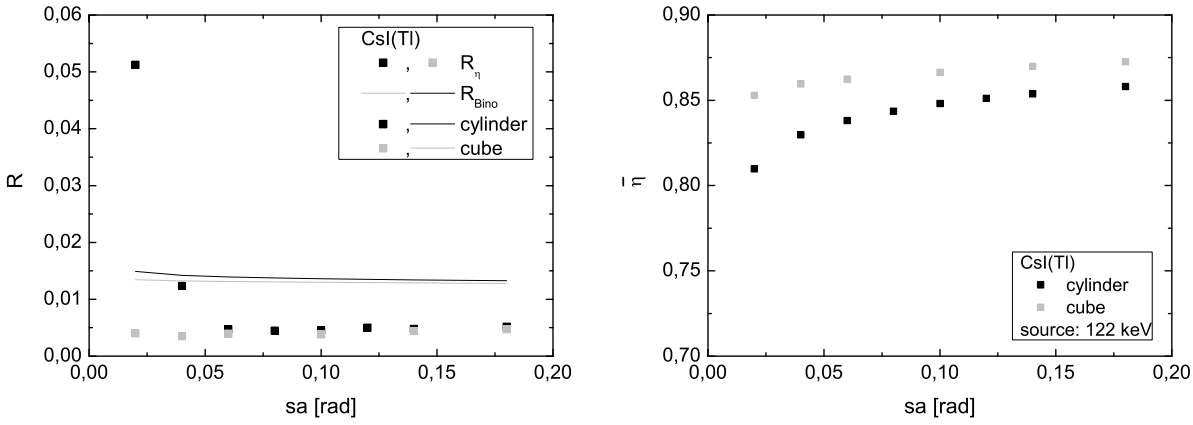

Figure 6.64.: *Effect of the degree of surface roughness, sa, on the energy resolution, R_η, and quantum efficiency of the system, η, for incident γ-rays of E = 122 keV. The CsI(Tl) scintillator has an absorption length of 2 m and it is cylindrical or cubical with the dimensions ⊘ = 4.5 mm and d = 10 mm or 4 x 4 x 10 mm^3. The reflector is diffuse with a reflectivity of 0.98.*

CsI(Tl) scintillator decreases with an increasing value of sa until sa = 0.06 rad and

remains almost constant, if the value of sa is increased further. For cubically shaped CsI(Tl) scintillators R_η remains almost constant for all illustrated values of surface roughness and it is equal to the values of cylindrically shaped CsI(Tl) for sa $\geq$ 0.06 rad. For sa $<$ 0.06 rad the light collection is more homogeneous inside cubically shaped CsI(Tl) scintillators, because the angular distribution of scintillation photons on the scintillator walls do not depend on their generation position compared to cylindrically shaped scintillators.

R_{Bino} is almost constant for all illustrated values of surface roughness and it is larger than R_η except for the cylindrical CsI(Tl) scintillator with a surface roughness of sa $<$ 0.04 rad.

$\overline{\eta}$ increases slowly with increasing surface roughness and it is larger for the cubically shaped scintillator. The ascending slope of $\overline{\eta}$ is larger for cylindrically than for cubically shaped scintillators. This results from a lower number of trapped scintillation photons in cubical compared to cylindrical scintillators, which has also been investigated in Sec. 6.2.2.

For an absorption length larger than 1 m, a surface roughness of the scintillator, sa $\geq$ 0.06 rad and a reflectivity of the diffuse reflector of 0.98 coupled to the SDD results into small contributions of R_η and R_{Bino} with values of about 0.005 and 0.015 for incident γ-rays of 122 keV.

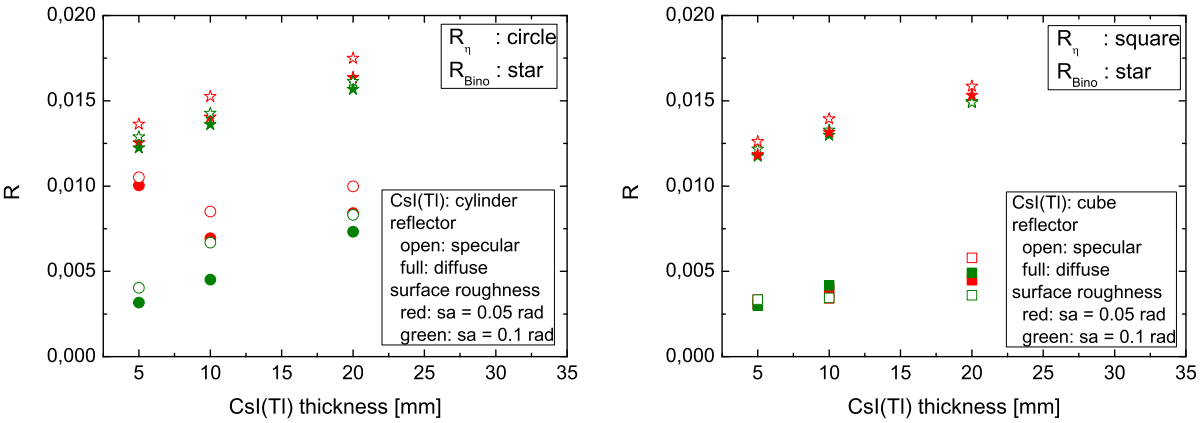

Figure 6.65.: *Simulations of $R_{Bino}(E)$ and $R_\eta(E)$ for SDD + CsI(Tl), with an absorption length of l = 2 m for scintillation photons in CsI(Tl), a light yield of $\overline{L}$(122 keV) = 69 photons/keV, a reflector reflectivity of 0.98 and a source of 122 keV.*

In Fig. 6.65 and 6.66 simulated results of $R_\eta(E)$, $R_{Bino}(E)$ and $\overline{N}_e(E)/E$ for incident γ-rays of 122 keV are analyzed as a function of scintillator surface roughness, thickness, shape and reflector type. The CsI(Tl) scintillators with an absorption length of 2 m are cylindrically shaped with a diameter of $\oslash$ = 4.5 mm or cubically shaped with a face of 4 x 4 mm^2 and thicknesses of 5 mm, 10 mm and 20 mm. The values of R_{Bino} and R_η increase from 5 mm to 20 mm thickness for the cylindrically and cubically shaped scintillator, except for the cylindrically shaped scintillator with a surface roughness of sa = 0.05 rad the value of R_η has a minimum at a scintillator thickness of 10 mm. Increasing the surface roughness from sa = 0.05 rad to sa = 0.1

rad improves the resolution in most cases. This improvement is largest for R_η of the system with the cylindrical scintillator with a thickness of 5 mm. The cubical CsI(Tl) scintillator has for both degrees of scintillator surface roughness, sa = 0.05 rad and 0.1 rad, lower values of R_{Bino} and R_η than the cylindrical one. The differences of R_{Bino} and $R_\eta(E)$ between the two surface roughnesses are not as pronounced for the cubically as for the cylindrically shaped CsI(Tl). The diffuse reflector yields usually slightly better resolutions than the reflector with the specular surface. For γ-rays with an energy of 122 keV the value of R_{Bino} is larger than the value of R_η.

A diffuse reflector and a larger surface roughness improves the energy resolution slightly for the cylindrically shaped scintillator. For the cubically shaped scintillator the improvement is smaller.

The results presented in Fig. 6.65 show the same tendencies as the measured dependencies of the energy resolution shown in Fig. 6.16.

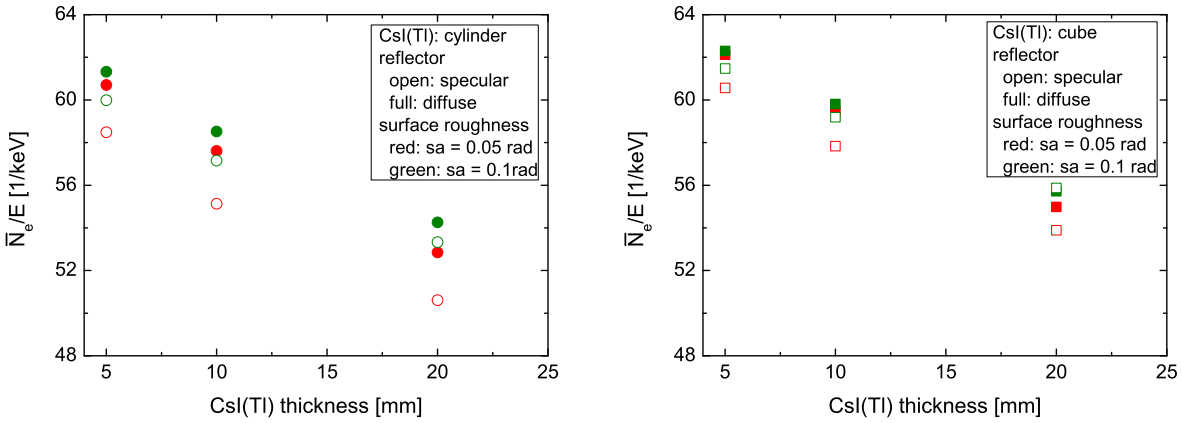

Figure 6.66.: *Simulations of $\overline{N}_e(E)/E$ for SDD + CsI(Tl), with an absorption length of l = 2 m for scintillation photons in CsI(Tl), a light yield of $\overline{L}(122\ keV)$ = 69 photons/keV, a reflector reflectivity of 0.98 and a source of 122 keV.*

In Fig. 6.66 the mean numbers of signal electrons per keV, $\overline{N}_e(E)/E$, are plotted against the thickness for cylindrical (on the left) and cubical CsI(Tl) (on the right). The value of $\overline{N}_e(E)/E$ reduces by about 10 % for an increase of the scintillator thickness from 5 to 20 mm. The cubical CsI(Tl) yields a slightly higher value of $\overline{N}_e(E)/E$ by about 1 to 2 signal electrons per keV compared to cylindrical CsI(Tl). The reflector with the rough surface is more efficient in the light collection and leads to a higher number of signal electrons $\overline{N}_e(E)/E$ than the one with the specular surface. These differences are decreasing with increasing surface roughness from sa = 0.05 rad to 0.1 rad of CsI(Tl).

The reason for the difference in $R_\eta(E)$, $R_{Bino}(E)$ and $\overline{N}_e(E)/E$ between cylindrical and cubical scintillators is that scintillation light has to travel longer paths, which includes more reflections, due to the geometry, until reaching the SDD. The probability of being absorbed in a cylindrical scintillator is higher and the scintillator and reflector surface become more important, because reflections are occurring more often. The scintillator absorption length, geometry and surface roughness, the

reflector type and reflectivity and the quantum efficiency of the SDD are parameters, which determine the light collection and its influence on R_η, R_{Bino} and $\overline{N}_e(E)/E$.

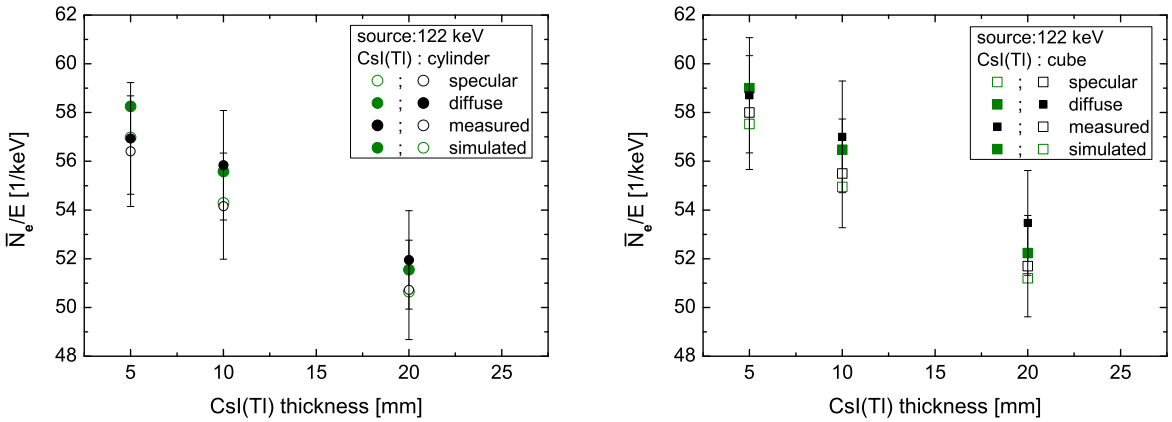

Figure 6.67.: *Results of $\overline{N}_e/E$ from measurements and simulations of cylindrically ($\oslash$ = 4.5 mm) and cubically (4 x 4 mm^2) shaped CsI(Tl) scintillators wrapped into a diffuse or specular reflector with a reflectivity of 0.98. The parameters of the absorption length and CsI(Tl) surface roughness are set to l = 2 m and sa = 0.1 rad. The light yield of CsI(Tl) is $\overline{L}$(122 keV) = 69 photons/keV. A ballistic deficit of 5 % has been assumed.*

The number of signal electrons per keV, $\overline{N}_e(E)/E$, from simulations and measurements for different scintillator lengths are presented in Fig. 6.67. These simulations include the loss of signal electrons, due to ballistic deficit of about 5 % at a shaping time of 12 μs, due to the long decay time of scintillation light in CsI(Tl). The measured number of signal electrons per keV, $\overline{N}_e(E)/E$, is in good agreement with the results from simulations within the error bars, so that the validity of our detector model, which is used in the simulations, can be confirmed. The values of the quantum efficiency of the system, $\overline{\eta}$, for scintillation photons is plotted in Fig. 6.68 for the three CsI(Tl) thicknesses. $\overline{\eta}$ is almost constant in the energy range 6 keV - 662 keV, because of the small scintillator sizes and large absorption length of scintillation light inside CsI(Tl), the high reflectivity of the reflector and the high quantum efficiency of the SDD entrance window.

The energy dependent relative energy resolutions, $R_{Bino}(E)$ and $R_\eta(E)$, for three cylindrical CsI(Tl) scintillators with an absorption length of 2 m, a scintillator surface roughness of sa = 0.1 rad and thicknesses of d = 5 mm, 10 mm and 20 mm respectively are illustrated in Fig. 6.69 on the left. R_{Bino} decreases with increasing energy and is larger for thicker scintillators. R_{Bino} is larger than $R_\eta(E)$ up to energies of 300 keV. $R_\eta(E)$ decreases for increasing energies up to 60 keV and increases, if the energy is increased further for scintillators with a thickness of 10 mm and 20 mm. This originates from an increase of the absorption depth range of γ-rays inside CsI(Tl) for γ-rays with an increasing energy and thicker scintillators, which enable the absorption in a larger volume.

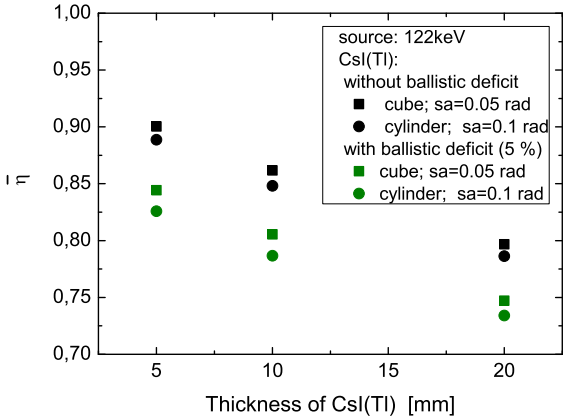

Figure 6.68.: *Simulated values of $\overline{\eta}$ for the system SDD coupled to cylindrical ($\oslash$ = 4.5 mm) or cubical (4 x 4 mm^2) CsI(Tl) scintillators with thicknesses of d = 5, 10 and 20 mm respectively and wrapped into a diffuse reflector with a reflectivity of 0.98. Green circles and squares are values, where the ballistic deficit of 0.05 of signal electrons is included. sa is the degree of surface roughness in rad. The mean light yield of CsI(Tl) is set to $\overline{L}$(122 keV) = 69 photons/keV.*

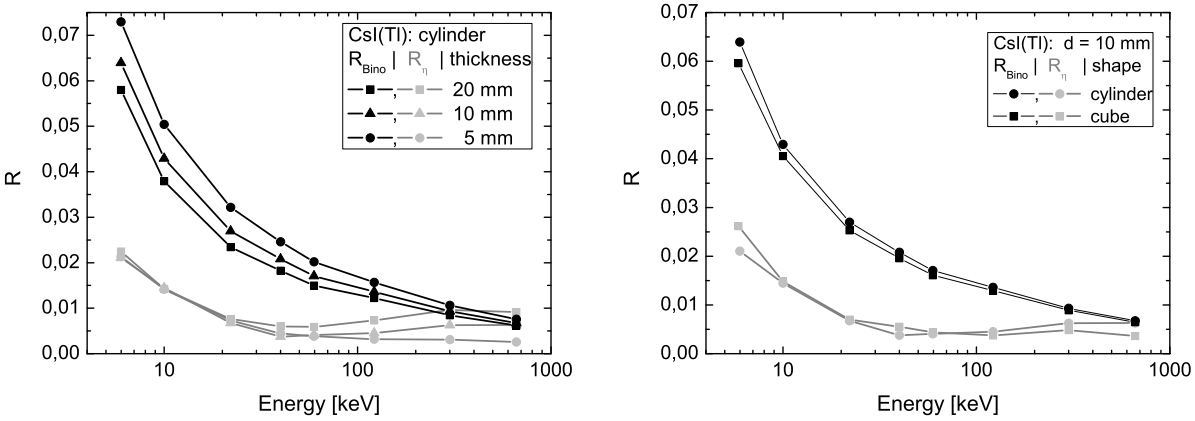

Figure 6.69.: *Simulated values of $R_{Bino}(E)$ and $R_\eta(E)$ as a function of the γ-energy, inside the system SDD coupled to the cylindrical CsI(Tl) scintillator (on the left) with the dimensions, $\oslash$ = 4,5 mm and d = 10 mm, an absorption length of 2 m, a degree of surface roughness of sa = 0.1 rad and a diffuse reflector with a reflectivity of 0.98. In the right figure the values of $R_{Bino}(E)$ and $R_\eta(E)$ for 10 mm thick cylindrical and cubical CsI(Tl) (4 x 4 mm^2) are illustrated.*

Fig. 6.69 on the right shows the energy dependence of R_{Bino} and $R_\eta(E)$ for a cylindrical and cubical CsI(Tl) scintillator with a thickness of 10 mm. For the cubical CsI(Tl) scintillator R_{Bino} is slightly better.

For the detector system CsI(Tl) + SDD the values of R_{Bino} and R_η are smaller compared to the contribution from the light yield non-proportionality, R_T (see Sec. 6.2.1).

The best detector performance for a detector system consisting of a single SDD coupled to CsI(Tl) or $LaBr_3(Ce)$ can be achieved for a SDD with a high quantum efficiency of ≥ 0.9, a cubical scintillator as thin as possible with a rough surface, wrapped into a diffuse reflector with a high reflectivity of ≥ 0.98. Furthermore the absorption length of scintillation photons should be larger than 1 m inside the scintillator. There should also be the possibility to couple the scintillator directly onto the SDD entrance window.

6.2.3. Total energy resolution and its contributions

The relative energy resolution, $R(E)$, of the detector system scintillator coupled to an SDD can be described by Eq.

$$R(E) \approx 2.35\sqrt{R^2_{Fano-Scint} + R^2_T + R^2_\eta + R^2_{Bino} + R^2_{el}}, \tag{6.34}$$

which has been derived and discussed in Sec. 4.1.

Fig. 6.70 shows the relative energy resolution, $R(E)$, and its contributions in the energy range from $E = 22$ to 662 keV for the detector system consisting of a cylindrical $LaBr_3(Ce)$ scintillator with a diameter of $\oslash = 5$ mm and a thickness of d = 10 mm coupled to a SDD. Due to the fact, that the Fano factor of $LaBr_3(Ce)$ is

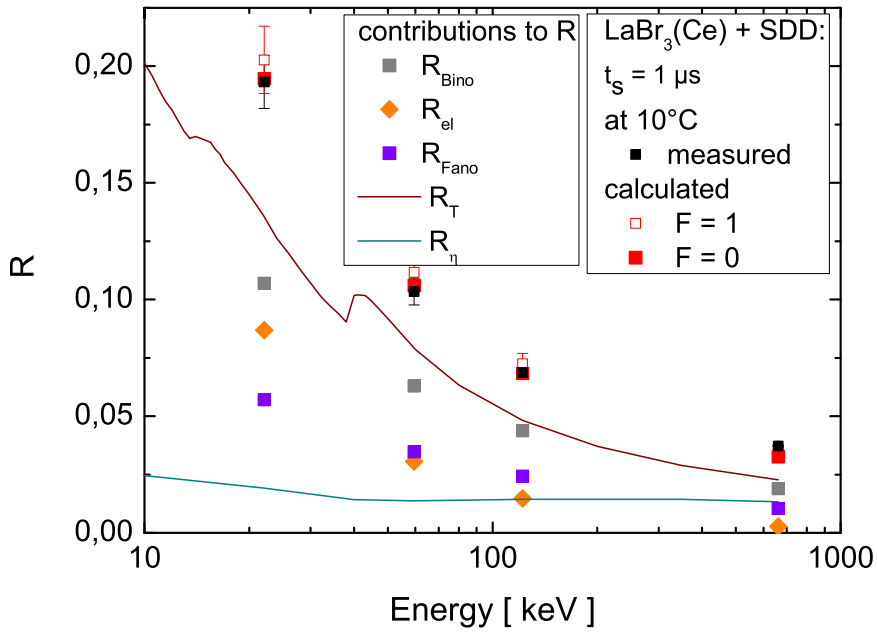

Figure 6.70.: *Calculated and measured energy resolution, $R(E)$, of $LaBr_3(Ce)$ + SDD (30 mm^2) and its contributions. R_{Fano} has been calculated for $F = 1$ and $\overline{w} = 13$ eV.*

not known yet, its value has been set to 0 and 1, so that the effect on the calculated value of $R(E)$ (black open circles in Fig. 6.70) can be visualized. The measured (black squares in Fig. 6.70) and the calculated values of $R(E)$ are in good agreement within the error bars. R_η has the lowest contribution to the energy resolution for energies E $<$ 122 keV and for larger energies it remains almost constant. The electronic noise contribution, R_{el}, has the lowest value of all noise contributions for energies E $\geq$ 122 keV. R_{el} can be reduced by cooling the detector to moderate temperatures, especially for low energies. The contribution of the binomial term, R_{Bino}, to the energy resolution is in the energy range from 22 keV to 662 keV below the contribution of the light yield non-proportionality, whereas their difference becomes smaller to higher energies. For the detector type SDD + $LaBr_3$(Ce) the dominant contributions to the energy resolution are R_T and R_{Bino}. Increasing the quantum efficiency of the SDD in the energy range 300 to 400 nm as supposed in Sec. 5.5.2 would reduce R_{Bino}.

In Fig. 6.71 the values of the energy resolution, $R(E)$, and its contributions are plotted against the γ-energy for the detector system consisting of a cylindrical CsI(Tl) scintillator with a diameter of $\oslash$ = 4.5 mm and a thickness of d = 10 mm coupled to a SDD.

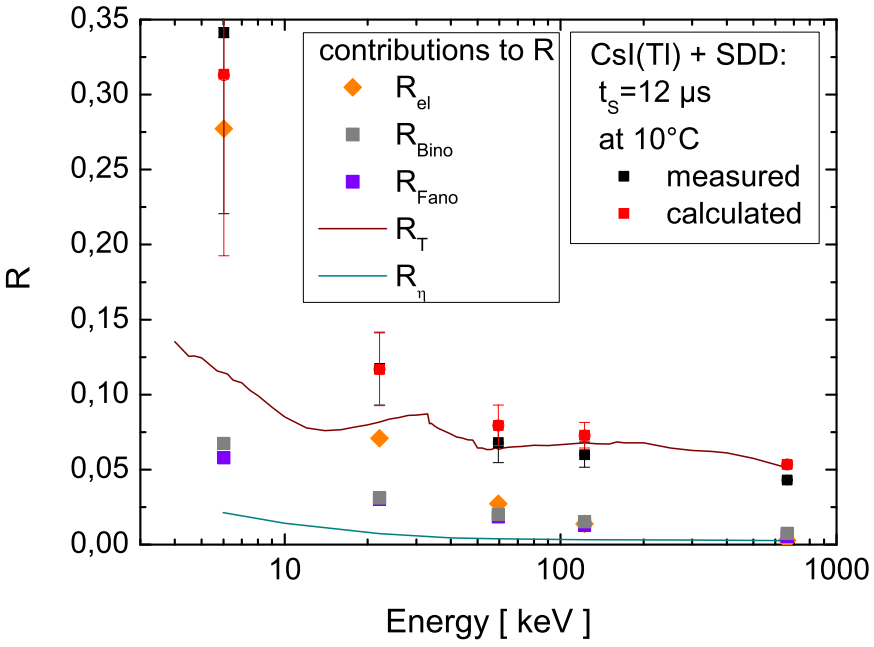

Figure 6.71.: *Calculated and measured energy resolution, $R(E)$, of CsI(Tl) + SDD (30 mm^2) and its contributions. R_{Fano} has been calculated for $F = 0.28$ and $\overline{w} = 14$ eV.*

The measured and calculated values of the energy resolution are in good agreement within the error bars. The contribution of the inhomogeneous light and charge collection, R_η, to the energy resolution is over the whole energy range the smallest contribution. The contributions of $R_{Fano-CsI}$ and R_{Bino} are larger than that of R_η.

The electronic noise contribution, R_{el}, becomes larger than $R_{Fano-CsI}$ and R_{Bino} for energies E $\leq$ 60 keV and larger than R_T for energies E $\leq$ 22 keV. R_{el} can be reduced to values below R_T over the whole energy range, if the detector is cooled to from 10°C to - 20°C. For the detector type SDD + CsI(Tl) the main contribution to the energy resolution originates from the non-proportional light yield of CsI(Tl).

In this chapter we could show that the non-proportional light yield is the main reason for the energy dependent degradation of the energy resolution. The origins of the non-proportional light yield of scintillators are of physical nature. Their impact can be influenced by increasing the crystal quality, because of a reduction of impurity concentration, by changing the doping concentration of the fluorescence ions and by co-doping [125, 126].

The other contributions to the energy resolution, except of $R_{Fano-Scint}$, can be optimized by improving the SDD entrance window and choosing the appropriate scintillator geometry, surface roughness and reflector type. These parameters have been already optimized for the SDD + CsI(Tl) detector, but there is still room to improve the $LaBr_3$(Ce) + SDD detector.

In order to improve the resolution of the detector system SDD + scintillator the most important task will be to develop scintillators with a high and almost proportional light yield. These would be scintillators with a smaller band gap and much higher and similar mobilities of electrons and holes, so that on the one hand the diffusion from regions with high ionization densities is fast enough to avoid Auger like quenching and on the other hand to reduce the separation distance of electrons and holes. Recently developed scintillators with a more proportional light yield are SrI_2(Eu) and $LaBr_3$(Ce) co-doped with Sr [25, 126].

7. Spectroscopy and imaging with SDD array/pnCCD + CsI(Tl) detectors

In this chapter we investigate the detector response of γ-ray cameras, consisting of a SDD array/pnCCD coupled to a scintillator. Results from measurements with a 77 cell SDD array + CsI(Tl) γ - detector are used to define the parameters for the Monte Carlo simulations. It is examined by simulations how a change of detector parameters affects the energy and spatial resolution. SDD array + CsI(Tl) detectors have been developed for energies of several 10 keV up to 300 keV. For this detector type the radiation is incident from the scintillator side.

The performance of a detector consisting of a pnCCD coupled to a CsI(Tl) is studied by Monte Carlo simulations, in order to find appropriate detector parameters, which make it possible to expand the excellent detector performance of a pnCCD with respect to the quantum efficiency, energy and spatial resolution up to 150 keV. In this case the detector system is irradiated from the pnCCD side to allow also the detection of X-rays down to 1 keV.

7.1. Principles of the Anger γ-camera

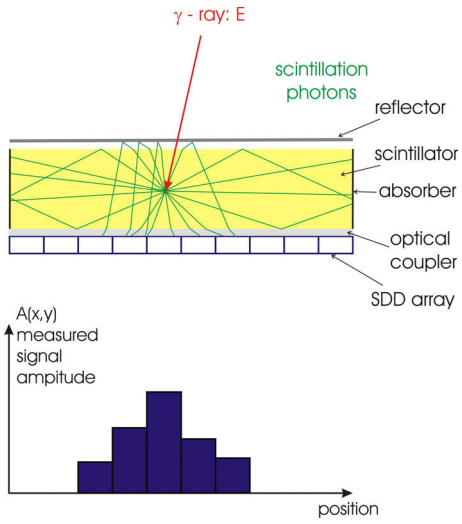

Figure 7.1.: *Setup of the Anger camera consisting of a continuous scintillator coupled to an SDD array.*

From the generation point, where the incident γ-ray deposits a part or its total energy inside the scintillator, scintillation photons are propagating isotropically in

all direction (Fig. 7.1). The aspect ratio of the scintillator, which is the cross section over the thickness, has to be large (>> 1), in order to assure an exact reconstruction of the position, where scintillation photons have been generated. A large aspect ratio reduces the interaction of scintillation photons on the scintillator side faces. This favors a distribution of scintillation photons on the SDD array/pnCCD with the maximum number inside the closest pixels below the generation point and a decreasing number inside pixels with an increasing distance (Fig. 7.1). This is because of a decreasing solid angle covering the area of a pixel at larger distances from the generation point (Fig. 7.2 blue). Also the ratio of scintillator thickness to the cross section of the pixel is very important, because it determines, together with the scintillator surface roughness and reflectivity, the distribution of scintillation photons and the number of pixels, which register a signal above the data acquisition (DAC) threshold.

A small scintillator thickness compared to its cross section, a diffuse Lambertian reflector on top of the scintillator, so that reflection is favored perpendicular to the scintillator top face, and absorbing paint of the scintillator side faces improve the collection of scintillation photons, because they are focused onto the pixels close to the generation point. A focus of scintillation photons on a lower number of pixels increases the signal to electronic noise ratio, hence the energy and spatial resolution. A low electronic noise level is very important, because it determines the height of the DAC threshold.

Nevertheless, a high fraction of photons is lost, due to the fact, that scintillation photons propagating from the generation point into the direction of the side faces are absorbed there (Fig. 7.2 dark yellow) and because of totally reflected photons on the detector entrance window.

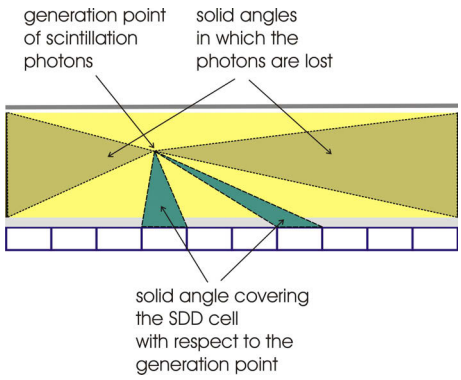

Figure 7.2.: *Dark yellow areas: scintillation photons inside these solid angles are lost, due to absorption on the scintillator side walls. Yellow areas: scintillation photons have a certain probability to penetrate into the SDD. Blue areas: solid angle covering one SDD cell for two distances from the generation point of the scintillation light.*

The depth of the generation point of scintillation light inside the scintillator is also a crucial parameter, because it defines the number of SDD cells over which scintillation photons are distributed.

If the γ-energy exceeds 200 keV (Fig. 2.1) the probability of Compton scattering in CsI or $LaBr_3$ is greater than the cross section for photo effect. For Compton

scattered γ-rays there is the probability of a second interaction via Compton or photo effect, so that one incident γ-ray could generate scintillation photons in two or more positions inside the scintillator. This complicates the reconstruction of the interaction points.

The intrinsic spatial resolution is defined as the full width at half maximum, FWHM, of a Gaussian fit through the spatial distribution of the reconstructed positions, (x,y), where scintillation photons have been generated. The intrinsic spatial resolution is denoted as $\widetilde{R}_i$.

In this work we investigate the energy and intrinsic spatial resolution of Anger γ-cameras, consisting of an SDD array of 77 hexagonal cells coupled to a 5 mm thick CsI(Tl) scintillator (Sec. 7.2).

If an image of an extended object, which emits γ-rays into several directions, is required, a collimator has to be placed in front of the scintillator. The collimator serves as an objective, which generates a projection of the object inside the scintillator. In App. E two types of collimators and their contribution to the spatial resolution are introduced.

7.2. 77 cells SDD array + CsI(Tl) γ-camera

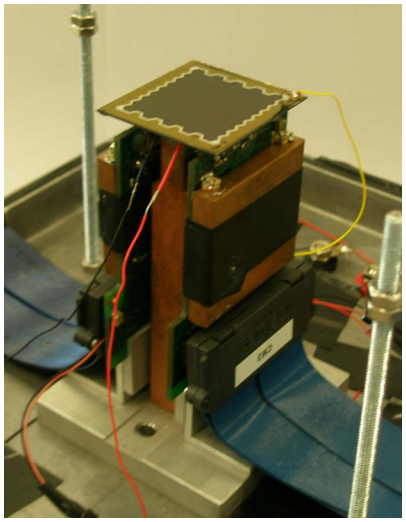

Figure 7.3.: *Bare 77 cell SDD array detector with front end electronics and a heat dissipater made of copper.*

SDD arrays of different shapes and sizes with anti-reflection coatings coupled to one CsI(Tl) scintillator have been developed for γ-ray imaging [127, 128, 129, 130, 131]. Such an Anger camera could be interesting in different fields such as medical application, astrophysics or as a monitor for the radiation inside a fusion plasma. The focus of these γ-detectors has been more on the imaging than on spectroscopy in the past. The benefits of SDD compared to PMT arrays are the monolithic integration of several SDD cells with a fill factor close to 100 %, lower bias voltages, a low sensitivity to magnetic fields and a quantum efficiency of QE > 0.6 compared to QE < 0.45 for PMTs ([132]). These advantages in combination with

more compact SDD arrays result in a better intrinsic spatial resolution of an Anger camera consisting of a SDD instead of a PMT array coupled to a scintillator. The lower electronic noise value of SDDs is furthermore an advantage compared to diode arrays. A very good intrinsic spatial resolution can be achieved with a relatively low number of photodetector cells, reducing the electronic complexity and costs compared to direct semiconductor γ-ray detectors such as CdTe, which need a high number of small pixels to achieve the same spatial resolution.

The investigated γ-ray Anger camera consists of a monolithic SDD array with 77 hexagonal cells (Fig. 7.3) and a total area of 2.9 cm $\cdot$ 2.6 cm = 7.6 cm^2. Each cell has a diameter of $\oslash$ = 3.2 mm and an area of 8.7 mm^2. The SDD array

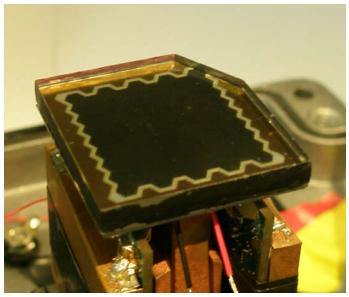

Figure 7.4.: *77 cell SDD array detector coupled to a 5 mm thick CsI(Tl) scintillator.*

is coupled to a CsI(Tl) scintillator with a thickness of 5 mm (Fig. 7.4), which covers all SDD cells. The absorbed fraction of the incident radiation in dependence on the energy is illustrated in Fig. 7.5. More than 50 % of the incident γ-rays with an energy of 200 keV are absorbed inside the 5 mm thick CsI scintillator. The

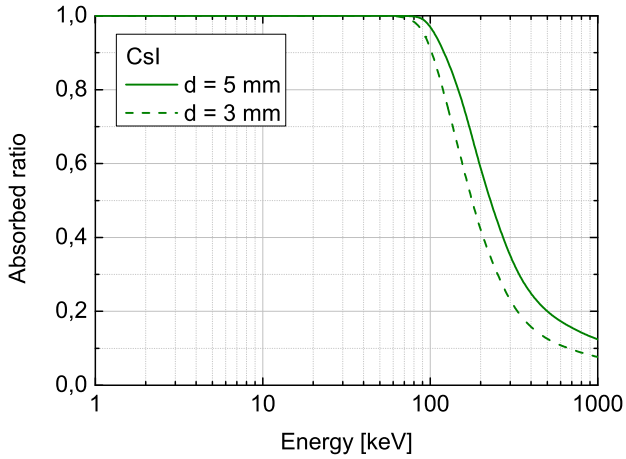

Figure 7.5.: *Absorbed fraction of the incident photons inside CsI with a thickness of 5 and 3 mm.*

scintillator has a polished surface. Its top face is covered with Millipore paper, which serves as a diffuse reflector. The side facets are painted black to absorb incident scintillation photons. This improves the accuracy of the reconstructed position of the generation point, especially close to the side faces. CsI(Tl) is the first choice

as a scintillator, because it has a high light yield, it is not hygroscopic, thus easy to handle and the spectrum of the scintillation photons covers an energy range for which the SDD quantum efficiency can reach a maximum value. Drawbacks are the relatively long decay times of the generated scintillation light and the afterglow. $LaBr_3$(Ce) is a faster scintillator with a similar light output, but the SDD has a lower quantum efficiency for scintillation photon from $LaBr_3$(Ce). It is also more difficult to handle, because it is hygroscopic. A brighter scintillator is SrI_2(Eu) with an emission maximum at 435 nm and a light yield of 115 photons/keV at 662 keV [133]. But this scintillator is also hygroscopic and can be handled only in dry atmosphere.

The entrance window of the SDD array has been optimized for scintillation light from CsI(Tl) and it is covered by a protective layer with a thickness of several μm, which reduces the quantum efficiency of the entrance window for wavelength below 700 nm. The quantum efficiency is shown in Fig. 7.6 for photons incident under an angle of 0 ° from the air on the left and from CsI(Tl) on the right.

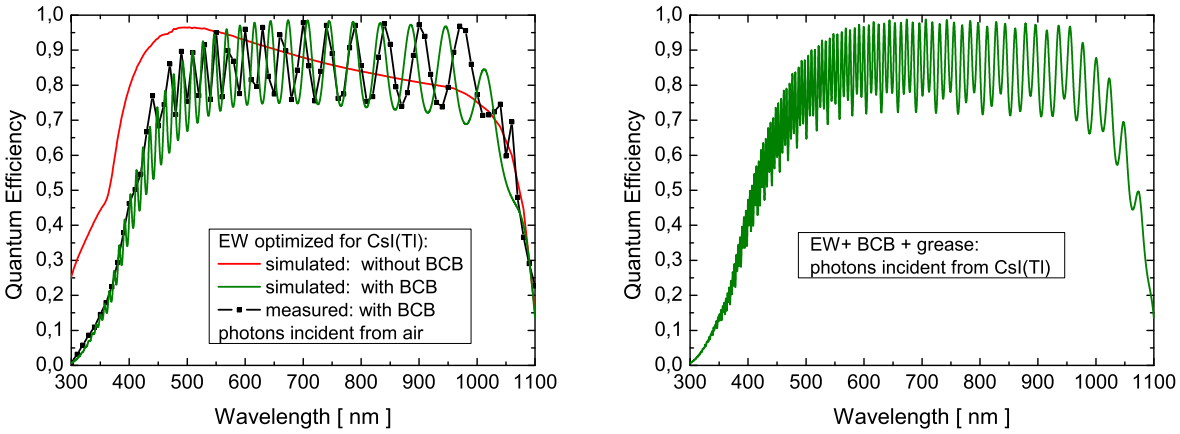

Figure 7.6.: *Quantum efficiency at room temperature for photons incident perpendicular onto the ARC-Window, which is optimized for light around 500 nm, with an additional protective layer (BCB) on top with a thickness of about 4000 nm. Photons incident from the air (on the left) and from CsI(Tl), which is coupled with optical grease to the SDD entrance window (on the right).*

The front end electronics consist of two boards with 5 application-specific integrated circuits (ASICs) on each board. On each ASIC there are 8 channels with a preamplifier, pole zero regulator, a Gaussian shaper with four possible shaping times (peaking time: 1.6, 2, 4, 6 μs), a baseline holder and a peak stretcher (Fig. 7.7). The preamplifier gain can be set to two values, low and high gain. The value of the high gain is twice the value of the low gain. There is also a shift register with the possibility to set the threshold for the data acquisition, above which incoming signals are accepted. The analog outputs of the 8 channels are multiplexed to one single output. The analog signals are then converted into digital signals by 5 two channel analog to digital converters (ADCs) of 2^{14} bits. Each ADC converts the output signals from two ASICs. The control signals are provided by 3 programmable

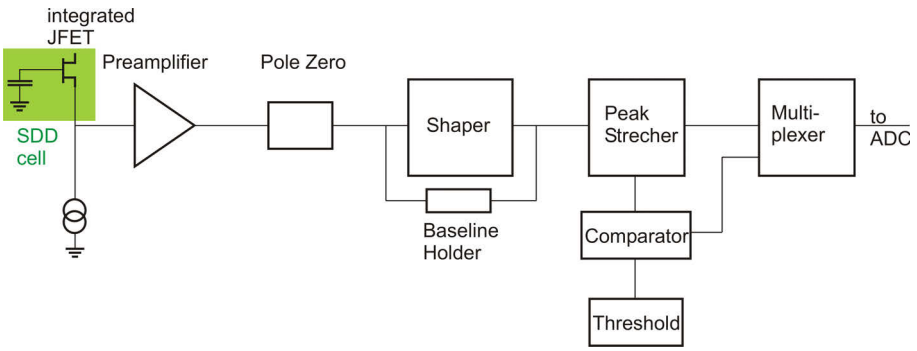

Figure 7.7.: *Schematics of the front end electronics, which is integrated onto the 8 channel ASIC, which processes the signals of 8 SDD cells.*

logic devices (CPLDs) and transferred to the PC via a USB 2 interface. The front end electronics and the data acquisition system have been developed by a group at Politecnico di Milano and INFN Milano [134, 129].

The electronic noise is limited to a value of about $\mathrm{ENC}_{el} = 15$ electrons per SDD cell at - 10°C, due to a not yet optimized front end electronics and data acquisition system.

7.2.1. Spatial and energy resolution at 60 and 122 keV

The data acquisition (DAC) threshold has been set for each SDD cell individually, which is in the range from 200 to 350 ADC channels in low gain mode. The conversion from the ADC channel number, N_{ch}, to the number of signal electrons, N_e, is given by [135]

$$N_e = N_{ch} \cdot \frac{1}{g} \tag{7.1}$$

where $g \approx 3.41$ is in the low gain and $g \approx 6.82$ in the high gain mode. Thus the DAC threshold is in the range from 60 to 100 electrons. In order to reduce events generated by electronic noise, only events are accepted, where at least 3 SDD cells register signal electrons above DAC threshold. To reduce ballistic deficit measurements have been performed with the maximal available peaking time of 6 μs, which corresponds to a shaping time of about 3 μs. This results into a ballistic deficit of about 20 % for scintillation light from CsI(Tl).

Fig. 7.8 shows drawings of the two measurement setups.

The detected number of signal electrons in each SDD cell after the interaction of a 59.5 keV γ-ray photon with the CsI(Tl) scintillator is presented in Fig. 7.9. Several SDD cells register a signal above the DAC threshold. The maximal number of signal electrons registered in one SDD cell is about 120.

The reconstruction for the lateral interaction positions of γ-rays with the scintillator is first calculated with the center of gravity method from the measured response (Fig. 7.9) of the 77 SDD cells, yielding (x_S,y_S). Then the values of the measured response are compared with results from Monte Carlo simulations within a grid of $\pm$ 1 mm around (x_S,y_S) and the whole scintillator thickness of 5 mm. A range of $\pm$ 1 mm around (x_S,y_S) has been chosen to limit the calculation time. The response of the 77 SDD cells has been simulated for scintillation photons propagating

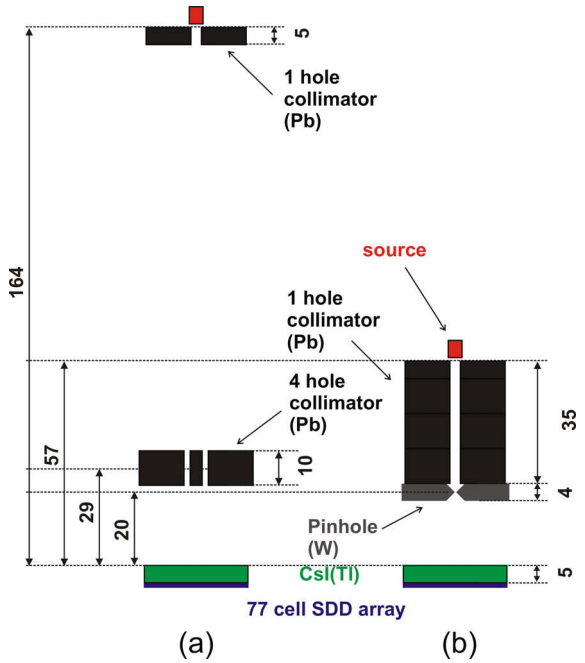

Figure 7.8.: *Drawing of the measurement setup. The 4 holes in the lead (Pb) collimator have a diameter of 0.5 mm and are located at the corners of a square with 4 mm side length. The one hole Pb collimators have a hole diameter of 2 mm. The pinhole in the tungstate (W) plate is 0.22 mm in diameter.*

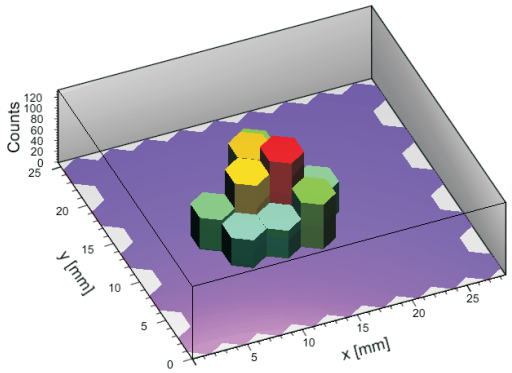

Figure 7.9.: *Measured response of the 77 SDD cells in number of signal electrons after the interaction of a 59.5 keV γ-ray photon. The drawing of the measurement setup is illustrated in Fig. 7.8 b.*

isotropically from the positions defined by the grid with a step size of 100 μm in x, y and 500 μm in z direction. The 3 dimensional position of the interaction point, $p_r(x_r,y_r,z_r)$, is determined by searching the minimum of

$$argmin_{p(x,y,z)} \left(\sum_{i=1}^{77} |A_i - A_{i,sim,p}| \right) \rightarrow p_r \tag{7.2}$$

where p is the positions inside the raster around (x_S,y_S), A_i the measured and $A_{i,sim,p}$ the simulated number of generated signal electrons inside the SDD cell i.

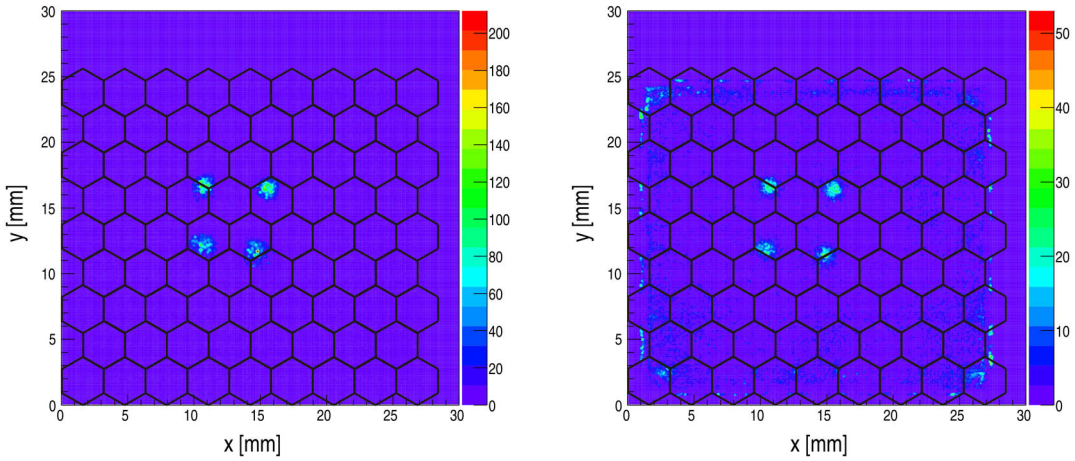

Figure 7.10.: *Image of the ^{241}Am (on the left) and ^{57}Co source (on the right) in the 4 hole collimator configuration illustrated in Fig. 7.8 a.*

Histograms of the reconstructed interaction points (x_r, y_r) of γ-rays from a ^{241}Am (on the left) and a ^{57}Co source (on the right) inside the scintillator CsI(Tl), are illustrated in Fig. 7.10 for the setup with the 4 hole collimator (Fig. 7.8 a). The diameter of the sources are 1 mm for ^{241}Am and 4 mm for ^{57}Co. The image of Fig. 7.10 on the right, results after irradiation with a ^{57}Co source and has more events originating from electronic noise, than the image of Fig. 7.10 on the left, because of a much lower activity of the ^{57}Co source. The events detected close to the scintillator side surfaces originate most probably from the interaction with γ-rays, which passed the Pb collimator ($\oslash$ = 30 mm) and interacted with the scintillator close to its side face. Also positions of events are reconstructed in this area where x_r and y_r coordinates are outside the 77 cell array. If the reconstruction is performed with the center of gravity method only, the reconstructed positions of events close to the scintillator border are shifted relatively to the real position into the direction of the detector center. The reason why there are no events at the border of the scintillator is that x_r or y_r has a maximum distance of 1 mm to x_s or y_s.

Histograms of the coordinates, x_r and y_r, of the reconstructed interaction points for the measurement setup with the pinhole with a diameter of 0.22 mm (Fig. 7.8 b) are presented in Fig. 7.11. The FWHMs of the Gaussian fits through the histograms yield a spatial resolution of about $\widetilde{R} \approx 1.1$ mm for the irradiation with the ^{241}Am and ^{57}Co sources. The total spatial resolution, $\widetilde{R}$, is larger than the intrinsic spatial resolution, $\widetilde{R}_i$, of the detector, due to the additional contribution of the source, collimator and scintillator geometry and distances.

Fig. 7.12 shows additionally the depth of the interaction point of incident γ-rays with the scintillator. γ-rays from ^{241}Am and ^{57}Co sources have mainly the energies E = 59.5 keV and 122 keV. Approximately all of the incident γ-rays with an energy of 59.5 keV are absorbed within the first 2 mm of the CsI(Tl) scintillator in contrast to γ-rays with an energy of 122 keV, which are absorbed over the whole scintillator thickness of 5 mm.

The relative energy resolutions for γ-rays with an energy of 59.5 keV (^{241}Am), 88 keV (^{109}Cd) and 122 keV (^{57}Co) determined from measurements are R(59.5 keV)

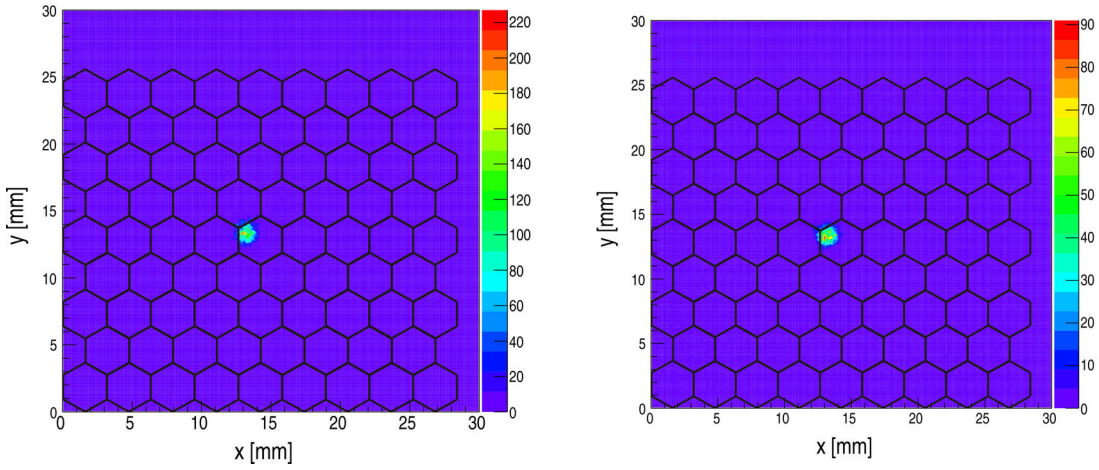

Figure 7.11.: *Image of the ^{241}Am (on the left) and ^{57}Co source (on the right) in the pinhole configuration illustrated in Fig. 7.8 b.*

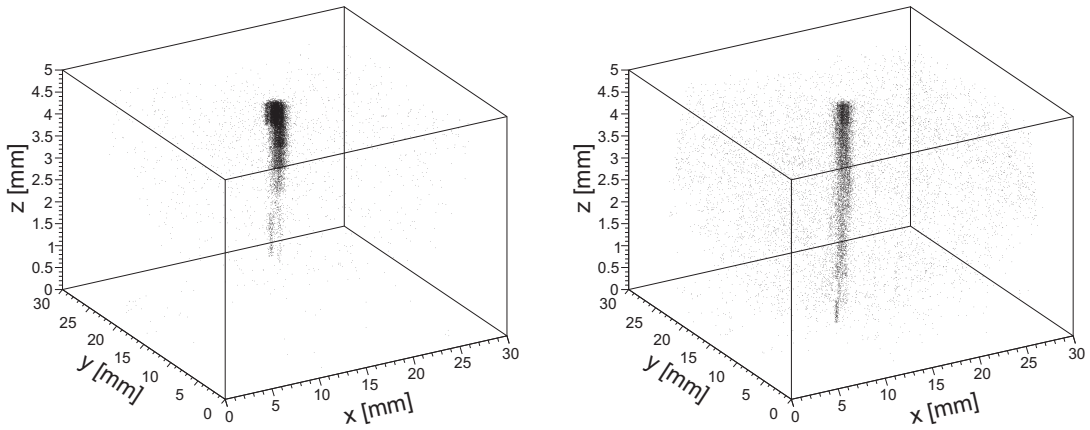

Figure 7.12.: *Reconstructed interaction points in three dimensions for ^{241}Am on the left and ^{57}Co source on the right. γ-rays of the ^{57}Co source penetrate deeper into the CsI(Tl) scintillator illustrated in Fig. 7.8 b.*

= 0.33 - 0.37, R(88 keV) = 0.31 - 0.34 and R(122 keV) = 0.36 - 0.41. The measured spectra of ^{241}Am, ^{109}Cd and ^{57}Co are illustrated in Fig. 7.13 and 7.14. The photo peak generated by the 122 keV photons (^{57}Co) is not Gaussian like. The reason for this deviation is discussed later in this section. In Fig. 7.13 there are partially visible peaks at lower energies than the photo peaks at 59.5 and 88 keV. In case of the spectrum generated by the ^{241}Am source the partially visible peak belongs to the escape peak and in case of the irradiation with ^{109}Cd it is the photo peak generated by the 22 keV γ-rays of the ^{109}Cd source. Fig. 7.14 shows the total pulse height distribution, if the detector is irradiated with a ^{57}Co source. Aside from the photo peak generated by the 122 and 136 keV γ-rays, there is also a shoulder or a peak at lower energies, which originates most probably from Pb X-ray fluorescence photons from the Pb collimator (75 keV) and γ-rays interacting close to the side

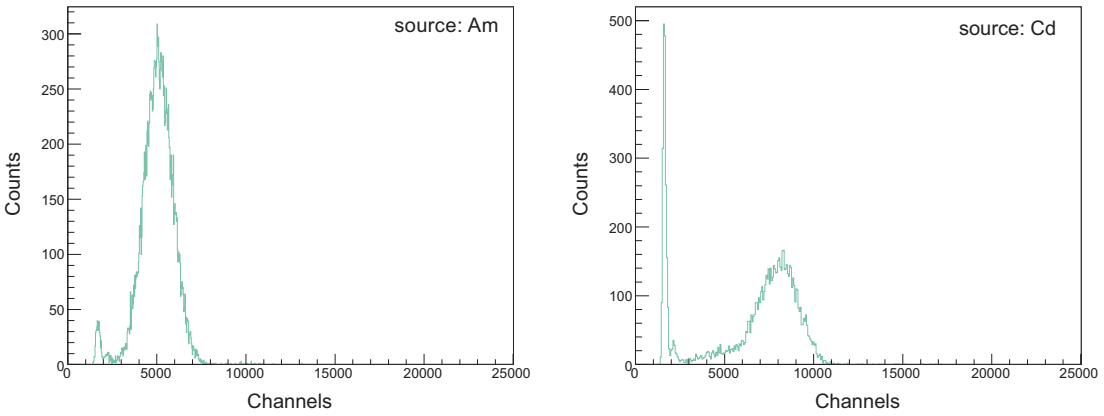

Figure 7.13.: *Measured pulse height distribution for the irradiation of the detector in the measurement setup illustrated in Fig. 7.8 (b) with ^{241}Am (on the left) and ^{109}Cd (on the right).*

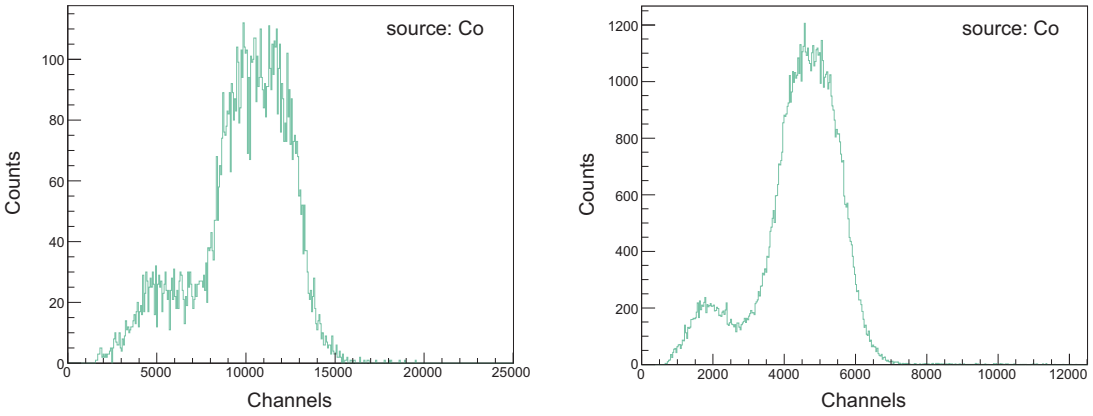

Figure 7.14.: *Histogram on the left: measured pulse height distribution for the irradiation with ^{57}Co in the measurement setup illustrated in Fig. 7.8 b. Histogram on the right: measured pulse height distribution for the irradiation with ^{57}Co and a similar measurement setup, but without the pinhole. The source is 10 mm closer to the detector. Also the gain of the preamplifier is 0.5 times the gain of the left histogram.*

faces of the scintillator, where a large number of scintillation photons are absorbed, due to the black coating. Also the high threshold for signal acceptance alters the shape of the spectrum. Measured results of the spatial resolution for γ-rays with an energy of 59.5 keV and the energy resolution for γ-rays with energies of 59.5 keV, 88 keV and 122 keV for the system 77 cell SDD array + 5 mm thick CsI(Tl) are presented for the first time in this work.

7.2.2. Results of the spatial and energy resolution from Monte Carlo Simulations

Results from Monte Carlo simulations with Geant4, where the response of the detector inside its measurement setup (Fig. 7.8) have been reproduced, are shown in the following.

The equivalent noise charge of the electronic noise has been set for each SDD cell to $\mathrm{ENC}_{el} = 15$ electrons, which has been determined from measurements. γ-rays are generated on a disc with a diameter as the real sources, $\oslash(^{241}\mathrm{Am}) = 1$ mm and $\oslash(^{57}\mathrm{Co}) = 4$ mm, and the photon momentum direction covers a solid angle of 11.5° to the normal of the disc surface. In the measurement setup this solid angle is larger. Increasing the solid angle in the simulations leads to a much higher calculation time. We made a compromise with the value of 11.5°. The top surface of the scintillator has been set polished. It is covered with a diffuse reflector. Its reflectivity has been set to 0.98 as in the simulations of the single SDD cell + CsI(Tl). The sides of the scintillator are set to absorb each incident photon, in order to reproduce the property of the black paint on the side faces of the scintillator.

In our simulations, we made the approximation that all 77 SDD cells have the same electronic noise value, $\mathrm{ENC}_{el} = 15$ electrons, and also the same DAC threshold, which has been set to 205 ADC channels for γ-rays of 59.5 keV and to 250 ADC channels for γ-rays of 122 keV in the low gain mode. This corresponds to a DAC threshold of 60 and 73 electrons.

To include the contribution of the CsI(Tl) light yield non-proportionality into the Geant4 simulations of the total detector response in the energy range 59.5 to 122 keV, the following approximation has been made. The number of scintillation photons, $\overline{N}_{ph} = \mathrm{E} \cdot \overline{L}$ for a certain light yield $\overline{L}$, is generated with a probability distribution given by a Gaussian distribution with an adjustable standard deviation, $\sigma(N_{ph})$. To match the value of the simulated to that of the measured energy resolution for the detector consisting of one SDD cell coupled to CsI(Tl) for energies around 75 keV, the distribution of the number of scintillation photons is approximated by a Gaussian distribution with the standard deviation, $\sigma(N_{ph}) = \mathrm{r}_{intr} \cdot \sqrt{\overline{N}_{ph}}$, where $\mathrm{r}_{intr} = 2.34$. The relative variance is $v(N_{ph}) = \mathrm{r}^2_{intr}/\overline{N}_{ph}$. The intrinsic contribution to the total energy resolution is then $\mathrm{R}_{intr} = 2.35 \cdot \sqrt{r^2_{intr}/(\overline{L}(E) \cdot E)}$, which replaces $\mathrm{R}_{Fano-CsI(Tl)}$ and R_T in formula 6.34. Inserting $v(N_{ph})$, $\overline{N}_{ph}$ and the system quantum efficiency, $\overline{\eta}$, into Eq. B.29 leads to the total variance of the number of signal electrons. With the value of the variance of signal electrons, the total energy resolution determined by Monte Carlo simulations, R_{sim}, is approximated by

$$R_{sim} \approx \sqrt{R^2_{intr} + R^2_{\eta} + R^2_{Bino,\eta} + R^2_{el}}, \tag{7.3}$$

where $\mathrm{R}_{Bino,\eta} = 2.35\sqrt{(1-\overline{\eta})/\overline{N}_e}$, $R_{el} = \sqrt{n_{cells}} \cdot R_{el,cell}$, n_{cells} is the number of SDD cells recording a signal above data acquisition threshold and $R_{el,cell}$ is the electronic noise of one SDD cell. Fig. 7.15 shows the values of $\sqrt{R^2_{Fano} + R^2_T + R^2_{Bino}}$ and $\sqrt{R^2_{intr} + R^2_{Bino,\eta}}$ in the energy range 25 to 150 keV with a deviation of less than 14 % in the energy range 60 to 122 keV.

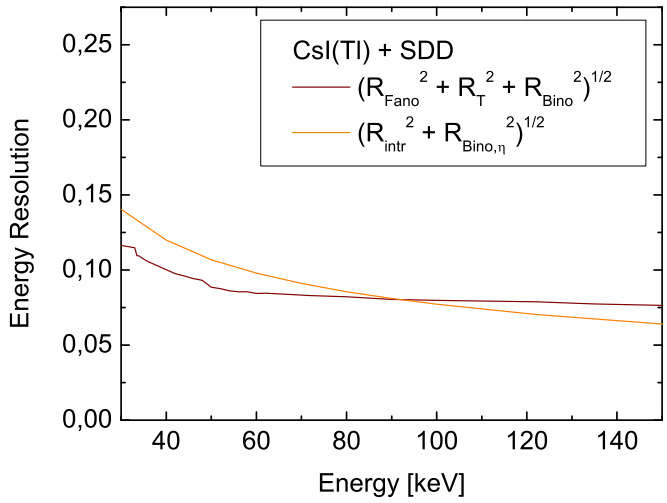

Figure 7.15.: *Energy resolution without the contributions of R_η and R_{el} calculated with Eq. 6.5 or 7.3. The energy resolution values illustrated by the orange curve results from simulations of the detector response with Geant4, where the number of scintillation photons is approximated by a Gaussian distribution with a variance of $Var(N_{ph}) = r_{intr}^2 \cdot \overline{N}_{ph}$.*

The ^{57}Co source is simulated by the generation of 122 and 136 keV photons with a probability of 91 % and 9 %.

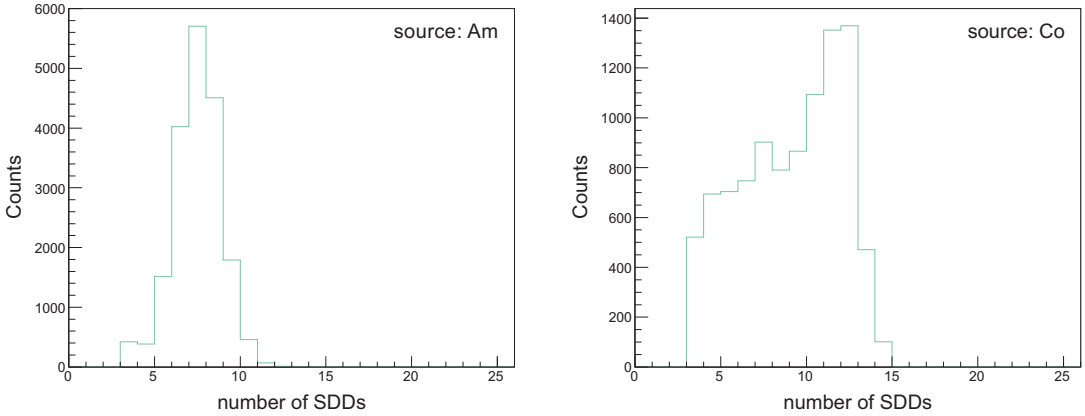

Figure 7.16.: *Measured number of SDD cells, which shared scintillation photons (above threshold) from one event.*

In Fig. 7.16 and 7.17 histograms are illustrated of the measured and simulated number of SDDs, which registered a number of signal electrons above DAC threshold after γ-interactions with the scintillator. A higher γ-energy generates more scintillation photons, so that the maximum number of SDD cells registering signal electrons above DAC threshold is larger. The distributions in the histograms strongly depend on the value of the DAC threshold. A high DAC threshold, due to a high electronic

noise, makes these distributions more sensitive to changes of the position where scintillation photons are generated, relative to the center of the closest SDD cell. Simulations show that, if scintillation photons are generated above the center of a SDD cell, the distribution in the histogram for incident γ-rays of 59.5 keV becomes narrower and the maximum of the histogram for incident γ-rays of 122 keV shifts to 7 SDD cells. The measured (Fig. 7.16) and simulated distributions (Fig. 7.17)

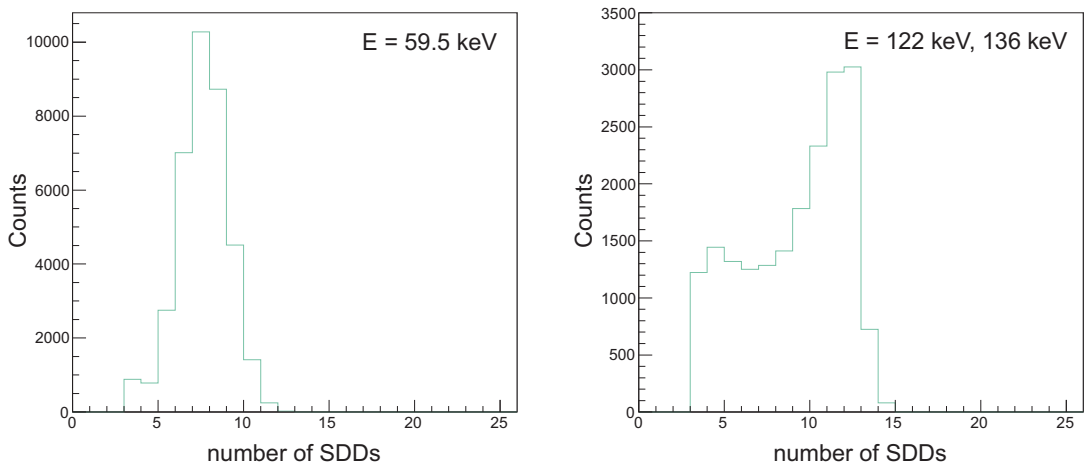

Figure 7.17.: *Simulated number of SDD cells, which shared scintillation photons (above threshold) from one event. Photon source of 59.5 keV on the left and 122 (91 %), 136 keV (9 %) on the right.*

for 59.5 keV photons are similar. The higher bin content in the range from 3 - 9 SDD cells in the measured histogram (Fig. 7.16 third picture) compared to the simulated histogram (Fig. 7.17 second picture) results most probably from the fact, that a larger number of events interact closer to the center of the SDD cell in the measurements compared to the simulations.

The energy dependent light yield for CsI(Tl), used in these simulations, is the same as the light yield used for the simulations of the system single SDD cell coupled to CsI(Tl). The reconstructed interaction points of γ-rays with energies of 59.5 keV or 122 + 136 keV incident onto the detector in the measurement setup, illustrated in Fig. 7.8 (b), is shown in Fig. 7.18. The spatial resolutions are $\approx$ 1.1 mm for γ-rays with energies of E = 59.5 keV and 0.9 mm for E = 122 keV, 136 keV. For photons of E = 59.5 keV the result from simulation is in good agreement to the measured value presented in Sec. 7.2.1. The spatial resolution for higher energies is slightly better for the simulated compared to measured values. In order to determine the intrinsic resolution of the detector, the position of the source, which generates γ-rays, has been set to a fixed point and the momentum of the incident γ-rays is perpendicular to the scintillator surface. This leads to an intrinsic spatial resolution of $\widetilde{R}_i \approx 1.1$ mm for E = 59.5 keV and 0.5 mm for E = 122 keV, 136 keV. There is no improvement of the spatial resolution at E = 59.5 keV, because of the low signal to DAC threshold.

The interaction depth of γ-rays inside the scintillator can be determined by a three dimensional reconstruction algorithm presented in Sec. 7.2.1. The recon-

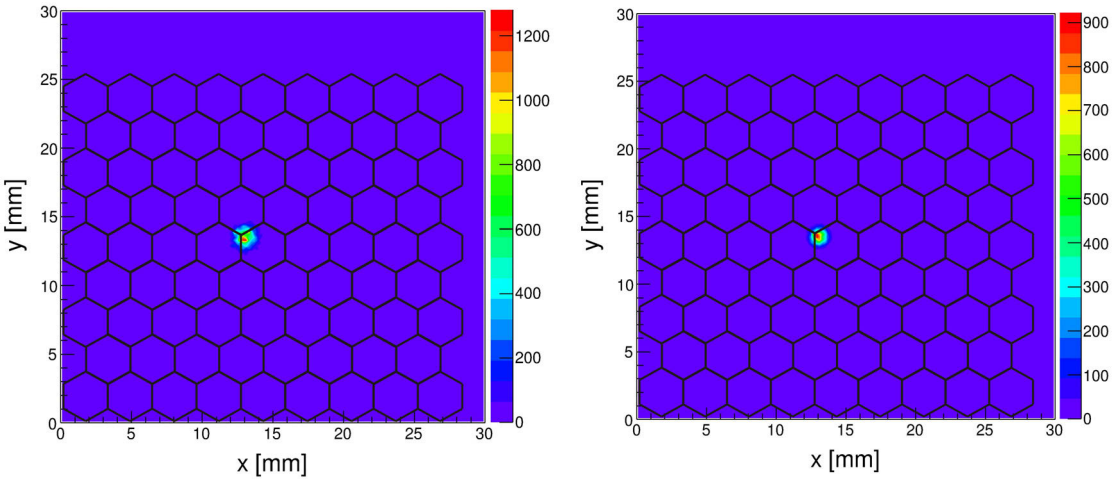

Figure 7.18.: *Reconstructed images from simulations generated by the irradiation of the detector in the measurement setup illustrated in Fig. 7.8 (b) with γ-rays of 59.5 keV (on the left) and 122 (91 %) + 136 keV (9 %) (on the right).*

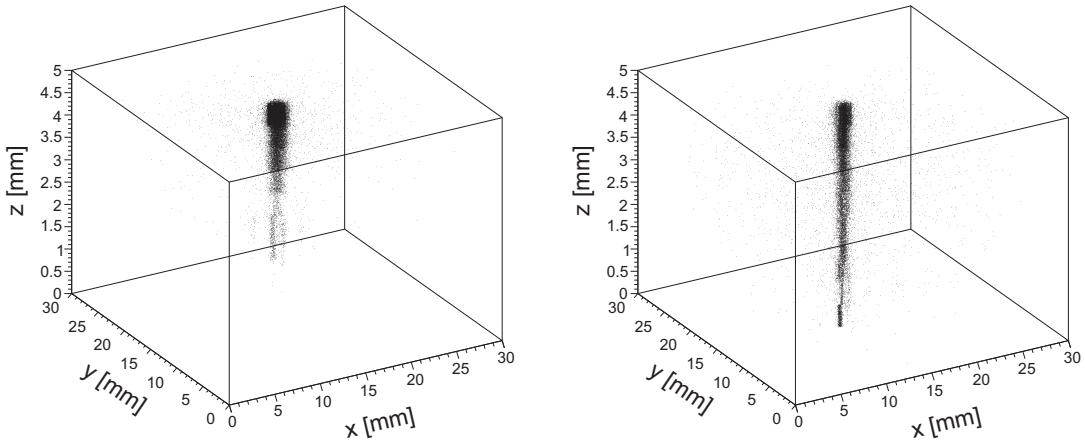

Figure 7.19.: *Reconstructed 3 dimensional images from simulations generated by the irradiation of the detector in the measurement setup illustrated in Fig. 7.8 (b) with γ-rays of 59.5 keV (on the left) and 122 (91 %) + 136 keV (9 %) (on the right).*

structed interaction points in three dimensions are illustrated in Fig. 7.19. This is also in a good agreement with the reconstructed image from the measured detector response in Fig. 7.12 for the same measurement setup and detector parameters. The knowledge of the interaction depth could be used to determine the direction of γ-rays incident under a cetrain angle into the scintillator and to improve the spatial resolution.

The results of the energy resolution from simulations are R(59.5 keV) $\approx$ 0.37 (Fig. 7.20 on the left) and R(122 keV) $\approx$ 0.38 (Fig. 7.20 on the right), which are in good agreement with the result from the measurement presented in Sec. 7.2.1.

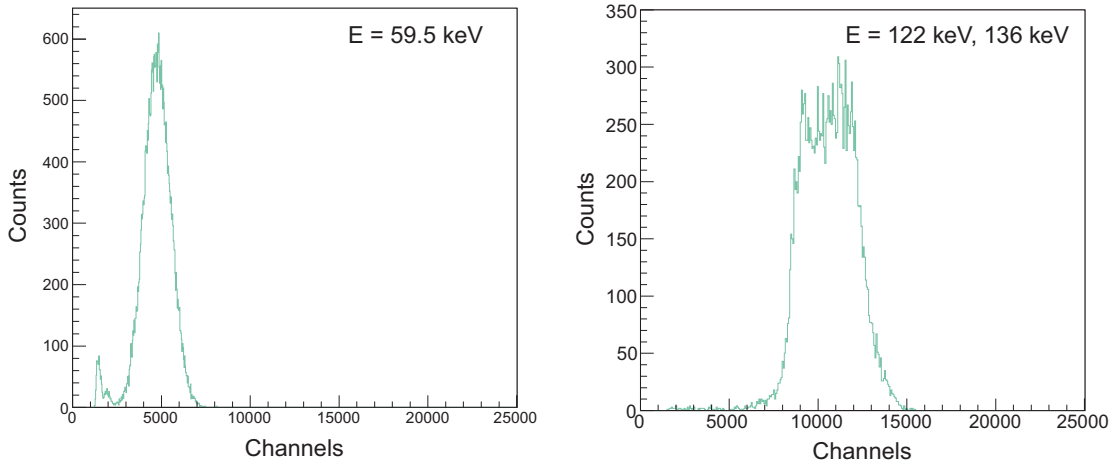

Figure 7.20.: *Results of the pulse height distribution from simulations generated by the irradiation of the detector in the setup with the pinhole configuration shown in Fig. 7.8 (b) with 59.5 keV (on the left) and 122 (91 %) + 136 keV (9 %) (on the right).*

The differences of the measured and simulated spectra for 122 keV γ-rays originates most probably from the fact that the energy resolution is very sensitive to the position, where scintillation photons are generated, relative to the center of the closest SDD cell. Contributions to the shoulder on the low energy side of the photo peak generated by the ^{57}Co source in the measured spectrum in Fig. 7.14 originate most probably from fluorescence photons from the Pb collimator and from γ-rays interacting with the scintillator close to the side faces, where a large fraction of scintillation photons hit the SDD surface outside of the active area, generating a lower signal amplitude.

Fig. 7.21 shows the contributions of R_{Fano}, R_T, R_η, R_{Bino} and R_{el} and their sum, R_{sum}, to the energy resolution, if the effect of the loss of signal electrons, due to ballistic deficit and the DAC threshold, is not included in the calculations. R_T, R_{Bino} and R_{el} are the main contributions, because of the low quantum efficiency of the system, which is about $\overline{\eta} \approx 0.32$ for scintillation photons and the large electronic noise of $ENC_{el} \approx 15$ electrons. The values of R_{sum} are much lower than the measured and simulated total energy resolution, R, due to the fact, that the loss of a large number of signal electrons, because of the DAC threshold, has not been taken into account. This contribution to the energy resolution and is examined in the following.

Fig. 7.22 shows the fraction of absorbed γ-rays in certain depths inside the CsI(Tl) scintillator. Almost all photons with an energy of 59.5 keV are absorbed within the first 1.5 mm of CsI(Tl). About 65 % of the photons with an energy of 122 keV are absorbed within the first 1.5 mm of CsI(Tl). The interaction depth of γ-rays inside the scintillator, hence the generation depth of scintillation photons inside the CsI(Tl) scintillator, is important, due to the fact, that the distribution of the scintillation photons over the SDD cells depends on their generation depth.

Fig. 7.23 shows the simulated response of the 77 SDD cells at two generation depths inside CsI(Tl) for 122 keV γ-rays with the DAC threshold set to 0. The

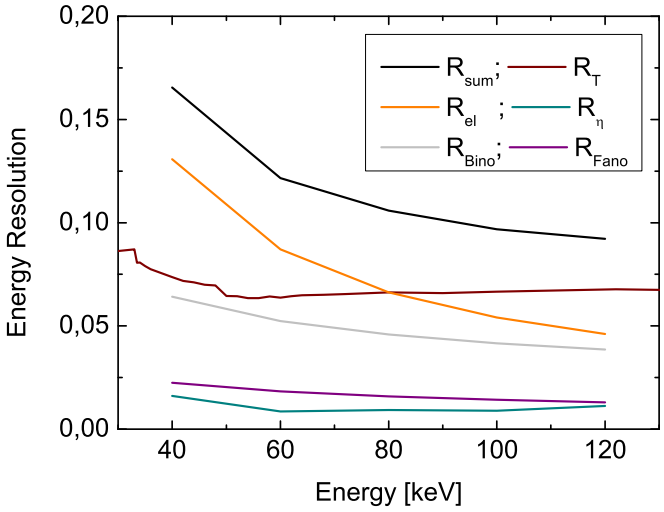

Figure 7.21.: *Contributions to the energy resolution of the 77 cell SDD array coupled to the 5 mm thick CsI(Tl) scintillator. The contribution of R_T has been determined in Sec. 6.2.1. $R_{el} = \sqrt{n_{cells}} R_{el,cell}$ with $n_{cells} = 12$ SDD cells and $R_{el,cell}$ the electronic noise contribution of one SDD cell with $ENC_{el} = 15$ electrons.*

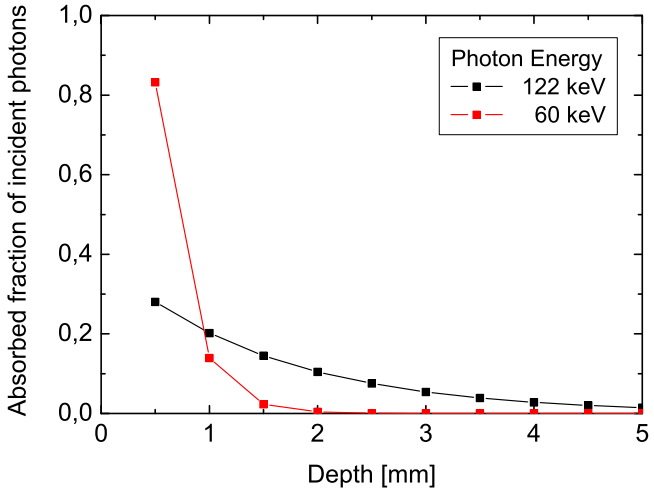

Figure 7.22.: *Absorbed fraction of incident photons in certain depths inside CsI(Tl).*

number of SDD cells recording signal electrons is larger, if the generation depth of scintillation photons is close to the top scintillator surface in a depth of 0.05 mm (Fig. 7.23(a)) compared to 2.55 mm (Fig. 7.23(b)). Furthermore the signal amplitude is about twice as large, if scintillation photons are generated in a depth of 2.55 mm compared to 0.05 mm from the top scintillator surface. In a generation depth of 0.05 mm the maximum number of detected signal electrons per SDD cell is about 250, if an energy of 122 keV is deposited inside the CsI(Tl) scintillator. The

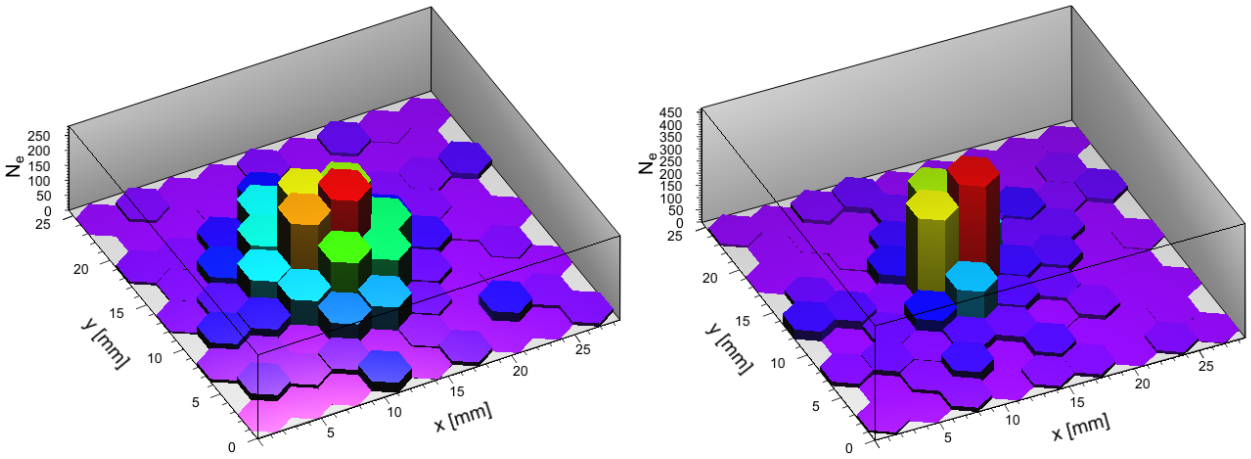

(a) *Energy deposition at 0.05 mm depth.* (b) *Energy deposition at 2.55 mm depth.*

Figure 7.23.: *Simulated amount of signal electrons detected by each SDD cell after the deposition of 122 keV. Electronic noise is included.*

data acquisition threshold is set to 73 electrons, so that a large amount of the signal falls below this threshold.

The mean quantum efficiency for scintillation photons is $\overline{\eta} \approx 0.32$. If the loss of signal electrons, due to ballistic deficit and DAC threshold, is not taken into account, the mean number of signal electrons is $\overline{N}_e = E \cdot \overline{L}(E) \cdot \overline{\eta} \approx 1390$ and 2690 scintillation photons, if an energy of 59.5 keV and 122 keV is deposited inside CsI(Tl). Due to the ballistic deficit and DAC threshold a fraction of about 0.5 of the generated signal electrons is lost.

Fig. 7.24 on the left shows the shift of the mean number of signal electrons as a function of the generation depth of scintillation photons. The mean number of signal

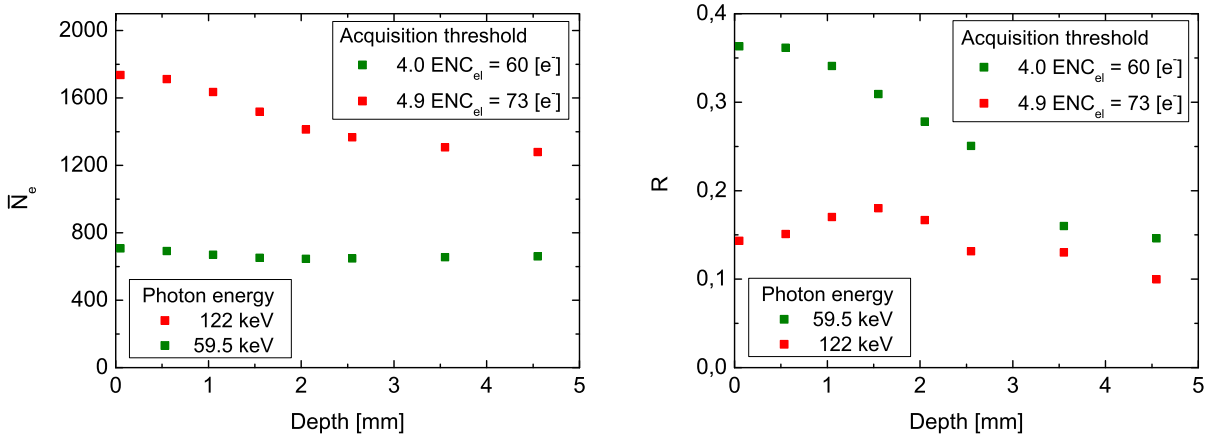

Figure 7.24.: *Mean number of signal electrons (on the left) and energy resolution (on the right) as a function of the generation depth of scintillation photons inside CsI(Tl). At 5 mm, there is the interface of CsI(Tl) to the optical coupler.*

electrons, generated after the deposition of 59.5 keV, remains almost constant, if the generation depth of scintillation photons is changed. In contrast to that, the mean number of signal electrons generated after the deposition of 122 keV decreases from 1700 to values close to 1250, if the generation depth increases above 2 mm. This leads to a relative broadening by about $450/1475 \approx 0.31$. This value in combination with the maximum value of the energy resolution, which is shown in Fig. 7.24 on the right (red points), add up to a total energy resolution of about 0.36. For 59.5 keV the large contribution to the energy resolution originates from the large value of the energy resolution of R = 0.37, if scintillation photons are generated close to the scintillator top face (green points in Fig. 7.24 on the right), due to the small signal to noise ratio at that position, because of the distribution of scintillation photons over a larger number of SDD cells compared to positions closer to the SDD surface.

In Fig. 7.25 the mean number of SDD cells, which record a signal above threshold during one event, and its standard deviation times 2.35 (approximation to the FWHM of a Gaussian peak) are plotted against the generation depth of scintillation photons. Up to 2.0 mm depth, there is a large difference in the number of SDD cells recording a signal after the interaction of 59.5 and 122 keV γ-rays with the CsI(Tl) scintillator. At a depth of 0.05 mm the mean number of SDD cells recording a signal

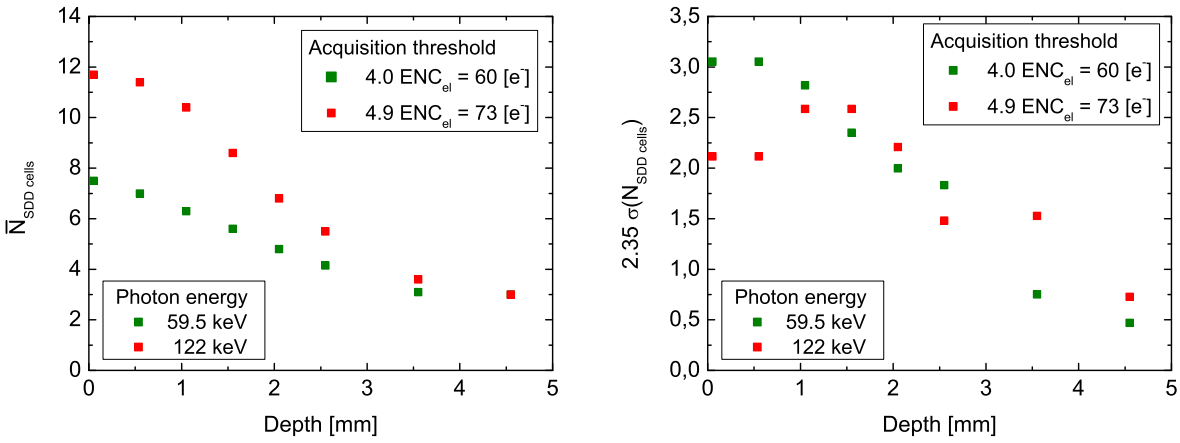

Figure 7.25.: *Mean number of SDD cells, which record a signal above threshold and its standard deviation expressed in rms.*

is about 7.5 respectively 12. In contrast to that, its standard deviation times 2.35 is about 3 respectively 2. Although the signal is distributed over a larger number of cells, if an energy of 122 keV is deposited compared to 59.5 keV, the standard deviation is smaller, due to a larger signal to noise ratio per SDD cell. This leads to a narrower variance of the number of signal electrons, hence to a better energy resolution in a certain depth, if an energy of 122 keV is deposited compared to 59.5 keV.

If the electronic noise value is reduced from ENC_{el} = 15 to 4 electrons and the DAC threshold from 60 or 73 to 16 electrons, the mean number of signal electrons decreases only slightly with an increasing generation depth of scintillation photons for incident γ-rays of 59.5 keV and 122 keV (Fig. 7.26 on the left). The larger

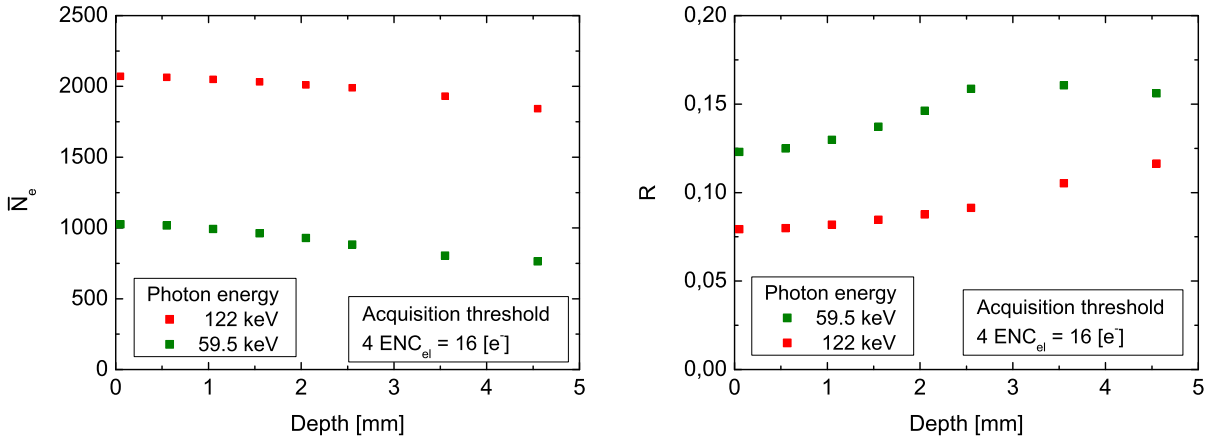

Figure 7.26.: *Mean number of the detected signal electrons and the energy resolution as a function of the generation depth of scintillation photons for an electronic noise is ENC_{el} = 4 electrons and a scintillator thickness of 5 mm.*

signal to noise ratio and lower DAC threshold improves the energy resolution and its dependence on the generation depth of scintillation photons (Fig. 7.26 on the right).

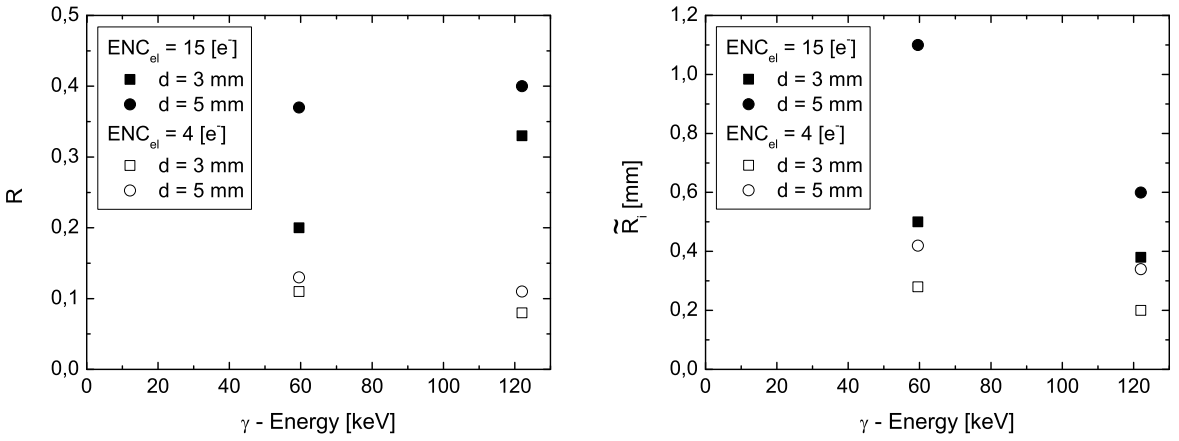

Figure 7.27.: *Energy and spatial resolutions for two electronic noise values and CsI(Tl) scintillator thicknesses.*

Fig. 7.27 shows the results for the intrinsic spatial and energy resolution for incident photons with energies of E = 59.5 and 122 keV and CsI(Tl) thicknesses of d = 5 mm (QE = 1 up to 100 keV) and 3 mm (QE = 1 up to 80 keV) for ENC_{el} = 4 (DAC = 16 e$^-$) and 15 (DAC = 60; 73 e$^-$) electrons. A reduction of the CsI(Tl) thickness from 5 to 3 mm improves the energy and spatial resolution, which is very large for γ-rays with an energy of E = 59.5 keV, if the electronic noise is ENC_{el} = 15 electrons. A reduction of the electronic noise from ENC_{el} = 15 to

4 electrons, improves strongly the relative energy resolution and spatial resolution. This improvement is the largest for the relative energy resolution at 122 keV.

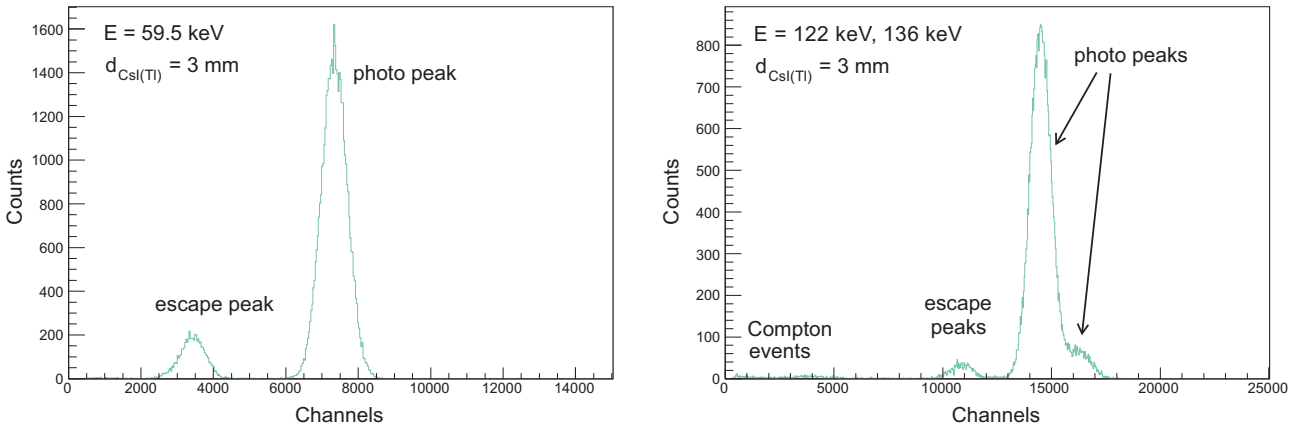

Figure 7.28.: *Simulated spectra after irradiation of the scintillator with photons of E = 59.5 keV (on the left) and 122 keV (Intensity = 91 %) + 136 keV (Intensity = 9 %) (on the right). The standard deviation of the electronic noise is set to ENC_{el} = 4 electrons with a DAC threshold of 16 electrons and a scintillator thickness of 3 mm.*

Fig. 7.28 shows the simulated spectra for the 3 mm thick CsI(Tl) scintillator for incident photons of E = 59.5 keV and 122 keV (91 %) + 136 keV (9 %).

The parameters of the detector during measurements are now recapitulated: The CsI(Tl) thickness is d = 5 mm, all CsI(Tl) faces are polished, the CsI(Tl) side faces are painted with an absorptive coating, the reflector is Millipore paper, the standard deviation of the electronic noise is ENC_{el} = 15 electrons and the DAC threshold is in the range from 60 to 100 electrons. In order to find parameters, which improve the detector performance, we examined the influence of the following modifications by simulations: a) Painting the scintillator top face with a diffuse reflector with the same reflectivity of 0.98; b) Reduction of the scintillator thickness from 5 mm to 3 mm; c) Reduction of the electronic noise value from ENC_{el} = 15 to 4 electrons.
Option a) increases the system quantum efficiency for scintillation photons (from $\overline{\eta} \approx 0.32$ to $\overline{\eta} \approx 0.44$ for $d_{CsI(Tl)} = 5$ mm). For $d_{CsI(Tl)} = 3$ mm the diffuse reflector yields a value of $\overline{\eta} \approx 0.55$. It also increases the spatial distribution of scintillation photons over a larger number of SDD cells at the same time, so that the electronic noise of a higher number of SDD cells is collected. It improves the energy and spatial resolution for ENC_{el} = 15 at E = 59.5 keV.
Options b) and c) improve the energy and spatial resolution the most (Fig. 7.27). Reducing the electronic noise from a value of ENC_{el} = 15 to 4 electrons, enables the reduction of the DAC threshold. A value of ENC_{el} = 4 has been determined from measurements of slightly larger circular SDD cells with an area of 10 mm^2, read out by the standard electronics for one cell SDDs.

We have shown in these sections that we can reproduce the measured results of the spatial and energy resolution by Monte Carlo simulations. Results from simulations with different detector parameters indicate, that there is much room to improve the

performance of the 77 cell SDD array + CsI(Tl) detector, mostly by reducing the electronic noise from the data acquisition hardware. This would yield a γ-camera with a good energy resolution and a sub millimeter spatial resolution in the range 60 to 122 keV.

7.3. pnCCD + CsI(Tl) camera for X- and γ-rays

The pn-junction Charged Coupled Device (pnCCD) is a silicon pixel detector. As for SDDs, its working principle is based on sideward depletion. The pnCCD enables measurements with a very good energy, spatial and timing resolution in the energy range from 100 eV up to several 10 keV, but with a decreasing quantum efficiency for X-rays above 10 keV. The pnCCD bulk is fully depleted by applying a high negative voltage to the back contact and a lower negative voltage to the registers on the front side relative to the substrate (Fig. 7.29). The voltages are adjusted in a way, that generated electrons inside the bulk propagate towards the potential minimum close to the storage registers, which have a distance of about 7 μm from the front side of the pnCCD [136] (Fig. 7.29). The registers are formed by pn-junctions on the front side of the detector. Voltages Φ_1, Φ_2 and Φ_3, are applied to the registers, in such an order that every third register has the same voltage. This forms a regular grid of potential minima parallel to the front side of the pnCCD [136] (Fig. 7.29). In regular

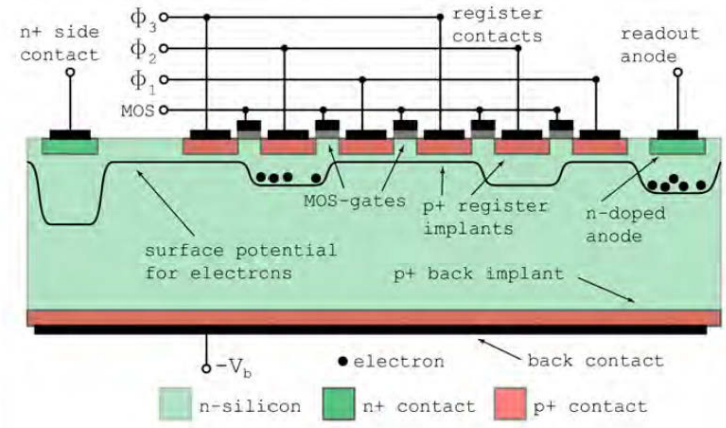

Figure 7.29.: *Block diagram of a pnCCD with two pixels, taken from [136].*

time intervals all the potential valleys are transferred laterally in the direction of the anodes, located at one side of the pnCCD. This is realized by changing sequentially the voltages, Φ_1, Φ_2 and Φ_3, on the transfer registers. The content of the pixels in one column is readout in series. The rows are readout in parallel. The anodes are connected to an on-chip JFET. The integration of the first JFET enables a low noise and fast readout, due to the small capacitance. A readout rate up to 1 kHz can be achieved. The number of readouts per column is variable. Reducing its number, reduces also the electronic noise from the readout process. A reduction of the number of readouts is equivalent to a reduction of the number of pixels per column, which leads to larger pixels. The electronic noise per pixel remains almost constant, due to a very low leakage current inside the pnCCD. With the reduction

of the number of readouts the electronic noise per pnCCD area can be reduced. A detailed description of the pnCCD and its operation can be found in [136].

pnCCDs with pixel sizes between 50 to 300 μm have been fabricated. The spatial resolution is in the order of the pixel size or less. The quantum efficiencies of SDDs (Sec. 5) and pnCCDs are equal, because they have the same thickness and compositions of the entrance window. Coupling a scintillator onto the backside of the pnCCD, while irradiating the detector from the front side (see Fig. 7.30), extends the energy range of the pnCCD to 100 keV and higher. Up to now there are no γ-cameras with a good spatial and energy resolution and a high quantum efficiency in the energy range from 1 to 150 keV. In this section we are investigating the response of a pnCCD + CsI(Tl) detector in the energy range from 1 to 150 keV by Monte Carlo simulations.

Recently pnCCDs have been utilized as an excellent detector for X-ray diffraction experiments. It has been used as a low noise and fast readout X-ray camera for experiments at free electron lasers. The solid state group at the University of Siegen uses the pnCCD as a detector for white synchrotron radiation in the spectral range from 5 to 40 keV. In these experiments the radiation hits the sample in one shot and generates a diffraction pattern on the pnCCD, which is positioned at a certain distance from the sample. From this diffraction pattern, the reciprocal lattice and the crystal lattice in real space coordinates can be reconstructed. Energies up to 200 keV can be generated inside synchrotron beam lines with bending magnets. The quantum efficiency for 450 μm thick pnCCDs and SDDs decrease exponentially for increasing X-ray energies above 10 keV. To exploit the energy range up to 200

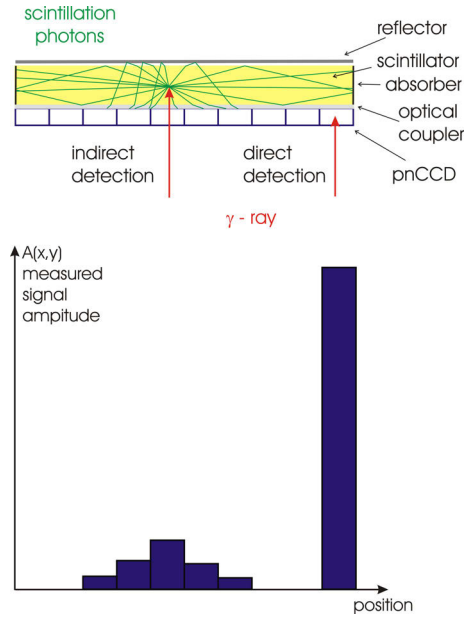

Figure 7.30.: *Schematics of the direct and indirect detection mode of the detector pnCCD + scintillator.*

keV with pnCCDs, a scintillator has to be coupled onto the back side of it and the pnCCD has to be used as a photodetector for scintillation light.

To maintain the good spatial (pixel and sub pixel resolution) and energy resolution of the pnCCD in the energy range 1 to several 10 keV the radiation has to enter the

pnCCD + scintillator detector from the pnCDD side (Fig. 7.30) to take advantage of the direct detection mode (Fig. 7.30). Most of the photons are interacting inside the pnCCD up to 15 keV (Fig. 7.31 violet line). Photons with higher energies are mainly absorbed inside the CsI(Tl) scintillator (Fig. 7.31 green line). Furthermore the probability for photo effect to occur inside the pnCCD decreases and becomes equal to that of Compton scattering around 50 keV (Sec. 2.1.1). This reduces the fraction of events generated by the photo effect to the total number of events inside the pnCCD at larger energies.

The scintillator on the back side of the pnCCD increases the system quantum efficiency (Fig. 7.31 black curves) and also the probability for photo effect relative to Compton scattering, due to the higher Z and density of the CsI scintillator material compared to Si. For CsI and $LaBr_3$ the probabilities for photo effect and Compton scattering are equal close to 200 keV (Sec. 2.1.1). In indirect detection mode (Fig. 7.30) the deposited energy inside the scintillator leads to a spread of the signal electrons over several pixels. The position of the interaction is calculated by the center of gravity method. The energy resolution in indirect detection mode suffers most from the loss of a large number of scintillation photons, due to the light collection efficiency and the distribution of signal electrons over a large number of pixels, which increases the electronic noise of the total signal by summing up the noise of all individual pixels.

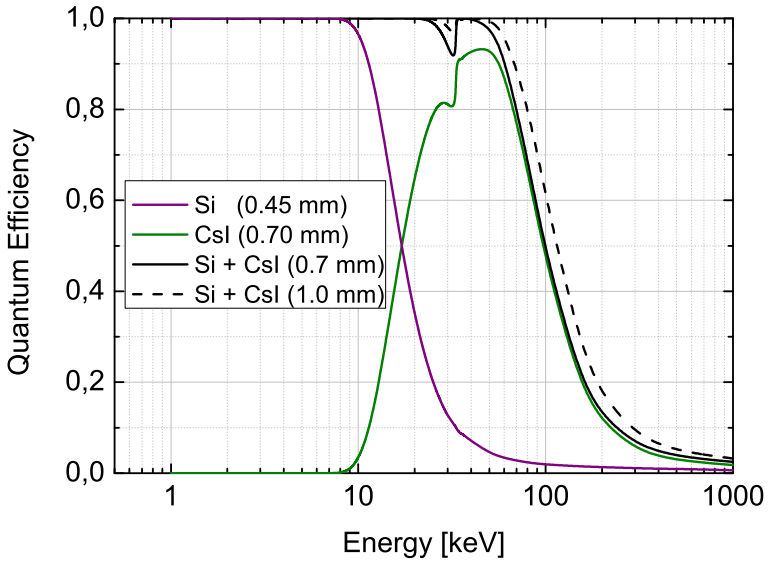

Figure 7.31.: *Quantum efficiency of the pnCCD without any losses at its entrance window, the 0.7 mm thick CsI crystal and the combined system pnCCD + CsI(Tl).*

Fig. 7.31 shows that the quantum efficiency for a pnCCD + CsI(Tl) detector with scintillator thicknesses of 0.7 mm and 1 mm. It is still above 0.5 at 100 keV and above 0.1 at 200 keV. Also for the Anger camera consisting of a pnCCD + scintillator as for the SDD array + scintillator, CsI(Tl) is the optimum scintillator for a prototype detector for practical reasons (see Sec. 7.2).

The most important requirements of the combined detector system in indirect detection mode, where the pnCCD serves as a photodetector for the scintillation light, are the following: The spatial resolution should be similar or better compared to that in direct detection mode, which is in the order of the pixel size. The energy resolution should be sufficiently good to enable a discrimination of the energies inside the Laue spots. These energies fulfill the Bragg condition or result from pile up events [137]. In both cases events are recorded with energies resulting from the multiplication of an integer to the first order Bragg energy. The Bragg condition for a crystal is fulfilled for photons with the energies

$$E_n = n\frac{2\pi\hbar c}{2dsin\theta} \approx n\frac{39}{d[\mathring{A}]sin\theta}[\text{keV}], \tag{7.4}$$

with n an integer, $\hbar$ the Planck constant, c the velocity of light, d the distance between adjacent crystal planes and θ the angle between the propagation direction of the incident photon to the crystal surface. The energy resolution should be sufficient to enable a discrimination of the energies E_n and E_{n+1}. For an increasing distance of the crystal planes and the angle θ the energy E_n decreases. E.g. inserting the lattice spacing of iron, which is 2.8 Å and an angle of $\theta = 45°$ into Eq. 7.4 results into $E_n \approx n \cdot 20$ keV.

Reducing the electronic noise, improves the resolution. The pnCCD has to be cooled to reduce the electronic noise from the leakage current. But due to the fact, that a decreasing temperature leads to a reduction of the light yield of CsI(Tl), the pnCCD + CsI(Tl) detector has to be cooled down to temperatures, where the light yield of the CsI(Tl) scintillator is still high enough to enable imaging and spectroscopy at the same time. The electronic noise of the 75 x 75 μm^2 pnCCD per pixel as a function of the temperature is illustrated in Fig. 7.32 on the left. At - 10°C

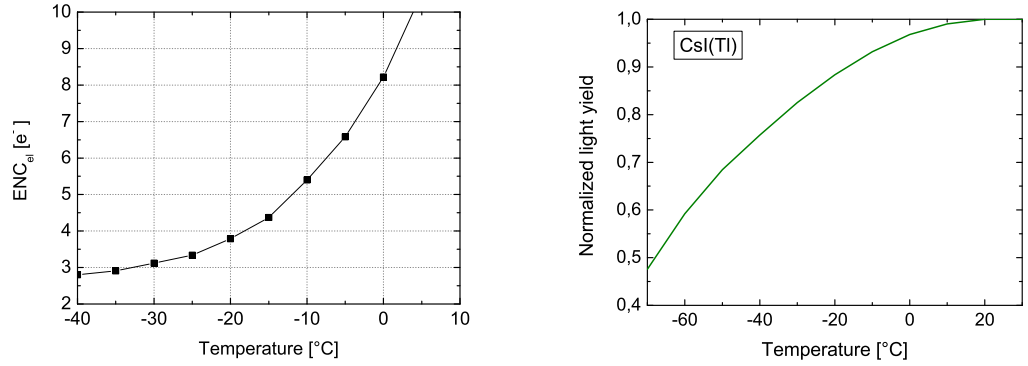

Figure 7.32.: *Electronic noise of a 75 x 75 μm^2 pixel pnCCD plotted against temperature (on the left). Light yield dependency of CsI(Tl) on temperature taken from S. Gobain crystals (on the right).*

the electronic noise value is ENC_{el} = 5.5 electrons and it drops below 3 electrons for temperatures ≤ - 35°C. We measured a decrease of the light yield of CsI(Tl) by about 10 %, if the temperature is decreased from room temperature to - 20°C. Fig. 7.32 on the right shows the dependency of the light yield of CsI(Tl) on the

temperature [69]. A compromise between a high light yield and low electronic noise could be reached at a detector temperature of about - 20°C, where the light yield of the CsI(Tl) scintillator is still 90 % compared to its value at room temperature and the electronic noise per pixel is $ENC_{el} \approx 3.8$ electrons.

Crucial for the energy resolution in the indirect mode is also the number of readouts. pnCCDs with pixel sizes of 75 x 75, 75 x 300 and 300 x 300 μm^2 have been investigated by simulations. The number of readouts of the pnCCD can be reduced. This is equivalent to an on chip binning in one direction, which leads to a decrease of the electronic noise per area. With this procedure a pixel size of 75 x 300 μm^2 can be realized by binning the number of signal electrons of a pnCCD with a pixel size of 75 x 75 μm^2 from 4 pixels in the readout direction.

In order to determine the optimal parameters for the Anger camera, consisting of a pnCCD + CsI(Tl), Monte Carlo simulations have been performed of the detector response for different sets of parameters, including scintillator thickness, light yield, reflector type, pnCCD pixel size and electronic noise.

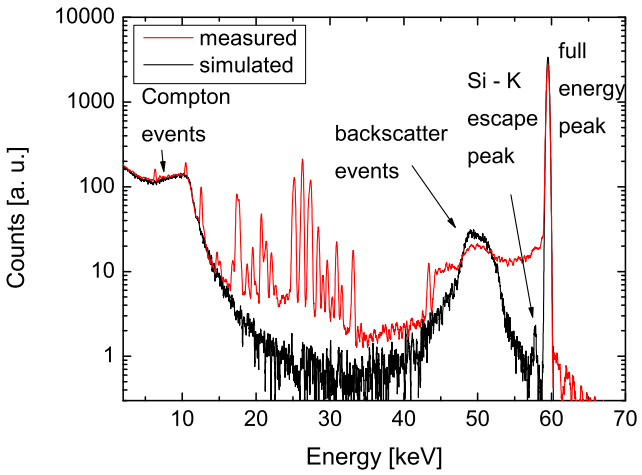

Figure 7.33.: *Measured (red curve) and simulated spectrum (black curve) with of a SDD irradiated with an ^{241}Am source or with photons of the energy 59.5 keV. The peaks, which are not labeled, originate from the ^{241}Am source or from fluorescence photons from the Pb collimator.*

The excellent performance of the pnCCD in direct detection mode degrades with increasing energies, due to a decreasing quantum efficiency and ratio of the photo effect to Compton scattering. Fig. 7.33 shows a measured spectrum with an SDD of an ^{241}Am source and a simulated spectrum for incident γ-rays with an energy of 59.5 keV. The spectral response of SDDs and pnCCDs are similar. The simulated spectrum reproduces the measured spectrum well, except for the shoulder on the left side of the photo peak. Simulations indicate that a charge collection efficiency less than 1 at the front side of the detector with a thickness of several μm could cause such a shoulder on the low energy side of the photo peak.

Fig. 7.34 shows two simulated spectra of the direct detection of γ-rays with an energy of 50 keV and 100 keV inside the pnCCD with the system pnCCD + CsI(Tl).

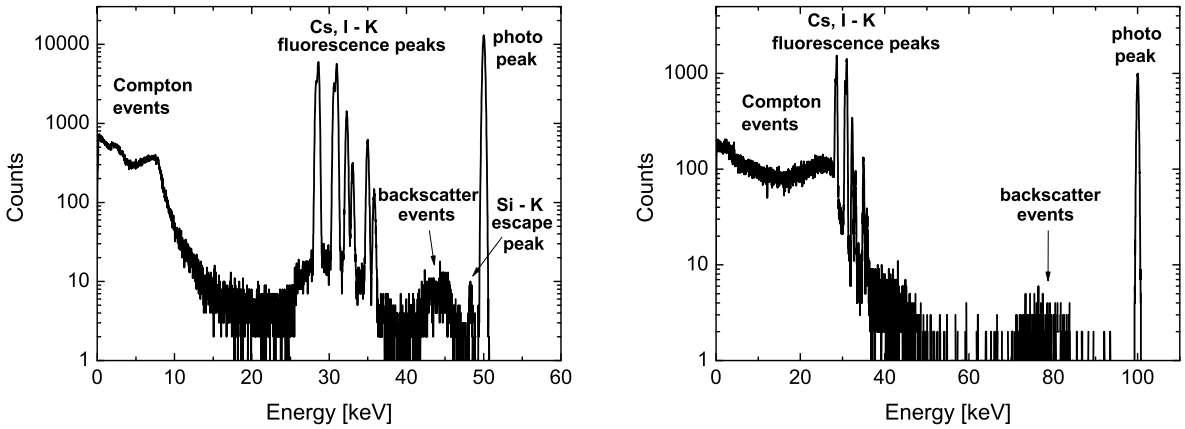

Figure 7.34.: *Simulated spectrum in the direct detection mode for pnCCD (0.45 mm) + optical pad (0.1 mm) + CsI (1 mm) for 50 and 100 keV photons.*

The pnCCD is coupled to a 1 mm thick CsI(Tl) crystal with a 100 μm thick optical pad. These spectra contain additional fluorescence peaks from the relaxation of the excited Cs and I atoms inside the scintillator. Fluorescence photons, which are generated inside the scintillator, can escape and can be absorbed with a certain probability inside the pnCCD. In Fig. 7.35 the fraction of events generated by

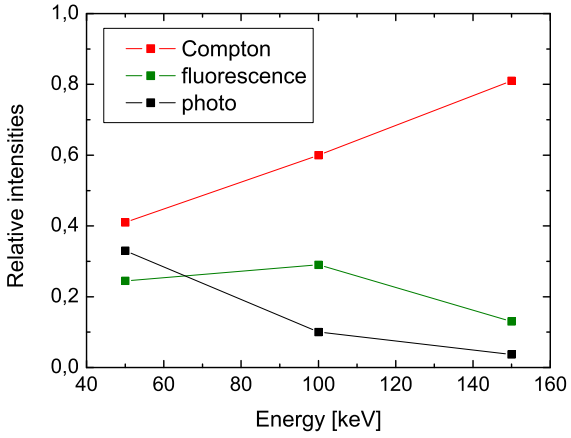

Figure 7.35.: *Simulated relative intensities of events generated by the photo effect and Compton scattering inside the pnCCD and fluorescence photons from the CsI(Tl) scintillator to the total number of events detected in the direct detection mode of the pnCCD + optical pad + CsI(Tl) system.*

photo effect and Compton scattering inside the pnCCD and fluorescence photons from the CsI(Tl) scintillator to the total number of directly detected X- or γ-rays are presented for 50, 100 and 150 keV. The number of events from Compton scattering increases and that from photo effect decreases with increasing γ-energy as expected from their cross section in Si (see Fig. 2.1). The fraction of detected fluorescence

photons increases slightly with increasing energy from 50 to 100 keV, because a larger fraction of γ-photons reaches the scintillator without any interaction inside the pnCCD at higher energies. From 100 keV to 150 keV the fraction of detected fluorescence photons decreases, because a larger ratio of incident photons penetrates deeper into the scintillator, from where fluorescence photons reach the pnCCD with a lower probability. The fraction of fluorescence photons is larger than the fraction of events from photo effect in the energy range 50 to 150 keV. For γ-energies E > 50 keV the quantum efficiency is smaller than 0.05 and the probability for photo effect becomes also smaller compared to the number of events from Compton scattering in silicon. The quantum efficiency for the detection of events generated by the photo effect is about 0.01 for 50 keV and 0.001 for 100 keV γ-ray photons respectively. The number of incident photons has to be large enough to detect sufficient photons inside the photo peak for an evaluation of the γ-ray energy. The background is generated mainly by fluorescence photons and events from Compton scattering. The knowledge of the exact energy of the fluorescence peaks can be used to attribute these events to γ-rays, which interacted inside the scintillator.

For a high number of detected events the relative energy resolution of the system pnCCD + CsI(Tl) determined in direct detection mode (R ≈ 0.01) is more than an order of magnitude better compared to the indirect detection mode.

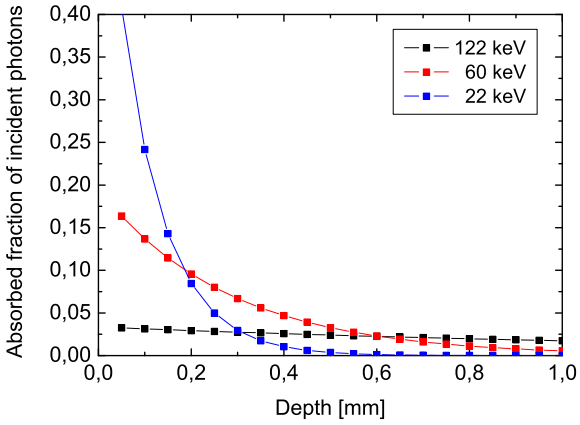

Figure 7.36.: *Fraction of absorbed γ-rays in intervals of 50 μm inside a 1 mm thick CsI(Tl) scintillator.*

Depending on the γ-energy the number of photons interacting inside a certain depth range of the scintillator follows from Beer-Lamberts law. For 22, 59.5 and 122 keV photons the absorbed fractions of photons inside intervals of 0.05 mm in CsI are illustrated in Fig. 7.36. For energies below 50 keV most of the photons are absorbed in the first 300 μm inside CsI(Tl), whereas larger energies are absorbed more uniformly inside the 1 mm thick CsI(Tl) scintillator. Because of that, it is important to know the distribution of scintillation photons over the pnCCD pixels as a function of their generation depth.

The quantum efficiency of the pnCCD for scintillation light is set to the same values as for the single SDD cell, which has been coupled to CsI(Tl) (see Fig. 5.13).

Fig. 7.37 shows the distribution of scintillation photons, generated inside a 0.7

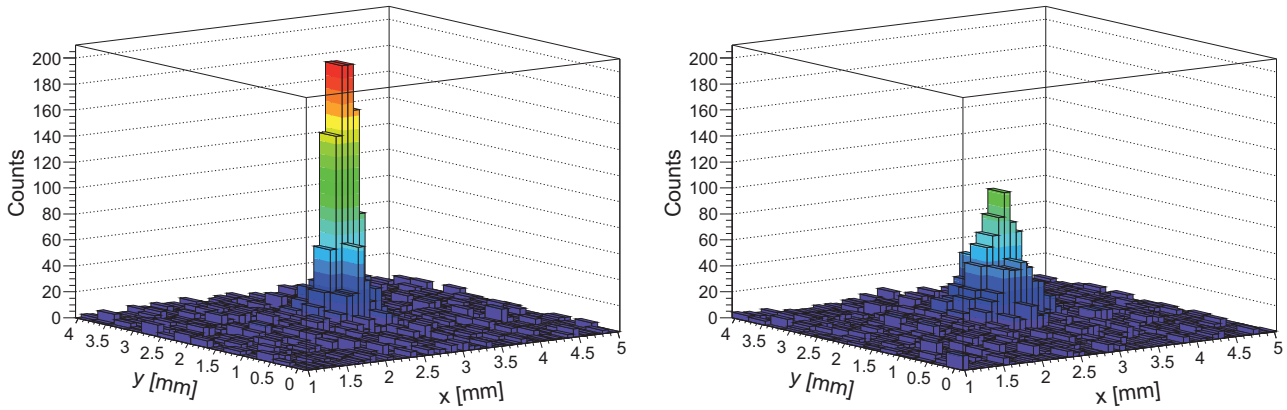

Figure 7.37.: *Simulated distribution of signal electrons inside the pixels with an area of 75* x *300* μm^2. *The electronic noise is* ENC_{el} = *3 electrons, the light yield* $\overline{L}$ = *70 photons/keV. An energy of 100 keV has been deposited at two depths inside the 0.7 mm thick CsI(Tl) at z = 0.05 (on the left) and 0.25 mm (on the right) from the pnCCD surface.*

mm thick CsI(Tl) scintillator, over the pnCCD pixels with the dimension 75 x 300 μm^2. At two depths inside the scintillator an energy of 100 keV has been deposited. With increasing distance to the pnCCD the same amount of scintillation photons is spread over an increasing number of pixels. The distribution over a larger number of pixels increases the electronic noise after summing up the signals of the pixels above threshold. Also the number of photons, which fall below the data acquisition threshold, increases. The standard deviations of the spatial distribution of signal electrons inside the pnCCD for two CsI(Tl) thicknesses, 0.7 and 1 mm, and two types of reflectors on top of the CsI(Tl) scintillator, are illustrated in Fig. 7.38. In one case a diffuse reflector is positioned on top of the scintillator with an infinitesimal thin air gap in between (reflector 1). In the other case the scintillator surface on top is painted with a diffuse reflective coating (reflector 2). The reflectivity is set to 0.98 in both cases. The sides of the scintillator are painted with an absorptive coating. Increasing the distance from the pnCCD surface into the scintillator increases the standard deviation of the spatial distribution until it saturates close to the top surface. The distribution width of scintillation photons reaches larger values for the 1 mm compared to the 0.7 mm thick scintillator, if the generation of scintillation photons is close to the top of the scintillator, because the photons have to cover longer lateral distances to reach the pnCCD. The photon distribution width is slightly larger in the center of the scintillator for the configuration with reflector 2.

A large fraction of generated scintillation photons do not contribute to the production of signal electrons. If the mean light yield of CsI(Tl) is 60 scintillation photons per keV, a 100 keV γ-photon generates $\overline{N}_{ph}$ = 6000 scintillation photons, if the whole energy is deposited inside the scintillator. The mean number of signal electrons, $\overline{N}_e$, results from the mean value of the light and charge collection efficiency, $\overline{\eta}$, times $\overline{N}_{ph}$. For the configuration with the 0.7 mm thick scintillator the

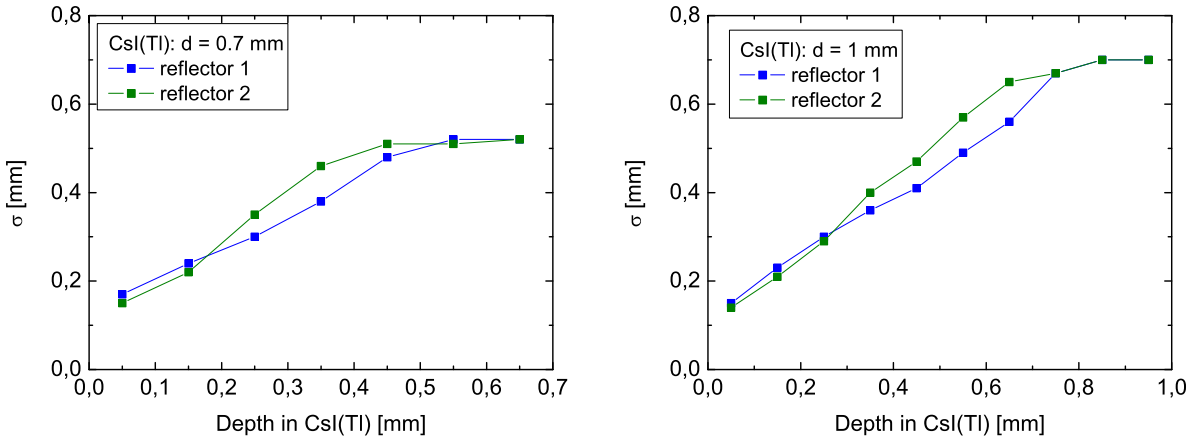

Figure 7.38.: *Standard deviation of the simulated distribution of signal electrons as a function of the generation depth for two reflector types and scintillator thicknesses.*

mean numbers of signal electrons are $\overline{N}_e \approx 0.7 \cdot \overline{N}_{ph} = 4200$ (reflector 2) and $\overline{N}_e \approx 0.39 \cdot \overline{N}_{ph} = 2340$ (reflector 1). For the configuration with the 1 mm thick scintillator the mean numbers of signal electrons are $\overline{N}_e \approx 0.62 \cdot \overline{N}_{ph} = 3720$ (reflector 2) and $\overline{N}_e \approx 0.39 \cdot \overline{N}_{ph} = 2280$ (reflector 1). A large fraction of the generated scintillation photons is not converted into signal electrons. If the number of scintillation photons generates a signal below the data acquisition threshold, they are not taken into account. This additional loss of scintillation photons depends crucially on the number of pixels over which they are distributed. The width of the photon distribution in dependence on the generation depth can lead to a shift of the signal electron peak for certain values of the electronic noise, the pixel size, the scintillator light yield and the reflector type.

The energy resolution of the system pnCCD + CsI(Tl) for the case that there is no loss of signal electrons, because of the data acquisition threshold, is illustrated in Fig. 7.39 for the configuration with reflector 1 (on the left) and reflector 2 (on the right). The main contributions to the energy resolution are R_T and R_{Bino}, if reflector 1 is used and only R_T, if reflector 2 is used. The sum of all contributions is given by R_{sum}, whose value is the lowest reachable value of the energy resolution, if no signal electrons are lost, due to a certain data acquisition threshold. Its influence on the detector response is investigated in the following.

Fig. 7.40 presents the mean number of signal electrons, which is given by the peak position in the simulated spectra, as a function of the generation depth of scintillation photons inside CsI(Tl). Scintillation photons are generated by depositing an energy of 100 keV at certain depths inside the CsI(Tl). Results for pixel sizes of 75 x 300 μm^2 and 300 x 300 μm^2 and CsI(Tl) thicknesses of 0.7 mm and 1 mm for the pnCCD + CsI(Tl) detector are illustrated. The light yield, $\overline{L}$, and the electronic noise, ENC_{el}, have been set in pairs to (50 $\overline{N}_{ph}/keV$, 5 e^-), (60 $\overline{N}_{ph}/keV$, 4 e^-) and (70 $\overline{N}_{ph}/keV$, 3 e^-). The data acquisition threshold is 4·ENC_{el}, if not stated otherwise. The configurations with reflector 1 or 2 are displayed by a solid or dotted curve

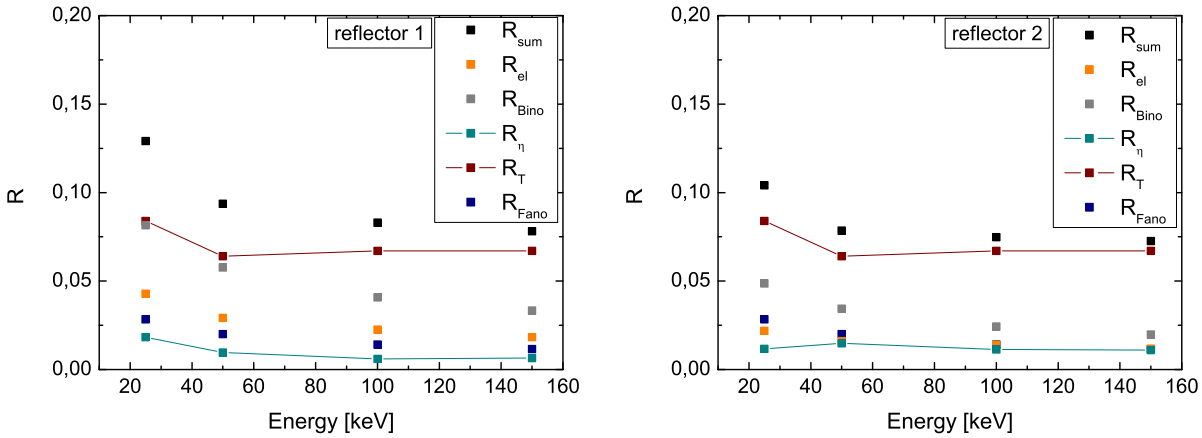

Figure 7.39.: *Contributions to the energy resolution for the configurations with reflector 1 (on the left) and 2 (on the right), if the loss of signal electrons, due to a certain data acquisition threshold value, is not taken into account. The pixel size is 75 x 300 μm^2, the CsI(Tl) scintillator thickness is 0.7 mm, the light yield $\overline{L}$ = 60 N_{ph}/keV and the electronic noise ENC_{el} = 4 electrons.*

respectively (Fig. 7.40). Most of the parameter assemblies lead to a large shift of the signal electron peak, if the generation depth of scintillation photons inside CsI(Tl) is changed. For the detector configuration with a pixel size of 75 x 300 μm^2 and reflector 1 applies that an increasing distance of the generation depth of scintillation photons to the pnCCD surface, decreases the number of signal electrons, because a higher number of scintillation photons fall below the data acquisition threshold, due the distribution of scintillation photons over a larger number of pixels (Fig. 7.40(a) and 7.40(c) solid curves). An exception is the configuration with the 0.7 mm thick CsI(Tl) scintillator and the light yield of 70 $\overline{N}_{ph}/keV$, where the number of signal electrons is slightly increasing.

In case of the detector configuration with reflector 2 and a pixel size of 75 x 300 μm^2 (Fig. 7.40(a) and 7.40(c) dashed curves) the number of signal electrons also decreases with an increasing distance of generation depth of scintillation photons to the pnCCD surface for a scintillator thickness of 1 mm and light yields of 50 and 60 $\overline{N}_{ph}/keV$. It increases otherwise, due to the fact, that more photons are reflected into a smaller number of pixels, if the generation point approaches the interface of reflector 2 and the scintillator.

If the pixel size of the pnCCD is 300 x 300 μm^2 the number of signal electrons increases with increasing distance of the generation depth of scintillation photons from the pnCCD surface, independent on the reflector type (Fig. 7.40(b) and 7.40(d)). For a pnCCD with a pixel size of 300 x 300 μm^2 the strongest increase of the mean number of signal electrons with increasing distance of the generation depth of scintillation photons to the pnCCD surface happens for the scintillator with a thickness of 1 mm and reflector 2. If the scintillator thickness is 0.7 mm, simulations indicate that the shift decreases with an increasing light yield from 50 to 70 photons per keV

for the configuration with reflector 2.

Five curves show a smaller shift of the signal electron peak. These are in Fig. 7.40(a) the brown (dotted), the green (solid) and the violet (solid) curves and in Fig. 7.40(b) the violet (dotted) curve of the 0.7 mm thick scintillator and in Fig. 7.40(d) the brown (solid) curve of the 1 mm thick scintillator. The shift of the mean number of signal electrons as a function of the generation depth, can have a large effect on the energy resolution, especially for γ-rays with higher energies, such as 100 and 150 keV, due to the more uniform absorption of γ-rays over the whole CsI(Tl) thickness. This leads to a degradation of the energy resolution. In case of

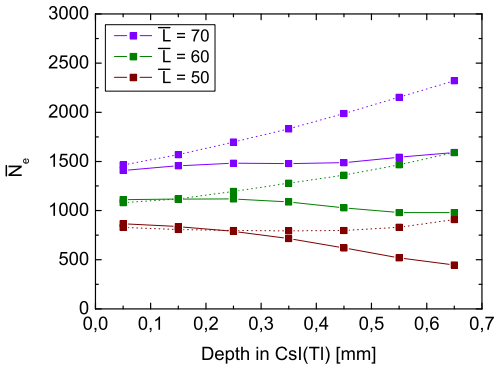

(a) *CsI(Tl) thickness of 0.7 mm; Pixel size of 75* x 300 μm^2.

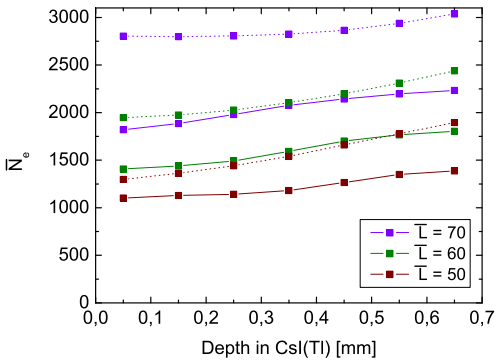

(b) *CsI(Tl) thickness of 0.7 mm; Pixel size of 300* x 300 μm^2.

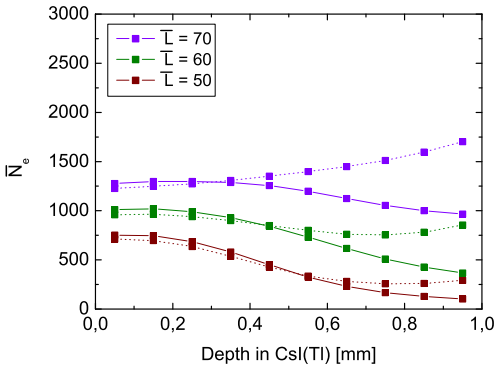

(c) *CsI(Tl) thickness of 1 mm; Pixel size of 75* x 300 μm^2.

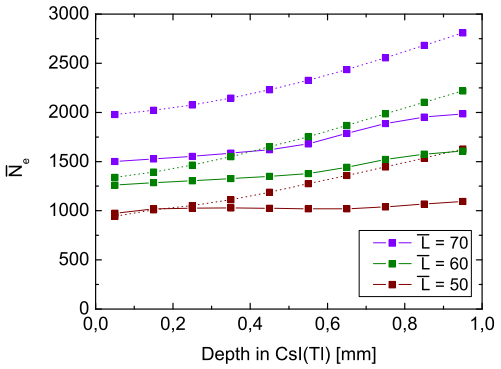

(d) *CsI(Tl) thickness of 1 mm; Pixel size of 300* x 300 μm^2.

Figure 7.40.: *Simulated mean number of signal electrons plotted against the generation depth of scintillation photons after the deposition of an energy of 100 keV. Solid lines belong to the reflector 1 and dotted lines to the reflector 2 configuration. A threshold for data acquisition of 4·ENC_{el} has been set. The light yields of $\overline{L}$ = 50, 60 and 70 $\overline{N}_{ph}$/keV have electronic noise values of ENC_{el} = 5, 4 and 3 electrons respectively.*

the detector with the set of parameters leading to the brown dotted curve in Fig. 7.40(a) the light yield of 50 photons per keV is too low to generate a spectrum with a clearly distinguishable signal electron peak for γ-energies of 25 and 50 keV.

The contribution of the intrinsic CsI(Tl) properties to the resolution is incorporated by the same approximation into the simulations as described in Sec. 7.2 with the same parameter value for r_{intr}.

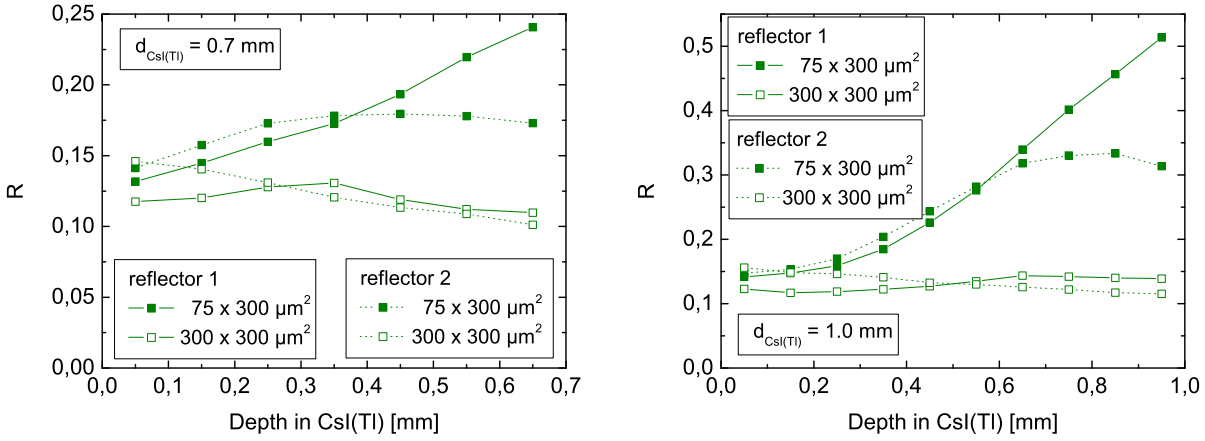

Figure 7.41.: *Energy resolution against generation depth of the scintillation photons inside a 0.7 and 1.0 mm thick CsI(Tl) scintillator. An energy of 100 keV is deposited.*

In Fig. 7.41 the energy resolution is plotted against the generation depth of scintillation photons, which are created after an energy of 100 keV is deposited inside the 0.7 and 1.0 mm thick CsI(Tl) scintillator respectively. If the CsI(Tl) scintillator is 0.7 mm thick, the poorest resolution occurs for the detector with a pixel size of 75 x 300 μm^2 and reflector 1. The resolution degrades to R = 0.24 at a depth of 0.65 mm from the pnCCD - CsI(Tl) interface. If the CsI(Tl) scintillator is 1 mm thick, the energy resolution degrades much faster with increasing generation depth of scintillation photons, from R $\approx$ 0.15 to a maximum value of 0.33 and 0.51 for reflector 2 and reflector 1 respectively and a pixel size of 75 x 300 μm^2. For the detector with the larger pixel size of 300 x 300 μm^2 the energy resolution remains in the range of R = 0.1 to 0.16.

For some detector configurations the simulated relative energy resolution in dependence on the γ-energy are plotted in Fig. 7.42. Values connected with solid lines belong to detector configuration, which lead to smaller peak shifts. A decrease of the light yield from 70 to 60 scintillation photons per keV and an increase of the electronic noise value from 3 to 4 electrons leads to an increase of the energy resolution, especially at 25 keV, if the pixel size is 75 x 300 μm^2 (Fig. 7.42 on the left). This effect is smaller for a pixel size of 300 x 300 μm^2. A larger pixel size improves also the energy resolution at 25 and 50 keV. An increase of the scintillator thickness has almost no effect on the energy resolution (Fig. 7.42 on the right) for a light yield of 50 scintillation photons per keV. For 100 and 150 keV the energy resolution can be improved in some cases by setting the data acquisition threshold to a higher value, e.g. 6·ENC$_{el}$.

The spatial resolution is better for events, where scintillation photons are generated close to the pnCCD entrance window, because they are distributed over a

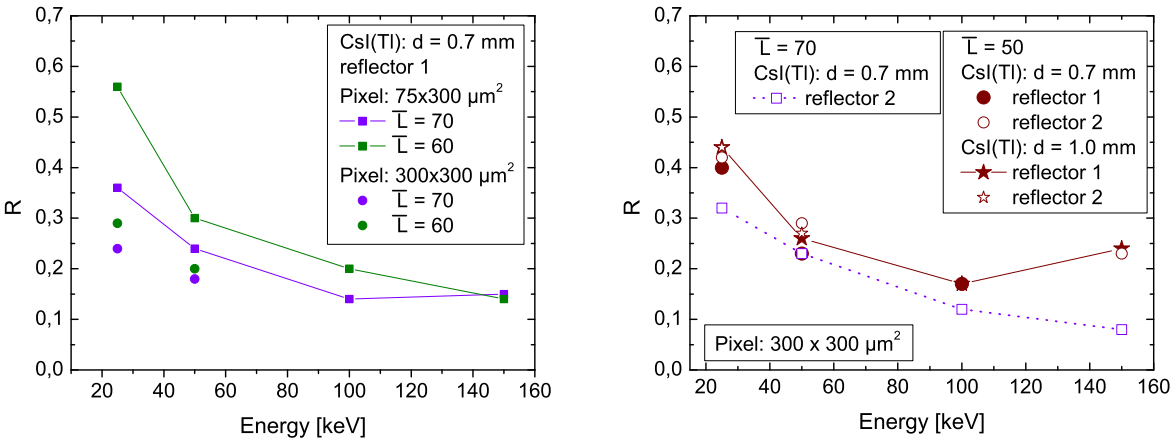

Figure 7.42.: *Simulated relative energy resolution for the energies 25, 50, 100 and 150 keV. The threshold for data acquisition has been set to 4·ENC$_{el}$.*

smaller number of pixels, leading to a larger signal to noise ratio. If an energy of 100 keV is converted into scintillation photons, the standard deviation of the spatial resolution can differ by a value up to 30 μm, if scintillation photons are generated close to the pnCCD entrance window or close to the CsI(Tl) top surface.

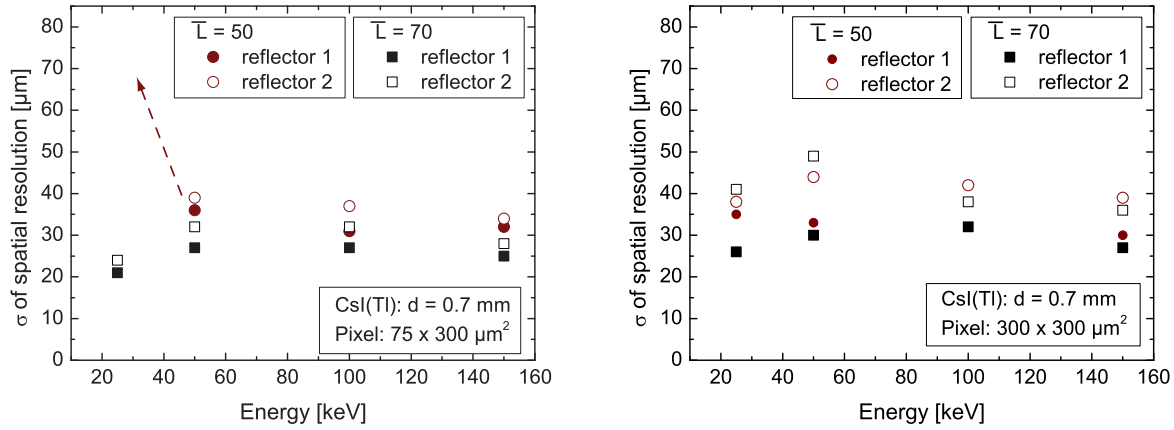

Figure 7.43.: *Simulated spatial resolution corresponding to the energy resolutions presented in Fig.7.42 for the energies 25, 50, 100 and 150 keV. The threshold for data acquisition has been set to 4·ENC$_{el}$.*

The standard deviation of the spatial resolution, determined from a Gaussian fit over the reconstructed coordinates, as a function of the γ-energy, for the sets of parameters with $\overline{L} = 50$ (ENC$_{el}$ = 5 electrons) and $\overline{L} = 70$ (ENC$_{el}$ = 3 electrons) scintillation photons per keV, a CsI(Tl) thickness of 0.7 mm and pixel sizes of 75 x 300 μm^2 and 300 x 300 μm^2 are presented in Fig. 7.43. Its value is in the range between 15 μm and 50 μm in Fig. 7.43. Except for energies E $<$ 50 keV and for the detector with a pixel size of 75 x 300 μm^2 and a light yield of $\overline{L} = 50$ (ENC$_{el}$ =

5 electrons) scintillation photons per keV, the spatial resolution degrades to values $\sigma > 50$ μm, due to the low signal to noise ratio. In contrast to that, the spatial resolution improves slightly at 25 keV compared to 50 keV, if the detector parameters are set to $\overline{L} = 70$ N_{ph}/keV with $ENC_{el} = 3$ electrons, due to the fact, that most of the events occur closer to the pnCCD surface, so that the signal to noise ratio is increased in spite of the lower energy.

Reflector 1 leads usually to a better spatial resolution than reflector 2. An increase of the CsI(Tl) thickness from 0.7 to 1 mm can degrade the spatial resolution at 25 and 50 keV by a value up to 15 μm (but the spatial resolution does not exceed a value of 55 μm), if the light yield is $\overline{L} = 50$ scintillation photons per keV (with $ENC_{el} = 5$ electrons) and the pixel size is 75 x 300 μm^2.

Results of simulations for pixel sizes of 75 x 75 μm^2, a light yield of 70 scintillation photons per keV, an electronic noise of 3 electrons and a threshold for data acquisition of $4 \cdot ENC_{el}$ show that no clear spectrum can be recorded in indirect detection mode for this set of detector parameters. The spatial resolution can be determined nevertheless for these detector parameters and their values are in the same range as shown in Fig. 7.43.

Spectra of the configuration with the pixel size of 75 x 300 μm^2, the electronic noise of $ENC_{el} = 4$ electrons, a data acquisition threshold of 16 electrons, a CsI(Tl) thickness of 0.7 mm and reflector 1 are shown in Fig. 7.44. On the left side of the

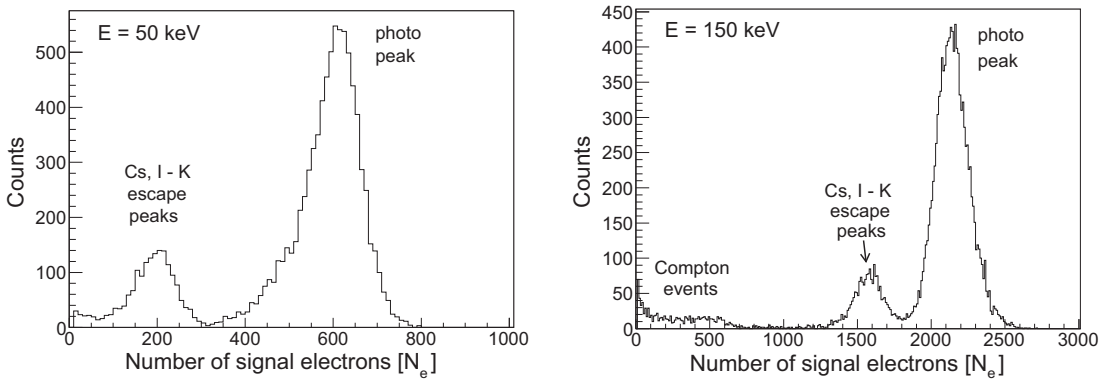

Figure 7.44.: *Simulated spectra for the detector parameters: pixel size 75 x 300 μm^2, $ENC_{el} = 3$ electrons, light yield of 70 photons/keV, CsI(Tl) thickness of 0.7 mm, reflector 1 and a data acquisition threshold of 4 ENC_{el} (on the left) and 6 ENC_{el} (on the right).*

photo peak, there is the escape peak, originating from the escape of $K_{\alpha,\beta}$ fluorescence photons from the relaxation of the excited Cs and I atoms in the scintillator.

Below 200 keV the probability for photo effect is larger than for Compton scattering inside CsI, so that events from Compton scattering play only a minor role, especially below 100 keV. Determined from simulated spectra, the ratio of the number of events inside the escape to the events inside the photo peak are in the range between 0.22 and 0.09. The increase of the CsI(Tl) thickness from 0.7 to 1 mm leads to a reduction of the ratio up to 35 % of the number of events inside the escape peak to the number of events inside the photo peak. The number of events inside the escape peaks together with the number of events generated by Compton

scattering and photo effect add up to the number of γ-rays, which interacted inside the scintillator. From this number and the number of events detected directly inside the pnCCD, the total number of incident γ-rays can be determined, if the QE of the detector system is known.

To conclude, it can be said, that for the considered parameters the best energy resolution in indirect detection mode can be expected for the pnCCD with the larger pixel size of 300 x 300 μm^2 and the thinner CsI(Tl) scintillator with a thickness of 0.7 mm. Whether reflector 1 or 2 leads to a better energy resolution, depends crucially on the energy of the γ-ray, the light yield of the CsI(Tl) scintillator, the electronic noise value per pixel and the value of the data acquisition threshold. An improvement of the energy resolution can be achieved for incident γ-rays with energies around 100 keV and higher by increasing the data acquisition threshold. By this method, events, which have generated scintillation photons above a certain distance from the pnCCD - CsI(Tl) interface, can be disregarded. The spatial resolution in the indirect detection mode is slightly better for the detector configuration with reflector 1.

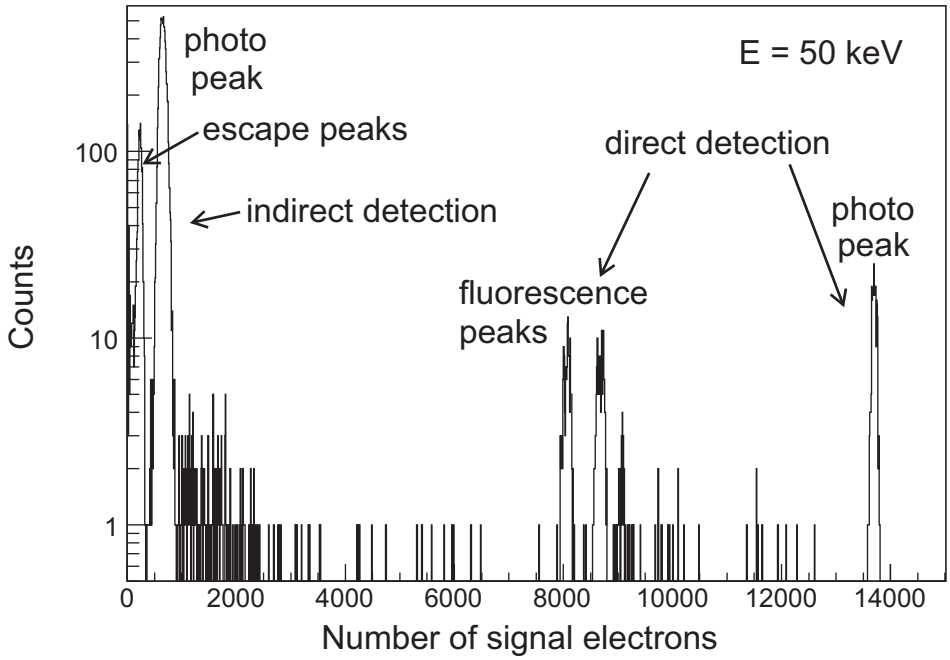

Figure 7.45.: *Simulated spectrum including the direct and indirect detection events for incident photons with an energy of 50 keV. The number of incident photons is 10000.*

A spectrum including directly and indirectly detected events is presented in Fig. 7.45. In order to reconstruct such a spectrum from the measured pnCCD response, the fingerprints of all possible interaction processes (e.g. Compton, photo, fluorescence, escape) have to be known, in order to assign the response of the pnCCD to the right process or processes and energy. Events from the direct and indirect detection mode can be discriminated by examining the distribution of signal electrons over the pixels and the number of signal electrons in each pixel.

Results from simulations indicate that the energy and spatial resolution in the indirect detection mode is suitable for distinguishing the energy inside and the positions of different Laue spots. The energy resolution at high energies can also be determined from the direct detection mode, if enough photons are incident onto the pnCCD to compensate its low quantum efficiency.

8. Summary and Conclusions

In this work we have investigated X- and γ-ray detectors consisting of SDDs or pnCCDs coupled to scintillators, such as CsI(Tl) and $LaBr_3$(Ce), in order to define limitations of the detector performance and to uncover possibilities to improve it.

In literature a detailed description of all relevant contributions to the energy resolution for the whole detector system consisting of a SDD / pnCCD coupled to a scintillator is still missing. In this work the relevant contributions to the energy resolution for a detector system consisting of a single SDD cell coupled to CsI(Tl) or $LaBr_3$(Ce) in the energy range from 6 keV to 662 keV and for a SDD array or pnCCD coupled to CsI(Tl) for energies smaller or equal 150 keV have been determined.

A formula for the relative energy resolution has been derived from a statistical treatment of the overall process, from the interaction of γ-rays with the scintillator to the collection of signal electrons at the detector anode. If the smallest terms in this formula are neglected, the remaining terms originate from the Fano noise inside the scintillator, the energy dependent conversion efficiency of the generated electrons and holes into scintillation photons, the inhomogeneous light and charge collection efficiency, the binomial term, which describes statistical fluctuations of the number of signal electrons, due to a mean conversion efficiency of generated electrons and holes inside the scintillator into signal electrons, and the electronic noise. The scintillator shape, thickness, surface roughness, the type and reflectivity of the reflector and the quantum efficiency of the SDD or pnCCD affect the value of the light and charge collection efficiency, hence the number of signal electrons. In literature the Fano noise contribution of the scintillator is generally not investigated and instead of the binomial term, a Poisson term is usually used to describe the statistical contribution, which is not a good approximation for modern scintillation detectors anymore.

In case of the γ-detector consisting of a single SDD cell coupled to the scintillator, one of the main contributions to the energy resolution can be attributed to the energy dependent conversion efficiency of electrons and holes into scintillation photons. Its contribution to the energy resolution and light yield as a function of γ-energy is determined by a combination of Monte Carlo simulations and analytical models. At first the interaction of the γ-ray inside the scintillator and the generation of photo, Compton and Auger electrons is simulated. To each of these electrons a number of scintillation photons is attributed. The electron light yield is used as an input to calculate the total mean number of generated scintillation photons. The conversion efficiency of the generated electrons and holes into scintillation photons, which is proportional to the electron light yield, is determined with analytical models proposed by Birks [84, 116] and Onsager [85, 86]. These models describe a reduction of the conversion efficiency at high and low energy densities. Landau fluctuations of the deposited energy along the track of the electrons through the scintillator lead to fluctuations of the conversion efficiency [25, 49, 100], hence to fluctuations of the

number of generated scintillation photons.

From these results, the so called scintillator "non-proportionality" contribution to the light yield and the energy resolution are extracted for incident γ-rays. The calculated energy dependent light yield of $LaBr_3$(Ce) and the calculated contribution of the non-proportionality of $LaBr_3$(Ce) and CsI(Tl) to the energy resolution in the energy range 6 keV - 662 keV are presented for the first time in this work.

The simulated values of the light yield and the total energy resolution are in good agreement with results from measurements within the error bars in the energy range from 6 to 662 keV for single SDD cells coupled to $LaBr_3$(Ce) and CsI(Tl).

The limitation for a further improvement of the energy resolution of γ-detectors consisting of a single SDD cell coupled to $LaBr_3$(Ce) or to CsI(Tl) is determined by the non-proportionality of the scintillators. Scintillators with a similar or higher light yield and a more proportional response, such as the recently developed SrI_2(Eu) and $LaBr_3$(Ce):Sr [25, 126], are promising candidates for a further improvement.

The energy and spatial resolution of a γ-camera consisting of a SDD array with 77 hexagonal cells and an active area of 29 x 26 mm^2 coupled to a 5 mm thick CsI(Tl) scintillator have also been investigated in this work. From measurements and simulations a spatial sub pixel resolution of 0.5 mm and 1.1 mm at 60 keV and 122 keV and a relative energy resolution of about 0.37 have been determined. Results from simulations of the detector response show that the main contributions to the energy and spatial resolution originate from the low signal to electronic noise ratio in combination with a high data acquisition threshold. This leads to large fluctuations in the number of signal electrons and to a dependence of the mean number of signal electrons on the distance of the generation depth of scintillation photons inside the scintillator from the SDD surface. These contributions can be decreased by using thinner CsI(Tl) scintillators, but mostly by a reduction of the electronic noise and data acquisition threshold.

In order to develop a detector with a good energy and spatial resolution in the energy range 1 keV - 150 keV a γ-camera has been investigated by simulations consisting of a pnCCD coupled to a CsI(Tl) scintillator with a thickness of 0.7 mm or 1 mm and pnCCD pixel sizes of 75 x 300 μm^2 and 300 x 300 μm^2. The detector is irradiated from the pnCCD side, so that photons with energies up to 15 keV are mainly detected directly by the pnCCD. Photons with higher energies are mainly absorbed inside the CsI(Tl) scintillator and the scintillation photons are then detected by the pnCCD, which is denoted as the indirect detection mode. Simulations indicate that the spatial resolution of these detectors is better than 80 μm. In indirect detection mode energy resolution values of about 10 keV to 15 keV could be possible in a narrow parameter range, determined by the electronic noise, the light yield of CsI(Tl), the type and reflectivity of the reflector and the pnCCD pixel size. These results suggest that this detector system can be used as a X- and γ-ray detector for diffraction analysis in the energy range 1 keV - 150 keV.

It can be said that the detector systems SDD or pnCCD coupled to $LaBr_3$(Ce) or CsI(Tl) have been understood, so that origins of limitations of the energy and spatial resolution are defined and possibilities for improvements are presented.

A. Physical background of solid state radiation detectors

A.1. Interaction of photons with matter

A.1.1. Interaction of X- and γ-rays with matter

In the energy range $2m_ec^2(1+m_e/M) \leq E < 4m_ec^2$ the pair production takes place close to the nucleus. A photon transforms near the nucleus into an electron and positron pair with kinetic energies $E_{kin} = 0.5(E - 2m_ec^2)$. For photon energies $E \geq 4m_ec^2$ the energy and momentum conservation enables the pair production also in the field of an atomic electron, which receives a part of the momentum and energy. The ratio of the pair production cross section near the atomic electron to that near the nucleus is

$$\frac{\Phi_{pair,elec}}{\Phi_{pair,nucl}} = \frac{1}{\widetilde{C}Z} \tag{A.1}$$

where $\widetilde{C} \approx 2.6$ at E = 6.5 MeV [19]. For Z = 35, which is the atomic number of Br, the Eq. A.1 yields 0.01, so that $\Phi_{pair,elec}$ can be neglected around E = 6.5 MeV. An approximate formula for the total pair creation cross section, valid in the energy range $2m_ec^2(1+m_e/M) \leq E < 7.5m_ec^2$ and for no screening of the field of the nucleus by the atomic electrons, has been calculated by Hough [138]:

$$\begin{aligned} \Phi_{pair,nucl} &= \alpha r_e^2 Z^2 \cdot \left(0.776\Phi_{pair,0} + 0.018\Phi_{pair,0}^2\right) \qquad (E > 2.1MeV) \\ \Phi_{pair,nucl} &= \alpha r_e^2 Z^2 \cdot 0.785\Phi_{pair,0} \qquad (E < 2.1MeV) \end{aligned} \tag{A.2}$$

where

$$\Phi_{pair,0} = 4\left(1 - \frac{2}{\kappa}\right)\left[\left(1 - \frac{1}{\kappa^2}\right)\left(\widetilde{K} - 1\right) - \frac{4\chi}{\kappa^2}\left(\chi - 1 - \frac{4}{\kappa^2}\left(\widetilde{K} - \chi\right)\right)\right] \tag{A.3}$$

and

$$\begin{aligned} \widetilde{K} &= \frac{1}{1 - \left(\frac{2}{\kappa}\right)^2} ln\left(\frac{\kappa}{2}\right) \\ \chi &= \frac{1}{\sqrt{1 - \left(\frac{2}{\kappa}\right)^2}} ln\left(\frac{\kappa}{2} + \sqrt{\left(\frac{\kappa}{2}\right)^2 - 1}\right). \end{aligned} \tag{A.4}$$

The field of the nucleus is not screened, because the pair creation occurs near the nucleus without atomic electrons in-between. For heavier elements the error of formula A.2 is expected to be larger, because of the Born approximation, which

is assumed in its derivation [19]. The ratio of the experimental, $\Phi_{pair,exp}$, to the theoretical, Φ_{pair}, cross section can be described by

$$\frac{\Phi_{pair,exp}}{\Phi_{pair}} = 1 - 1.5 \cdot 10^{-5} Z^2 \tag{A.5}$$

for energies E > 5 MeV [19]. Eq. A.5 yields for La with Z = 57 a ratio of 0.95.

A.1.2. Interaction of UV−Vis photons with matter

The absorption coefficient for direct transitions, where the electron has the same wave vector **k** in the initial and final state, from the valence into the conduction band is given by [139, 40]

$$\alpha = \frac{\pi e^2 \hbar}{\epsilon_0 m_e^2 ncE} \sum_{\mathbf{k}} |P_{cv}|^2 f_v(\mathbf{k})(1 - f_c(\mathbf{k}))\delta\left(E_c(\mathbf{k}) - E_v(\mathbf{k}) - E\right) \tag{A.6}$$

where e is the electron charge, $\hbar$ the Planck constant h over 2π, ϵ_0 the dielectric constant, m_e the electron mass, n the refraction index, c the velocity of light, E_c and E_v the electron energy in the conduction and valence band, $|P_{cv}|^2$ the momentum matrix element of the electric dipole transition and $f_{k,v}$ and $f_{k,c}$ the Fermi-Dirac distributions for electrons to occupy the valence and the conduction band at **k**. The summation in Eq. A.6 over all **k**, fulfilling the relation $E = E_c(\mathbf{k}) - E_v(\mathbf{k})$, can be replaced by an integral over a constant energy surface [139]. For double degenerate conduction and valence bands the sum over **k** can be expresses by

$$\sum_{\mathbf{k}} \rightarrow \int D_j\left(E_{cv}\right) dE_{cv} = \frac{2}{(2\pi)^3} \int \oint_{E_{cv}=const} \frac{dS_{\mathbf{k}}}{|\nabla_{\mathbf{k}}\left(E_{cv}\right)|} dE_{cv} \tag{A.7}$$

where D_j is the joint density of states, E_{cv} = E_c - E_v the excitation energy, $S_{\mathbf{k}}$ the constant energy surface defined by E_{cv} = constant. Inserting Eq. A.7 into A.6 yields

$$\alpha = \frac{e^2 \hbar}{4\pi\epsilon_0 m_e^2 ncE} \int \oint_{E_{cv}=const} |P_{cv}|^2 f_v(\mathbf{k})(1 - f_c(\mathbf{k})) \frac{dS_{\mathbf{k}}}{|\nabla_{\mathbf{k}}\left(E_{cv}\right)|} dE_{cv}. \tag{A.8}$$

For certain photon energies the joint density of states of the conduction and valence band becomes maximum. For these energies $|\nabla_k\left(E_{cv}\right)| = 0$, where E_{cv} = E_c - E_v. This leads to so called Van Hove singularities [140] in the joint density of states. In Fig. 2.8 the band structure of intrinsic silicon is illustrated [41]. Two regimes with excitation energies, E_1 and E_2, give rise to Van Hove singularities in the joint density of states, hence to characteristic points of the absorption coefficient of silicon at E = E_1 and E_2 (Fig. A.1).

For photon energies close to the energy gap, phonons have to participate in the absorption process, because silicon is an indirect semiconductor. Thus the excitation of an electron from the valence into the conduction band is a second order process with a lower absorption coefficient compared to the direct transitions. Eq. A.6 has to be extended by the electron phonon matrix element, which describes the probability for electron phonon scattering, and the phonon occupation number, $\overline{n}_{ph}$, which is temperature dependent. In the parabolic band approximation, for photon energies

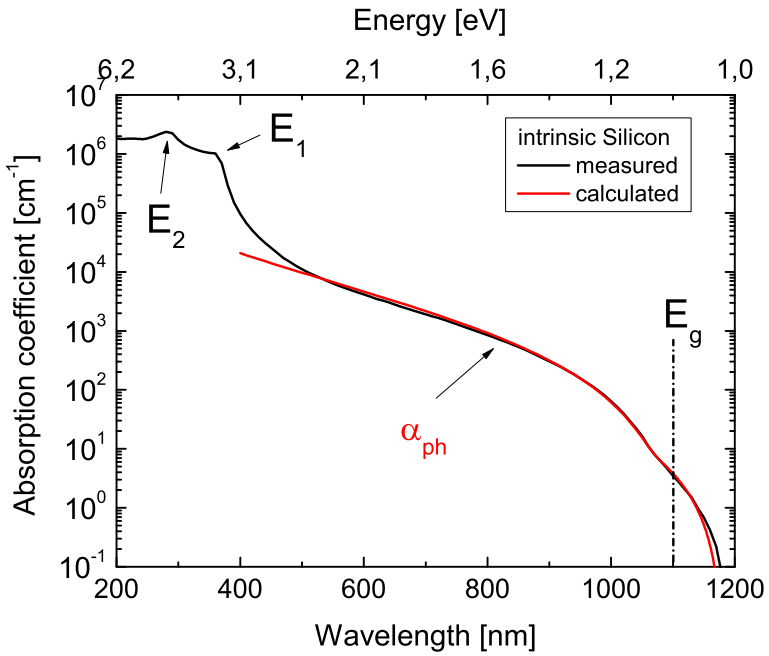

Figure A.1.: *Absorption length and coefficient of intrinsic silicon at 300 Kelvin. Data of the absorption coefficient are taken from [42].*

close to the energy gap, the absorption coefficient for indirect semiconductors can be described by [141]

$$\alpha_{ph} = D^2 \cdot \left[\overline{n}_{ph} \left(E - E_g + E_{ph}\right)^2 + \left(\overline{n}_{ph} + 1\right) \left(E - E_g - E_{ph}\right)^2\right] \tag{A.9}$$

where D is depending on material properties and temperature, E_g is the energy gap,

$$\overline{n}_{ph} = \frac{1}{exp\left(\frac{E_{ph}}{k_B T_{emp}}\right) - 1}, \tag{A.10}$$

where E_{ph} is the phonon energy and T_{emp} the temperature. The first term in Eq. A.9 describes the absorption process with the absorption and the second term with the emission of a phonon. For photon energies $E \leq E_g + E_{ph}$ only the first term of Eq. A.9 determines the absorption coefficient, because only the process where a phonon is absorbed is possible.

Fig. A.1 shows the absorption coefficients of intrinsic silicon presented in [42] (black curve) and calculated with formula A.9 and the parameters D = 64 cm$^{-0.5}$eV^{-1}, E_g = 1.1 eV and E_{ph} = 0.05 eV [141] (red curve). The curves are in good agreement in the wavelength range from 500 to 1150 nm.

For doped semiconductors, formula A.9 changes, because of a shift of the Fermi level, due to the filling of the conduction band with electrons or the valence band

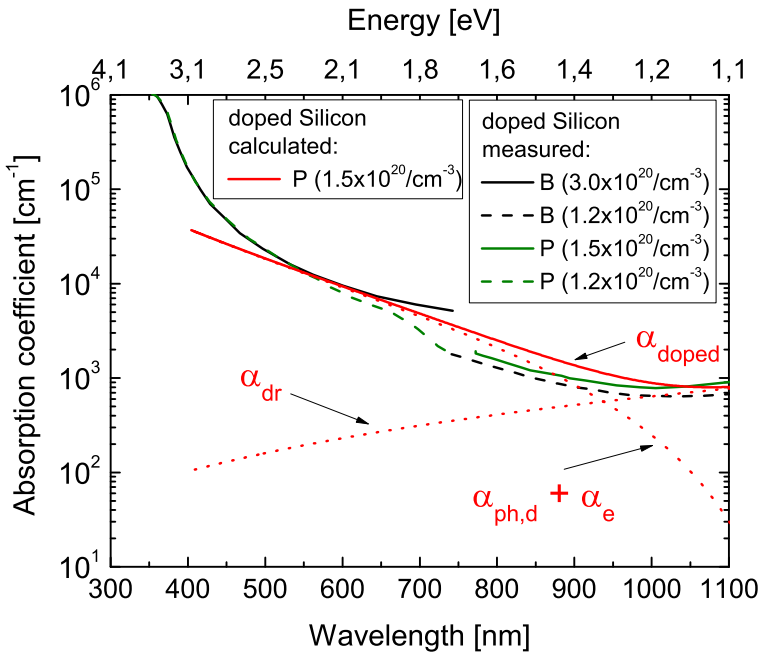

Figure A.2.: *Absorption length and coefficient of Boron doped p^+ and Phosphor doped n^--type silicon at 300 Kelvin. Data of the absorption coefficient are taken from [43, 44, 45].*

with holes, to [43]

$$\alpha_{ph,d} = \frac{8D^2}{\pi} \cdot \left[\frac{(E - E_g + E_{ph})^2}{exp\left(\frac{E_{ph}}{k_B T_{emp}}\right) - 1} \int_0^1 \frac{x^{1/2}(1-x)^{1/2}}{1 + exp\left(\frac{E_F - (E - E_g + E_{ph})x}{k_B T_{emp}}\right)} dx \right] + \frac{8D^2}{\pi} \cdot \left[\frac{(E - E_g - E_{ph})^2}{1 - exp\left(-\frac{E_{ph}}{k_B T_{emp}}\right)} \int_0^1 \frac{x^{1/2}(1-x)^{1/2}}{1 + exp\left(\frac{E_F - (E - E_g - E_{ph})x}{k_B T_{emp}}\right)} dx \right] \tag{A.11}$$

where E_F is the distance of the Fermi level to the conduction band minimum or the valence band maximum. E_g decreases with increasing doping concentrations. In addition in doped semiconductors, there is also the possibility to conserve the momentum of the excitation process by electron-electron or impurity scattering [142, 143]. This contribution to the absorption coefficient of doped indirect semiconductors can be written as [43]

$$\alpha_e = \frac{8\widetilde{B}^2}{\pi} \cdot (E - E_g)^2 \int_0^1 \frac{x^{1/2}(1-x)^{1/2}}{1 + exp\left(\frac{E_F - (E - E_g)x}{k_B T_{emp}}\right)} dx \tag{A.12}$$

where $\widetilde{B}$ is a parameter, depending on the doping concentration.

There is a third absorption process in heavily doped semiconductors. This is the free carrier absorption, where electrons or holes are excited within the same band:

$$\alpha_{dr} = \frac{e^3 h^2 N}{4\pi^2 \epsilon_0 m_e^{*2} n c \mu_e} \cdot \frac{1}{E^2}. \tag{A.13}$$

where N is the concentration of electrons in the conduction band, m_e^* the effective electron mass and μ_e the mobility of the electron. The total absorption coefficient in doped semiconductors is then

$$\alpha_{doped} = \alpha_{ph,d} + \alpha_e + \alpha_{dr}. \tag{A.14}$$

In Fig. A.2 the measured and calculated values of the absorption coefficient ($\alpha_{ph,d}$ + α_e, α_{dr}, α_{doped}) are presented. The parameters for n-doped Si, which are inserted into the equations A.11, A.12 and A.13 are $\widetilde{B}^2$ = 1200 $\mathrm{cm}^{-1/2}\mathrm{V}^{-2}$, E_g = 1.045 eV [43], N = $1.5{\cdot}10^{20}\mathrm{cm}^{-3}$, n ≈ 3.63 around 1000 nm [76], μ_e = 50 cm^2/Vs [144] for electrons in doped Si and an impurity concentration of $1.3{\cdot}10^{20}$ cm^3. The calculated absorption coefficient, α_{doped}, describes well the measured values of highly doped silicon for photon energies E < 2.5 eV ($\lambda > 500$ nm).

A.2. Light generation in scintillators

Possibilities for scintillation induced by thermalized electrons and holes are:

- $e + h \rightarrow h\nu$
- $e + h \rightarrow ex \rightarrow h\nu$
- $e + V_k \rightarrow STE \rightarrow h\nu$
- $e + h + A \rightarrow ex + A \rightarrow A^* \rightarrow A + h\nu$
- $e + V_k A \rightarrow STE$ *perturbed by* $A \rightarrow A + h\nu$
- $e + h + A \rightarrow A^{1+} + e \rightarrow A^* \rightarrow A + h\nu$
- $e + h + A \rightarrow A^{1-} + h \rightarrow A^* \rightarrow A + h\nu$
- $A \rightarrow A^* \rightarrow A + h\nu$

where ex is the exciton, V_k the center consisting of a hole localized between two Anions, I^-, in CsI and two Br^- in LaBr_3, A and A^* luminescence centers in the ground and excited state [14, 48]. Self-trapped excitons (STEs) are generated after the V_k center captures an electron.

The spontaneous transition probability for the electric dipole transition between two states, a and b, can be described by [62]

$$\begin{aligned} W(ed) &= \frac{8\pi^2 n}{3\hbar\epsilon_0\lambda^3}\left(\frac{E_{loc}}{E_{mac}}\right)^2 \frac{1}{g_b}\left|\langle\Psi_a(\vec{r})\left|e\mathbf{r}\right|\Psi_b(\vec{r})\rangle\right|^2 \\ &= \frac{8\pi^2 n}{3\hbar\epsilon_0\lambda^3}\left(\frac{E_{loc}}{E_{mac}}\right)^2 \frac{1}{g_b}\left|\mathbf{d}_{ba}\right|^2 \end{aligned} \tag{A.15}$$

where λ is the wavelength of the transmitted photon, n the refraction index of the scintillator, E_{loc} the local electric field, E_{mac} the macroscopic electric field amplitude, g_b the degeneracy of the excited state, Ψ_a and Ψ_b the electronic wave functions of the ground and excited state, $e\mathbf{r}$ the electric dipole moment operator and $\mathbf{d}_{ba}$ the

expectation value of the electric dipole moment operator. The decay time constant of an electric dipole transition is given by

$$\tau(ed) \propto \frac{1}{W(ed)}. \tag{A.16}$$

Thermal quenching causes a decrease of the luminescence and also of the decay time of the luminescence process, because $\tau(T_{emp}) = \tau(ed)\overline{Q}(T_{emp})$ [48], where $\tau(ed)$ is the decay time of the electric dipole transition. Additionaly, there is the probability of energy transfer P_t from one luminescence center to the next one, which increases the luminescence decay time to

$$\frac{1}{\tau_{tot}(T_{emp})} = \frac{1}{\tau(ed)\overline{Q}(T_{emp})} + \frac{1}{\tau_t(T_{emp})} \tag{A.17}$$

where $\tau_t(T_{emp}) = 1/P_t(T_{emp})$.

The transition probability characterized in Eq. A.15 does not include the contribution of lattice vibrations. In order to take this effect into account two approximations are made. The first approximation is to decouple the electronic and nuclear motion, which leads to the adiabatic (Born Oppenheimer 1927) approximation for the overall wave function

$$\Psi(\vec{r}, \vec{R}_l) = \Psi(\vec{r}, \vec{R}_l(0)) \cdot \chi_n(\vec{q}_l) \tag{A.18}$$

where $\vec{r}$ is the electron coordinate, $\vec{R}_l = \vec{R}_l(0) + \vec{q}_l$ the coordinate of the l^{th} ion with $\vec{R}_l(0)$ its average value and $\vec{q}_l$ its displacement, Ψ the electronic wave functions for the static case and χ the vibrational wavefunctions with regard to the motion of the ions. The second approximation is made by regarding only one vibrational mode ω, out of many, in which the ligand ions pulsate about a central ion, so that only one nuclear coordinate X, the so called configurational coordinate, can describe the distance between the ligand and the central ion [64]. The mean distance between the ligand and the central ion in the ground and relaxed, excited state can be described by the normal coordinates, $X_{a,0}$ and $X_{b,0}$. With this additional approximation the wave functions of the ground and excited state take the form

$$\begin{aligned} \Psi_{a,n} &= \Psi_a(\vec{r}, X_{a,0}) \cdot \chi_{a,n}(X) \\ \Psi_{b,m} &= \Psi_b(\vec{r}, X_{b,0}) \cdot \chi_{b,m}(X). \end{aligned} \tag{A.19}$$

The solution of the Schrödinger equation in the adiabatic approximation, considering only one normal mode described by the frequency ω, the configurational coordinate X and the approximation of a linear harmonic oscillator, yields [62]:

$$\begin{aligned} E_a &= E_{a,0} + \hbar\omega_a \left(n + \frac{1}{2}\right) \\ E_b &= E_{b,0} + \hbar\omega_b \left(m + \frac{1}{2}\right) \end{aligned} \tag{A.20}$$

for the total energy of the ground and excited state E_a and E_b including the energy, due to lattice vibrations, with the phonon energies $E_{ph,a} = \hbar\omega_a$ and $E_{ph,b} = \hbar\omega_b$.

The ionic potential energy is given by [62]

$$\begin{aligned} E_a(X) &= E_{a,0} + V_a(X) = E_{a,0} + \frac{1}{2} m\omega_a^2 (X - X_{a,0})^2 \\ E_b(X) &= E_{b,0} + V_b(X) = E_{b,0} + \frac{1}{2} m\omega_b^2 (X - X_{b,0})^2 \end{aligned} \tag{A.21}$$

where $V(X)$ is the potential of a harmonic oscillator and m the ion mass. Fig. A.3 shows the ground, a, and excited state, b, of a luminescence centers described by the Eqs. A.21 and A.20. Inserting the wave functions presented in Eq. A.19 into Eq.

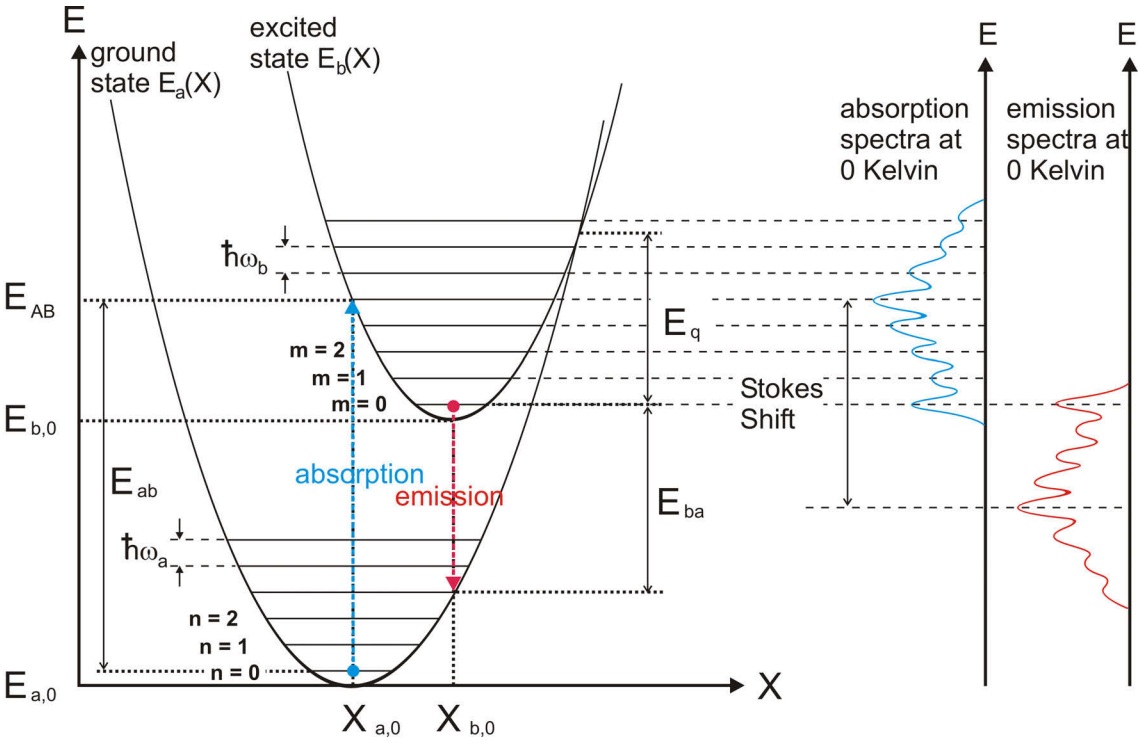

Figure A.3.: *Configurational diagram in the harmonic approximation for a luminescence center in the ground and excited state. (after [62, 64])*

A.15 yields the spontaneous transition probability from the excited into the ground state including the contribution of lattice vibrations [62, 64]:

$$\begin{aligned} & W(ed, vib) \\ &= \frac{8\pi^2 n}{3\hbar\epsilon_0 \lambda^3} \left(\frac{E_{loc}}{E}\right)^2 \frac{1}{g_b} \sum_{an,bm} \left| \langle \Psi_a(\vec{r}, X_{a,0}) \cdot \chi_{a,n}(X) \left| e\mathbf{r} \right| \Psi_b(\vec{r}, X_{b,0}) \cdot \chi_{b,m}(X) \rangle \right|^2 \\ &= \frac{8\pi^2 n}{3\hbar\epsilon_0 \lambda^3} \left(\frac{E_{loc}}{E}\right)^2 \frac{1}{g_b} \sum_{an,bm} \left| \langle \Psi_a(\vec{r}, X_{a,0}) \left| e\mathbf{r} \right| \Psi_b(\vec{r}, X_{b,0}) \rangle \right|^2 \cdot \left| \langle \chi_{a,n}(X) | \chi_{b,m}(X) \rangle \right|^2 \\ &= W(ed) \cdot \sum_{an,bm} \left| \langle \chi_{a,n}(X) | \chi_{b,m}(X) \rangle \right|^2 \\ &= W(ed) \end{aligned} \tag{A.22}$$

where $\sum_{an,bm} |\langle\chi_{a,n}(X)|\chi_{b,m}(X)\rangle|^2 = 1$. The result of the spontaneous dipole transition probability including the dynamic lattice is the same as for the static case. The effect of lattice vibrations reveals itself on the emission probability from a certain vibrational state m of the excited state b into a vibrational state n of the ground state by

$$W_{bm,an}(ed, vib) = W_{ba}(ed) \cdot |\langle\chi_{a,n}(X)|\chi_{b,m}(X)\rangle|^2 , \tag{A.23}$$

where $|\langle\chi_{a,n}(X)|\chi_{b,m}(X)\rangle|^2$ the relative emission probability, due to the overlap of the vibrational functions.

The shape of the emission band at 0 Kelvin can be described by the following function [62]

$$\begin{aligned} I_{ba}(E) &= I_0 \cdot \sum_n |\langle\chi_{a,n}(X)|\chi_{b,0}(X)\rangle|^2 \cdot \delta(E_{b0} - E_{an} - E) \\ &= I_0 \cdot \sum_n \frac{exp(-H)H^n}{n!} \delta(E_{b0} - E_{an} - E) \end{aligned} \tag{A.24}$$

where H is the Hyang-Rhys parameter, defined by [64]

$$E_{AB} - E_{b0} = \frac{1}{2} M\omega^2 (X_{b,0} - X_{a,0})^2 = H\hbar\omega_b. \tag{A.25}$$

Results of the Eq. A.24 are illustrated in Fig. A.4. Increasing values of the Hyang-

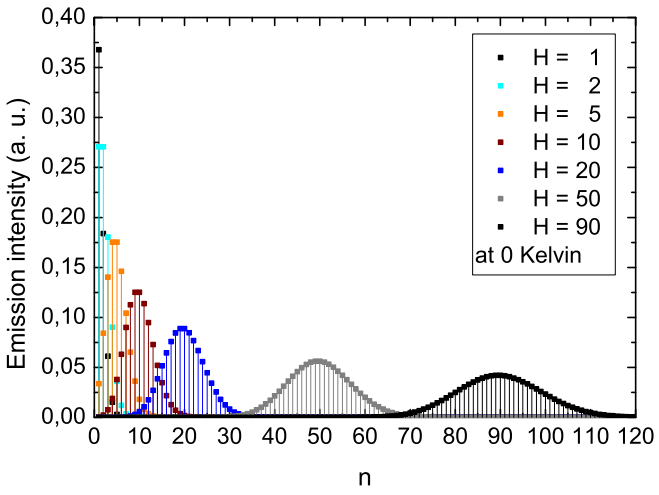

Figure A.4.: *Intensity of the emission at 0 Kelvin from the excited vibrational state $\chi_{b,0}$ into the vibrational ground states $\chi_{a,n}$ for several Hyang-Rhys parameters, H.*

Rhys parameter, H, lead to broader emission bands, due to the distribution of the overall emission rate among an increasing number of vibrational states. For large H, Eq. A.24 can be approximated by a Gaussian function [62]. The Stokes Shift (Fig. A.3), E_{Stokes}, is defined as the energy difference between the absorption and emission band maximum [64]

$$E_{Stokes} = E_{ab} - E_{ba} = 2\frac{1}{2} m\omega^2 (X_{b,0} - X_{a,0})^2 - 2\frac{1}{2}\hbar\omega = (2H - 1)\hbar\omega \tag{A.26}$$

for the approximation $\omega = \omega_a = \omega_b$. A stronger coupling between electronic states and lattice vibrations (phonons) leads to a larger shift between the ground and excited state parabolas with respect to the configurational coordinate, X, which increases the Hyang-Rhys parameter, hence the Stokes Shift.

There is also the possibility that the ground and excited state parabolas intersect each other (Fig. A.3), so that there is the chance for an electron in the excited state for temperatures > 0 K to reach the ground state through the emission of several phonons without the emission of a photon. The non-radiative transition probability $W(nr)$, due to multi-phonon emission, which decreases the scintillator light yield, decreases strongly with increasing energy difference ΔE between ground and excited state and increases with increasing temperature (thermal quenching) as [145, 48, 64]

$$W(nr)(T_{emp}) \approx F \cdot exp(-a\Delta E) \cdot exp\left(-\frac{E_q}{k_B T_{emp}}\right), \tag{A.27}$$

where F and a are material parameters, k_B the Boltzmann factor, T_{emp} the temperature and E_q the quenching energy illustrated in Fig. A.3.

The dependence of the radiative recombination efficiency $\overline{Q}$ on ΔE and T_{emp} can be written as [145, 48]

$$\overline{Q}(T_{emp}) \approx \frac{W(ed)}{W(ed)+W(nr)} = \frac{1}{1+\frac{F}{W_{ed}} \cdot exp\left(-\alpha\Delta E - \frac{E_q}{k_b T_{emp}}\right)}, \tag{A.28}$$

whereas the non-radiative recombination through traps is not taken into account here. The non-radiative transition probability $W(nr)$ in $LaBr_3$(Ce) and CsI(Tl) should be negligible after Eq. A.27, because of the large energy gap between the ground and excited states, ΔE, which is in the range from 2 to 4 eV (Tab. 2.2). For very small ΔE, $W(nr)$ becomes larger and $W(ed)$ smaller. Due to the $1/\lambda^3$ dependence (Eq. A.15), the non-radiative transitions dominate [64].

Another important issue is the light yield dependence on the concentration of luminescence centers. $\overline{L}$ increases up to a certain concentration and decreases after the concentration is further increased. This is due to the fact, that the travel distances of electrons and holes to the luminescence centers is reduced, hence the probability of charge carriers being trapped is also reduced. These processes lead to an increase of the transfer efficiency $\overline{S}(T_{emp})$. At a certain concentration the probability for the transfer of the excitation energy and charges from one center to the next increases in that way, that the probability to de-excite non-radiatively, increases again [14].

The same processes leading to an increase of $\overline{S}(T_{emp})$ with an increasing concentration of luminescence centers, described in the previous paragraph, lead also to a decrease of the luminescence (scintillation) rise time τ_r. The time dependence of the luminescence intensity $J(t) = \frac{dN_{ph}}{dt}$ is usually approximated by a sum of exponential functions [59, 145, 146]

$$J(t) = \sum_{i=0}^{N_l} \frac{a_i}{\tau_{tot,i}} \cdot exp(-\frac{t}{\tau_{tot,i}}) - \frac{a_i}{\tau_{r,i}} \cdot exp(-\frac{t}{\tau_{r,i}}), \tag{A.29}$$

where N_l is the number of possibilities for electrons and holes to recombine radiatively, t the time and a the scaling factor. The total number of generated photons results from the integration of $J(t)$ over the time: $N_{ph} = \int_0^\infty J(t)dt$.

B. Statistical background

A method to determine the mean value and the variance of probability distributions of statistical processes is to define their probability generating functions, which have been introduced by Laplace in 1812 [147]. The descriptors of statistical processes are defined by derivations of the probability generating functions.

B.1. Determination of the mean value and variance from generating functions

Considering a process, named G, with possible scores s = 0,1,2,...,n and the respective probabilities $p_0, p_1, p_2, ..., p_n$. The probability generating function, G(x), for such a process is defined as [148, 78, 149]:

$$G(x) = \sum_{s=0}^{n} x^s p_s. \tag{B.1}$$

where x is an auxiliary variable. G(1) = 1, because it is the sum over the probabilities of all possible scores. The average score results from the first derivative of the probability generating function, G(x), at x = 1:

$$\frac{dG(x)}{dx}_{x=1} = G^{'}(1) = \sum_{s}^{n} s p_s = \overline{s}. \tag{B.2}$$

The variance, Var(G), the square of the standard deviation, σ^2(G), of the process G is defined by [77]

$$Var(G) = \sigma^2(G) = \overline{s^2} - \overline{s}^2. \tag{B.3}$$

The second derivation of the generating function, G(x), at x = 1 is

$$\frac{d^2G(x)}{dx^2}_{x=1} = G^{''}(1) = \sum_{s}^{n} s(s-1) p_s = \overline{s^2} - \overline{s}. \tag{B.4}$$

Substituting $\overline{s^2}$ and $\overline{s}^2$ in Eq. B.3 by the first and second derivative of the generating function, G(x), yields

$$Var(G) = G^{''}(1) + G^{'}(1) - \left[G^{'}(1)\right]^2. \tag{B.5}$$

For example the probability generating function of a process constituting a Bernoulli trial with the scores 1 or 0, i.e. photon is transferred from the scintillator into the SDD or not, is

$$G(x) = x^0 p_0 + x^1 p_1 = p_0 + x p_1. \tag{B.6}$$

From G(1) = 1 results that $p_0 = 1 - p_1$. With the notation $p_1 = p$, the probability generating function can be written as

$$G(x) = (1 - p) + xp. \tag{B.7}$$

The mean value for the Bernoulli trial is

$$\overline{s} = G^{'}(1) = p \tag{B.8}$$

and the variance

$$Var(G) = G^{''}(1) + G^{'}(1) - \left[G^{'}(1)\right]^2 = 0 + p - p^2 = p(1 - p) \tag{B.9}$$

Knowing the probability generating function of a process, implies the possibility to calculate its mean value and variance.

B.1.1. Simultaneous processes

The generating function G(x) of two simultaneous independent processes with their probability generating functions A(x) and B(x), where the overall mean value $\overline{s}_G$ of the total process G is calculated by adding the mean values $\overline{s}_A$ and $\overline{s}_B$ of the processes A and B, is given by [78, 149]

$$G(x) = A(x)B(x). \tag{B.10}$$

The mean value $\overline{s}_G$ can be calculated by applying formula B.2 onto the probability generating function in B.10, which yields the expected mean value:

$$\overline{s}_G = A^{'}(1)B(1) + A(1)B^{'}(1) = \overline{s}_A + \overline{s}_B. \tag{B.11}$$

Applying formula B.5 onto the probability generating function in B.10 yields the variance of the overall process, G:

$$\begin{aligned}
&Var(G)\\
&= A^{''}(1)B(1) + 2A^{'}(1)B^{'}(1) + A(1)B^{''}(1) + A^{'}(1) + B^{'}(1) - \left[A^{'}(1) + B^{'}(1)\right]^2\\
&= A^{''}(1) + 2A^{'}(1)B^{'}(1) + B^{''}(1) + A^{'}(1) + B^{'}(1) - \left[A^{'}(1) + B^{'}(1)\right]^2\\
&= A^{''}(1) + B^{''}(1) + A^{'}(1) + B^{'}(1) - A^{'}(1)^2 - B^{'}(1)^2\\
&= [A^{''}(1) + A^{'}(1) - A^{'}(1)^2] + [B^{''}(1) + B^{'}(1) - B^{'}(1)^2]\\
&= Var(A) + Var(B)\\
&= \sigma(A)^2 + \sigma(B)^2
\end{aligned} \tag{B.12}$$

B.1.2. Processes in a cascade

Considering two independent processes A and B happening after each other, where the first process A has the score s_A, which serves as the number of trials for the

second process B. The overall mean value of this so called cascade process is then $\overline{s}_G = \overline{s}_A \overline{s}_B$ with the probability generating function [149, 150, 151]

$$G(x) = A[B(x)]. \tag{B.13}$$

Applying formula B.2 yields the expected result for the overall mean value

$$\overline{s}_G = A^{'}[B(1)]B^{'}(1) = A^{'}(1)B^{'}(1) = \overline{s}_A \overline{s}_B. \tag{B.14}$$

Applying formula B.5 yields the variance of the overall process, G:

$$\begin{aligned}
&Var(G) \\
&= A^{''}(1)B^{'}(1)^2 + A^{'}(1)B^{''}(1) + A^{'}(1)B^{'}(1) - \left[A^{'}(1)B^{'}(1)\right]^2 \\
&= A^{''}(1)B^{'}(1)^2 + A^{'}(1)B^{'}(1)^2 - A^{'}(1)^2 B^{'}(1)^2 \\
&+A^{'}(1)B^{''}(1) + A^{'}(1)B^{'}(1) - A^{'}(1)B^{'}(1)^2 \\
&= B^{'}(1)^2 \left[A^{''}(1) + A^{'}(1) - A^{'}(1)^2\right] \\
&+A^{'}(1) \left[B^{''}(1) + B^{'}(1) - B^{'}(1)^2\right] \\
&= \overline{s}_B^2 \cdot Var(A) + \overline{s}_A \cdot Var(B) \\
&= \overline{s}_B^2 \cdot \sigma(A)^2 + \overline{s}_A \cdot \sigma(B)^2.
\end{aligned} \tag{B.15}$$

The variances of processes happening in a cascade add up with different weighting factors compared to the variances of processes happening simultaneously (Eq. B.12) with weighting factors equal to 1. The variance originating from processes in a cascade is usually specified in relative units, $v(\mathrm{X}) = \mathrm{Var}(\mathrm{X})/\overline{s}_X^2$ where X is a random variable and $\overline{s}_X$ its mean value. The relative variance of G is then

$$\begin{aligned}
v(G) &= \frac{Var(G)}{\overline{s}^2} = \frac{\overline{s_B}^2 \cdot Var(A)^2 + \overline{s_A} \cdot Var(B)^2}{\left(\overline{s}_A \overline{s}_B\right)^2} \\
&= \frac{Var(A)}{\overline{s_A}^2} + \frac{Var(B)}{\overline{s}_A \overline{s}_B^2} \\
&= v(A) + \frac{v(B)}{\overline{s}_A}.
\end{aligned} \tag{B.16}$$

For example lets assume, that process B can be described by a Bernoulli trial with the probability p for success. Then the relative variance can be written as

$$v(G) = v(A) + \frac{1-p}{\overline{s}_A p} = \left(v(A) - \frac{1}{\overline{s}_A}\right) + \frac{1}{\overline{s}_A p}. \tag{B.17}$$

If the number of scores of process A is constant for each event, then the relative variance of process A is zero, $v(A) = 0$.

If the scores of process A follow a Poisson distribution, then $v(A) = 1/\overline{s}_A$ and Eq. B.17 changes to

$$v(G) = \frac{1}{\overline{s}_A p}. \tag{B.18}$$

B.1.3. Alternative processes

Process, B, can be of composite nature in such a way, that each event is described by one of several processes B_i. The probability generating function for this process can be defined by [78]

$$B(x) = \sum_i q_i B_i(x), \tag{B.19}$$

which is the weighted mean of the generating function $B_i(x)$ for the process B_i, where q_i is the frequency of B_i to happen. The mean value of process B is

$$\overline{s}_B = B^{'}(1) = \sum_i q_i \overline{s}_{B_i}. \tag{B.20}$$

Considering two processes A and B happening after each other to form a cascade with process B being of the form described in Eq. B.19. The overall probability generating function, G(x), is then

$$G(x) = \sum_i q_i A\left[B_i(x)\right]. \tag{B.21}$$

Assuming that each B_i process can be described by a Bernoulli trial (compare Eq. B.7) with a probability generating function

$$B_i(x) = (1 - p_i) + p_i x \tag{B.22}$$

and inserting Eq. B.22 into Eq. B.21 yields the total probability generating function [78]

$$G(x) = \sum_i q_i A\left[(1 - p_i) + p_i x\right]. \tag{B.23}$$

The first derivation of G(x) is

$$G^{'}(x) = \sum_i q_i A^{'}\left[(1 - p_i) + p_i x\right] p_i \tag{B.24}$$

with the mean value

$$\overline{s}_G = G^{'}(1) = \sum_i q_i A^{'}(1) p_i = A^{'}(1) \sum_i q_i p_i = A^{'}(1)\overline{p} = \overline{s}_A \overline{p}. \tag{B.25}$$

The second derivation of G(x) is

$$G^{''}(x) = \sum_i q_i A^{''}\left[(1 - p_i) + p_i x\right] p_i^2, \tag{B.26}$$

which becomes for x = 1

$$G^{''}(1) = \sum_i q_i A^{''}\left[1\right] p_i^2 = A^{''}(1) \sum_i q_i p_i^2 = A^{''}(1)\overline{p^2}. \tag{B.27}$$

The variance of the overall process results by inserting Eq. B.27 and B.25 into Eq. B.2:

$$
\begin{aligned}
& Var(G) \\
&= A^{''}(1)\overline{p^2} + A^{'}(1)\overline{p} - \left[A^{'}(1)\overline{p}\right]^2 \\
&= A^{''}(1)\overline{p^2} - A^{''}(1)\overline{p}^2 + A^{''}(1)\overline{p}^2 + A^{'}(1)\overline{p}^2 - A^{'}(1)^2\overline{p}^2 - A^{'}(1)\overline{p}^2 + A^{'}(1)\overline{p} \\
&= A^{''}(1)\left[\overline{p^2} - \overline{p}^2\right] + \overline{p}^2\left[A^{''}(1) + A^{'}(1) - A^{'}(1)^2\right] - A^{'}(1)\overline{p}^2 + A^{'}(1)\overline{p} \\
&= A^{''}(1)Var(p) + \overline{p}^2 Var(A) - A^{'}(1)\overline{p}^2 + A^{'}(1)\overline{p} \\
&= A^{''}(1)Var(p) + A^{'}(1)Var(p) - A^{'}(1)^2 Var(p) \\
&+\overline{p}^2 Var(A) - A^{'}(1)\overline{p}^2 + A^{'}(1)\overline{p} - A^{'}(1)Var(p) + A^{'}(1)^2 Var(p) \\
&= Var(A)Var(p) + \overline{p}^2 Var(A) - A^{'}(1)\overline{p}^2 \\
&+A^{'}(1)\overline{p} - A^{'}(1)Var(p) + A^{'}(1)^2 Var(p) \\
&= Var(A)Var(p) + \overline{p}^2 Var(A) - \overline{s}_A\overline{p}^2 + \overline{s}_A\overline{p} - \overline{s}_A Var(p) + \overline{s}_A^2 Var(p)
\end{aligned}
\tag{B.28}
$$

The result for the relative variance can be written as

$$
\begin{aligned}
v(G) &= \frac{Var(G)}{\overline{s}_G^2} = v(A)v(p) + v(A) - \frac{1}{\overline{s}_A} + \frac{1}{\overline{s}_A\overline{p}} - \frac{v(p)}{\overline{s}_A} + v(p) \\
&= \left(v(A) - \frac{1}{\overline{s}_A}\right) + v(p)\left(1 + v(A) - \frac{1}{\overline{s}_A}\right) + \frac{1}{\overline{s}_A\overline{p}}
\end{aligned}
\tag{B.29}
$$

For $v(p) = 0$, the variance in B.29 changes to the variance described in B.17 for a mean value p, which doesn't change frequently from one event to another.

If the scores of process A follow a Poisson distribution, then $v(A) = 1/\overline{s}_A$ and Eq. B.29 results into

$$
v(G) = v(p) + \frac{1}{\overline{s}_A\overline{p}} \tag{B.30}
$$

B.2. Derivation of the formula for the relative energy resolution

The overall process G, composed of the processes denoted by A, B and D has the generating function (Sec. B.1.3):

$$
\begin{aligned}
G(x) &= \sum_i\sum_j q_i k_j A[B_i[D_j(x)]] = \sum_i\sum_j q_i k_j A[1 - \overline{T}_i + \overline{T}_i[1 - \overline{\eta}_j + \overline{\eta}_j x]] \\
&= \sum_i\sum_j q_i k_j A[1 - \overline{T}_i\overline{\eta}_j + \overline{T}_i\overline{\eta}_j x],
\end{aligned}
\tag{B.31}
$$

with the mean value

$$
\overline{N}_e = G^{'}(1) = \sum_i\sum_j q_i k_j A^{'}(1)\overline{T}_i\overline{\eta}_j = A^{'}(1)\sum_i q_i\overline{T}_i\sum_j k_j\overline{\eta}_j = \overline{N}_{eh}\overline{T}\overline{\eta}. \tag{B.32}
$$

For the calculation of the relative variance of N_e the result of the second derivative of G(x) at x = 1 is needed:

$$G^{''}(1) = \sum_i \sum_j q_i k_j A^{''}(1) \overline{T}_i^2 \overline{\eta}_j^2 = A^{''}(1) \sum_i q_i \overline{T}_i^2 \sum_j k_j \overline{\eta}_j^2 = A^{''}(1) \overline{T^2} \cdot \overline{\eta^2}. \quad \text{(B.33)}$$

The relative variance of the overall process G can be determined in analogy to Eq. B.28 and B.29 with the result

$$v(N_e) = v(N_{eh}) - \frac{1}{\overline{N}_{eh}} + v(T \cdot \eta) \left(1 + v(N_{eh}) - \frac{1}{\overline{N}_{eh}}\right) + \frac{1}{\overline{N}_{eh} \overline{T} \overline{\eta}}. \quad \text{(B.34)}$$

C. Transmission and reflection of optical photons through thin films

The interaction of optical photons at an interface between two isotropic media can be described by a plane electromagnetic wave, which is partly reflected and transmitted at the interface. The propagation of the electric, $\vec{E}(\vec{r},t)$, and magnetic field, $\vec{H}(\vec{r},t)$, components can be described by the formulas

$$\vec{E}(\vec{r},t) = \vec{E_0} exp(i(\vec{k}\vec{r} - \omega t)) \tag{C.1}$$

$$\vec{H}(\vec{r},t) = \vec{H_0} exp(i(\vec{k}\vec{r} - \omega t)), \tag{C.2}$$

where $\vec{E_0}$ and $\vec{H_0}$ are the amplitudes of the electric and magnetic field respectively and $\vec{k}$ is the wave vector, r the position, ω the angular frequency and t the time. The relation between the magnetic field strength $\vec{H}$ and the magnetic flux density $\vec{B}$ is $\vec{B} = \mu\mu_0\vec{H}$, where μ and μ_0 are the relative and the vacuum permeability. $\mu = 1$ for non magnetic materials. The vectors $\vec{E}$, $\vec{H}$ and $\vec{k}$ are orthogonal to each other. From the Maxwell equation

$$\nabla \times \vec{E} = -\mu_0 \frac{d\vec{H}}{dt} \quad \Leftrightarrow \quad \vec{k} \times \vec{E} = \omega\mu_0\vec{H}$$

and the fact, that $\vec{k}$ and $\vec{E}$ are orthogonal to each other, results in the equation $k\left|\vec{E}\right| = \omega\mu_0\left|\vec{H}\right|$. With the dispersion relation of plane waves

$$\omega = \frac{c}{n}k,$$

where c is the velocity of light and n the energy dependent complex index of refraction. The relation between the magnitude of the electric and the magnetic field can be deduced to

$$\left|\vec{E}\right| = \frac{c}{n}\mu_0\left|\vec{H}\right|. \tag{C.3}$$

In case of an arrangement of several thin layers on top of each other with parallel interfaces, the electromagentic field at a point of the considered interface, z_1 (Fig. C.1), can be described by the superposition of two electromagnetic waves on each side of the interface respectively. The incident and reflected waves are on one side and the transmitted and the other incident wave on the opposite side of the interface at z_1. The incident wave from the opposite side of the interface results from the interference of the reflected waves on the interfaces below z_1 (Fig. C.1). The boundary condition for electromagnetic waves in isotropic, isolating and non magnetic materials is given by the continuity of the parallel component of the electric,

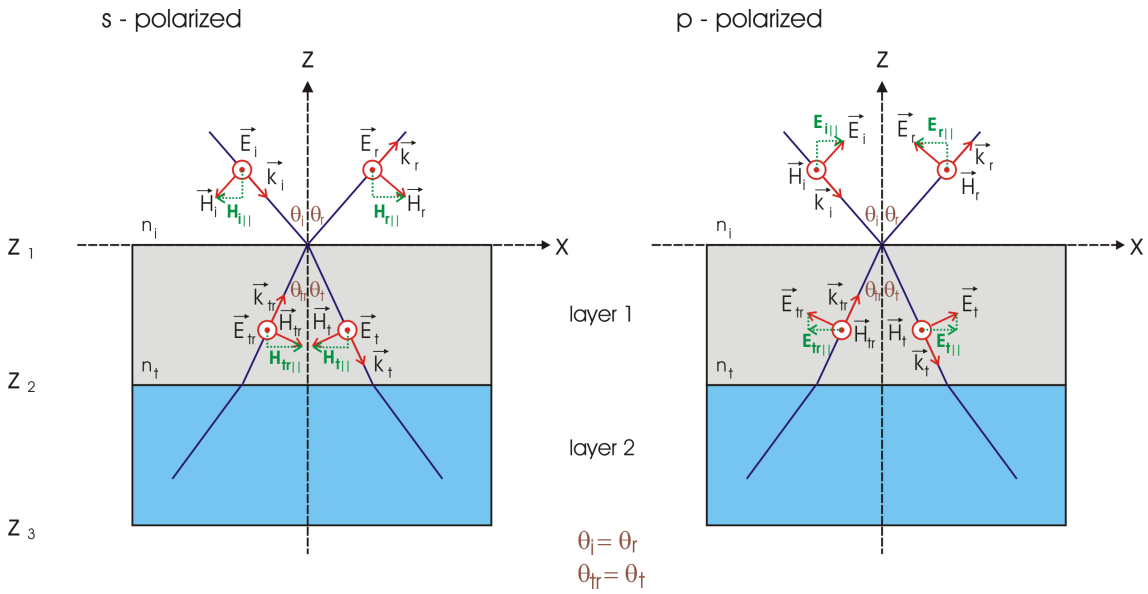

Figure C.1.: *Schematics of the amplitudes of the electric and magnetic field vectors for s- and p-polarized electromagnetic waves.*

$\vec{E}$, and magnetic, $\vec{H}$, field at the interface. The electromagnetic wave exhibits a polarization, which can be described by a linear combination of a s- and p-polarized electromagnetic wave. The s-polarized wave has the electric and the p-polarized wave the magnetic field parallel to the interface. The boundary condition for s- and p-polarized electromagnetic waves leads to the following equations [152]:
s-polarization:

$$E_i(z_1) + E_r(z_1) = E_t(z_1) + E_{tr}(z_1) \tag{C.4}$$

$$\begin{aligned} -H_i(z_1)cos\theta_i + H_r(z_1)cos\theta_i &= -H_t(z_1)cos\theta_t + H_{tr}(z_1)cos\theta_t \Leftrightarrow \\ -n_i E_e(z_1)cos\theta_i + n_i E_r(z_1)cos\theta_i &= -n_t E_t(z_1)cos\theta_t + n_t E_{tr}(z_1)cos\theta_t \end{aligned} \tag{C.5}$$

with Eq. C.3.

p-polarization:

$$\begin{aligned} H_i(z_1) + H_r(z_1) &= H_t(z_1) + H_{tr}(z_1) \Leftrightarrow \\ n_i E_i(z_1) + n_i E_r(z_1) &= n_t E_t(z_1) + n_t E_{tr}(z_1) \end{aligned} \tag{C.6}$$

with Eq. C.3,

$$E_i(z_1)cos\theta_i - E_r(z_1)cos\theta_i = E_t(z_1)cos\theta_t - E_{tr}(z_1)cos\theta_t \tag{C.7}$$

where i, r, t and tr are the indices for the parameters of the incident, reflected, transmitted and reflected after being transmitted electric or magnetic fields respectively. θ is the angle between the wave vector and the surface normal. After some transformations Eq. C.4 and C.5, respectively C.6 and C.7 can be written in a matrix

notation:
s-polarization

$$\begin{pmatrix} E_i(z_1) \\ E_r(z_1) \end{pmatrix} = \begin{pmatrix} \frac{1+a}{2} & \frac{1-a}{2} \\ \frac{1-a}{2} & \frac{1+a}{2} \end{pmatrix} \begin{pmatrix} E_t(z_1) \\ E_{tr}(z_1) \end{pmatrix} \tag{C.8}$$

where

$$a = \frac{n_t cos\theta_t}{n_i cos\theta_i}$$

p-polarization

$$\begin{pmatrix} E_i(z_1) \\ E_r(z_1) \end{pmatrix} = \begin{pmatrix} \frac{b+c}{2} & \frac{b-c}{2} \\ \frac{b-c}{2} & \frac{b+c}{2} \end{pmatrix} \begin{pmatrix} E_t(z_1) \\ E_{tr}(z_1) \end{pmatrix} \tag{C.9}$$

where

$$b = \frac{n_t}{n_i}; \quad c = \frac{cos\theta_t}{cos\theta_i}$$

The matrices in Eq. C.8 and C.9 are named $M_{s;n,n-1}$ and $M_{p;n,n-1}$. The propagation within one layer from one interface (n,n-1) to the other interface (n-1,n-2) has not been described yet. This can be done by the following equation:

$$\begin{pmatrix} E_{t;n,n-1} \\ E_{tr;n-1} \end{pmatrix} = \begin{pmatrix} exp(i\Theta_{n-1}) & 0 \\ 0 & exp(-i\Theta_{n-1}) \end{pmatrix} \begin{pmatrix} E_{i;n-1,n-2} \\ E_{r;n-1,n-2} \end{pmatrix} \tag{C.10}$$

[152] where

$$\Theta_{n-1} = kd_{n-1}cos\theta_{n-1} = \frac{2\pi n}{\lambda} d_{n-1} cos\theta_{n-1}, \tag{C.11}$$

d_{n-1} is the layer thickness of the layer with the index n-1 and λ the wavelength of the electromagnetic wave. Combining the matrices, which describe the Fresnel reflection and refraction (Eq. C.8 and C.9) with the matrix, which describes the propagation through the layers from one interface to the other (Eq. C.11), leads to the following equations:
s-polarized

$$\begin{pmatrix} E_{t;n,n-1} \\ E_{tr;n,n-1} \end{pmatrix} =$$

$$\begin{pmatrix} exp(i\Theta_{n-1})\frac{n_n cos\theta_n + n_{n-1} cos\theta_{n-1}}{2n_n cos\theta_n} & exp(-i\Theta_{n-1})\frac{n_n cos\theta_n - n_{n-1} cos\theta_{n-1}}{2n_n cos\theta_n} \\ exp(i\Theta_{n-1})\frac{n_n cos\theta_n - n_{n-1} cos\theta_{n-1}}{2n_n cos\theta_n} & exp(-i\Theta_{n-1})\frac{n_n cos\theta_n + n_{n-1} cos\theta_{n-1}}{2n_n cos\theta_n} \end{pmatrix} \begin{pmatrix} E_{i;n-1,n-2} \\ E_{r;n-1,n-2} \end{pmatrix} \tag{C.12}$$

p-polarized

$$\begin{pmatrix} E_{t;n,n-1} \\ E_{tr;n,n-1} \end{pmatrix} =$$

$$\begin{pmatrix} exp(i\Theta_{n-1})\frac{n_{n-1} cos\theta_n + n_n cos\theta_{n-1}}{2n_n cos\theta_n} & exp(-i\Theta_{n-1})\frac{n_{n-1} cos\theta_n - n_n cos\theta_{n-1}}{2n_n cos\theta_n} \\ exp(i\Theta_{n-1})\frac{n_{n-1} cos\theta_n - n_n cos\theta_{n-1}}{2n_n cos\theta_n} & exp(-i\Theta_{n-1})\frac{n_{n-1} cos\theta_n + n_n cos\theta_{n-1}}{2n_n cos\theta_n} \end{pmatrix} \begin{pmatrix} E_{i;n-1,n-2} \\ E_{r;n-1,n-2} \end{pmatrix} \tag{C.13}$$

The matrices, which describe the Fresnel refraction and reflection and the propagation of the waves through the layers are named $L_{s;n,n-1}$ and $L_{p;n,n-1}$. Let us suppose that two thin layers are deposited on a substrate and we would like to calculate the reflection on and transmission through the two layers. It can be done in the following way:

$$\begin{pmatrix} E_{i;3,2} \\ E_{r;3,0} \end{pmatrix} = L_{3,2} L_{2,1} M_{1,0} \begin{pmatrix} E_{t;1,0} \\ 0 \end{pmatrix} \tag{C.14}$$

Dividing the Eq. C.14 through $E_{i;3,2}$ leads to

$$\begin{pmatrix} 1 \\ r \end{pmatrix} = L_{3,2} L_{2,1} M_{1,0} \begin{pmatrix} t \\ 0 \end{pmatrix} \tag{C.15}$$

which can be transformed into

$$\begin{pmatrix} 1/t \\ r/t \end{pmatrix} = L_{3,2} L_{2,1} M_{1,0} \begin{pmatrix} 1 \\ 0 \end{pmatrix} \tag{C.16}$$

so that on the right hand side of Eq. C.16 remain only the matrices L and M and the vector (1 0) as input for the calculation of the complex reflection r and transmission coefficients, t.

D. Effect of the charge collection and quantum efficiency on the spectral response

D.1. Direct X-ray detection

The mean number of signal electrons, $\overline{N}_e$(E,z), reaching the anode after an energy deposition of one X - or γ-ray photon at a certain depth, z, is

$$\overline{N}_e(E,z) = \frac{E}{\overline{w}} \cdot CCE(z(E)) = \overline{N}_{eh}(E) \cdot CCE(z(E)), \tag{D.1}$$

The transmissivity through the inactive parts of the entrance window is set to 1, so that no partial events resulting from that part of the entrance window is considered. The relative variance of $N_e(E,z)$ can be calculated by the use of Eq. B.16 assuming in this case a simple cascade process:

$$v(N_e(E,z)) = v(N_e) + \frac{1 - CCE(z(E))}{\overline{N}_{eh-SDD}(E) \cdot CCE(z(E))}, \tag{D.2}$$

where $v(N_e)$ is the contribution of the so called Fano noise, whereas the second term in Eq. D.2 describes the z dependent noise contribution, due to a CCE(z) < 1. The second noise term in Eq. D.2 decreases with increasing absorption depths, z, of X-ray photons, because of an increasing CCE(z) close to 1.

The mean number of signal electrons, $\overline{N}_e$(E), summed over all absorption depths, results from

$$\overline{N}_e(E) = \overline{N}_{eh-SDD}(E) \cdot \overline{CCE}(E), \tag{D.3}$$

where $\overline{CCE}$ is defined in Eq. D.6. Due to the fact, that the CCE(z) changes from event to event (alternative cascade process) the relative variance $v(N_e(E))$ has to be calculated according to Eq. B.29:

$$v(N_e(E)) = \frac{F}{\overline{N}_{eh-SDD}} + v(CCE(E)) \left(1 + \frac{F-1}{\overline{N}_{eh-SDD}}\right) + \frac{1 - \overline{CCE}(E)}{\overline{N}_{eh-SDD} \cdot \overline{CCE}(E)}, \tag{D.4}$$

where

$$v(CCE(E)) = \frac{\overline{CCE^2}(E) - \overline{CCE}^2(E)}{\overline{CCE}^2(E)}. \tag{D.5}$$

Eq. D.4 changes for CCE(z) = CCE = 1 to $v(N_e(E)) = F/\overline{N}_{eh-SDD}$, which is the contribution of the Fano noise. $\overline{CCE}(E)$ and $\overline{CCE^2}(E)$ can be evaluated by

$$\overline{CCE}(E) = \frac{\int_0^d CCE(z) dA(E,z)}{\int_0^d dA(E,z)}, \tag{D.6}$$

and

$$\overline{CCE^2}(E) = \frac{\int_0^d CCE(z)^2 dA(E,z)}{\int_0^d dA(E,z)} \tag{D.7}$$

where dA(E,z) is given in Eq. 5.7. Including the variance of the electronic noise, $\mathrm{Var}_{el} = \mathrm{ENC}_{el}^2$, yields the overall variance of the spectrum

$$Var_{tot}(E) = Var(N_e(E)) + Var_{el} = v(N_e(E)) \cdot \overline{N}_e^2(E) + ENC_{el}^2. \tag{D.8}$$

The standard deviation σ_{tot} in eV determined by the contributions of Fano noise, CCE noise and electronic noise, is hence

$$\sigma_{tot}(N_e(E)) = \overline{w} \cdot \sqrt{Var(N_e(E)) + ENC_{el}^2}, \tag{D.9}$$

where $\overline{w}$ is the mean energy in eV to create an eh-pair. Eq. D.9 changes to Eq. 3.3 (Sec. 3.1.1) for CCE(z) = 1 with FWHM = 2.35 $\cdot \sigma_{tot}(N_e(E))$. In Fig. D.1 on the left the calculated values of σ_{tot} for a CCE(z) = 1 function and CCE functions specified by the pn- and ARC-Window are plotted against the energy for two electronic noise levels. The CCE(z) = 1 and the CCE(z) of the pn-Window have almost the same

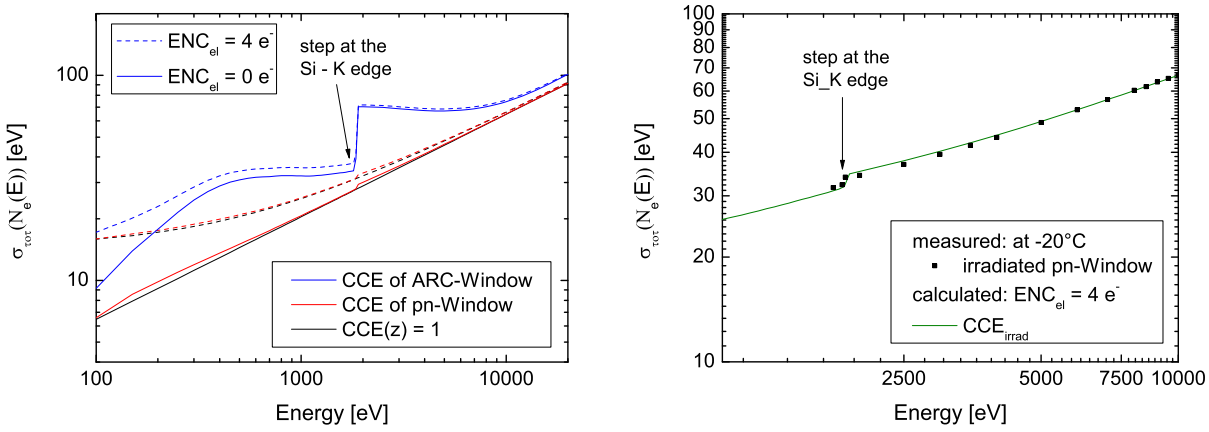

Figure D.1.: *Standard deviation, $\sigma_{tot}(N_e(E))$, of the number of detected signal electrons, $N_e(E)$, for a SDD window with CCE(z) = 1 (black line), pn- (orange line) and ARC-Window (blue line) for two electronic noise levels (left Fig.). Measured (- 20° C) and calculated FWHM = 2.35σ_{tot} of $N_e(E)$ for an SDD with a pn-Window, after X-ray irradiation with a dose of $3 \cdot 10^{11}$ (right Fig.). The discontinuities at the Si-K (1839 eV) absorption edge is smaller for the pn- compared to the ARC-Window, because of an improved CCE.*

values of σ_{tot}, whereas the values of the CCE(z) of the ARC-Window leads to a large degradation of σ_{tot} compared to CCE(z) = 1. On the right of Fig. D.1 the measured and calculated values of σ_{tot}, which are in a good agreement, are illustrated. In this case the SDD with the pn-Window has been irradiated with an X-ray dose of about $3 \cdot 10^{11}$ before recording the spectra and determining the FWHM of its photo peak.

After the irradiation of the pn-Window with that dose, a high number of defects are created at the SiO_2-Si interface, which degrade the value of the CCE in that region (Fig. D.2).

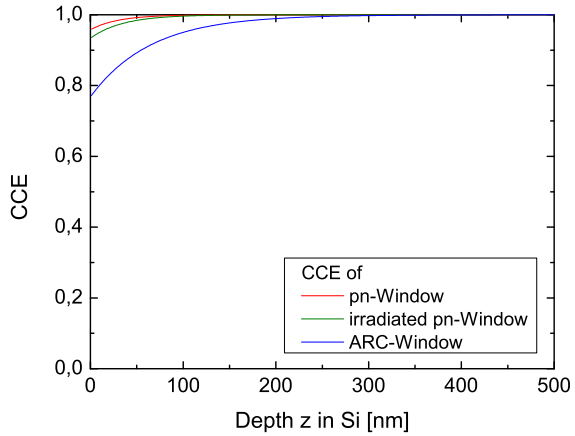

Figure D.2.: *CCE of the pn-Window, the irradiated pn-Window (X-ray dose of* $3 \cdot 10^{11}$*) and the ARC-Window.*

In Fig. D.2 the depth dependent charge collection efficiency functions of the pn-, ARC-Window and that of the irradiated pn-Window (X-ray dose of $3 \cdot 10^{11}$) are illustrated. The appropriate parameters for the CCE of the irradiated pn-Window are determined from the best agreement of the simulated and measured spectra in Fig. D.5.

The spectrum generated by incident X-rays involves several processes. These are the absorption of X-rays, the generation and collection of signal electrons at the SDD anode. These processes, which are summarized in an event, j, lead to a number of detected signal electrons, $N_{e,j}(E, z_j)$:

$$N_{e,j}(E, z_j) = N_{eh-SDD,j}(E) \cdot CCE(z_j(E)), \tag{D.10}$$

where $N_{eh-SDD,j}(E)$ is the number of generated eh-pairs inside the SDD of event j, and $CCE(z_j(E))$ the charge collection efficiency of event j and the absorption depth z_j. The number of generation eh-pairs, $N_{eh-SDD,j}(E)$, is approximated by a Gaussian distribution with a standard deviation, $\sqrt{F \cdot \overline{N}_{eh-SDD}}$. Each electron is collected with a probability of $CCE(z_j)$. This can be computed by Monte Carlo methods. The absorption depth, $z_j(E)$, following the absorption law, results from Eq. 5.6 , if it is resolved for z:

$$z_j(E) = -l(E) \cdot log(1 - r_j) \tag{D.11}$$

where l(E) is the absorption length, r a random number between [0,1] and j the considered event. A random number generator determines the value of r_j for each energy deposition, j. The absorption depth, $z_j(E)$, changes frequently from event to event.

Fig. D.3 shows the spectra of a SDD with ARC- and pn-Window generated by incident X-ray photons with energies of $E = 1830$ eV and 1860 eV (before and after

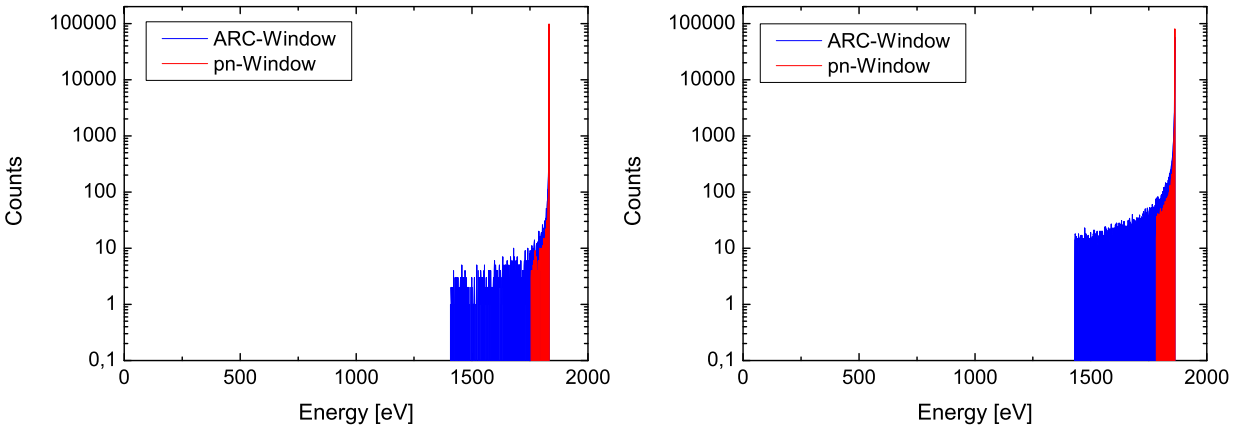

Figure D.3.: *Simulated spectral response of a SDD with ARC-Window regarding the effect of the CCE only for X-ray energies of E = 1830 eV (left Fig.) and 1860 eV (right Fig.), before and after the Si-K absorption edge.*

the Si-K absorption edge) including the contribution of the $\overline{CCE}$ without any noise. The number of counts is plotted against the value of $N_e(E) \cdot \overline{w}$ in units of eV. The influence of the CCE is larger for X-rays with an energy of $E = 1860$ eV, because of their shorter absorption length in silicon (Fig. 5.5), compared to photons with an energy of 1830 eV. This circumstance leads to a higher number of events with a partial charge collection (CCE < 1), hence with $N_e(E) < N_{eh-SDD}(E)$ (comp. Eq. D.10) for X-ray photons with an energy of $E = 1860$ eV. It is also recognizable that the fraction of events with $N_e(E) < N_{eh-SDD}(E)$ (comp. Eq. D.10) is larger for a SDD with an ARC- rather than a pn-Window, due to a poorer CCE (Fig. D.3).

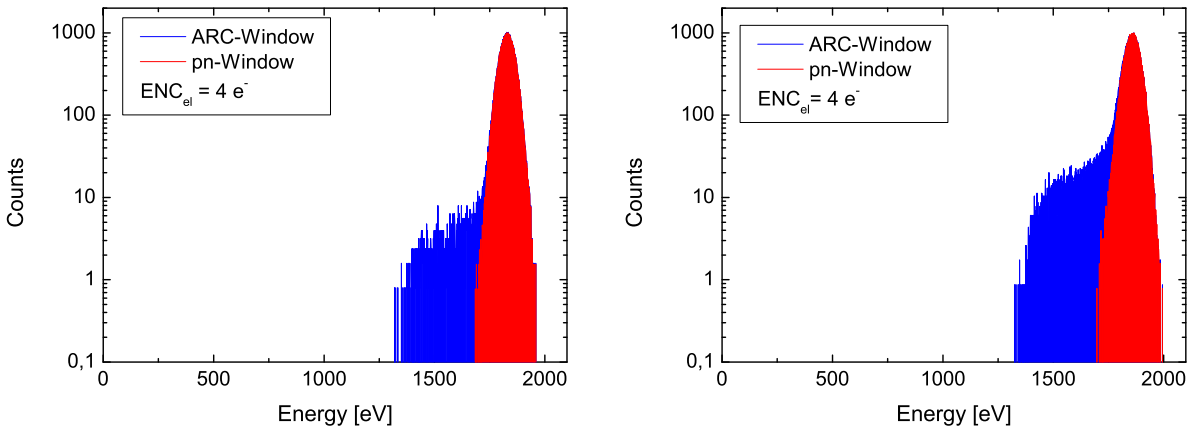

Figure D.4.: *Simulated spectral response of a SDD with pn-Window, due to the effect of the CCE and the contributions of the Fano and electronic noise for X-ray energies of E = 1830 eV (left Fig.) and 1860 eV (right Fig.).*

Fig. D.4 includes contributions from the CCE, Fano and electronics, noise to the

spectra shown in Fig. D.3. The CCE generates a more or less pronounced shoulder on the left side of the photo peak. This shoulder is smaller for a CCE, optimized for X-rays, as realized in the pn-Window compared to the ARC-Window, which is optimized for coupling the SDD to a scintillator.

Fig. D.5 shows the measured and calculated spectra of an SDD with pn-Window for incident X-ray energies of 1830 and 1860 eV. We have not performed measurements with an ARC-Window at these energies yet. The measured spectrum of a SDD with the irradiated pn-Window compared to the simulated ones, includes the noise peak at 0 eV and partial events resulting after the interaction of X-rays with the dielectric top layers. The number of these partial events is higher for incident X-rays with energies of 1860 eV compared to 1830 eV, because of the shorter absorption length inside the SiO_2-layer of the pn-Window at 1860 eV compared to 1830 eV. The measured and simulated photo peak spectra are in good agreement. Energy resolutions determined from a Gaussian fit to the photo peak neglect to a big part the contribution of partial events, so that the effect of the CCE is almost not visible in the value of the FWHM.

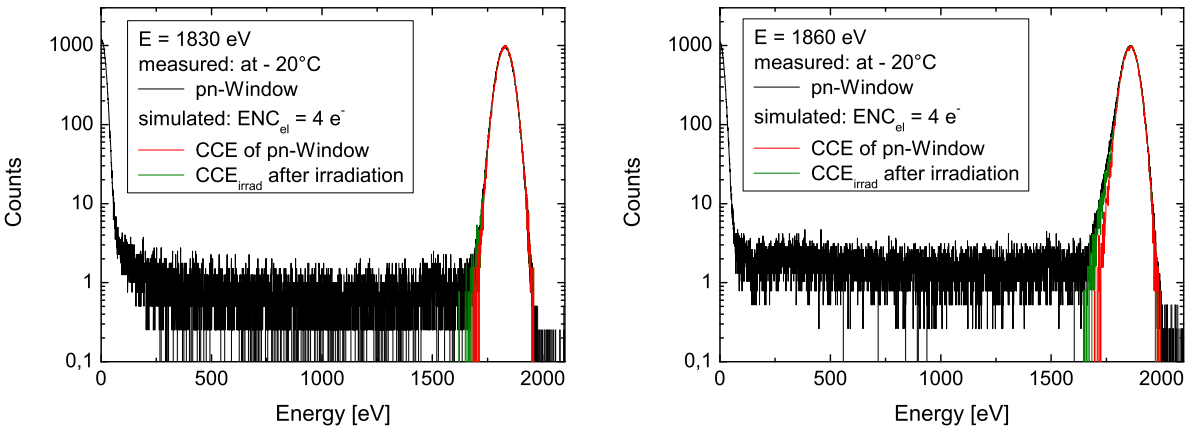

Figure D.5.: *Measured and calculated spectral response at 1830 and 1860 eV for a SDD with a pn-Window, including the contribution of the CCE, Fano and electronic noise.*

We can conclude that the presented analytical formula of the standard deviation of the energy resolution, including the CCE contribution besides the Fano and the electronic noise and the Monte Carlo simulations of the generated spectra reproduce the results from measurements accurately. Eq. D.9 includes the effect of the CCE for the first time in an analytical expression for the energy resolution of the SDD.

D.2. Direct detection of ultra violet and visible photons

The influence of quantum efficiency (QE) on the standard deviation of the number of the signal electrons, $\sigma(N_e)$, and the spectral response function is discussed in this chapter. The effect of the CCE on the spectral response of SDDs for incident X-rays has already been discussed in previous works [153, 154, 155] and a short overview has been given in App. D.1 (In addition to previous works we have derived formulas for the analytical calculation of the standard deviation of the number of signal electrons, $\sigma(N_e)$).

In the following, the number of scintillation photons, N_{ph}, is set to be constant in order to examine the effect of the QE only. The mean number of signal electrons, $\overline{N}_e$, detected at the anode is

$$\overline{N}_e = N_{ph} \cdot \overline{QE}. \tag{D.12}$$

The dependence of $\overline{QE}$ on the CCE is described in Eq. 5.10. A lower CCE decreases the mean quantum efficiency, $\overline{QE}$. This experiment corresponds to N_{ph} Bernoulli trials with $\overline{QE}$ the probability for one photon to be detected, so that the variance can be calculated as

$$Var(N_e) = (1 - \overline{QE}) \cdot \overline{QE} \cdot N_{ph}. \tag{D.13}$$

Including the variance of the electronic noise $\mathrm{Var}_{el} = \mathrm{ENC}_{el}^2$ yields

$$Var_{tot}(N_e) = Var(N_e) + Var_{el}. \tag{D.14}$$

The total standard deviation is then

$$\sigma_{tot}(N_e) = \sqrt{(1 - \overline{QE}) \cdot \overline{QE} \cdot N_{ph} + ENC_{el}^2}. \tag{D.15}$$

In Fig. D.6 the standard deviation, $\sigma_{tot}(N_e)$, is plotted against the number of incident photons for two quantum efficiencies and three electronic noise values. It is remarkable that the electronic noise contribution becomes more pronounced with decreasing number of incident photons.

The spectra resulting from incident light pulses, consisting of a constant number of photons, are determined by a binomial distribution with the parameters $\overline{QE}$ and N_{ph}. This can be simulated by Monte Carlo methods in the following way

$$N_e = \sum_{i=1}^{N_{ph}} P(\overline{QE})_i \tag{D.16}$$

with $P(\overline{QE})_i$ equal to 1 or 0 depending on whether the generation of a random number, r, in the interval [0,1] is $\mathrm{r} \leq \overline{QE}$ or $\mathrm{r} > \overline{QE}$. Fig. D.7 shows the dependence of the peak position and its standard deviation on the value of $\overline{QE}$. A decreasing $\overline{QE}$ value increases the distance of the peak from the value 2000, which is the number of incident photons per pulse and the value of the standard deviation $\sigma_{tot}(N_e)$. The CCE, which is part of the QE, does not generate a shoulder on the left side of the

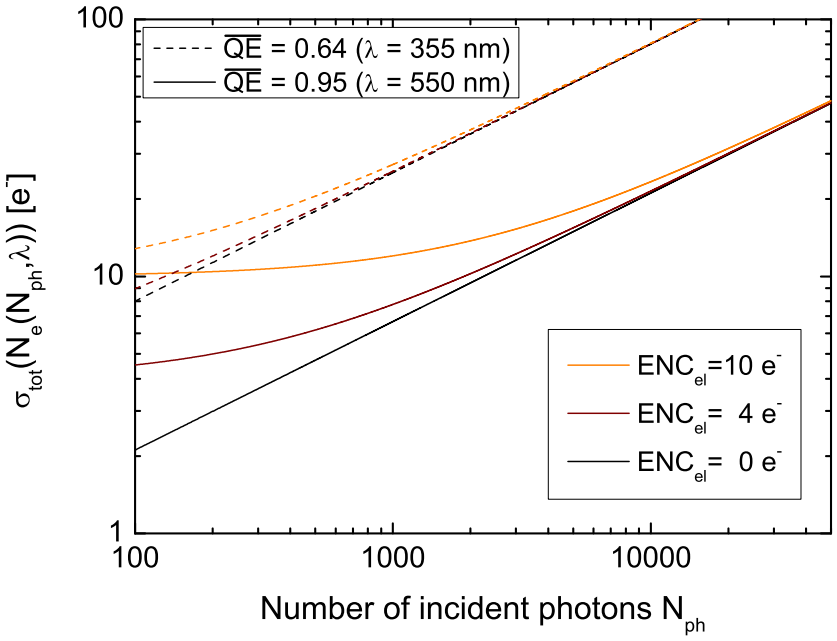

Figure D.6.: *Standard deviation for two $\overline{QE}$ values and three electronic noise values, ENC_{el}.*

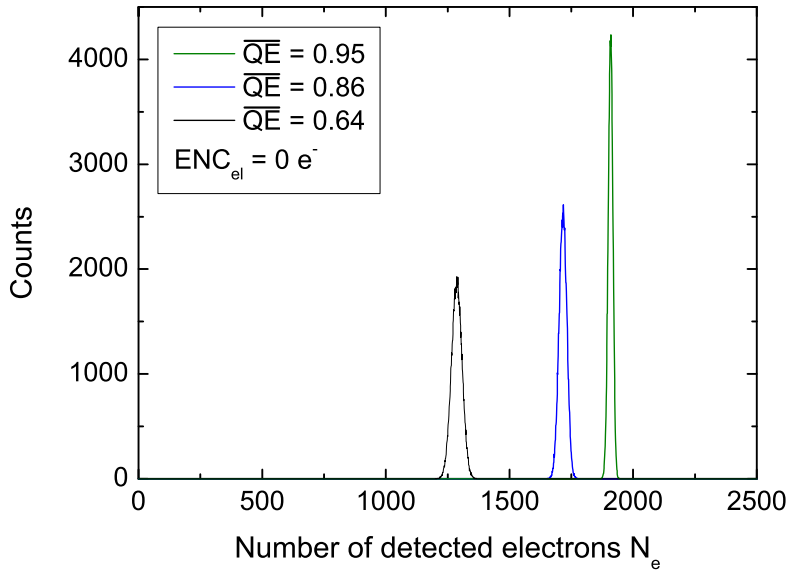

Figure D.7.: *Spectra after the absorption of incident light pulses with N_{ph} = 2000 per pulse and three different $\overline{QE}$ values. Each spectrum consists of 100000 detected pulses, simulated by a Monte Carlo algorithm.*

peak, as after the absorption of X-rays, but it has an impact on the peak position and its standard deviation.

If the pulse originates from scintillation generated after an interaction of γ-rays inside the scintillator, than the $\overline{QE}$ for scintillation photons varies from event to event. The $\overline{QE}$ varies, due to the fact, that the position, where the scintillation photons are generated inside the scintillator, varies frequently from event to event, so that the angular distribution of the incident scintillation photons onto the SDD varies too. Additionally the number of photons, N_{ph}, reaching the SDD surface is also varying, due to scintillator properties and scintillation photon collection inside the scintillator. In this case the relative variance of N_e has to be expressed by Eq. 4.7, where QE is one parameter of the system quantum efficiency, η.

E. Contribution of collimators to the spatial resolution

The spatial resolution determined by the collimator and detector assembly, which is also called geometrical resolution, is denoted by $\widetilde{R}_g$. In Fig. E.1 are the definitions of the geometrical resolutions, $\widetilde{R}_g$ and $\widetilde{R}'_g$, of two collimator types illustrated. The parallel hole collimator creates a one to one relation between the γ-ray object and its image inside the scintillator [156] and the pinhole collimator, produces a magnified or demagnified image of the γ-ray object inside the scintillator [157], depending on whether $b' < a'$ or $b' > a'$. a' is the distance of the scintillator to the pinhole and b' is the distance of the pinhole to the γ-ray source (Fig. E.1). A certain position, P, inside the scintillator can be reached by $\gamma-$rays emitted by an extended source inside a certain solid angle, which is defined by the collimator geometry and the detector assemply (Fig. E.1). The geometrical resolution, $\widetilde{R}_g$ (Fig. E.1), of a parallel hole

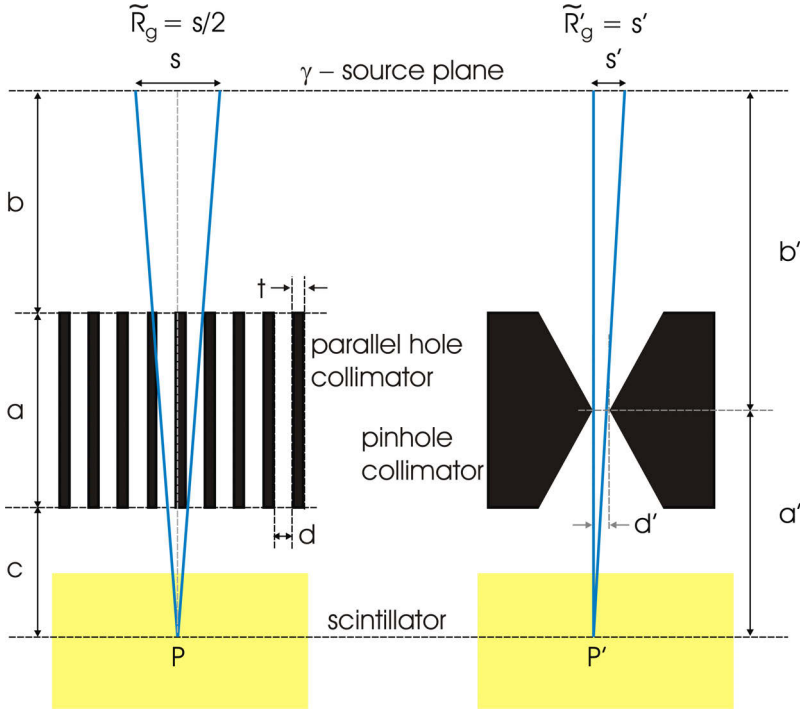

Figure E.1.: *Geometrical resolutions of parallel and pinhole collimators, $\widetilde{R}_g$ and $\widetilde{R}'_g$, of an extended γ-ray object in the source plane.*

collimator is defined by [156, 158]

$$\widetilde{R}_g = \frac{d}{a}(a+b+c) \tag{E.1}$$

where d is the hole width, a the effective hole length, c the scintillator collimator distance and b the distance of the collimator to the $\gamma-$ray source object. The geometrical resolution, $\widetilde{R}_g^{'}$, of a pinhole collimator is defined by [159]

$$\widetilde{R}_g^{'} = \frac{d^{'}}{a^{'}}(a^{'} + b^{'}). \tag{E.2}$$

where $d^{'}$ is the effective hole diameter, $a^{'}$ the scintillator pinhole distance and $b^{'}$ the distance of the pinhole to the $\gamma-$ray source object. Narrower holes, d, and smaller distances of the γ-source to the collimator, b, improve the geometrical object resolution.

The overall spatial resolution $\widetilde{R}$, also called object resolution, is generally defined by the FWHM of the intensity distribution, generated by a moving point source at a certain position, P, (Fig. E.1) inside the scintillator. It is a convolution of the spatial $\gamma-$ray flux distribution, due to the scintillator + collimator + source geometry and the spatial intrinsic intensity distribution of the reconstructed image, which is projected onto the source plane, due to fluctuations generated by the detector noise. If the spatial distributions are approximated by Gaussian distributions, their convolution is again a Gaussian distribution.

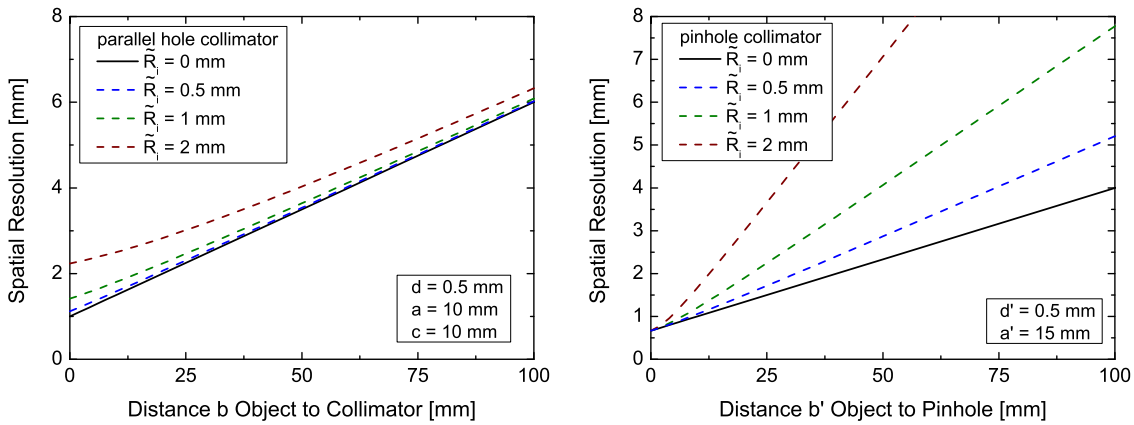

Figure E.2.: *Overall resolution of Anger cameras with parallel hole (left) and pinhole (right) collimator for four different intrinsic spatial resolutions $\widetilde{R}_i$ = 0, 0.5, 1, 2 mm.*

In the Gaussian approximation the object resolution of an Anger camera with a parallel hole collimator is given by [158]

$$\widetilde{R} = \sqrt{\widetilde{R}_i^2 + \widetilde{R}_g^2} \tag{E.3}$$

and for a pinhole collimator by [157]

$$\widetilde{R} = \sqrt{\left(\frac{b'}{a'}\widetilde{R}_i\right)^2 + \widetilde{R}_g^{'2}} \tag{E.4}$$

where $b^{'}/a^{'}$ is the magnification factor. The term $((b'/a')\widetilde{R}_i)^2$ can be neglected only for the case $a' >> b'$. Fig. E.2 shows the object resolution for an Anger camera with parallel (on the left) or pinhole (on the right) collimators calculated with the formulas E.3 and E.4 for three intrinsic spatial resolutions, $\widetilde{R}_i$, values. If a parallel hole collimator is used, the contribution of the intrinsic spatial resolution, $\widetilde{R}_i$, to the overall resolution is larger for small distances, b, of the object to the collimator. If a pinhole collimator is used the contribution of the intrinsic spatial resolution, $\widetilde{R}_i$, becomes larger for increasing distances, b', of the object to the pinhole.

Bibliography

[1] E. Rutherford, H. Geiger (Eds.), An Electrical Method of Counting the Number of α -Particles from Radio-Active Substances, Vol. 81 of Series A, Containing Papers of a Mathematical and Physical Character, Royal Society of London, The Royal Society, 1908.

[2] F. N. Flakus, Detecting and measuring ionizing radiation - a short history, IAEA Bulletin 23 (4) (1981) 31–36.

[3] S. M. Sze, K. K. Ng, Physics of Semiconductor Devices, 3rd Edition, John Wiley & Sons, 2001.

[4] S. Wang, Fundamentals of Semiconductor Theory and Device Physics, Prentice Hall, Englewood Cliffs, New Jersey, 1989.

[5] J. Butler, C. Lingren, F. Doty, $Cd_{1-x}Zn_xTe$ gamma ray detectors, Trans. Nucl. Sci. 39 (4) (1992) 605–609.

[6] T. Takahashi, S. Watanabe, Recent progress in CdTe and CdZnTe detectors, Trans. Nucl. Sci. 48 (4) (2001) 950–959.

[7] J. Baciak, Z. He, 1 cm thick HgI_2 gamma-ray spectrometers, in: Nucl. Sci. Symp. Conf. Rec., Vol. 5, 2003, pp. 3532–3536.

[8] E. Gatti, P. Rehak, J. T. Walton, Silicon drift chambers - First results and optimum processing of signals, Nucl. Instr. and Meth. 226 (1984) 129–141.

[9] D. Schlosser, P. Lechner, G. Lutz, A. Niculae, H. Soltau, L. Strüder, R. Eckhardt, K. Hermenau, G. Schaller, F. Schopper, O. Jaritschin, A. Liebel, A. Simsek, C. Fiorini, A. Longoni, Expanding the detection efficiency of silicon drift detectors, Nucl. Instr. and Meth. A: Accelerators, Spectrometers, Detectors and Associated Equipment 624 (2) (2010) 270–276.

[10] C. Fiorini, A. Longoni, F. Perotti, C. Labanti, P. Lechner, L. Strüder, Gamma ray spectroscopy with CsI(Tl) scintillator coupled to silicon drift chamber, Trans. Nucl. Sci. 44 (6) (1997) 2553–2560.

[11] C. Fiorini, A. Longoni, F. Perotti, C. Labanti, E. Rossi, P. Lechner, L. Strüder, First prototype of a gamma-camera based on a single CsI(Tl) scintillator coupled to a silicon drift detector array, Trans. Nucl. Sci. 47 (6) (2000) 1928–1932.

[12] M. Moszyński, C. Plettner, A. Nassalski, T. Szczęńiak, Ł. Świderski, A. Syntfeld-Każuch, W. Czarnacki, G. Pausch, J. Stein, A. Niculae, H. Soltau, A comparative study of silicon drift detectors with photomultipliers, avalanche

photodiodes and PIN photodiodes in gamma spectroscopy with $LaBr_3$ crystals, Trans. Nucl. Sci. 56 (3) (2009) 1006 – 1011.

[13] C. Fiorini, A. Longoni, F. Perotti, C. Labanti, E. Rossi, P. Lechner, H. Soltau, L. Strüder, A monolithic array of silicon drift detectors for high-resolution gamma-ray imaging, Trans. Nucl. Sci 49 (3) (2002) 995–1000.

[14] P. Lecoq, Inorganic Scintillators for Detector Systems, Springer-Verlag Berlin Heidelberg, 2006.

[15] W. Heitler, The Quantum Theory of Radiation, 3rd Edition, Oxford University Press, 1957.

[16] W. Leo, Techniques for Nuclear and Particle Physics Experiments, 2nd Edition, Springer-Verlag New York Berlin Heidelberg, 1994.

[17] F. Sauter, Über den atomaren Photoeffekt bei großer Härte der anregenden Strahlung, Ann. d. Phys. 401–248 (1931) 217.

[18] M. Stobbe, Zur Quantenmechanik photoelektrischer Prozesse, Ann. d. Phys. 399 (6) (1930) 661–715.

[19] H. A. Bethe, J. Ashkin, Experimental Nuclear Physics, Vol. 1, John Wiley & Sons, 1960.

[20] K. Debertin, R. G. Helmer, Gamma- and X-Ray Spectrometry with Semiconductor Detectors, North-Holland, 1988.

[21] B. L. Henke, E. M. Gullikson, J. C. Davis, X-ray interactions: Photoabsorption, scattering, transmission, and reflection at E = 50 - 30000 eV, Z = 1 - 92, Atomic Data and Nuclear Data Tables 54 (2) (1993) 181–342.

[22] J. H. Hubbell, S. M. Seltzer, Tables of X-ray mass attenuation coefficients and mass energy-absorption coefficients from 1 keV to 20 MeV for elements Z = 1 to 92 and 48 additional substances of dosimetric interest, National Institute of Standards and Technology (1996).

[23] Stopping power and range tables for electrons, National Institute of Standards and Technology, http://physics.nist.gov/PhysRefData/.

[24] D. C. Joy, S. Luo, An empirical stopping power relationship for low-energy electrons, Scanning 11 (4) (1989) 176–180.

[25] S. A. Payne, W. W. Moses, S. Sheets, L. Ahle, N. J. Cherepy, B. Sturm, S. Dazeley, G. Bizarri, W.-S. Choong, Nonproportionality of scintillator detectors: Theory and experiment. II, Trans. Nucl. Sci 58 (6) (2011) 3392 – 3402.

[26] L. Landau, On the energy loss of fast particles by ionization, J. Phys. U.S.S.R 8 (1944) 201–205.

[27] J. Moyal, Theory of ionization fluctuations, Philosophical Magazine Series 7 46 (374) (1955) 263–280.

[28] R. Devanathan, L. Corrales, F. Gao, W. Weber, Signal variance in gamma-ray detectors—A review, Nucl. Instr. and Meth. A 656 (2006) 637–649.

[29] R. C. Alig, S. Bloom, C. W. Struck, Scattering by ionization and phonon emission in semiconductors, Phys. Rev. B 22 (12) (1980) 5565–5582.

[30] R. C. Alig, Scattering by ionization and phonon emission in semiconductors. II. Monte Carlo calculations, Phys. Rev. B 27 (2) (1983) 968–977.

[31] F. Scholze, H. Rabus, G. Ulm, Mean energy required to produce an electron-hole pair in silicon for photons of energies between 50 and 1500 eV, J. Appl. Phys. 84 (5) (1998) 2926–2939.

[32] F. Scholze, H. Henneken, H. Kuschnerus, P. amd Rabus, M. Richter, G. Ulm, Determination of the electron-hole pair creation energy for semiconductors from spectral responsitivity of photodiodes, Nucl. Instr. and Meth. A 439 (2000) 208–215.

[33] M. J. Lipp, C. H. Yoo, D. Strachan, W. B. Daniels, Band-structure parameters and Fermi resonances of exciton-polaritons in CsI and CsBr under hydrostatic pressure, Phys. Rev. B 73 (2006) 1–8.

[34] M. E. McIlwain, D. Gao, N. Thompson, First principle quantum description of the energetics associated with $LaBr_3$, $LaCl_3$, and Ce doped scintillators, Nucl. Sci. Symp. Conf. Rec. N57-1 (2007) 2460–2465.

[35] S. Sasaki, H. Tawara, K. Saito, M. Miyajima, E. Shibamura, Average energies required per scintillation photon and energy resolutions in NaI(Tl) and CsI(Tl) crystals for gamma rays, Jpn. J. Appl. Phys. 45 (2006) 6420–6430.

[36] F. Gao, Y. Xie, S. Kerisit, L. Campbell, W. Weber, Yield, variance and spatial distribution of electron-hole pairs in CsI, Nucl. Instr. and Meth. A: Accelerators, Spectrometers, Detectors and Associated Equipment 652 (1) (2011) 564–567.

[37] U. Fano, On the theory of ionization yield of radiations in different substances, Phys. Rev. 70 (1-2) (1946) 44–52.

[38] U. Fano, Ionization yield of radiations. II. The fluctuations of the number of ions, Phys. Rev. 72 (1) (1947) 26–29.

[39] G. Alkhazov, A. Komar, A. Vorob'ev, Ionization fluctuations and resolution of ionization chambers and semiconductor detectors, Nucl. Instr. and Meth. 48 (1) (1967) 1–12.

[40] M. Balkanski, R. F. Wallis, Semiconductor Physics and Applications, Oxford University Press, 2000.

[41] P. Lautenschlager, M. Garriga, L. Vina, M. Cardona, Temperature dependence of the dielectric function and interband critical points in silicon, Phys. Rev. B 36 (1987) 4821.

[42] M. A. Green, M. J. Keevers, Optical properties of intrinsic silicon at 300 K, Prog. Photovolt.: Res. Appl. 3 (3) (1995) 189–192.

[43] M. Balkanski, A. Aziza, E. Amzallag, Infrared absorption in heavily doped n-type Si, Phys. Stat. Sol. 31 (1969) 323–330.

[44] G. E. Jellison, Jr., F. A. Modine, C. W. White, R. F. Wood, R. T. Young, Optical properties of heavily doped silicon between 1.5 and 4.1 eV, Phys. Rev. Lett. 46 (21) (1981) 1414–1417.

[45] P. E. Schmidt, Optical absorption in heavily doped silicon, Phys. Rev. B 23 (10) (1981) 5531–5536.

[46] R. Hartmann, K.-H. Stephan, L. Strüder, The quantum efficiency of pn-detectors from the near infrared to the soft X-ray region, Nucl. Instr. and Meth. A 439 (2000) 216–220.

[47] M. J. Weber, Inorganic scintillators: today and tomorrow, J. Lum. 100 (1-4) (2002) 35–45.

[48] P. A. Rodnyi, Physical Processes in Inorganic Scintillators, CRC Press, 1997.

[49] S. A. Payne, N. Cherepy, G. Hull, J. Valentine, W. W. Moses, W.-S. Choong, Nonproportionality of scintillator detectors: Theory and experiment, Trans. Nucl. Sci 56 (4) (2009) 2506 – 2512.

[50] J. Valentine, D. Wehe, G. Knoll, C. Moss, Temperature dependence of absolute CsI(Tl) scintillation yield, Nucl. Sci. Symp. and MIC Conf. Rec. 40 (4) (1991) 1267–1273.

[51] P. R. Menge, G. Gautier, A. Iltis, C. Rozsa, V. Solovyev, Performance of large lanthanum bromide scintillators, Nucl. Instr. and Meth. A: Accelerators, Spectrometers, Detectors and Associated Equipment 579 (1) (2007) 6–10.

[52] W. Setyawan, R. Gaume, R. Feigelson, S. Curtarolo, Comparative study of nonproportionality and electronic band structures features in scintillator materials, Trans. Nucl. Sci 56 (5) (2009) 2989–2996.

[53] R. T. Williams, J. Q. Grim, Q. Li, K. B. Ucer, W. W. Moses, Excitation density, diffusion-drift, and proportionality in scintillators, Phys. Stat. Sol. (b) 248 (2) (2011) 426–438.

[54] Q. Li, J. Q. Grim, R. T. Williams, G. A. Bizarri, W. W. Moses, A transport-based model of material trends in nonproportionality of scintillators, J. Appl. Phys. 109 (12) (2011) 1–17.

[55] P. Dorenbos, E. van Loef, A. Vink, E. van der Kolk, C. van Eijk, K. Krämer, H. Güdel, W. Higgins, K. Shah, Level location and spectroscopy of Ce^{3+}, Pr^{3+}, Er^{3+}, and Eu^{2+} in $LaBr_3$, J. Lum. 117 (2) (2006) 147–155.

[56] R. Bartram, L. Kappers, D. Hamilton, A. Lempicki, C. Brecher, V. Gaysinskiy, E. Ovechkina, V. Nagarkar, Afterglow suppression and non-radiative charge-transfer in CsI:Tl,Sm, Trans. Nucl. Sci. 55 (3) (2008) 1232 – 1236.

[57] Y. Zorenko, T. Voznyak, R. Turchak, A. Fedorov, K. Wiesniewski, M. Grinberg, Luminescent and scintillation properties of CsI:Tl films grown by the liquid phase epitaxy method, Phys. Stat. Sol. (a) 207 (10) (2010) 2344–2350.

[58] V. Nagirnyi, A. Stolovich, S. Zazubovich, V. Zepelin, E. Mihokova, E. Nikl, G. P. Pazzi, L. Salvini, Peculiarities of the triplet relaxed excited-state structure and luminescence of a CsI:Tl crystal, J. Phys.: Condens. Matter 7 (18) (1995) 3637–3653.

[59] J. D. Valentine, W. W. Moses, S. E. Derenzo, D. K. Wehe, G. F. Knoll, Temperature dependence of CsI(Tl) gamma-ray excited scintillation characteristics, Nucl. Instr. and Meth. A 325 (1993) 147–157.

[60] V. Nagirnyi, S. Zazubovich, V. Zepelin, M. Nikl, G. Pazzi, A new model for the visible emission of the CsI: Tl crystal, Chem. Phys. Lett. 227 (1994) 533–538.

[61] V. Babin, K. Kalder, A. Krasnikov, S. Zazubovich, Luminescence and defects creation under photoexcitation of CsI:Tl crystals in Tl+ -related absorption bands, J. Lum. 96 (1) (2002) 75–85.

[62] B. Henderson, G. F. Imbusch, Optical Spectroscopy of Inorganic Solids: Monographs on the Physics and Chemistry of Materials 44, Oxford University Press, 2010.

[63] E. V. D. van Loef, P. Dorenbos, C. W. E. van Eijk, K. W. Krämer, H. U. Güdel, Scintillation properties of $LaBr_3$:Ce^{3+} crystals: fast, efficient, and high-energy resolution scintillators, Trans. Nucl. Sci 486 (2002) 254–258.

[64] J. G. Sole, L. E. Bausa, D. Jaque (Eds.), An Introduction to the Optical Spectroscopy of Inorganic Solids, John Wiley & Sons, 2005.

[65] J. Andriessen, E. van der Kolk, P. Dorenbos, Lattice relaxation study of the 4f - 5d excitation of Ce^{3+}- doped $LaCl_3$, $LaBr_3$, and $NaLaF_4$: Stokes shift by pseudo Jahn-Teller effect, Phys. Rev. B 76 (7) (2007) 1–9.

[66] Richman, Isaac, Satten, A. Robert, Wong, Y. Eugene, Lattice vibrations of $LaCl_3$ and $LaBr_3$ from vibronic spectra, J. Chem. Phys. 39 (7) (1963) 1833–1846.

[67] B. Liu, M. Gu, Z. Qi, X. Liu, S. Huang, C. Ni, First-principles study of lattice dynamics and thermodynamic properties of $LaCl_3$ and $LaBr_3$, Phys. Rev. B 76 (6) (2007) 1–7.

[68] M. D. Birowosuto, P. Dorenbos, K. W. Kramer, H. U. Gudel, Ce^{3+} activated $LaBr_{3-x}I_x$: High-light-yield and fast-response mixed halide scintillators, J. Appl. Phys. 103 (10) (2008) 1–6.

[69] S.-G. Crystals, Scintillation material, www.crystals.saint-gobain.com.

[70] E. Gatti, P. Rehak, Semiconductor drift chamber - an application of a novel charge transport scheme, Nucl. Instr. and Meth. A 225 (1984) 524–532.

[71] A. Longoni, C. Fiorini, Handbook of Practical X - Ray Fluorescence Analysis, Springer Verlag Berlin/Heidelberg, 2006.

[72] G. Lutz, Semiconductor Radiation Detectors, Springer-Verlag Berlin Heidelberg New York, 1999.

[73] A. Niculae, P. Lechner, H. Soltau, G. Lutz, L. Strüder, C. Fiorini, A. Longoni, Optimized readout methods of silicon drift detectors for high-resolution X-ray spectroscopy, Nucl. Instr. and Meth. A 568 (2006) 336–342.

[74] P. Lechner, A. Pahlke, H. Soltau, Novel high-resolution silicon drift detectors, X-Ray Spectrometry 33 (2004) 256–261.

[75] P. Lechner, C. Fiorini, A. Longoni, G. Lutz, A. Pahlke, H. Soltau, L. Strüder, Silicon drift detectors for high resolution, high count rate X - ray spectroscopy at room temperature, International Centre for Diffraction Data 2004, Advances in X-ray Analysis 47 (2004) 53–58.

[76] E. D. Palik (Ed.), Handbook of Optical Constants of Solids, Academic Press, 1985.

[77] D. Blumenfeld, Operations Research Calculations, CRC Press, 2001.

[78] E. Breitenberger, Scintillation spectrometer statistics, Progress in Nucl. Phys 4 (1955) 56–94.

[79] H. Crystals, Personal correspondence (2012).

[80] C. Zerby, A. Meyer, R. Murray, Intrinsic line broadening in NaI(Tl) gamma-ray spectrometers, Nucl. Instr. and Meth. 12 (1961) 115–123.

[81] P. Iredale, The effect of the non-proportional response of NaI(Tl) crystals to electrons upon the resolution for $\gamma-$rays, Nuclear Instruments and Methods 11 (0) (1961) 340–346.

[82] J. Valentine, B. Rooney, J. Li, The light yield nonproportionality component of scintillator energy resolution, Trans. Nucl. Sci. 45 (3) (1998) 512–517.

[83] B. Rooney, J. Valentine, Benchmarking the compton coincidence technique for measuring electron response nonproportionality in inorganic scintillators, Trans. Nucl. Sci 43 (3) (1996) 1271–1276.

[84] J. B. Birks, Scintillations from organic crystals: Specific fluorescence and relative response to different radiations, Proc. Phys. Soc. A 64 (1951) 874–877.

[85] L. Onsager, Initial recombination of ions, Phys. Rev. 54 (8) (1938) 554–557.

[86] G. J. Hoffman, A. C. Albrecht, Near-threshold photoionization spectra in nonpolar liquids: A geminate pair based model, J. Phys. Chem. 95 (6) (1991) 2231–2241.

[87] Q. Li, J. Q. Grim, R. T. Williams, G. A. Bizarri, W. W. Moses, The role of hole mobility in scintillator proportionality, Nucl. Instr. and Meth. A 652 (2011) 288–291.

[88] S. E. Derenzo, J. K. Riles, Monte Carlo calculations of the optical coupling between Bismuth Germanate crystals and photomultiplier tubes, Trans. Nucl. Sci 29 (1) (1982) 191–195.

[89] C. Carrier, R. Lecomte, Effect of geometrical modifications and crystal defects on light collection in ideal rectangular parallelepipedic BGO scintillators, Nucl. Instr. and Meth. A294 (1990) 355–364.

[90] J. Bea, L. Gadea, A.and Garcia-Raffi, J. Rico, B. Rubio, T. J. L., Simulation of light collection in scintillators with rough surfaces, Nuclear Instruments and Methods in Physics Research A 350 (1994) 184–191.

[91] M. Janecek, W. W. Moses, Simulating scintillator light collection using measured optical reflectance, Trans. Nucl. Sci 57 (3) (2010) 964–970.

[92] M. Globus, B. Grinyov, Operation characteristics of ionizing radiation detectors based on inorganic and plastic scintillators for nuclear physics and medical instrumentation, Trans. Nucl. Sci 43 (3) (1996) 1287–1294.

[93] S. M. Sze, Semiconductor Devices Physics and Technology, 2nd Edition, John Wiley & Sons, 2002.

[94] P. Lechner, L. Strüder, Ionization statistics in silicon X - ray detectors - New experimental results, Nucl. Instr. and Meth. A 354 (1995) 464–474.

[95] F. Pedrotti, L. Pedrotti, W. Bausch, H. Schmidt, Optik für Ingenieure Grundlagen, Springer Verlag Heidelberg, 2002.

[96] H. Stöcker (Ed.), Taschenbuch der Physik, Vol. 3, Verlag Harri Deutsch, 1998.

[97] MF-Millipore filters, Tech. rep., Merck Millipore, http://www.millipore.com/catalogue/module/c152.

[98] Enhanced specular reflector (ESR), Tech. rep., 3M Optical Systems, http://www.3m.com/product/information/Vikuiti-Enhanced-Specular-Reflector.html.

[99] H. T. van Dam, S. Seifert, W. Drozdowski, P. Dorenbos, D. R. Schaart, Optical absorption length, scattering length, and refractive index of $LaBr_3$(Ce), Trans. Nucl. Sci. 59 (3) (2012) 656–664.

[100] N. Cherepy, S. Payne, S. Asztalos, G. Hull, J. Kuntz, T. Niedermayr, S. Pimputkar, J. Roberts, R. Sanner, T. Tillotson, E. van Loef, C. Wilson, K. Shah, U. Roy, R. Hawrami, A. Burger, L. Boatner, W.-S. Choong, W. Moses, Scintillators with potential to supersede Lanthanum Bromide, Trans. Nucl. Sci. 56 (2009) 873–880.

[101] E. V. D. van Loef, P. Dorenbos, C. W. E. van Eijk, K. Kramer, H. U. Gudel, High-energy-resolution scintillator: Ce^{3+} activated $LaBr_3$, Appl. Phys. Lett. 79 (10) (2001) 1573–1575.

[102] R. Gwin, R. B. Murray, Scintillation process in CsI(Tl). I. Comparison with activator saturation model, Phys. Rev. 131 (2) (1963) 501–508.

[103] P. Schotanus, R. Kamermans, Scintillation characteristics of pure and Tl-doped CsI crystals, Nucl. Sci. Trans. 37 (2) (1990) 177–182.

[104] L. Trefilova, T. Charkina, A. Kudin, N. Kosinov, L. Kovaleva, A. Mitichkin, Radiation defects creation in CsI(Tl) crystals and their luminescence properties, J. Lum. 102-103 (0) (2003) 543–550.

[105] A. Iltis, M. Mayhugh, P. Menge, C. Rozsa, O. Selles, V. Solovyev, Lanthanum halide scintillators: Properties and applications, Nuclear Instruments and Methods in Physics Research Section A: Accelerators, Spectrometers, Detectors and Associated Equipment 563 (2) (2006) 359–363.

[106] J. Glodo, W. W. Moses, W. M. Higgins, E. V. D. van Loef, P. Wong, S. E. Derenzo, M. J. Weber, K. S. Shah, Effects of Ce concentration on scintillation properties of $LaBr_3$:Ce, Trans. Nucl. Sci. 52 (5) (2005) 1805–1808.

[107] W. Drozdowski, P. Dorenbos, A. Bos, J. de Haas, S. Kraft, E. Maddox, A. Owens, F. Quarati, C. Dathy, V. Ouspenski, Effect of proton dose, crystal size, and cerium concentration on scintillation yield and energy resolution of $LaBr_3$:Ce, Trans. Nucl. Sci. 54 (3) (2007) 736–740.

[108] S. Agostinelli, J. Allison, K. Amako, J. Apostolakis, H. Araujo, P. Arce, M. Asai, D. Axen, S. Banerjee, G. Barrand, F. Behner, L. Bellagamba, J. Boudreau, L. Broglia, A. Brunengo, H. Burkhardt, S. Chauvie, J. Chuma, R. Chytracek, G. Cooperman, G. Cosmo, P. Degtyarenko, A. Dell'Acqua, G. Depaola, D. Dietrich, R. Enami, A. Feliciello, C. Ferguson, H. Fesefeldt, G. Folger, F. Foppiano, A. Forti, S. Garelli, S. Giani, R. Giannitrapani, D. Gibin, J. J. Gómez Cadenas, I. González, G. Gracia Abril, G. Greeniaus, W. Greiner, V. Grichine, A. Grossheim, S. Guatelli, P. Gumplinger, R. Hamatsu, K. Hashimoto, H. Hasui, A. Heikkinen, A. Howard, V. Ivanchenko, A. Johnson, F. W. Jones, J. Kallenbach, N. Kanaya, M. Kawabata, Y. Kawabata, M. Kawaguti, S. Kelner, P. Kent, A. Kimura, T. Kodama, R. Kokoulin, M. Kossov, H. Kurashige, E. Lamanna, T. Lampén, V. Lara, V. Lefebure, F. Lei, M. Liendl, W. Lockman, F. Longo, S. Magni, M. Maire, E. Medernach, K. Minamimoto, P. Mora de Freitas, Y. Morita, K. Murakami, M. Nagamatu, R. Nartallo, P. Nieminen, T. Nishimura, K. Ohtsubo, M. Okamura, S. O'Neale, Y. Oohata, K. Paech,

J. Perl, A. Pfeiffer, M. G. Pia, F. Ranjard, A. Rybin, S. Sadilov, E. Di Salvo, G. Santin, T. Sasaki, N. Savvas, Y. Sawada, S. Scherer, S. Sei, V. Sirotenko, D. Smith, N. Starkov, H. Stoecker, J. Sulkimo, M. Takahata, S. Tanaka, E. Tcherniaev, E. Safai Tehrani, M. Tropeano, P. Truscott, H. Uno, L. Urban, P. Urban, M. Verderi, A. Walkden, W. Wander, H. Weber, J. P. Wellisch, T. Wenaus, D. C. Williams, D. Wright, T. Yamada, H. Yoshida, D. Zschiesche, Geant4–a simulation toolkit, Nuclear Instruments and Methods in Physics Research Section A: Accelerators, Spectrometers, Detectors and Associated Equipment 506 (3) (2003) 250–303.

[109] B. D. Rooney, J. D. Valentine, Scintillator light yield nonproportionality: Calculating photon response using measured electron response, Trans. Nucl. Sci. 44 (3) (1997) 509–516.

[110] H. Tawara, S. Sasaki, K. Saito, E. Shibamura, A Monte-Carlo method for determining absolute scintillation-photon yields and energy resolution of scintillators for gamma rays, in: KEK Proceedings of the Second International Workshop on EGS, Tsukuba, Japan, 2000, pp. 152–160.

[111] B. Reutter, W. Moses, W.-S. Choong, G. Hull, S. Payne, N. Cherepy, J. Valentine, Experimental and Monte Carlo investigation of intrinsic limits of scintillator energy resolution, 2007, pp. 1447 – 1451.

[112] G. Bizarri, N. Cherepy, W. Choong, G. Hull, W. Moses, S. Payne, J. Singh, J. Valentine, A. Vasilev, R. Williams, Progress in studying scintillator proportionality: Phenomenological model, Trans. Nucl. Sci. 56 (4) (2009) 2313–2320.

[113] M. Moszyński, C. Plettner, A. Nassalski, T. Szczęśniak, Ł. Świderski, A. Syntfeld-Każuch, W. Czarnacki, G. Pausch, J. Stein, A. Niculae, H. Soltau, A comparative study of silicon drift detectors with photomultipliers, avalanche photodiodes and pin photodiodes in gamma spectrometry with labr$_3$ crystals, IEEE Trans. Nucl. Sci. 56 (3) (2009) 1006 – 1011.

[114] I. V. Khodyuk, P. Dorenbos, Nonproportional response of $LaBr_3$:Ce and $LaCl_3$:Ce scintillators to synchrotron x-ray irradiation, J. Phys.: Condens. Matter 22 (48) (2010) 1–7.

[115] S. Guatelli, A. Mantero, B. Mascialino, P. Nieminen, M. Pia, Geant4 atomic relaxation, Trans. Nucl. Sci. 54 (3) (2007) 585 – 593.

[116] J. B. Birks, The Theory and Practice of Scintillation Counting, Pergamon Press, Oxford, 1964.

[117] A. Jablonski, S. Tanuma, C. J. Powell, New universal expression for the electron stopping power for energies between 200 eV and 30 keV, Surf. Interface Anal. 38 (2) (2006) 76–83.

[118] W. Mengesha, T. Taulbee, B. D. Rooney, J. Valentine, Light yield nonproportionality of CsI(Tl), CsI(Na), and YAP, Trans. Nucl. Sci 45 (3) (1998) 456–461.

[119] I. N. Bronstein, K. A. Semendjajew, G. Musiol, H. Mühlig, Taschenbuch der Mathematik, Vol. 5, Verlag Harri Deutsch, 2001.

[120] I. V. Khodyuk, J. T. M. de Haas, P. Dorenbos, Nonproportional response between 0.1–100 keV energy by means of highly monochromatic synchrotron X-rays, Trans. Nucl. Sci. 57 (3) (2010) 1175–1181.

[121] M. O. Krause, Atomic radiative and radiationless yields for K and L shells, J. Phys. Chem. Ref. Data 8 (2) (1979) 307–327.

[122] D. W. Aitken, B. L. Beron, G. Yenicay, H. R. Zulliger, The fluorescent response of NaI(Tl), CsI(Tl), CsI(Na) and CaF_2(Eu) to X-rays and low energy gamma rays, Trans. Nucl. Sci. 14 (1) (1967) 468–477.

[123] A. Syntfeld-Każuch, Ł. Świderski, W. Czarnacki, M. Gierlik, W. Klamra, M. Moszyński, P. Schotanus, Non-proportionality and energy resolution of CsI(Tl), Trans. Nucl. Sci. 5 (2007) 1836–1841.

[124] Ł. Świderski, R. Marcinkowski, M. Szawlowski, M. Moszyński, W. Czarnacki, A. Syntfeld-Każuch, T. Szczęśniak, G. Pausch, C. Plettner, K. Roemer, Non-proportionality of electron response and energy resolution of Compton electrons in scintillators, Nucl. Sci. Symp. Conf. Rec. (2010) 285–290.

[125] G. Hull, W.-S. Choong, W. W. Moses, G. Bizarri, J. Valentine, S. Payne, N. Cherepy, B. W. Reutter, Measurements of NaI(Tl) electron response: Comparison of different samples, Trans. Nucl. Sci. 56 (1) (2009) 331–336.

[126] M. S. Alekhin, J. T. M. de Haas, I. V. Khodyuk, K. W. Krämer, P. R. Menge, V. Ouspenski, P. Dorenbos, Improvement of γ-ray energy resolution of $LaBr_3$(Ce) scintillation detectors by Sr^{2+} and Ca^{2+} co-doping, Appl. Phys. Lett. 102 (2013) 1–4.

[127] C. Fiorini, A. Longoni, F. Perotti, C. Labanti, E. Rossi, P. Lechner, L. Strüder, Detectors for high-resolution gamma-ray imaging based on a single CsI(Tl) scintillator coupled to an array of silicon drift detectors, Trans. Nucl. Sci 48 (3) (2001) 346–350.

[128] C. Fiorini, F. Perotti, Small prototype of Anger camera with submillimeter position resolution, Rev. Sci. Instrum. 76 (2005) 1–8.

[129] C. Fiorini, A. Gola, M. Zanchi, A. Longoni, H. Soltau, L. Strüder, Silicon drift photodetectors for scintillation readout in medical imaging, Nucl. Instr. and Meth. A 571 (2007) 126–129.

[130] C. Fiorini, A. Gola, R. Peloso, A. Longoni, P. Lechner, H. Soltau, L. Strüder, Imaging performances of the DRAGO gamma camera, Nucl. Instr. and Meth. A 604 (2009) 101–103.

[131] C. Fiorini, P. Busca, R. Peloso, A. Abba, A. Geraci, C. Bianchi, G. L. Poli, G. Virotta, K. Erlandsson, B. F. Hutton, P. Lechner, H. Soltau, L. Struder, A. Pedretti, P. Van Mullekom, L. Ottobrini, G. Lucignani, The HICAM gamma camera, Trans. Nucl. Sci 59 (3) (2012) 537–544.

[132] Photonic devices, Tech. rep., Hamamatsu (2014).

[133] New: SrI_2:Eu scintillation crystals available, Tech. rep., Hellma Materials GmbH, http://www.hellma-materials.com/text/989/en/ausblenden/hellma-materials-scintillation-crystals.html.

[134] A. Gola, C. Fiorini, M. Porro, M. Zanchi, The readout electronics and the DAQ system of the DRAGO anger camera, Nucl. Sci. Symp. Conf. Rec. 270 (2006) 1334–1337.

[135] B. Riccardo, La gamma camera Drago: Caratterizzazione sperimentale, Master's thesis, Politecnico Di Milano Facolta' Di Ingegneria Dell'informazione (2008).

[136] N. Kimmel, Analysis of the charge collection process in solid state X-ray detectors, Ph.D. thesis, Universität Siegen (2008).

[137] S. Send, Utilization of a frame store pnCCD for energy-dispersive Laue diffraction with white synchrotron radiation, Ph.D. thesis, Naturwissenschaftlich-Technische Fakultät der Universität Siegen (2013).

[138] P. V. C. Hough, Low energy pair production, Phys. Rev. 73 (1947) 266–267.

[139] P. Y. Yu, M. Cardona, Fundamentals of Semiconductors Physics and Materials Properties, 3rd Edition, Springer-Verlag Berlin Heidelberg New York, 2003.

[140] L. V. Hove, The occurrence of singularities in the elastic frequency distribution of a crystal, Phys. Rev. 89 (6) (1953) 1189–1193.

[141] G. G. Macfarlane, V. Roberts, Infrared absorption of silicon near the lattice edge, Phys. Rev. 98 (1955) 1865–1866.

[142] J. I. Pankove, Optical absorption of Arsenic-doped degenerate Germanium, Phys. Rev. 126 (3) (1962) 956–962.

[143] C. Haas, Infrared absorption in heavily doped n-type Germanium, Phys. Rev. 125 (6) (1962) 1965–1971.

[144] M. Auslender, S. Hava, Free carrier contribution to dynamic dielectric function of heavily doped semiconductors, Phys. Stat. Sol. (b) 174 (1992) 565–574.

[145] D. Curie, G. F. J. Garlick, Luminescence in Crystals, Methuen and Co Ltd, 1963.

[146] J. Valentine, V. Jordanov, D. Wehe, G. Knoll, Charge calibration of CsI(Tl)/photodiode spectroscopy systems, Nucl. Instr. and Meth. A: Accelerators, Spectrometers, Detectors and Associated Equipment 314 (1) (1992) 119–124.

[147] P.-S. d. Laplace, Oeuvres complètes de Laplace, Vol. 7, Gauthier-Villars (Paris), 1886.

[148] T. Jorgensen, Jr., On probability generating functions, Am. J. Phys. 16 (5) (1948) 285–289.

[149] N. T. J. Bailey, The Elements of Stochastic Processes with Applications to the Natural Sciences, Wiley & Sons, 1990.

[150] F. Seitz, D. W. Mueller, On the statistics of luminescent counter systems, Phys. Rev. 78 (5) (1950) 605–612.

[151] A. W. Drake, McGraw-Hill Series in Probability and Statistics: Fundamentals of Applied Probability Theory, Mc-Graw-Hill Book Company, 1967.

[152] Z. Knittl, Optics of Thin Films, John Wiley & Sons, Inc., 1976.

[153] P. Lechner, Zur Ionisationsstatistik in Silizium, Ph.D. thesis, Fakultät für Physik der Technischen Universität München (1998).

[154] M. W. F. Popp, Untersuchung und analytische Modellierung der Systemantwort von pn-CCD Detektoren, Ph.D. thesis, Fakultät für Physik der Ludwig-Maximilians-Universität München (2000).

[155] T. Eggert, Die spektrale Antwort von Silizium-Röntgendetektoren, Ph.D. thesis, Fakultät für Physik der Technischen Universität München (2004).

[156] H. O. Anger, Scintillation camera with multichannel collimators, J. Nucl. Med. 5 (7) (1964) 515–531.

[157] G. J. Hine (Ed.), Instrumentation in Nuclear Medicine, Vol. 1, Academic Press, 1967.

[158] J. A. Sorenson, M. E. Phelps (Eds.), Physics in Nuclear Medicine, W. B. Saunders Company, 1987.

[159] J. R. Mallard, M. J. Myers, The performance of a gamma camera for the visualization of radioactive isotopes in vivo, Phys. Med. and Biol. 8 (2) (1963) 165–182.

Acknowledgments

Finally I would like to thank all my colleagues and all the people, who supported my work for this thesis:

- First I would like to express my gratitude to my advisor Prof. Dr. Lothar Strueder for his guidance and support over the last years and Prof. Dr. Ullrich Pietsch for the chance to work in one of his projects and for being my second advisor for this thesis.
- I would like to thank Dr. Heike Soltau for her patience, her interest in my work and the many fruitful discussions.
- I am grateful to Dr. Adrian Niculae, who supported me with his knowledge concerning the working principle of the SDD and front end electronics many times. He had always an open door to listen to my questions.
- I am thankful to Dr. Gerhard Lutz for the detailed discussions about processes inside the SDD.
- I give thanks to Robert Hartmann for his help concerning the entrance window of the detector and the working principle of the pnCCD.
- I am very thankful to Peter Holl for his advice, where to get a high calculation power for simulations.
- Many thanks to all my colleagues, who supported me and my work with their knowledge and encouragements.
- I would like to thank Dr. Florian Schopper and Dr. Georg Weidenspointer for the discussions about the entrance window and Geant4 simulations.
- I am grateful to my parents and my brother for their constant support and encouragement.
- I am grateful to my parents, who made it possible for me to study, and my brother for his mental assistance and proofreading. I could always count on their support and encouragement.
- I would like to thank my wife Teresa for her patience, support and love. She gave me the strength to finish this work successfully.

Eidesstattliche Erklärung

Ich erkläre hiermit, dass ich die vorliegende Arbeit ohne unzulässige Hilfe Dritter und ohne Benutzung anderer, nicht angegebener Hilfsmittel angefertigt habe. Die aus anderen Quellen direkt oder indirekt übernommenen Daten und Konzepte sind unter Angabe der Quelle gekennzeichnet. Die Arbeit wurde bisher weder im In- noch im Ausland in gleicher oder ähnlicher Form einer anderen Prüfungsbehörde vorgelegt. Es wurden keine Dienste eines Promotionsvermittlers oder einer ähnlichen Organisation in Anspruch genommen.